CYCLICALLY LOADED FOUNDATIONS AND PIPELINES IN COHESIVE SOILS

A Dissertation

by

HUSHAM ATALLA MOHAMMED AL-JANABI

Submitted to the Office of Graduate and Professional Studies of
Texas A&M University
in partial fulfillment of the requirements for the degree of

DOCTOR OF PHILOSOPHY

Chair of Committee,	Charles Aubeny
Committee Members,	Robert Lytton
	Marcelo Sanchez
	Jerome Schubert
Head of Department,	Robin Autenrieth

August 2020

Major Subject: Civil Engineering

ABSTRACT

This research addresses three thrust areas associated with cyclically loaded foundations and pipelines in cohesive soils. The first is thixotropy and sensitivity of Gulf of Mexico (GoM) clay. The second thrust area investigates the cumulative displacements due to nonuniform cyclic amplitudes using finite element method. The third studies seabed-riser interaction at the Touchdown Zone (TDZ) of pipelines/risers subjected to vertical, lateral, and zig-zag monotonic and cyclic loading.

The first thrust area measures the remolded strength and the thixotropic strength recovery in GoM clay. To fill the existing gap in long-term measurements of thixotropic strength recovery in this clay, two techniques are used: the full-flow penetrometer (T-bar) and the miniature vane shear test.

The second thrust area presents two parts 1) experimental results and 2) finite element (FE) investigations. The experimental tests investigate the degradation of vertical and lateral resistance and calibrate a constitutive model. The FEA investigates the cumulative deformations for different aspect ratios (*L/D* = 4, 5, and 6) of caissons subjected to inclined cyclic loading and different load angles.

The third thrust area provides data for developing a model for 1) vertical cyclic loading tests of risers-soil interaction at TDZ, 2) lateral cyclic loading tests of pipelines/riser-soil interaction at TDZ and/or at seabed, and 3) zig-zag cyclic loading tests of pipelines/riser-soil interaction at TDZ and/or at seabed. The vertical cyclic loading tests

evaluate the effects of cyclic loading, loading rate, load amplitude, riser embedment depth, and consolidation on the vertical stiffness of the soil supporting the riser in the TDZ.

The lateral and zigzag cyclic loading tests of pipelines/risers evaluate the fundamental mechanism of the pipeline/riser-soil interaction in the lateral direction subjected to monotonic and cyclic loading, the evolution of lateral resistance with different (small to large) displacement amplitudes, the degradation of lateral resistance, and the recovery of the soil strength with time.

DEDICATION

All the praises and thanks be to Almighty Allah!

I am thankful to my parents, my brothers, and my sisters for everything!

Relatives and friends, thank you!

ACKNOWLEDGEMENTS

It has been truly a privilege working under the supervision of Professor Charles Aubeny. Thank you for your patience, guidance and mentoring. Thank you for all the motivation that kept me learning through my Doctor of Philosophy degree.

Thanks to Dr. Marcelo Sanchez, Dr. Robert Lytton, Dr. Jerome Schubert, and Dr. Jinbo Chen for contributing as committee members.

I would like to thank the staff at the Zachry Department of Civil Engineering at Texas A&M University. Thank you to the Texas A&M High Performance Research Computing facility for providing resources needed to perform numerical simulations.

I would like to extend a big thank you to my mother, my father, my siblings, and my relatives for supporting me throughout my life. Thanks to my friends, fellow classmates, and coworkers at Texas A&M University.

CONTRIBUTORS AND FUNDING SOURCES

Contributors

This work was supervised by committee members as fellows:

- Professor Charles P. Aubeny, P.E., Professor, Zachry Department of Civil Engineering, Texas A&M University, College Station, Texas, USA [Chair]
- Professor Robert Lytton, Professor, Zachry Department of Civil Engineering, Texas A&M University, College Station, Texas, USA [Member]
- Professor Marcelo Sanchez Castilla, Associate Professor, Zachry Department of Civil Engineering, Texas A&M University, College Station, Texas, USA [Member]
- Professor Jerome Schubert, Associate Professor, Petroleum Engineering, Texas A&M University, College Station, Texas, USA [Member]
- Dr. Jinbo Chen, Geotechnical Engineer, Shell Global Solution Inc., Houston, Texas, USA [Special member]

All the work for this dissertation was completed by the student independently.

Funding Sources

Graduate studies were supported through a Scholarship for Doctoral Studies sponsored by The Higher Committee for Education Development (HCED) in Iraq. Additional support has been provided by Shell Global Solutions (US) Inc. and Shell International Exploration and Production. Parts of this work were made possible by the National Science Foundation under Grant Number CMMI-1463431.

TABLE OF CONTENTS

Page

ABSTRACT ii

DEDICATION...iv

ACKNOWLEDGEMENTS v

CONTRIBUTORS AND FUNDING SOURCES vi

TABLE OF CONTENTS vii

LIST OF FIGURES xii

LIST OF TABLES...xix

1. INTRODUCTION 1

1.1. Thixotropy and Sensitivity 2
1.2. Pile Foundations...4
1.3. Suction Caissons 6
1.4. Offshore Risers 9
1.5. Steel Catenary Riser Behavior...9
1.6. Riser Installation 11
1.7. Trench Formation Process 12
1.8. Cyclic Loading..13
1.9. Objectives 14
  1.9.1. Thixotropy and sensitivity 14
  1.9.2. Cyclically loaded piles/caissons in cohesive soils 15
  1.9.3. Risers and pipelines 15
1.10. Dissertation Outline...18
1.11. Nomenclature...19
1.12. References...21

2. EXPERIMENTAL FACILITY 26

2.1. Introduction..26
2.2. Model Setup..26
  2.2.1. Steel Loading Frame..26
  2.2.2. Robotic System (Smart Motors)...27

2.2.3. Steel Basin....28
2.2.4. Force Transducers....29
2.2.5. Laser Displacement Sensor....29
2.2.6. Tilt Transducer....30
2.2.7. Torque Sensor....31
2.2.8. Miniature Vane Shear Test Apparatus (MVT)....31
2.2.9. Vane Blade....32
2.2.10. Full-Flow (T-bar) Penetrometer Model,....33
2.2.11. Piles/ Caisson Models....34
2.2.12. Riser Models....35
2.2.13. Aluminum Basins....36
2.2.14. Smart Motor Interface (SMI)....37
2.2.15. Data Acquisition (DAQ), National Instruments (NI)....38
2.2.16. LabVIEW Software....39
2.3. Nomenclature....40
2.4. References....40

3. SOIL PREPARATION....42

3.1. Introduction....42
3.2. Model Soil Properties Used in This Research....42
3.3. Soil Index Properties....43
3.4. Test Program (Undrained Shear Strength)....44
3.5. Undrained Shear Strength....45
3.5.1. Undrained Shear Strength, Monotonic T-bar Penetrometer....45
3.5.2. Undrained Shear Strength, Miniature Vane Shear Test (MVT)....48
3.6. Nomenclature....53
3.7. References....54

4. EXPERIMENTAL MEASUREMENT OF THIXOTROPY AND SENSITIVITY IN GULF OF MEXICO CLAY....56

4.1. Introduction....56
4.2. Background....59
4.3. Research Objective and Scope....60
4.4. Test Program....61
4.5. Full-Flow Penetrometer, T-bar Penetrometer....63
4.5.1. Full-Flow Penetrometer Penetration Resistance....63
4.6. Undrained Shear Strength of The Soil....65
4.6.1. Undrained Shear Strength Using Full-Flow Penetrometer....66
4.7. Cyclic Full-Flow Penetrometer....66
4.7.1. Undrained Shear Strength Using Miniature Vane Shear Tests....69
4.8. Remolded Undrained Shear Strength....77
4.8.1. Remolded Undrained Shear Strength Using T-Bar Tests....77

4.8.2. Remolded Undrained Shear Strength Using MVTs 78
4.9. Penetration Resistance Degradation..80
4.10. Sensitivity And Acquired Sensitivity..81
4.10.1. Acquired Sensitivity Using MVTs 82
4.10.2. Acquired Sensitivity Using Full-Flow Penetrometer 82
4.11. The Percentage Of Thixotropy Strength Regain..84
4.12. Nomenclature...86
4.13. References..88

5. EXPERIMENTAL AND NUMERICAL INVESTIGATION OF THE PERFORMANCE OF PILES AND SUCTION CAISSONS SUBJECTED TO INCLINED CYCLIC LOADING IN COHESIVE SOILS 92

5.1. Introduction...92
5.2. Background...95
5.2.1. Suction Caissons Analysis 95
5.2.2. P-Y Curves for Flexible Piles in Clay 99
5.3. Finite Element Analysis 101
5.3.1. Mesh and Boundary Conditions..101
5.3.2. Constitutive Model 102
5.3.3. Model Validation (Comparison to Existing Monotonic Solutions) 106
5.4. Experimental Program..107
5.4.1. Caisson Models 107
5.4.2. Test Program 108
5.4.3. Test Bed Strength Profile...110
5.5. Experimental Measurements of Uplift Loading 111
5.5.1. Pullout Resistance 111
5.5.2. Cyclic Amplitudes of 0.2% *D* 115
5.5.3. Cyclic Amplitude of 0.45% *D*..116
5.5.4. Cyclic Amplitudes of 0.95% and 2% *D*..117
5.6. Results for Lateral Load Tests...119
5.6.1. Lateral Monotonic Resistance...119
5.6.2. Lateral Cyclic Loading Test, Tilt ~ 0.5° and 1.5° 120
5.7. Calibrate the Constitutive Model Using the Experimental Results 124
5.8. Numerical Analysis Methodology 125
5.9. Comparisons to Previous Measurements...128
5.10. Parametric Study 129
5.10.1. Effect of Soil Properties and Adhesion Factor....................................131
5.10.2. Effect of Variable Load Amplitudes..132
5.10.3. Effect of Aspect Ratio, L/D = 4, 5, & 6..138
5.10.4. Effect of Load Inclination for Different Aspect Ratios 144
5.11. Nomenclature...148
5.12. References..150

6. EXPERIMENTAL MEASUREMENT OF TOUCHDOWN ZONE STIFFNESS FOR SCR IN GULF OF MEXICO CLAY..157

- 6.1. Introduction..157
- 6.2. Background...161
  - 6.2.1. Load-Deflection (P-y) Curves...161
- 6.3. Objectives...163
- 6.4. Test Program...164
- 6.5. Test Equipment..167
- 6.6. Model Seabed Properties...167
- 6.7. Undrained Shear Strength of the Soil...167
  - 6.7.1. Penetration Resistance of T- bar Penetrometer.....................................168
- 6.8. Buoyancy Effect...170
- 6.9. Rate Effect Results and the Comparison With Existing Results...................173
  - 6.9.1. Monotonic Tests...173
  - 6.9.2. Cyclic Tests..176
- 6.10. Erosion (Scour)...177
- 6.11. Stiffness Degradation Under Cyclic Loading..178
  - 6.11.1. Large Cyclic Amplitude (2-way 5% *D*)..178
  - 6.11.2. Shallow Penetration Depth, *h/D*= 0.25 to 1.0.......................................178
  - 6.11.3. Deep penetration, *h/D*= 2.0 *D*...179
  - 6.11.4. Small Cyclic Amplitude (2-way 2% *D*)..182
- 6.12. Pause period..184
  - 6.12.1. Large Cyclic Amplitude (2-way 5% *D*), Test 11a -11j...........................184
- 6.13. Reconsolidation Effects During Test 11a to Test 11j...................................186
  - 6.13.1. Small Cyclic Amplitude (2% *D*), *h/D*=0.5...188
  - 6.13.2. Reconsolidation Effects During Test 12a to test 12d..............................189
- 6.14. Recommendations..190
- 6.15. Nomenclature..190
- 6.16. References..192

7. EXPERIMENTAL MEASUREMENT OF MONOTONIC AND CYCLIC LATERAL RESISTANCE OF RISERS AND PIPELINES IN GULF OF MEXICO CLAYS..197

- 7.1. Introduction..197
- 7.2. The Properties of Soil..202
- 7.3. Test Equipment..202
- 7.4. Test Program...202
- 7.5. Undrained Shear Strength of the Soil...207
- 7.6. Mechanism Response of The Lateral Resistance..209
- 7.7. Pipe Trajectory and Vertical Penetration...211
- 7.8. Results and Data Interpretation..213

7.8.1. Series 1: Vertical Monotonic Loading Tests With Different Penetration Rates and The Comparison With Existing Results 213
7.8.2. Series 2: Backbone Curve Resistance (*U/D* ~ 3.0) at Different Embedment Depths, *W/D* of 0.5 and 1.0 215
7.8.3. Simulate the Riser Initial Vertical Penetration (and Then Apply Very Small Lateral Cyclic Amplitudes)..220
7.8.4. Monotonic Tests (Backbone Curve) With a Small Deformation, u/D ~ 0.3, for w/D = 0.5 and 1.0...220
7.8.5. Small Cyclic Amplitude $\Delta u/D$ of 0.15 *D* at *w/D* = 0.5 and 1.0..............222
7.9. Rest Period and Strength Recovery...225
7.9.1. Monotonic Tests (Backbone Curve) Large Deformation, u/D ~ 1.0 for w/D = 0.5 and 1.0 and Pause Period Effect 226
7.9.2. Large Cyclic Amplitude, $\Delta u_{cyc}/D$ ~ 0.5, w/D = 0.5 and 1.0....................228
7.10. Trench Formation 231
7.11. The Following Observations Can Be Made for the Entire Test Program: ...232
7.12. Nomenclature 233
7.13. References...235

8. CYCLIC LOADING OF PIPELINES/RISERS IN COHESIVE SOILS 239

8.1. Introduction...239
8.2. The Properties of The Seabed Model 242
8.3. Test Equipment 242
8.4. Test Program...242
8.5. Results and Data Interpretation..251
8.5.1. Series 1 and Series 2: Zig-zag Loading Tests 251
8.5.2. Series 2: Zig-zag Loading 258
8.6. Nomenclature...264
8.7. References 264

9. CONCLUSION...268

9.1. Experimental Measurement of Thixotropy and Sensitivity in Gulf of Mexico Clay 268
9.2. Experimental and Numerical Investigation of The Performance of Piles and Suction Caissons Subjected To Inclined Cyclic Loading in Cohesive Soils..270
9.3. Experimental Measurement of Touchdown Zone Stiffness for SCR in Gulf of Mexico Clay 273
9.4. Experimental Measurement of Monotonic and Cyclic Lateral Resistance of Risers and Pipelines in Gulf of Mexico Clays...275
9.5. Cyclic Loading of Pipelines/Risers in Cohesive Soils 276

LIST OF FIGURES

Page

Figure 1.1 Full and partial thixotropy. 3

Figure 1.2 Measured thixotropy strength ration vs. time. 4

Figure 1.3 Driven Piles, courtesy of Dr. James D. Murff. 5

Figure 1.4 Jack-up platform, courtesy of Dr. Aubeny. 5

Figure 1.5 Suction caisson (reprinted from Colliat et al. 2011). 6

Figure 1.6 Suction caisson installation. 7

Figure 1.7 Effect of padeye depth on suction anchor response. 9

Figure 1.8 A typical SCR. 10

Figure 1.9 Moving platform. 11

Figure 1.10 J-lay Method. 11

Figure 1.11 S-lay Method. 12

Figure 1.12 Sketch of Allegheny gas export SCR trench and b- Multiple pictures of Allegheny trench, seven months after installation (reprinted from Bridge & Howells, 2007). 13

Figure 2.1 Steel loading frame. 27

Figure 2.2 Robotic system (Smart Motors). 28

Figure 2.3 Steel basin. 28

Figure 2.4 Vertical force transducers. 29

Figure 2.5 Lateral force transducer. 29

Figure 2.6 Laser displacement sensor. 30

Figure 2.7 Tilt Transducer. 30

Figure 2.8 Torque transducer. 32

Figure 2.9 Small vane blade. 33

Figure 2.10 Big vane blade...33

Figure 2.11 Full-flow penetrometer, T-bar penetrometer model...............................34

Figure 2.12 A sketch of the T-bar penetrometer model. 34

Figure 2.13 Suction caisson models. 35

Figure 2.14 Riser Model. 36

Figure 2.15 A sketch of riser model with other fabrications. 36

Figure 2.16 Aluminum basins and mixing tools...37

Figure 2.17 Smart Motor Interface (SMI) software..38

Figure 2.18 DAQ system...38

Figure 2.19 LabVIEW software. 39

Figure 3.1 Plastic drums..44

Figure 3.2 A photograph shows the dense state of the clay. 44

Figure 3.3 T-bar model connected to the robotic system. 46

Figure 3.4 A sketch of the T-bar model. 46

Figure 3.5 Some selected T-bar tests. 47

Figure 3.6 Some selected T-bar tests. 47

Figure 3.7 Some selected T-bar tests. 47

Figure 3.8 Miniature vane shear test apparatus. 49

Figure 3.9 Undrained shear strength s_u vs. water content w_c%. 49

Figure 3.10 Different miniature vane shear test at w_c% = 80.4. 50

Figure 3.11 Miniature vane shear test at w_c % = 73.4. 51

Figure 3.12 Miniature vane shear test at w_c% = 77.4. 51

Figure 3.13 Miniature vane shear test at w_c% = 77. 51

Figure 3.14 Miniature vane shear test at w_c% = 81. 52

Figure 3.15 Miniature vane shear test at w_c% = 76. 52

Figure 3.16 Miniature vane shear test at w_c% = 73.9. 52

Figure 3.17 Miniature vane shear test at w_c% = 75. 53

Figure 3.18 Miniature vane shear test at w_c% = 74.8. 53

Figure 4.1 Measured thixotropy strength ration vs. time. 57

Figure 4.2 Thixotropy strength ratio vs. plasticity (reprinted from Andersen & Jostad, 2002). 58

Figure 4.3 Net and measured penetration resistance. 65

Figure 4.4 Directly after mixing. 67

Figure 4.5 Two days after mixing the soil. 67

Figure 4.6 Four days after mixing the soil. 68

Figure 4.7 Six days after mixing the soil. 68

Figure 4.8 Eight days after mixing the soil. 68

Figure 4.9 Ten days after mixing the soil. 68

Figure 4.10 22 days after mixing the soil. 69

Figure 4.11 31 days after mixing the soil. 69

Figure 4.12 114 days after mixing the soil. 69

Figure 4.13 Vane shear tests MVTs (1 hour after mixing). 71

Figure 4.14 Vane shear tests MVTs (3 hours after mixing). 72

Figure 4.15 Vane shear tests MVTs (1 day after mixing). 72

Figure 4.16 Vane shear tests MVTs (2 days after mixing). 73

Figure 4.17 Vane shear tests MVTs (4 days after mixing). 73

Figure 4.18 Vane shear tests MVTs (6 days after mixing). 74

Figure 4.19 Vane shear tests MVTs (8 days after mixing). 74

Figure 4.20 Vane shear tests MVTs (10 days after mixing). 75

Figure 4.21 Vane shear tests MVTs (20 days after mixing). 75

Figure 4.22 Vane shear tests MVTs (30 days after mixing). 76

Figure 4.23 Vane shear tests MVTs (112 days after mixing). 76

Figure 4.24 Normalized penetration resistance vs. the number of cycles..................79

Figure 4.25 Comparison of Acquired sensitivity for different studies vs. time. 84

Figure 4.26 Percentage thixotropy regain vs. time. 85

Figure 5.1 Effect of padeye depth on suction anchor response.................................94

Figure 5.2 Non-uniform load amplitude history...94

Figure 5.3 A sketch of a suction caisson with compression axial force. 96

Figure 5.4 A sketch of a suction caisson with tension force.....................................98

Figure 5.5 Failure Mechanisms of Suction Caissons: (a) three-dimensional failure...99

Figure 5.6 Finite element mesh. 102

Figure 5.7 Hardening model (reprinted from Simulia, 2014). 104

Figure 5.8 Force and strain controlled loading (reprinted from Simulia, 2014). 105

Figure 5.9 Comparisons between FEA and previous studies..................................107

Figure 5.10 Suction caisson models. 108

Figure 5.11 Undrained shear strength profiles selected from T-bar tests................111

Figure 5.12 Normalized pullout resistance vs. time. 113

Figure 5.13 photographs with vented and sealed caissons......................................114

Figure 5.14 Vertical cyclic test with cyclic amplitude ~ 0.002 *D*...........................115

Figure 5.15 Vertical cyclic test with cyclic amplitude ~ 0.0045 *D*.........................116

Figure 5.16 Vertical cyclic test with cyclic amplitude ~ 0.0095 *D*.........................118

Figure 5.17 Vertical cyclic test with cyclic amplitude ~ 0.02 *D*. 119

Figure 5.18 Lateral monotonic resistance with previous studies. 120

Figure 5.19 Lateral cyclic test with a tilt of ~ 0.5°. 121

Figure 5.20 Lateral cyclic test with a tilt of ~1.5°. 122

Figure 5.21 Lateral cyclic test with a tilt of ~1.5°. 123

Figure 5.22 Comparison between the experimental results and FE results. 126

Figure 5.23 Lateral load vs. time (experimental and numerical results). 126

Figure 5.24 Vertical load vs. time (experimental and numerical results). 127

Figure 5.25 Experimental and numerical results. 129

Figure 5.26 Cumulative lateral displacement for $L/D = 5$ and $\psi = 20°$. 133

Figure 5.27 Cumulative lateral displacement for $L/D = 5$ and $\psi = 45°$. 134

Figure 5.28 Cumulative lateral displacement for $L/D = 5$ and $\psi = 60°$. 135

Figure 5.29 Cumulative lateral displacement for $L/D = 5$ and $\psi = 75°$. 136

Figure 5.30 Cumulative vertical and resultant displacement for $L/D = 5$ and $\psi = 20°$. 137

Figure 5.31 Cumulative displacements for different aspect ratios. 140

Figure 5.32 Cumulative displacements for different aspect ratios. 141

Figure 5.33 Effect of load inclination on tilt. 145

Figure 5.34 Effect of load inclination on cumulative displacement for different aspect ratios. 146

Figure 6.1 Steel catenary risers in the touchdown zone. 160

Figure 6.2 Typical *P-y* Behavior. 161

Figure 6.3 Measured vs. corrected penetration resistance. 169

Figure 6.4 Some of the T-bars test results. 169

Figure 6.5 Undrained shear strength s_u vs. water content w%. 170

Figure 6.6 Some sketches illustrate the steps of penetrating and cycling the riser. ..172

Figure 6.7 Some photos show the heave and the formed trenches..........................173

Figure 6.8 Different loading rates for monotonic loading tests...............................175

Figure 6.9 Comparison with previous studies for monotonic tests. 175

Figure 6.10 Cyclic tests with different loading rates. 177

Figure 6.11 Cloudy water wave (scour)..177

Figure 6.12 Cyclic tests with different penetration depths, h/D..............................180

Figure 6.13 Soil resistance degradation while increasing the number of cycles for different penetration depths. 182

Figure 6.14 Soil resistance, P/D vs. normalized displacement for $h/D = 0.5$. 183

Figure 6.15 soil resistance, P/D vs. No. of cycles. 183

Figure 6.16 Test 11-a: normalized secant stiffness vs. Normalized cyclic displacement (unloading stage). 186

Figure 6.17 Normalized stiffness during pause periods...187

Figure 6.18 Soil Resistance vs. number of cycles. 188

Figure 6.19 Test 12: Soil resistance vs. number of cycles. 190

Figure 7.1 Steel Catenary Riser (SCR). 200

Figure 7.2 A sketch and Multiple pictures of Allegheny trench, seven months after instillation (reprinted from Bridge & Howells, 2007). 201

Figure 7.3 General sketches show the test program for $w/D = 0.5$ with nomenclature. 206

Figure 7.4 Undrained shear strength profiles from different tests............................208

Figure 7.5 Typical lateral response of pipelines..210

Figure 7.6 Effect of pipe weight..212

Figure 7.7 Vertical monotonic tests...214

Figure 7.8 Lateral resistance vs. normalized displacement. 218

Figure 7.9 Photographs are taken during testing. 219

Figure 7.10 Normalized lateral resistance vs. normalized lateral displacement for u/D ~ 0.3 and w/D = 0.5 and 1.0. 221

Figure 7.11 Normalized lateral resistance vs. normalized lateral displacement. 223

Figure 7.12 Lateral resistace vs. number of cycles for $\Delta u_{cyc}/D$ ~ 0.15 and w/D = 0.5 and 1. 224

Figure 7.13 Pipe settlement with time. 226

Figure 7.14 Normalized lateral resistance vs. normalized lateral displacement. 227

Figure 7.15 Normalized lateral resistance vs. normalized lateral displacement. 230

Figure 7.16 Lateral resistance vs. number of cycles for u/D ~1 and w/D = 0.5 and 1. 231

Figure 8.1 H-u Behavior of Steel Catenary Riser (SCR). 242

Figure 8.2 General sketch shows series 1 and series 2 with nomenclature. 246

Figure 8.3 Photographs are taken during testing. 249

Figure 8.4 Backbone curve and hysteresis cycles (zig-zag loading). 254

Figure 8.5 Backbone curve and hysteresis cycles (zig-zag loading). 255

Figure 8.6 Backbone curve and hysteresis cycles (zig-zag loading). 257

Figure 8.7 Pipe trajectory (series 2). 257

Figure 8.8 Backbone curve and hysteresis cycles (zig-zag loading). 259

Figure 8.9 Backbone curve and hysteresis cycles (zig-zag loading). 260

Figure 8.10 Backbone curve and hysteresis cycles (zig-zag loading). 262

Figure 8.11 Lateral resistance vs. number of cycles Test 1f and Test 2f. 262

Figure 8.12 Pipe trajectory (series 2-3). 263

LIST OF TABLES

Page

Table 3.1 The index properties of the soil. 43

Table 3.2 Summary of the test program. 45

Table 3.3 Undrained shear strength profiles using T-bar tests. 48

Table 4.1 Summary of the second thrust area test program. 61

Table 5.1 Caisson models. 108

Table 5.2 Series 1: Installation at different penetration rate effects. 109

Table 5.3 Series 2: Summary of the vertical cyclic loading tests. 109

Table 5.4 Series 3: Summary of the lateral monotonic and cyclic tests. 110

Table 5.5 Series 4: Pullout tests. 110

Table 5.6 Ultimate and allowable load cases. 130

Table 6.1 Series 1: Monotonic Penetration at Different Loading Rates. 164

Table 6.2 Series 2: Cyclic Testing with No Rest Periods. 165

Table 6.3 Series 3: Large Amplitude Cyclic Loading with Rest Periods. 166

Table 6.4 Series 4: Small Amplitude Loading with Rest Periods. 166

Table 6.5 Undrained Shear Strength Using (T-bars Test). 170

Table 7.1: The index properties of the soil. 202

Table 7.2 Series 1: Vertical Monotonic Penetration at Different Loading Rates. 203

Table 7.3 Series 2: Summary of Pure Monotonic Tests. 204

Table 7.4 Series 3 and Series 4: Summary of Monotonic and Cyclic Tests. 204

Table 7.5 Undrained Shear Strength Using (T-bars Tests). 208

Table 8.1 Series 1 and Series 2: Summary of Zig-Zag Loading Tests. 244

1. INTRODUCTION

This research addresses three thrust areas associated with cyclically loaded foundations and pipelines in cohesive soils:

The first thrust area addresses cyclically loaded caissons. Traditionally, the design of caissons is based on ultimate load capacity, with relatively little attention given to accumulated displacements under cyclic loading. This phase of the research involves single-gravity laboratory models tests of caissons subjected to both horizontal and vertical cyclic loading, supported by finite element studies using a bounding surface plasticity model capable of predicting permanent cyclic displacements.

The second thrust studies seabed-riser interaction at the Touchdown Zone (TDZ) of a Steel Catenary Riser (SCR) subjected to vertical monotonic and cyclic loading. Fatigue life of risers and pipelines is sensitive to seabed stiffness; therefore, this component of the research aims to improve the reliability and accuracy of existing vertical and horizontal seabed models. The primary research tool in this effort is a single-gravity laboratory model testbed capable of simulating horizontal vertical pipeline motions.

A critical mechanism influencing both studies discussed above is remolding and strength recovery of cohesive soils. Remolding effects are described in terms of soil sensitivity. Following remolding, two processes affect strength recovery: thisxotropy and reconsolidation. Thixotropy in particular is an area requiring additional understanding and date. The third component of this research, therefore, investigates sensitivity and thixotopic properties of Gulf of Mexico (GoM) clay.

1.1. Thixotropy and Sensitivity

Processes such as pile penetration and cyclic loading can cause a loss of soil strength, some of which is recovered through re-consolidation and thixotropic strength gain. As defined by Mitchell (1960), thixotropy is an isothermal, reversible, time-dependent process where a material stiffens while at rest, then softens or liquefies upon remolding. Thixotropy refers to time-dependent strength gain in soil at constant water content after remolding. This process is in contrast to the strength gain in soil associated with consolidation, which occurs under conditions of changing water content. There are multiple factors affecting the strength of the soil (e.g. Plasticity index (I_p), Sensitivity of the soil (S_t), Activity of the soil (A_c), etc.). Figure 1.1a-b depicts shear strength versus time. Figure 1.1a shows purely thixotropy material, where the original strength will ultimately be recovered. Figure 1.1b illustrates partially thixotropy, where the original strength will never be regained again.

Figure 1.2 shows some examples of a measured thixotropy strength ratio with different plasticity indexes and different types of soils which are kaolin, Bentonite, and Gulf of Mexico clay. The thixotropy strength ratio can be defined as the ratio of the gain in undrained shear strength with time (s_{u_t}) to remolded undrained shear strength (s_{ur}). It shows how the gain in strength differs depending on the soil properties. Thixotropy is considered as a significant factor for offshore geotechnical design (e.g. subsea structure, anchoring systems, piles, etc.). According to Terzaghi (1944), sensitivity of the clay can be defined as the ratio between the undisturbed strength $s_{u(undisturbed)}$ and remolded strength (s_{ur}). It is not an easy number to predict, especially after remolding the soil and waiting for the curing period to occur. Furthermore, it can be estimated differently depending on the used equipment and the used methods of calculations.

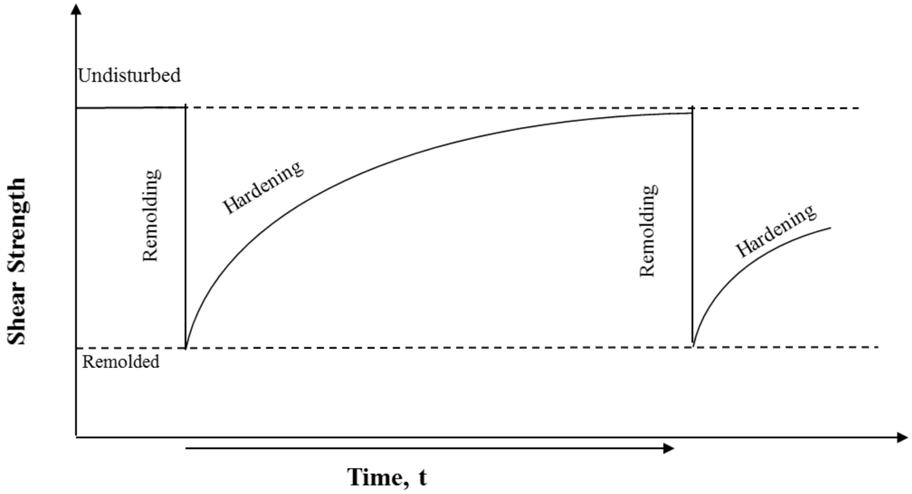

a) Full thixotropy material.

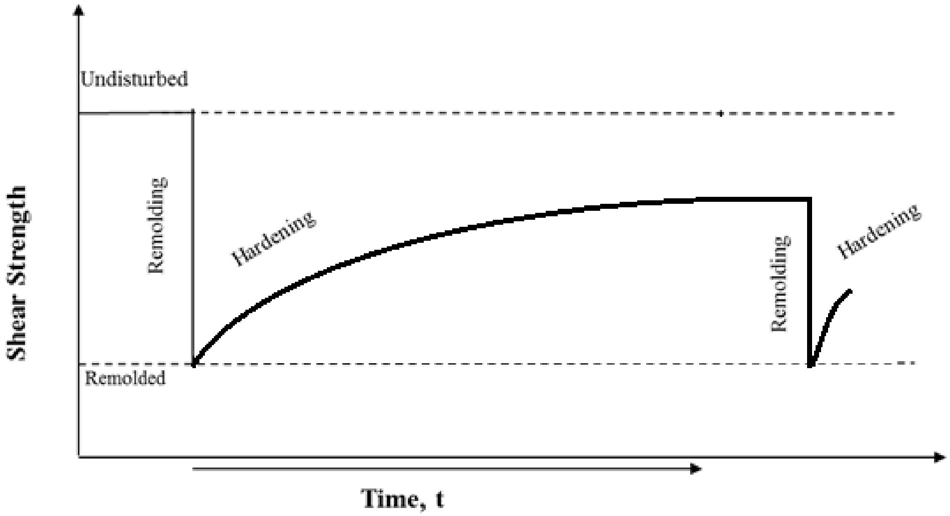

b) Partially thixotropic material.

Figure 1.1 Full and partial thixotropy.

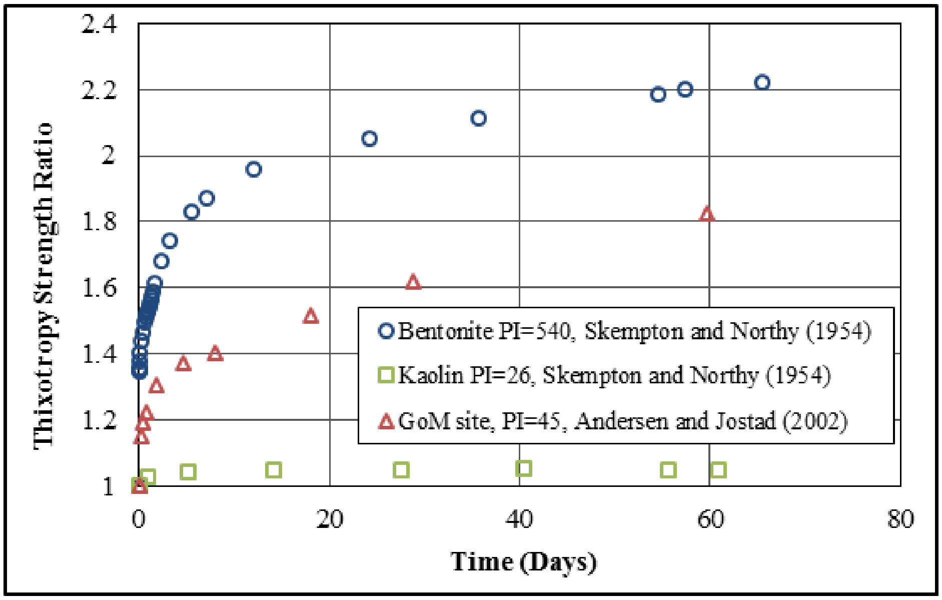

Figure 1.2 Measured thixotropy strength ration vs. time.

1.2. Pile Foundations

Pile foundations are considered the most commonly used types of foundations in onshore and offshore applications. There are two types of piles, which are 1) driven piles and 2) grouted piles. The typical aspect ratios of driven piles (L/D) ranges from 20 to 70 According to Schneider and Senders, (2010) and diameter to wall thickness (D/t_w) ranges from 25 to 100. Since the offshore structures are large and massive, they require a large number of piles. Figure 1.3 shows a photograph for driven piles. The driven piles require auxiliary platforms such as jack-up rigs in order to be installed as shown in Figure 1.4.

On the other hand, the most common foundations for offshore wind turbines are monopiles. The monopiles have large diameters ranging from 3 to 5 m with aspect ratios of 4 to 20. When the soil conditions include calcareous or rock sediments, the grouted piles are used as an alternative to driven piles. The difference between the procedure of offshore and onshore grouted piles is that onshore grouted piles use a reinforcement cage, and offshore grouted piles use a steel pipe.

Figure 1.3 Driven Piles, courtesy of Dr. James D. Murff.

Figure 1.4 Jack-up platform, courtesy of Dr. Aubeny.

1.3. Suction Caissons

The oil-gas industry has developed and used suction caissons (Figure 1.5) as alternatives to drag anchors (Colliat et al. 1997). Some advantages of suction caissons as an alternative to drag anchors are (1) relative ease of installation and (2) reliable predictions of the vertical and lateral capacity compared to other anchor types such as drag anchors, and (3) precise vertical and horizontal positioning.

Suction caissons are installed partially by self-weight penetration and then penetrated to full installation depth accomplished by the application of "suction". The suction is actually a differential pressure induced by pumping through a valve in the top

Figure 1.5 Suction caisson (reprinted from Colliat et al. 2011).

cap (Aubeny, 2017) (Figure 1.6). One of the advantages of using suction caissons over piles is that they do not require auxiliary platforms such as jack-up rigs (Figure 1.4) to support the installation operation with heavy underwater hammers (Aubeny, 2017). The aspect ratio (length to diameter, *L/D*) of suction caissons typically range from 1.5-3 for stiff clay, less than 1.5 for dense sands, and greater than 5 for soft clays.

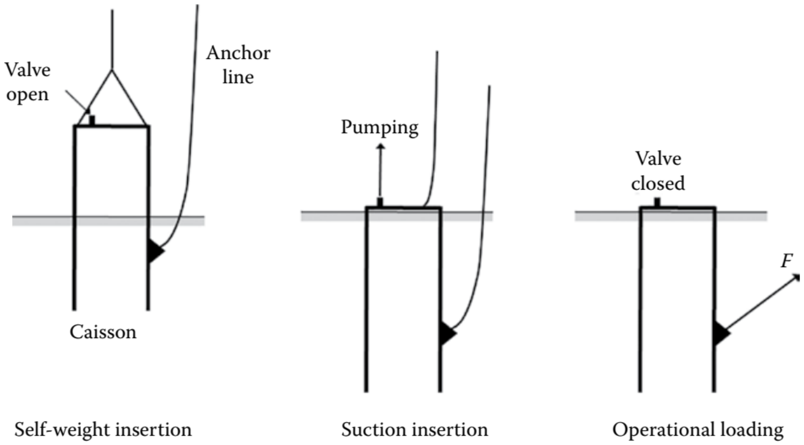

Figure 1.6 Suction caisson installation.

Some studies using scale model tests to predict the capacity of suction caissons have been performed (Clukey and Morrison, 1995; Fuglsang & Steensen-Bach, 1991). Other numerical analyses and upper bound plastic limit analysis methods are used to evaluate the suction caisson capacity (Aubeny & Murff, 2003; Sparrevik, 2002). A quasi-monotonic analysis is typically employed for suction caissons. In existing design methodologies, the caisson must resist a peak cyclic load when assessing the effect of cyclic loading on quantifying the reduction in shear strength. For predicting displacements, Winkler springs can be employed using *p-y* curves for lateral loads and *Q-z* and *t-z* for axial loads (API 2003; DNV 2014). Since the cumulative deformations significantly depend on the number of cycles and load amplitudes (Li et al. 2015), the cumulative deformation should be accounted in the design methodologies.

This study involves two methodologies: 1) experimental and 2) finite element analyses. For the experimental study, laboratory model tests are used to impose displacement-controlled cyclic loading. The soil degradation with increasing numbers of load cycles is measured for both vertical and lateral cyclic loading. This study investigated suction caissons with spect ratios of L/D = 2, 4, 5, and 6 and load inclination angles ψ = 20°, 45°, 60°, and 75°. Suction anchors in moderate water depths can be used for catenary moorings with loading angles generally around 25° or less to provide primarily horizontal loading of the suction anchor (Randolph, 2012). In some cases, the loading angles can be varied depending on the location of the suction pile from the structure. Furthermore, suction piles in soft soils with a large length to diameter ratio can provide relevant solutions for conductor installation (Sparrevik, 2002). The aspect ratios of the suction piles and the load inclination are investigated in this study.

When possible, a padeye is attached at about two-thirds of the caisson length, which approximates the optimal load location for maximizing load capacity when the soil strength increases approximately linearly with depth. The load attachment for the anchoring chain is generally between 50 to 70% of the total suction caisson embedment, in order to maximize the lateral resistance and to give a pure translation of the caisson rather than rotation (Randolph et al. 1998; Randolph, 2012) (Figure 1.7). Storms in offshore anchor and foundation applications are comprised of non-uniform load amplitudes (Anderson, 2015).

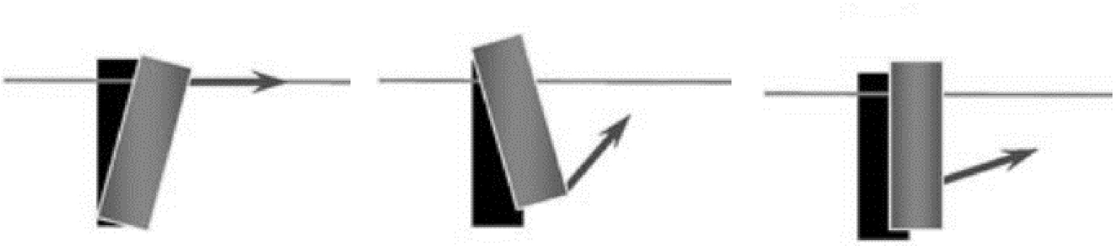

Figure 1.7 Effect of padeye depth on suction anchor response.

1.4. Offshore Risers

Risers are conduits for conveying hydrocarbon materials (oil or gas) from seabed to floating production platform. Steel catenary risers (SCRs) have been one of attractive options at offshore industry after first use in 1994 by Shell on the Auger tension leg platform moored in 872 m off water (Mekha, 2001). The Diameter of the riser typically ranges from 8-12 inches and the operation pressure about 13790-34474 kPa (2000-5000 psi) (Howells, 1995).

1.5. Steel Catenary Riser Behavior

Steel Catenary Risers (SCRs) are long steel pipes that hang freely between the seabed and floating production facilities. The basic concept of the riser system is to connect between a floating production vessel and pipelines on the bottom by way of a flex joint. Because of the weight of entire riser length, the tension forces at the top connection are high. The steel catenary riser is linked to a receptacle on the floating platform and hangs at a prescribed angle to keep a stable catenary shape. It extends down in a curve shape to the touchdown point (TDP). The pipe will be buried in a trench at the TDP. Figure 1.8 shows an SCR and how it can be divided into three sections, Catenary zone, Buried zone, and Surface zone (Bridge et al., 2003). At the surface zone, the riser lays on the surface where it is effectively a static pipeline.

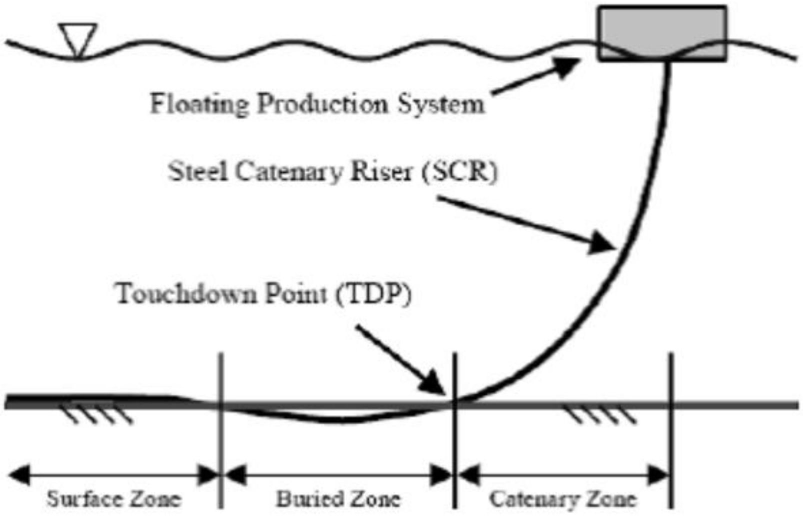

Figure 1.8 A typical SCR.

Some factors due to the harsh environments in deepwater such as wind, current, and slow-drift wave motions cause large wave-induced motions on the platform and large vessel offsets. These factors lead to some design challenges of the application of SCRs.Platforms or vessels move back and forth and/or up and down by wave motions as shown in Figure 1.9. Most movements of the platforms and vessels are lateral. It is important to note that the TDP changes location along the SCR due to the platform movements. Therefore, the TDZ is more applicable to describe this location.

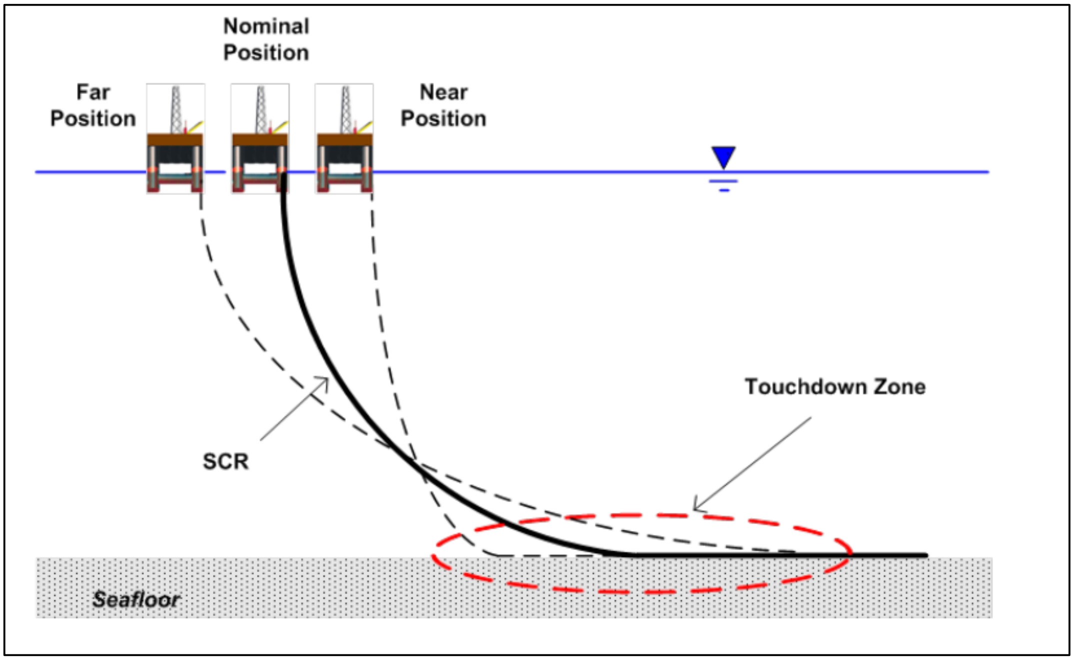

Figure 1.9 Moving platform.

1.6. Riser Installation

Riser installation is a critical process because it can directly affect the fatigue life of SCRs if any damages happened. There are different types of steel catenary riser installation. For example J-lay, S-lay, reel, and hybrid. J-lay (Figure 1.10 and Figure 1.11).

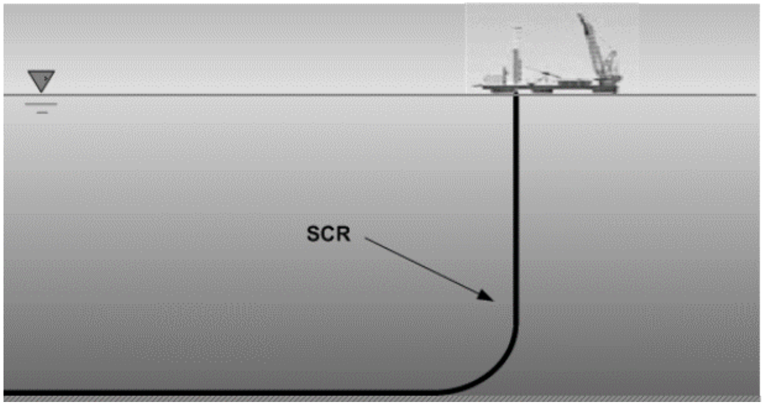

Figure 1.10 J-lay Method.

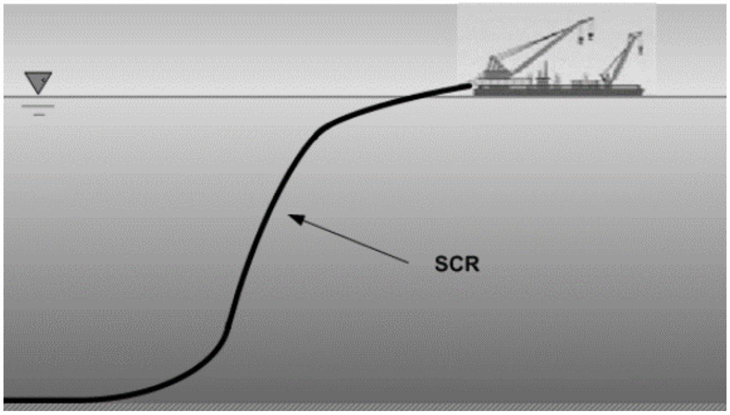

Figure 1.11 S-lay Method.

1.7. Trench Formation Process

During the operating conditions of SCRs, the trenches will be formed in the spot where the pipe touches the seabed TDZ, which is known as the dynamic motion. The SCR can be swept into several diameters in the horizontal and the vertical directions that will lead to forming the trenches with different diameters (Bridge & Howells, 2007). The SCR can be decided into three regions: catenary zone, buried zone, and surface zone Figure 1.8. The hanging part of the riser is the catenary zone. The buried zone is where the riser buries in a trench at the seabed. The last part is the surface zone, which statically rests on the seafloor. Figure 1.12 shows the trench formation seven months after the riser installation (Bridge & Howells, 2007).

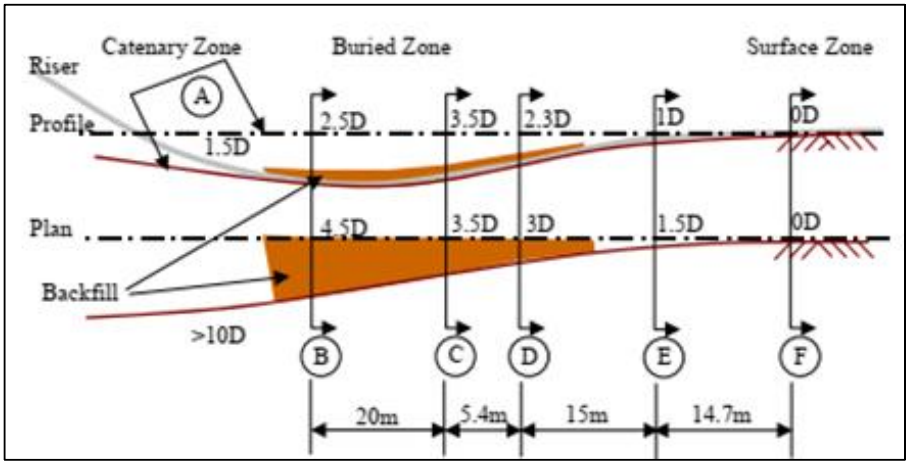

a) A sketch of Allegheny gas export SCR trench.

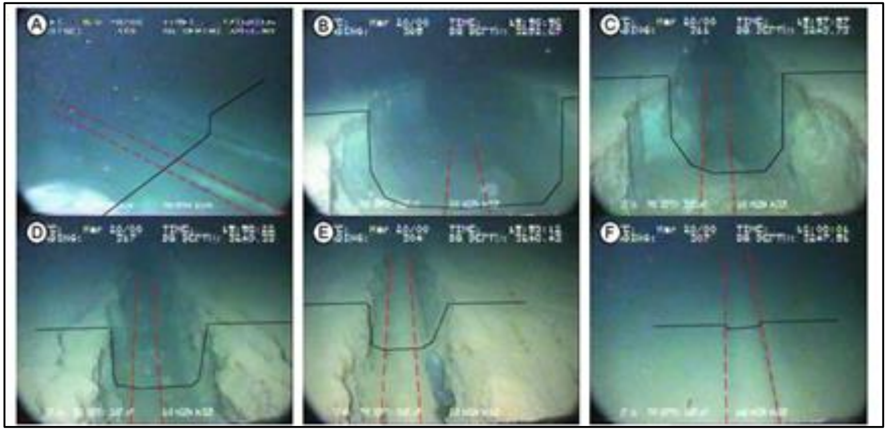

b) Multiple pictures of Allegheny trench, seven months after installation.

Figure 1.12 Sketch of Allegheny gas export SCR trench and b- Multiple pictures of Allegheny trench, seven months after installation (reprinted from Bridge & Howells, 2007).

1.8. Cyclic Loading

Offshore structures (e.g. foundations and risers) are subjected to cyclic loads from winds, waves, currents, and tides. A typical loading period (similar to wave loading) ranges from 7 to 16 seconds. All tests, including the T-bar, are conducted with a dimensionless velocity vD/c_v exceeding 100s, where v is the pipe/T-bar velocity and c_v is the coefficient of consolidation. The loading rates satisfy the criterion of Chatterjee et al. (2013) for ensuring fully undrained conditions.

1.9. Objectives

This research presents experimental and numerical results for cyclically loaded piles/caissons and pipes. Three thrust areas in this research are studied 1) thixotropy and sensitivity (chapter 4), 2) experimental and numerical investigations of cyclically loaded piles/caissons (chapter 5), and 3) monotonic and cyclic vertical, lateral, and zig-zag resistance of risers and pipelines in cohesive soils (Chapter 6-8).

1.9.1. Thixotropy and sensitivity

Single gravity displacement-controlled laboratory model tests, which are used to perform the cyclic T-bar and miniature vane shear tests. In this study, monotonic T-bar tests, cyclic T-bar tests, as well as vane shear tests are conducted to find:

1) The gain in undrained shear strength with time using cyclic T-bar tests (s_{u_t}),
2) The gain in undrained shear strength with time using vane shear tests ($s_{u\_t(MVT)}$),
3) Acquired sensitivity of soil using cyclic T- bar ($AS_{t(T\text{-}bar)}$) and how it is affected over time,
4) Soil sensitivity using vane shear tests ($A_{St(MVT)}$) and how it is affected over a prolonged period of time, and
5) Cyclic T-bar and vane shear results compared with other existing results.

This study is performed to fill the existing gap in longterm measurements.

1.9.2. Cyclically loaded piles/caissons in cohesive soils

This study involves experimental and numerical investigations. The experimental study is conducted in fine-grained soil to predict degradation of soil-resistance and to calibrate a constitutive model (nonlinear kinematic hardening model). The calibrated model had to match monotonic and cyclic lateral and vertical loading tests as well as pullout tests. This calibrated model can be considered as a good benchmark to investigate the accumulative displacements of piles and caissons subjected to vertical, lateral, or inclined loads. A parametric study using a 3-*D* finite element model using non-uniform load amplitudes is conducted to evaluate:

1. Lateral and vertical resistance of monotonic loading as well as the pullout resistance for an open and closed vent,
2. Degradation of the lateral and vertical resistance with increasing numbers of load cycles,
3. Calibration of the nonlinear kinematic hardening model using a commercial software (ABAQUS) package, and
4. Cumulative plastic deformations using non-uniform load amplitudes for different aspect ratios (L/D = 4, 5, and 6) and load inclinations ($\psi = 20^{\circ}$ to 75° from the horizontal).

1.9.3. Risers and pipelines

Monotonic and cyclic model tests are conducted using single gravity, displacement-controlled laboratory model tests of soil stiffness. All tests used high plasticity Gulf of Mexico clay with undrained shear strength corresponding to typical normally consolidated conditions. This thrust area is divided into three parts 1) vertical cyclic loading tests of risers-soil interaction at TDZ, 2) lateral cyclic loading tests of pipelines/riser-soil interaction at TDZ and/or at seabed, and zig-zag cyclic loading tests of pipelines/riser-soil interaction at TDZ and/or at seabed.

5.2.3. Vertical cyclic loading tests (Chapter 6)

The test program adds to the database evaluating the influence of the major variables (displacement magnitude, embedment depth, etc.) affecting soil stiffness for SCR fatigue-assessment. Additionally, it presents new results on stiffness recovery during rest periods, stiffness reduction after resumed cyclic loading, and gradual gains in stiffness under prolonged cyclic loading. The findings on stiffness recovery are particularly important, as this has been a major source of uncertainty in prior investigations. The study investigated the following aspects of soil-riser interaction:

1. Rate effects for monotonic and cyclic loading,
2. Vertical stiffness for displacement amplitudes ranging from 0.02-0.05 *D*,
3. Soil stiffness degradation with increasing in the number of cycles,
4. Siffness recovery during rest periods, and
5. Stiffness recovery under prolonged cyclic loading.
6. Effect of riser embedment depth *h* over a range h/D = 0.25-2,
7. Effect of loading rate during monotonic penetration, with load rates varying from 1 to 15 mm/sec,
8. Vertical stiffness degradation as a function of load cycle under cyclic displacement amplitudes in the range $\Delta y_{cyc}/D$ = 0.02-0.05, and

9. Stiffness recovery during rest (pause) periods ranging from 1 to 16 hours for $\Delta y_{cyc}/D = 0.02$ and 1 to 13 hours for $\Delta y_{cyc}/D = 0.05$.

5.2.3. Lateral cyclic loading tests (Chapter 7)

There are some empirical expressions for lateral resistance and the subsequent steady residual resistance as a result of experimental Investigations. These methods are commonly used in practice, but are subject to significant scatter and uncertainty. The test program expands database and serves to reduce the level of uncertainty. The study investigates the following aspects of soil-pipeline/riser interaction:

1. Fundamental mechanism of pipeline/riser-soil interaction in the lateral direction subjected to monotonic and cyclic loading,
2. Evolution of lateral resistance with different (small to large) displacement amplitudes,
3. Degradation of lateral resistance while increasing the number of cycles, and
4. Recovery of soil strength with time.

5.2.3. Zig-zag cyclic loading tests (Chapter 8)

As with the lateral cyclic loading tests, these tests aim to expand the database and reduce the level of uncertainty in model predictions. In contrast to the procedure utilized in the lateral tests in keeping the vertical position constant, the pile in the zigzag tests is subjected to a constant (self-weight) vertical load. this study investigates the following aspects:

1. better understanding the behavior of the trench formation process,

2. Lateral resistance behavior after a rest period, and
3. Shape of trenches and berms formed during the lateral and the zig-zag movements with different embedment depths.

1.10. Dissertation Outline

This dissertation comprises eight chapters. Every chapter starts with an introduction section, background, and finishes with a summary and conclusion section. It should be noted that due to journal style, some overlap occurs across different chapters.

Chapter 1 introduces an overview of thixotropy and sensitivity, piles/caissons, and pipelines/risers-soil interaction.

Chapter 2 looks at 1-g experimental design and apparatus that are used in the entire study.

Chapter 3: studies soil properties, soil parameters, and soil preparation for the laboratory testbed soils. In this chapter, two techniques are used (monotonic T-bar and miniature vane shear tests) to predict the undrained shear strength.

Chapter 4: presents a study that is performed to predict thixotropy and sensitivity in Gulf of Mexico clay. In this chapter, two techniques are used (cyclic T-bar tests and miniature vane shear tests) to estimate the undrained shear strength and remolded undrained shear strength under a prolonged period of time in order to estimate thixotropy and sensitivity of soil.

Chapter 5: Experimental and Finite element investigations of performance of piles and suction caissons to predict the cumulative deformations due to inclined cyclic loading in cohesive clay.

Chapter 6: presents on the findings of a series of single-element, single-gravity laboratory model tests investigating *P-y* behavior for SCRs in high plasticity Gulf of Mexico (GOM) clay. The objective isto acquire data on soil resistance during monotonic and cyclic loading and to assess the effect of recovery during rest periods.

Chapter 7: evaluates the fundamental mechanism of the pipeline/riser-soil interaction in the lateral direction subjected to monotonic and cyclic loading, the evolution of lateral resistance with different (small to large) displacement amplitudes, the degradation of lateral resistance while increasing the number of cycles, and the recovery of the soil strength with time.

Chapter 8: studies the fundamental mechanism of the pipeline/riser-soil interaction in zig-zag direction (combined vertical and lateral movements), the degradation of lateral resistance while increasing the number of cycles, and the recovery of the soil strength with time.

1.11. Nomenclature

A_c	Activity of Soil
AS_t	Acquired Sensitivity
$AS_{t(MVT)}$	Acquired Soil Sensitivity Using Vane Shear Tests
$AS_{t(T\text{-}bar)}$	Acquired Sensitivity Of Soil Using Cyclic T-bar
CPTu	Conventional Piezocone Penetration Test
D	Pile/Caisson, Pipe, or T-bar Diameter
D_v	Vane Diameter

FVTs	Field Vane Shear Tests
GoM clay	Gulf of Mexico clay
h	Embedment Depth for Risers
H_v	Measured Height of The Vane Blade
I_P	Plasticity Index
K	Vane Blade Constant
L	Pile/Caisson, Pipe, or T-bar Length
MVT	Miniature Vane Test
MVTs	Miniature Vane Tests
N	Number of Cycles
$N_{T\text{-}bar}$	T-bar Bearing Factor
$N_{T\text{-}bar(r)}$	Remolded T-bar Bearing Factor
$q_{T\text{-}bar(ext)}$	Extraction Resistance
$q_{T\text{-}bar(m)}$	Measured Penetration Resistance
$q_{T\text{-}bar(n)}$	Penetration Resistance At Cycle Number (n)
$q_{T\text{-}bar(net)}$	Net Penetration Resistance
SCR	Steel Catenary Riser
S_t	Sensitivity of Soil
$S_{t(FVT)}$	Sensitivity From Field Vane Shear Tests
s_u	Undrained Shear Strength
$s_{u(MVT)}$	Undrained Shear Strength Using Miniature Vane Test
$s_{u(MVT)r}$	Remolded Undrained Shear Strength Using Miniature Vane Test

$s_{u(undisturbed)}$	Undisturbed (Intact) Strength
s_{u_t}	Thixotropy Strength Ratio (The Gain In Undrained Shear Strength With Time)
$s_{u\_t(MVT)}$	The Gain In Undrained Shear Strength With Time Using Vane Shear Tests
s_{u0}	Undrained Shear Strength at the surface
s_{ur}	Remolded Undrained Shear Strength
t_w	Pile wall thickness
TDZ	Touch Down Zone
y	Vertical Displacement
Δy	Change In Vertical Displacement
Δy_{cyc}	Cyclic Displacement Amplitude
ψ	Load Inclination

1.12. References

Al-Janabi, H. A., Aubeny, C. P., Chen, J., & Luo, M. (2019, April). Experimental Measurement of Touchdown Zone Stiffness for SCR in Gulf of Mexico Clay. In *Offshore Technology Conference*. Offshore Technology Conference.

Andersen, K. H. (2015). Cyclic soil parameters for offshore foundation design. Frontiers in offshore geotechnics III, 5.

API (2003). Recommended practice for planning, designing and constructing fixed offshore platforms–working stress design (RP 2A-WSD), American Petroleum Institute.

Aubeny, C. (2017). *Geomechanics of Marine Anchors*. CRC Press.

Aubeny, C. P., Han, S. W., & Murff, J. D. (2003). Inclined load capacity of suction caissons. International Journal for Numerical and Analytical Methods in Geomechanics, 27(14), 1235-1254.

Aubeny, C. P., Shi, H., & Murff, J. D. (2005). Collapse loads for a cylinder embedded in trench in cohesive soil. *International Journal of Geomechanics*, *5*(4), 320-325.

Bridge, C. D., & Howells, H. A. (2007, January). Observations and modeling of steel catenary riser trenches. In *The Seventeenth International Offshore and Polar Engineering Conference*. International Society of Offshore and Polar Engineers.

Bridge, C., & Willis, N. (2002, May). Steel catenary risers–results and conclusions from large scale simulations of seabed interaction. In *Proc. of the Int. Conf. on Deep Offshore Technology* (pp. 40-60).

Bridge, C., Howells, H., Toy, N., Parke, G. A. R., & Woods, R. (2003). Full-scale model tests of a steel catenary riser. *WIT Transactions on The Built Environment*, *71.*

Chatterjee, S., White, D. J., & Randolph, M. F. (2013). Coupled consolidation analysis of pipe–soil interactions. *Canadian Geotechnical Journal*, *50*(6), 609-619.

Clukey, E. C., Morrison, M. J., Gamier, J., & Corté, J. F. (1995, January). The response of suction caissons in normally consolidated TLP loading conditions. In Offshore Technology Conference. Offshore Technology Conference.

Clukey, E., Jacob, P., & Sharma, P. P. (2008, January). Investigation of riser seafloor interaction using explicit finite element methods. In *Offshore Technology Conference*. Offshore Technology Conference.

Colliat, J. L., Boisard, P., Gramet, J. C., & Sparrevik, P. (1997, December). Geotechnical design and installation behaviour of suction anchor piles-comparison with drag anchors. In Proc., 7th Int. Conf. on Behaviour of Offshore Struct., Pergamon, Delft, The Netherlands (Vol. 1, p. 133).

Colliat, J. L., Dendani, H., Puech, A., & Nauroy, J. F. (2011). Gulf of Guinea deepwater sediments: Geotechnical properties, design issues and installation experiences. In *Proceedings of the 2nd International Symposium on Frontiers in Offshore Geotechnics (ISFOG), Perth, Australia* (pp. 59-86).

DNV (2014). "Design of Offshore Wind Turbine Structures, DET NORSKE VERITAS AS."

Fuglsang, L.D., and Steensen-Bach, J.O. (1991). "Breakout Resistance of Suction Piles in Clay," Proceedings of the International Conference on Centrifuge 1991, Boulder, Colorado, pp.153–159.

Howells, H. (1995). “Advances in steel catenary riser design.” The 2nd Annual International Forum on Deepwater Technology, DEEPTEC, Aberdeen, UK.

Howells, H. (1995). “Advances in steel catenary riser design.” *The 2nd Annual International Forum on Deepwater Technology, DEEPTEC*, Aberdeen, UK.

Hu, H. J. E., Leung, C. F., Chow, Y. K., & Palmer, A. C. (2011). Centrifuge modelling of SCR vertical motion at touchdown zone. *Ocean Engineering*, *38*(7), 888-899.

Li, W., Igoe, D., & Gavin, K. (2015). Field tests to investigate the cyclic response of monopiles in sand. Proceedings of the Institution of Civil Engineers-Geotechnical Engineering, 168(5), 407-421.

Matlock, H. (1970). Correlations for design of laterally loaded piles in soft clay. *Offshore technology in civil engineering’s hall of fame papers from the early years*, 77-94.

Mekha, B. B. (2001). “New frontiers in the design of steel catenary risers for floating production systems.” *Journal of Offshore Mechanics and Arctic Engineering*, 123, 153–158.

Mitchell JK (1960). “Fundamental aspects of thixotropy in soils,” *Journal of the Soil Mechanics and Foundations Division*, ASCE, 86(SM3), pp. 19-52.

Randolph, M. F. (2012). Offshore design approaches and model tests for sub-failure cyclic loading of foundations. In Mechanical behaviour of soils under environmentally induced cyclic loads (pp. 441-480). Springer, Vienna.

Randolph, M. F., O'neill, M. P., Stewart, D. P., & Erbrich, C. (1998, January). Performance of suction anchors in fine-grained calcareous soils. In Offshore technology conference. Offshore Technology Conference.

Skemption, A., and Northey, R. (1952). “The Sensitivity of Clays,” Géotechnique, 3(1), 30-53.

Sparrevik, P. (2002, January). Suction pile technology and installation in deep waters. In *Offshore technology conference*. Offshore Technology Conference.

Terzaghi. (1944). “Ends and means in soils mechanics,” Eng. Journ. (Canada), 27:608.

You, J. H. (2012). Numerical Modeling of Seafloor Interaction With Steel Catenary Riser. Texas A&M University, College Station, USA. Doctor of Philosophy.

2. EXPERIMENTAL FACILITY

2.1. Introduction

This chapter covers the designs and the fabrications of all laboratory equipment associated with conducting the model tests as well as with soil characterization needed to support model test interpretation. Some of this equipment isalready existed in the geotechnical laboratory, but needed to be modified depending on test requirements.

2.2. Model Setup

In this section, all the apparatus, equipment, sensors, etc., which are used in all five thrust areas will be explained in detail. It includes a steel loading frame, robotic system (smart motors), steel basin, force transducers, laser displacement transducers, tilt transducer, torque transducer, miniature vane shear test apparatus (MVT), full-flow (T-bar) penetrometer model, vane blade, riser models, suction caisson models, mixing equipment, aluminum basins, smart motor interface (SMI), National Instruments (NI), and LabVIEW Software.

2.2.1. Steel Loading Frame

A steel frame supported the smart motors used in the tests. The steel loading frame ables to move to the top and the bottom. These two movements are controlled by a drill attached to the top of the frame as shown in Figure 2.1. The steel loading frame is already fabricated from another study (Beemer, 2016). Some fabrications and modifications are made in order to to make the steel loading frame fits the requirements of this research.

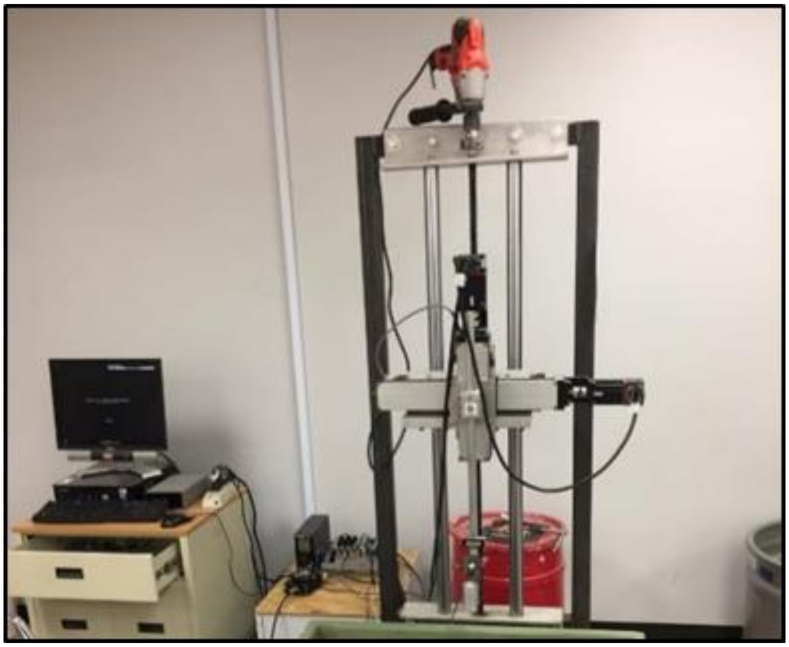

Figure 2.1 Steel loading frame.

2.2.2. Robotic System (Smart Motors)

To control the smart motors (SMs) in both vertical, horizontal or/and zig-zag directions, the Smart Motor Interface (SMI) software is used. The SMs have four degrees of freedom. Multiple scripts are written and uploaded into the SMI depending on the velocity of displacement, acceleration/ deceleration, etc. of the motors. Displacement-controlled loading was used (Mohammed, 2013; Al-janabi et al., 2014; Beemer, 2016). Figure 2.2 shows a photograph of the robotic system.

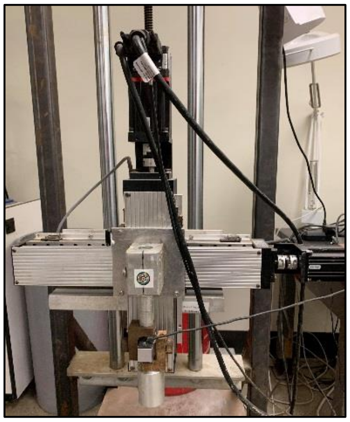

Figure 2.2 Robotic system (Smart Motors).

2.2.3. Steel Basin

A steel box containing the soil test bed with dimensions 80 cm long, 50 cm width and 50 cm height with a wall thickness of 4.76 cm is used in this study. The basin has a removable base plate to control the height of the test bed (Fattah et al. 2014, 2014a, 2015; Al-janabi et al. 2014). Figure 2.3 shows the basin, the removal plate, and the drainage valve.

Figure 2.3 Steel basin.

2.2.4. Force Transducers

Three force transducers are used to conduct the test program in this study. Two of them are used to measure vertical forces, and the third one is used to measure lateral forces. Therefore, there classify as very precise transducers. Figure 2.4 and Figure 2.5 show the vertical force transducers and the lateral load transducers. All of these transducers are connected to the national instruments DAQ, which will be explained in section (0) and section (0).

Figure 2.4 Vertical force transducers.

Figure 2.5 Lateral force transducer.

2.2.5. Laser Displacement Sensor

Two high-resolution laser displacement sensors (BANNER) are used to collect the required data during testing. These sensors are very precise, but they are limited to a specific displacement distance. Figure 2.6 shows one of the laser sensors.

Figure 2.6 Laser displacement sensor.

2.2.6. Tilt Transducer

A MEMSIC CXTLA02 tilt sensor is used to measure the tilt of the caisson in two orthogonal directions and had a full range of ± 70o with a linear range of ± 20o. The angle of tilt measured using the tilt meter is theoretically proportional to the sine of the ratio of the change in output voltage to the sensitivity. However, for small angles within the linear range, the angle of tilt can be assumed to be proportional to the change in output voltage with a nonlinearity of 2% full-scale as reported by the manufacturer. Figure 2.7 shows the tilt sensor that isused for the third thrust area.

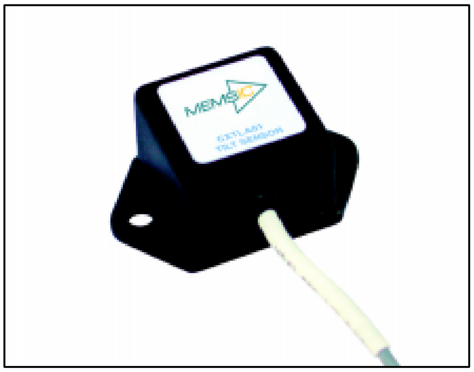

Figure 2.7 Tilt Transducer.

2.2.7. Torque Sensor

A TRT 50 torque transducer is used in this study to measure the torque in order to find the undrained shear strength of the soil. This traducer is connected to a smart motor (with a gearbox) at the upper side and to a vane at the lower side as shown in Figure 2.8.

2.2.8. Miniature Vane Shear Test Apparatus (MVT)

A miniature vane shear test apparatus MVT, Figure 2.8., is one of the apparatuses that is used to predict thixotroy effect by predicting the undrained shear strength and sensitivity at different times. In addition, a relationship between water content and undrained shear strength is found. the MVT is fabricated to be installed on a frame. This frame is adjustable height manually by rotating a small steering wheel as shown in Figure 2.8. The steering wheel is connected to a ball screw, which helps to lower/raise the vane base. That leads to insert the vane into the required soil embedment depths. The vane can be replaced with any vane size depending on the test requirements.

A variable speed smart motor with a gearbox isused to control penetration rates. Furthermore, this apparatus features a torque transducer that is connected to the data acquisition system to collect the required readings in a very precise way. The undrained shear strength is found according to ASTM D4648/D4648M-16, (2016).

Figure 2.8 Torque transducer.

2.2.9. Vane Blade

In this study, two different vanes are used to find the relationship of the undrained shear strength versus the water contents. One of them has dimensions of 25.4 mm (1.0 inch) in diameter and 50.4 mm (2.0 inches) in height. The second vane has dimensions of 50.8 mm (2.0 inches) in diameter and 101.6 mm (4.0 inches) in height. Figure 2.9 and Figure 2.10 show both of the vanes.

Figure 2.9 Small vane blade.

Figure 2.10 Big vane blade.

2.2.10. Full-Flow (T-bar) Penetrometer Model,

A T-bar with a diameter of 12.7 mm (0.5 inches) and length of 50.8 mm (2 inches) used for this study to predict the undrained shear strength of the Gulf of Mexico clay with time. It is fabricated to be connected to a load cell as shown in Figure 2.11. The T-bar rod is connected to the robotic actuator and to the data acquisition system. Figure 2.12 shows a sketch of the T- bar model and other fabrications. T-bar tests are conducted directly on test bed soils to provide independent measurements of the undrained shear strength of the soil.

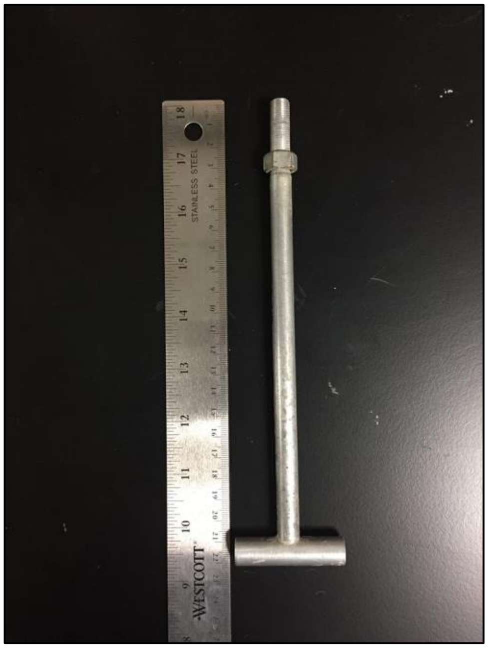

Figure 2.11 Full-flow penetrometer, T-bar penetrometer model.

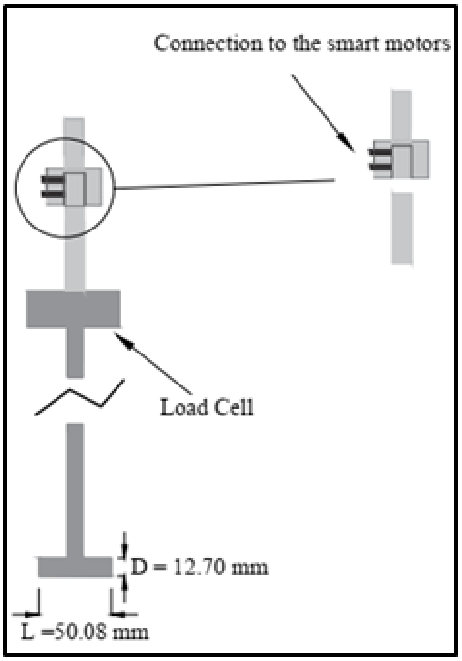

Figure 2.12 A sketch of the T-bar penetrometer model.

2.2.11. Piles/ Caisson Models

Eight foundations (piles/suction caissons) models are used in this study. These foundations are comprised of aluminum with outer diameter (*D*) of 50.8 mm (2 inches), inner diameter (D_{in}) of 47 mm ~ (1.9 inches), projected (embedment) length (*L*) of 99 mm (3.9 inches), and a total length (L_t) of 111.3 mm (4.38 inches). Figure 2.13a-b shows a sketch and a photograph of the model foundations used in this study along with the applied forces and moments.

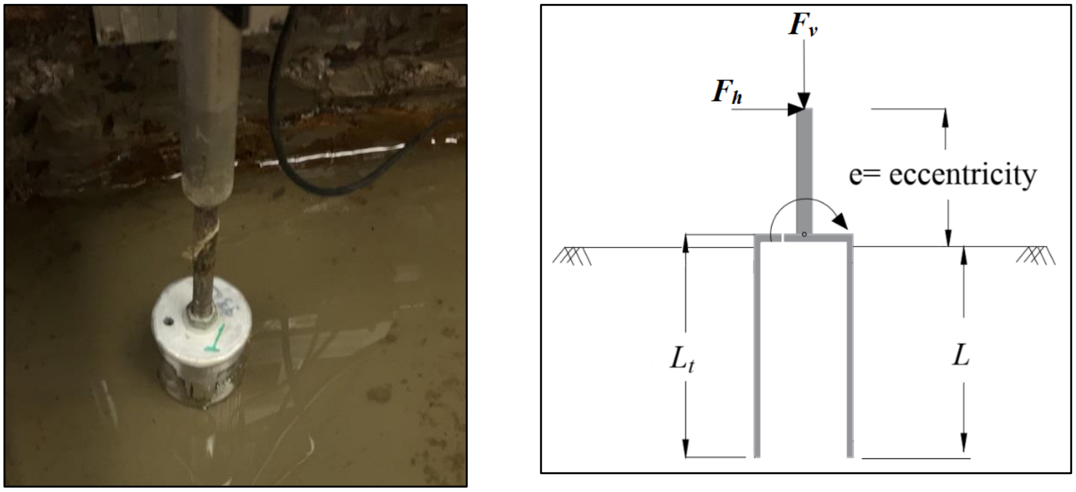

a) Caisson installation (open vent)

b) A sketch shows the vertical, horizontal forces and the moment for *L*/*D* = 2.

Figure 2.13 Suction caisson models.

2.2.12. Riser Models

Three riser models are fabricated for the third thrust area to simulate the pipeline/riser with aspect ratio *L/D* of 6. Length (*L*) of 30.48 cm (12 inches) and diameter (*D*) of 5.08 cm (2 inches). All three pipes have the same properties, steel with a wall thickness of about 4.76 mm. The pipes are judged to be sufficiently stiff so as to approximate a rigid body. It has a screwed hole to connect the other fabrications and the load cells into it as shown in Figure 2.14 and Figure 2.15.

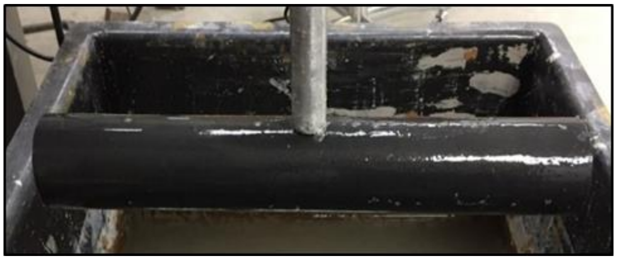

Figure 2.14 Riser model.

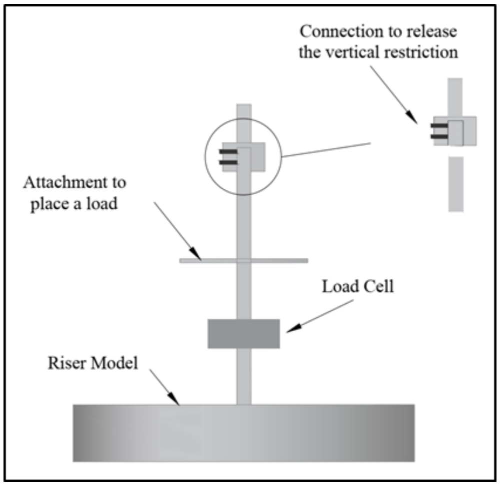

Figure 2.15 A sketch of riser model with other fabrications.

2.2.13. Aluminum Basins

During the storage of soil in plastic drums, self-weight consolidation occurred, which required re-working of the soil to achieve the target strength and density for the soil testbed. Therefore, the soil is removed from the barrels and placed in several small (approximately 3 ft long by 2 ft wide) aluminum basins as shown in Figure 2.16. Mixing tools are attached to both a big and small motor and are used to remix the soil as shown in Figure 2.16. Reconstituting the soil to the target density used only native (salt) water to ensure that the salt content of the pore fluid is minimally affected.

Figure 2.16 Aluminum basins and mixing tools.

2.2.14. Smart Motor Interface (SMI)

The SMI software is used to control the smart motors (SMs) in both vertical, horizontal or/and zig-zag directions (see Figure 2.17). The SMs have four degrees of freedom. In order to run them, two scripts need to be written and uploaded into the SMI. Multiple scripts are written and uploaded into the SMI depending on the desired velocity, displacement, and acceleration/ deceleration, of the motors. Displacement-controlled loading is used (Mohammed, 2013; Al-janabi et al., 2014; Beemer, 2016).

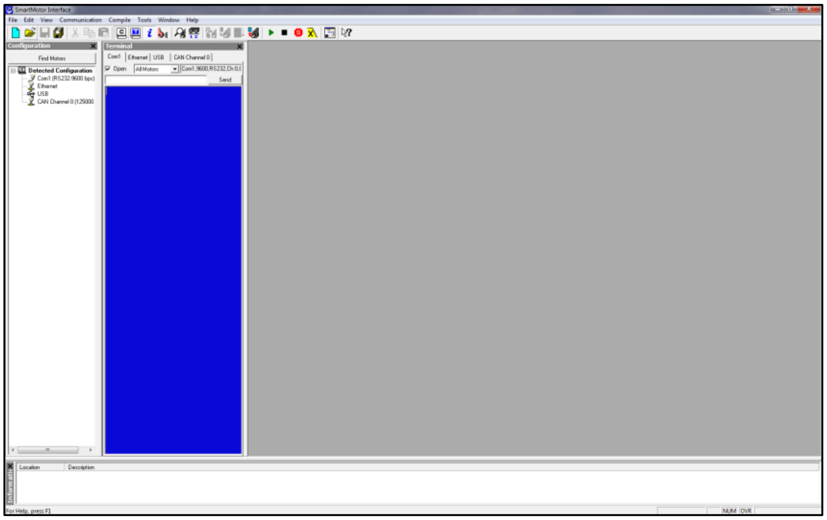

Figure 2.17 Smart Motor Interface (SMI) software.

2.2.15. Data Acquisition (DAQ), National Instruments (NI)

Data Acquisition System (NI) for force, displacement, and tilt sensing with LabVIEW Software is used. Six modules are connected to the DAQ system to collect the measurements. Two NI-9237, two NI-9239, and two NI-9219 are used to measure forces, displacements, and tilts of the suction caisson, respectively. Figure 2.18 shows the DAQ system with the modules and an external power supply.

Figure 2.18 DAQ system.

2.2.16. LabVIEW Software

Lab View software is coded to be used in this study. It is coded to collect the required data during testing. Since some tests are performed at 1.5 mm/sec, and others, like T-bar tests, at 20 mm/sec, it is required to collect more than one sample per second to capture more data and plot it with more accuracy. The software helps to collect whatever samples needed per second (e.g. 1=< samples/sec >=100) with high precision. Figure 2.19 shows the LabVIEW front page.

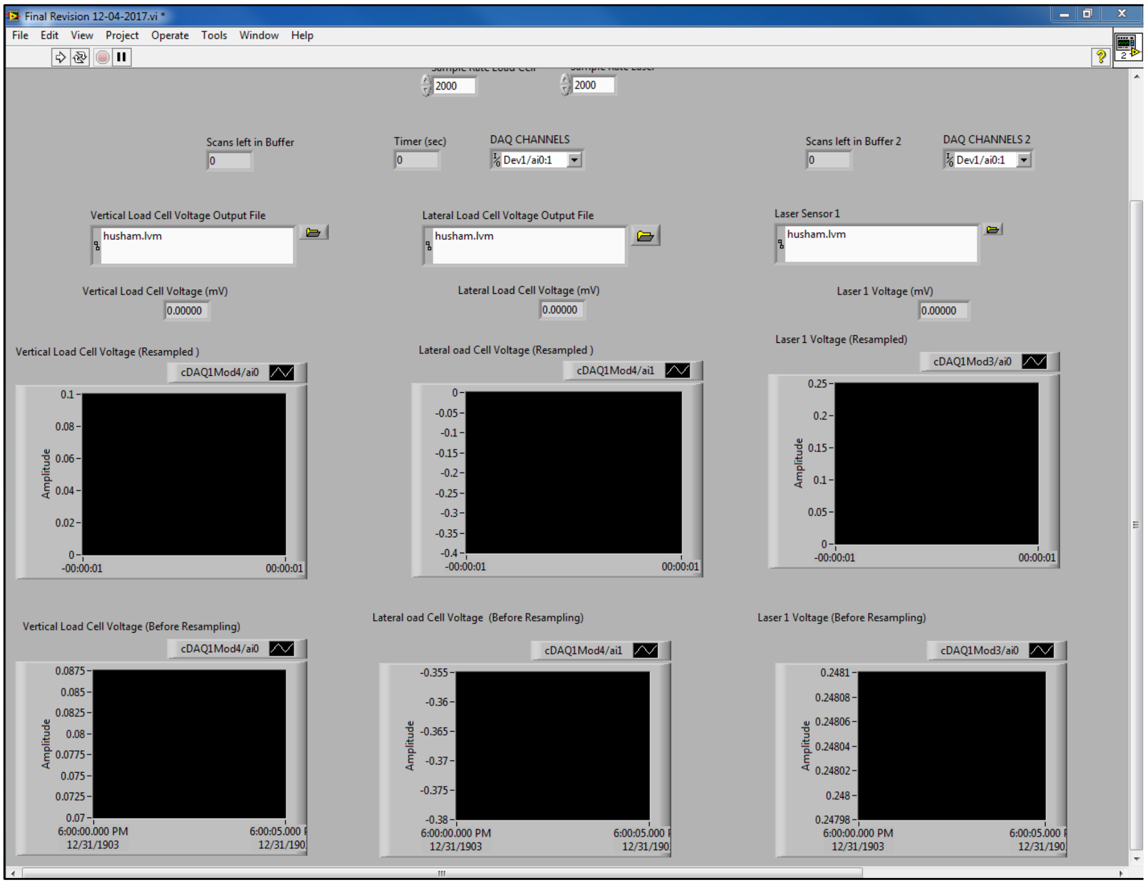

Final Revision 12-04-2017.vi *

2000

2000

Scans left in Buffer: 0

Timer (sec): 0

DAQ CHANNELS: Dev1/ai0:1

Scans left in Buffer 2: 0

DAQ CHANNELS 2: Dev1/ai0:1

Vertical Load Cell Voltage Output File: husham.lvm

Lateral Load Cell Voltage Output File: husham.lvm

Laser Sensor 1: husham.lvm

Vertical Load Cell Voltage (mV): 0.00000

Lateral Load Cell Voltage (mV): 0.00000

Laser 1 Voltage (mV): 0.00000

Figure 2.19 LabVIEW software.

2.3. Nomenclature

SCR	Steel Catenary Riser
TDZ	Touch Down Zone
MVT	Miniature Vane Test
SMs	Smart Motors
SMI	Smart Motor Interface
NI	National Instruments
DAQ	Data Acquisition
TRT	Tourqe Transducer
D	Diameter of (Piles, Caissons, Pipe, or T-bar)
D_{in}	Inner Diameter of The Caisson
L	Length of pipe or Embedded Pile/Caisson
L_t	Total length of the caisson with the lid

2.4. References

Al-janabi, H. A., Shlash, K. T., and Fattah, M. Y. (2014). "The Behavior of Bounded Foundations on Sandy Soil Bounded Shallow Foundations on Iraqi Sandy Soil with Different Densities," In. Saarbrücken: LAP LAMBERT Academic Publishing.

ASTM D4318-17e1, A. I. (2017). "Standard Test Methods for Liquid Limit, Plastic Limit, and Plasticity Index of Soils," West Conshohocken, PA.

ASTM D4648/D4648M-16, A. I. (2016). “Standard Test Methods for Laboratory Miniature Vane Shear Test for Saturated Fine-Grained Clayey Soil,” West Conshohocken, PA.

Beemer, R. D. (2016). “Experimental studies of squat gravity caissons and monopiles for offshore applications,” (Ph.D.), Texas A&M University.

Fattah, M. Y., Shlash, K. T., and Mohammed, H. A. (2014). “Bearing capacity of rectangular footing on sandy soil bounded by a wall,” Arabian Journal for Science and Engineering, 39(11), 7621-7633.

Fattah, M. Y., Shlash, K. T., and Mohammed, H. A. (2014a). “Experimental Study on the Behavior of Bounded Square Footing on Sandy Soil,” Engineering and Technology Journal, 32(5 Part (A) Engineering), 1083-1105.

Fattah, M. Y., Shlash, K. T., and Mohammed, H. A. (2015). “Experimental study on the behavior of strip footing on sandy soil bounded by a wall,” Arabian Journal of Geosciences, 8(7), 4779-4790.

3. SOIL PREPARATION

3.1. Introduction

In this chapter, soil preparation and index properties of the used soil will be explained in detail. A typical Gulf of Mexico (GoM) clay is used in this study. Seabed deposits consist of very soft clays with low undrained shear strength ratio. Therefore, marine clays tend to have high void ratios. The undrained shear strength varies with depth and it can be defined as a function of depth (w). Equation 3.1 shows the undrained shear strength and how it varies linearly with depth.

$$s_u = s_{uo} + s_u * w \qquad \textbf{Equation 3.1}$$

where: s_{uo} is the undrained shear strength at the surface of the seabed and s_u is the shear strength gradient with depth.

s_{uo} may generally be taken as 0 to 4 kPa while the intact strength gradient may be as high as 0 to 20 kPa (Willis and West, 2001). Full-Flow Penetrometers (T-bar and ball penetrometers) and vane shear test are widely used to predict the in-situ soil strength for the low shear strength near the mudline.

3.2. Model Soil Properties Used in This Research

A typical clay from the the Gulf of Mexico is used in this study. During storage in plastic drums, self-weight consolidation occurred, which required re-working of the soil to achieve the target strength and density for the soil testbed. Reworking of the soil is accomplished by adding native (salt) water and mixing to achieve a target undrained shear strength in the range 1.12 to 1.68 kN/m^2 (25 to 35 psf). The soil is removed out of the barrels in several small (approximately 3 ft long by 2 ft wide) basins. The soil is remixed and the salty water is added to achieve the target strength. After achieving the required undrained shear strength, the soil is placed in the test basin in about four to five layers to create a total soil depth of about 35 to 40 cm. A sharp tool is used to level the layers and remove any cavities. The basin is sealed using a nylon sheet and left for about 48 hours to permit thixotropic strength recovery to occur. Free water is added to a level of about 10 to 12 cm to create a submerged condition. After finishing a given riser load test, the affected oil is removed and replaced by new soil using the same placement procedure as described above. Figure 3.1 and Figure 3.2 show the plastic barrels and the dense state of the soil after storage, respectively.

3.3. Soil Index Properties

The index properties of the clayey soil are determined by using standard tests ASTM D4318-00, (2018). The details of these properties are listed in Table 3.1. Laboratory characterization tests consisted of liquid limit, plastic limit, and water content. The table below shows the details.

Table 3.1 The index properties of the soil.

Index Properties	Values (%)
Liquid Limit (LL)	59
Plastic Limit (PL)	30
Plasticity Index (PI)	29

Figure 3.1 Plastic drums.

Figure 3.2 A photograph shows the dense state of the clay.

3.4. Test Program (Undrained Shear Strength)

The test program consists of two series of tests. The first series is the monotonic T-bar test, which is performed to find the undrained shear strength profile for GoM clay with different moisture water content as presented in Table 3.2. The second series of tests is miniature vane shear tests (MVTs), which is conducted to find a relationship between the undrained shear strengths and the moisture water contents as shown in Table 3.2.

Table 3.2 Summary of the test program.

Series No.	Test No.	Loading rate	Test description
1	1-8	20 mm/sec	Monotonic T-bar tests with different water contents
3	19-25	ASTM D4648/D4648M-16, (2016)	Miniature vane shear Tests with different water contents

3.5. Undrained Shear Strength

Two different techniques, monotonic T-bar penetrometer and miniature vane shear tests are used in this research to measure the undrained shear strength and confirm that it is in the desired range for about 1.12 to 1.68 kN/m^2 (25 to 35 psf).

3.5.1. Undrained Shear Strength, Monotonic T-bar Penetrometer

A T-bar with a diameter of 12.7 mm (0.5 inches) and length of 50.8 mm (2 inches) used for this study to predict the undrained shear strength of the Gulf of Mexico clay with time. It is fabricated to be connected to a load cell as shown in Figure 3.3. The T-bar rod is connected to the robotic actuator and to the data acquisition system. The penetration rate is 20 mm/sec (0.787 in/sec) to present undrained loading condition (Langford &

Aubeny, 2008; Yafrate el al., 2009). All undrained shear strengths are interpreted by using a T- bar bearing factor of 10.5. Accurate measurement of test soils is essential to properly interpret thixotropy effect with time. Figure 3.4 shows a sketch of the T- bar model and other fabrications. T-bar tests are conducted directly on test bed soils to provide independent measurements of the undrained shear strength of the soil.

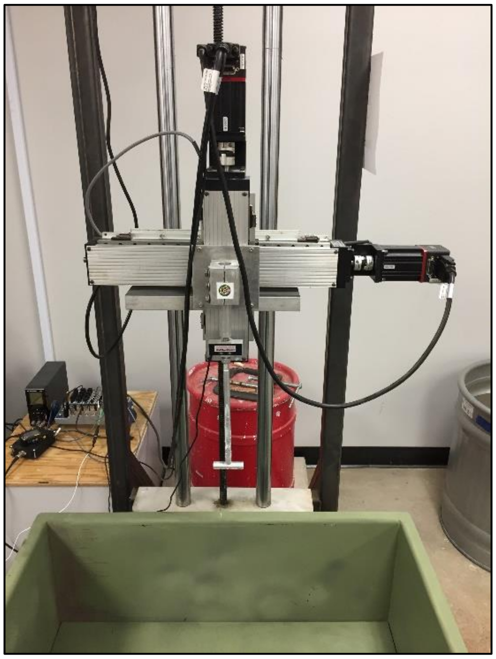

Figure 3.3 T-bar model connected to the robotic system.

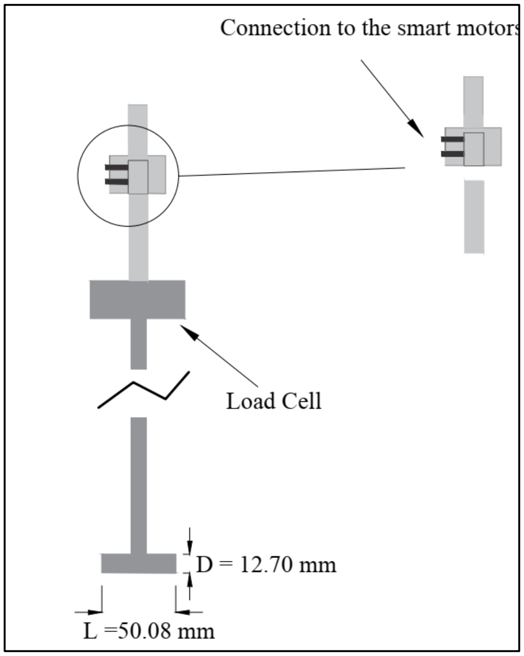

Figure 3.4 A sketch of the T-bar model.

5.2.3. Undrained shear strength with different moisture water content (*w* %)

In order to find the undrained shear profiles, monotonic full-flow penetrometer and T-bar penetrometer tests are conducted with different water contents. Figure 3.5, Figure 3.6, and Figure 3.7 show the relationship between the undrained shear strength and depths for selected monotonic T-bar tests for different moisture water contents. Table 3.3 shows the undrained shear strength profiles with different water contents.

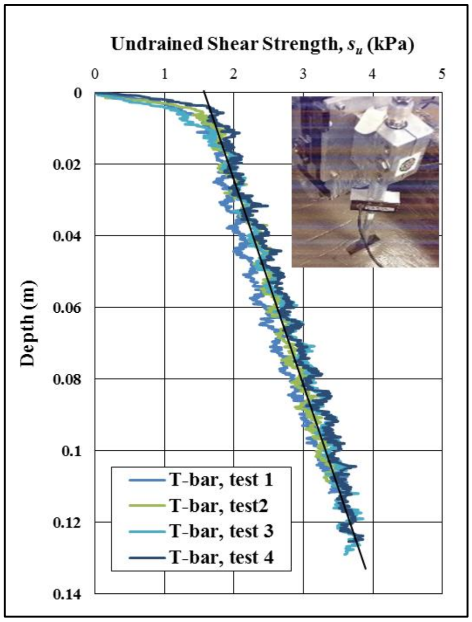

Figure 3.5 Some selected T-bar tests.

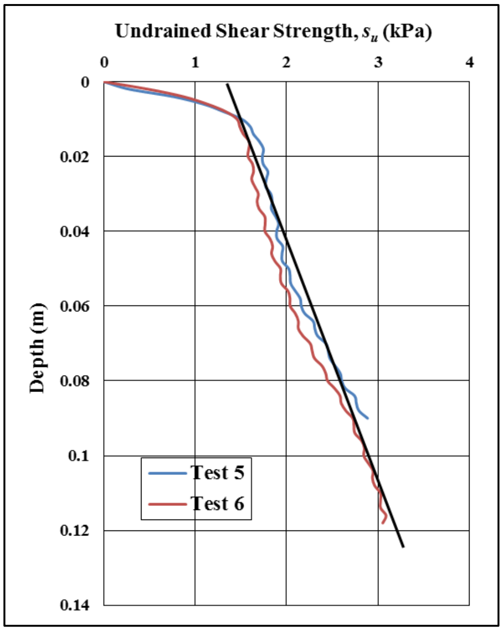

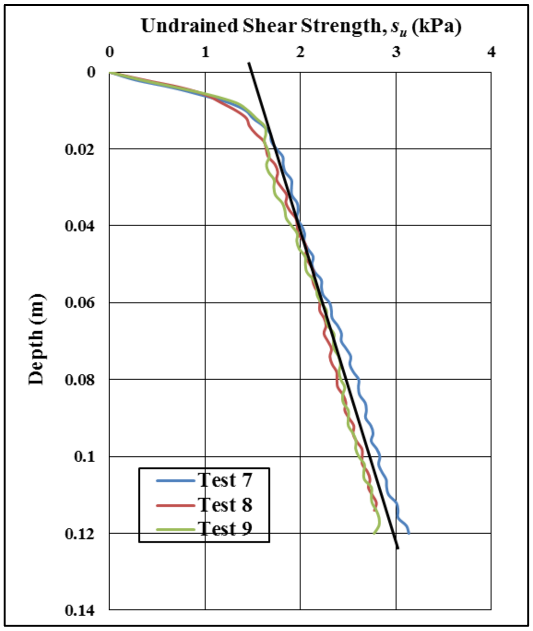

Figure 3.6 Some selected T-bar tests.

Figure 3.7 Some selected T-bar tests.

It is clear from Figure 3.5 to Figure 3.7 that the profile of shear strength versus depth is nearly linear. Since the T-bar factor of the first few diameters of penetration is not constant, it should be treated with some caution, as discussed in (White and Randolph 2007).

Table 3.3 Undrained shear strength profiles using T-bar tests.

Water content (*w* %)	**s_{uo} (kPa)**	**Strength gradient (kPa /m)**	**Undrained Shear Strength, s_u (kPa)**
80	1	16.7	1.053+16.7*w*
77.2	1.5	18.8	1.436+18.8*w*
78	1.3	14	1.292+14*w*
76.3	1.5	16.3	1.484+16.3*w*
77.5	1.4	12.3	1.412+12.3*w*

3.5.2. Undrained Shear Strength, Miniature Vane Shear Test (MVT)

The miniature vane shear test apparatus (Figure 3.8) is used to establish relationships between water content and undrained shear strength as shown in Figure 3.9. This apparatus features a torque transducer that is connected to the data acquisition system described above. A variable-speed motor with gears is used to control rotation rates. The undrained shear strength is computed from vane measurements in accordance with ASTM D4648/D4648M-16, (2016). The soil is mixed using the mixer apparatus (Chapter 1) and then placed in three compaction models. These models are sealed using nylon sheets and left for about 48 hours to permit thixotropic strength recovery to occur. After that, the test program of the vane shear tests is conducted. Figure 3.9 shows how the undrained shear strength decreases while increasing moisture water content.

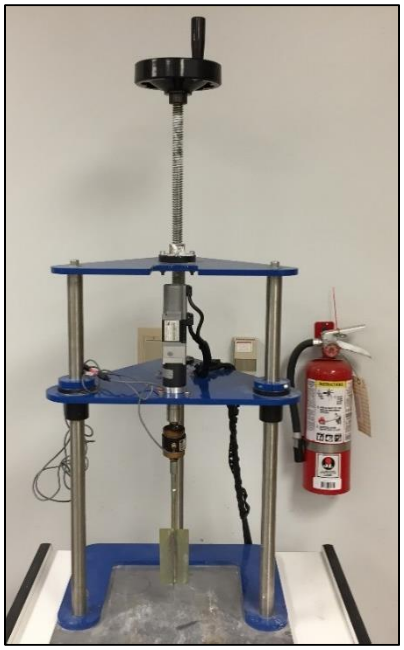

Figure 3.8 Miniature vane shear test apparatus.

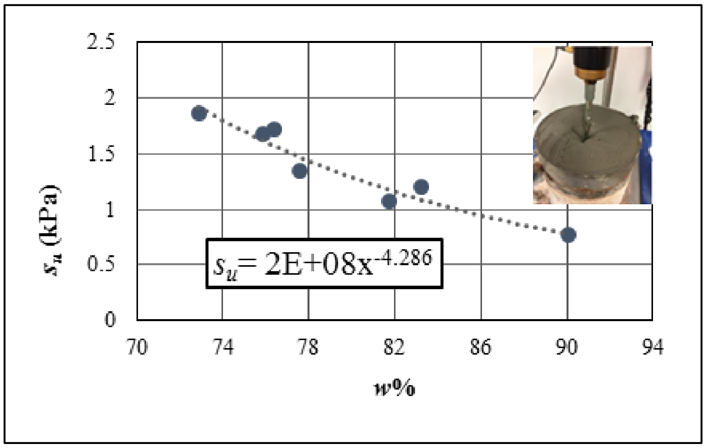

Figure 3.9 Undrained shear strength s_u vs. water content w_c%.

Equation 3.2 and Equation 3.3 are used to find the undrained shear strength ($s_{u(MVT)}$) according to the ASTM D4648/D4648M-16 (2016).

$$s_{u(MVT)} = T / K$$ **Equation 3.2**

$$K = \frac{\pi D_V{}^2 H_V}{2*10^9}\left[1+\frac{D_V}{3H_V}\right]$$ **Equation 3.3**

where: T= maximum torque, K= vane blade constant, D_v = measured diameter of the vane blade (see section 0), and H_v= measured height of the vane blade (see section0).

The strength is determined by applying a torque at a constant rotation as explained in ASTM D4648/D4648M-16 (2016). Some selected miniature shear tests are shown in Figure 3.10 to Figure 3.18. These figures show some of the undrained shear strength angular rotation (degrees) for different water content.

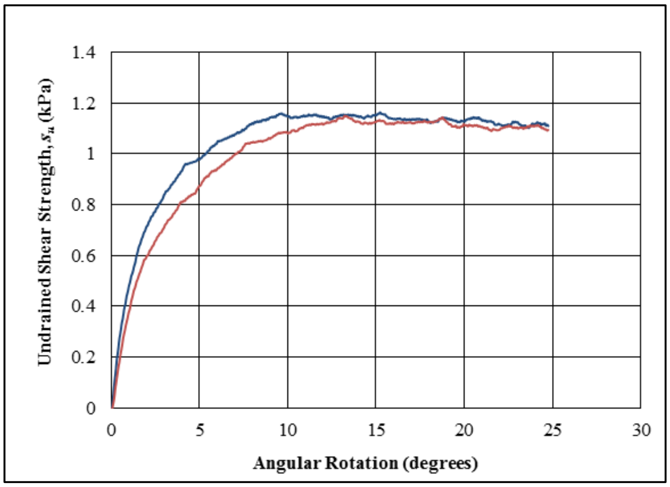

Figure 3.10 Different miniature vane shear test at w_c% = 80.4.

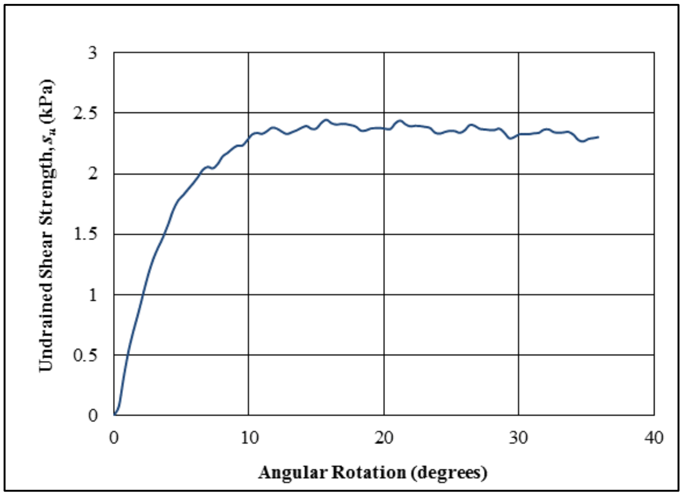

Figure 3.11 Miniature vane shear test at w_c % = 73.4.

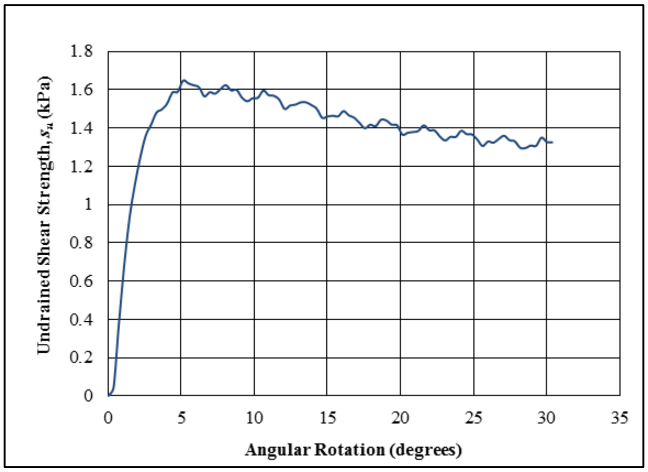

Figure 3.12 Miniature vane shear test at w_c% = 77.4.

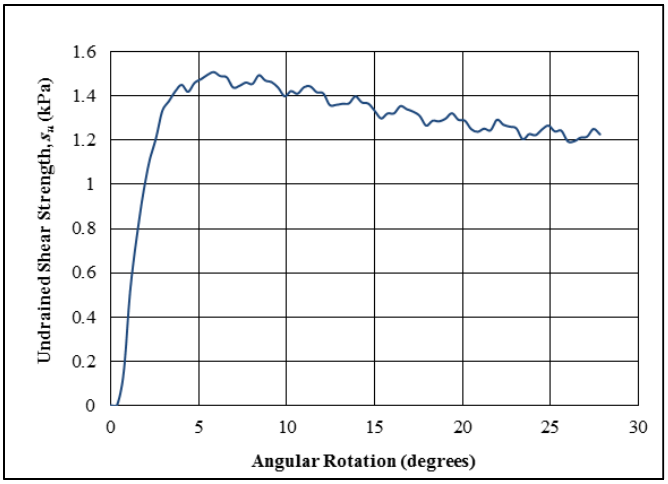

Figure 3.13 Miniature vane shear test at w_c% = 77.

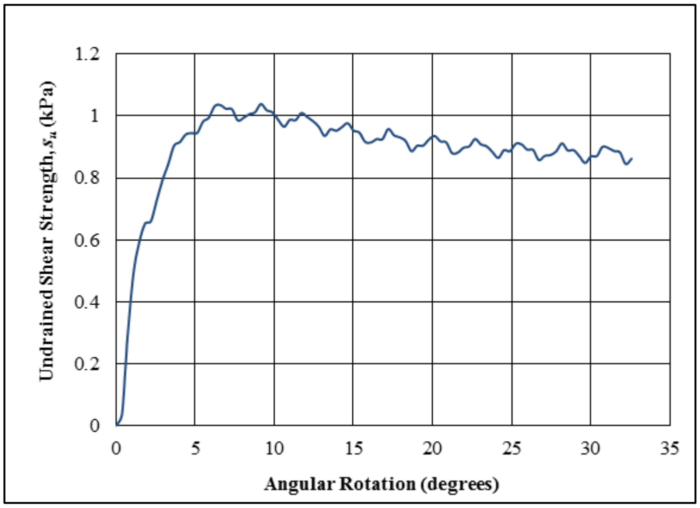

Figure 3.14 Miniature vane shear test at w_c% = 81.

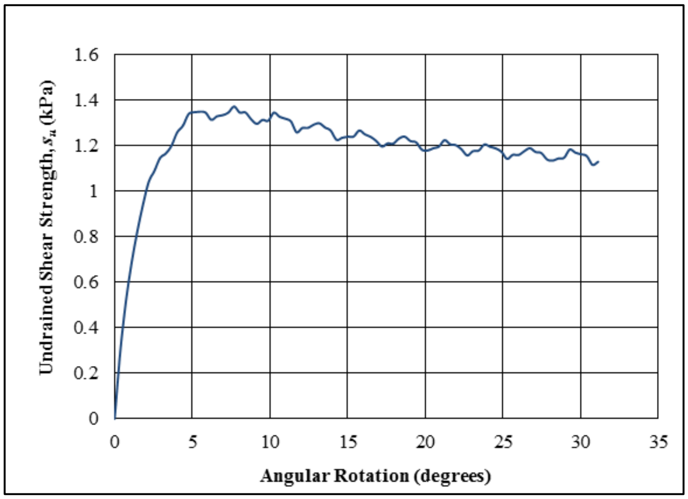

Figure 3.15 Miniature vane shear test at w_c% = 76.

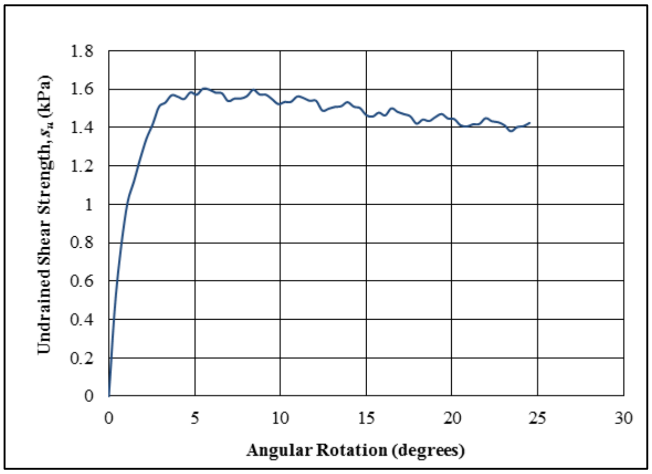

Figure 3.16 Miniature vane shear test at w_c% = 73.9.

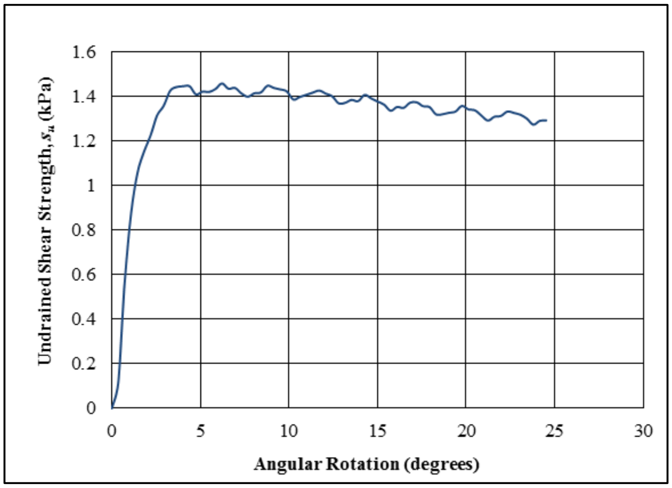

Figure 3.17 Miniature vane shear test at w_c% = 75.

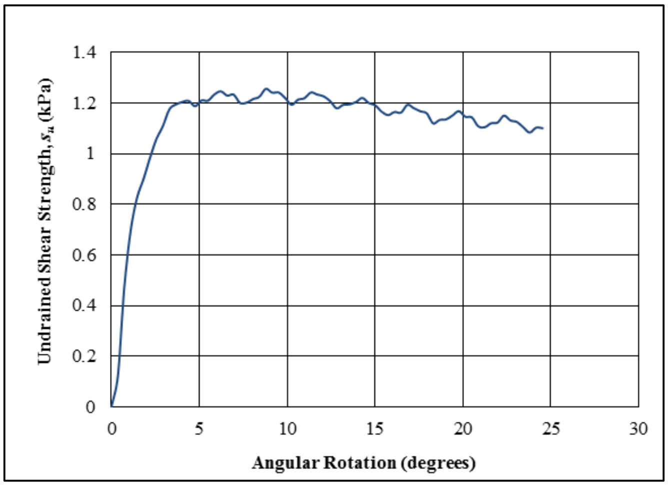

Figure 3.18 Miniature vane shear test at w_c% = 74.8.

3.6. Nomenclature

D_v	Vane Diameter
GoM clay	Gulf of Mexico clay
H_v	Measured Height of The Vane Blade
K	Vane Blade Constant
LL	Liquid Limit
MVTs	Miniature Vane Tests

PI	Plasticity Index
PL	Plastic Limit
s_u	Undrained Shear Strength
$s_{u(MVT)}$	Undrained Shear Strength Using Miniature Vane Test
s_{u0}	Undrained Shear Strength at the surface
T	Maximum Torque
w	Embedment depth
$w_c\%$	Water Moisture Content

3.7. References

ASTM D4318-17e1, A. I. (2017). “Standard Test Methods for Liquid Limit, Plastic Limit, and Plasticity Index of Soils,” West Conshohocken, PA.

ASTM D4648/D4648M-16, A. I. (2016). “Standard Test Methods for Laboratory Miniature Vane Shear Test for Saturated Fine-Grained Clayey Soil,” West Conshohocken, PA.

Langford, T., and Aubeny, C. P. (2008). “Model Tests for Steel Catenary Riser in Marine Clay,” *Paper presented at the Offshore Technology Conference*, Houston, OTC-19495.

White, D. J., & Randolph, M. F. (2007). Seabed characterisation and models for pipeline-soil interaction. International Journal of Offshore and Polar Engineering, 17(03).

Willis, N. R. T., & West, P. T. J. (2001, January). Interaction between deepwater catenary risers and a soft seabed: large scale sea trials. In *Offshore Technology Conference*. Offshore Technology Conference.

Yafrate, N., DeJong, J., DeGroot, D., and Randolph, M. (2009). "Evaluation of remolded shear strength and sensitivity of soft clay using full-flow penetrometers," Journal of Geotechnical and Geoenvironmental Engineering, 135(9), 1179-1189.

4. EXPERIMENTAL MEASUREMENT OF THIXOTROPY AND SENSITIVITY IN GULF OF MEXICO CLAY[*]

4.1. Introduction

As defined by Mitchell (1960), thixotropy is an isothermal, reversible, time-dependent process where a material stiffens while at rest, then softens or liquefies upon remolding. Thixotropy refers to time-dependent strength gain in soil at constant water content after remolding. This process is in contrast to the strength gain in soil associated with consolidation, which occurs under conditions of changing water content. There are multiple factors affecting the strength of the soil (e.g. Plasticity index (I_p), Sensitivity of the soil (S_t), Activity of the soil (A_c), etc.). Figure 4.1 shows some examples of a measured thixotropy strength ratio with different plasticity indexes and different types of soils which are kaolin, Bentonite, and Gulf of Mexico clay. The thixotropy strength ratio can be defined as the ratio of the gain in undrained shear strength with time (s_{u_t}) to remolded undrained shear strength (s_{ur}). It shows how the gain in strength differs depending on the soil properties. Thixotropy is considered a significant factor for offshore geotechnical design (e.g. subsea structure, anchoring systems, piles, etc.).

Full-flow penetrometers in use today are either spherical (ball) or cylindrical (T-bar) as a part of offshore geotechnical site investigations. Vane shear tests also are widely

---

[*] Reprinted with permission from "Experimental Measurement of Thixotropy and Sensitivity in Gulf of Mexico Clay" by Authors' Husham A. Al-Janabi and Charles P. Aubeny, 2019. the International Society of Offshore and Polar Engineers (ISOPE), Volume Number, 2259-2267, Copyright [2019] by the International Society of Offshore and Polar Engineers (ISOPE).

used as a part of geotechnical site investigation to predict the undrained shear strength and other geotechnical parameters. In this study, a full-flow penetrometer T-bar penetrometer and a miniature vane shear test (MVT) are used.

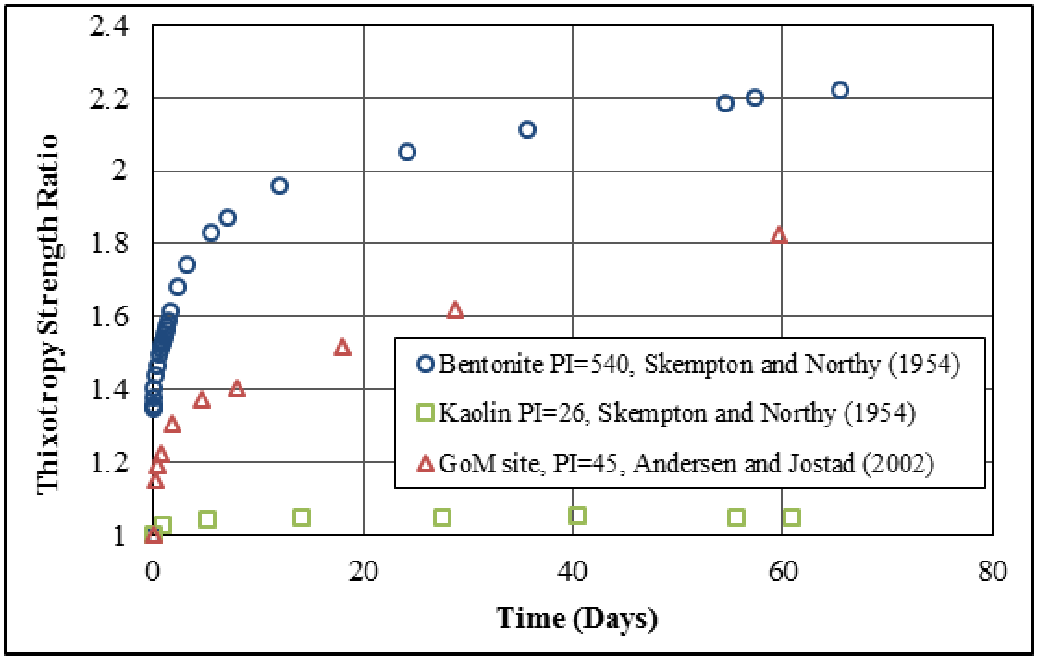

Figure 4.1 Measured thixotropy strength ration vs. time.

Penetration installation of a foundation - such as a skirt foundation, suction caisson, or pile - remolds the soil near the soil-foundation interface, usually leading to a reduction in soil strength. After installation, the shear strength starts to increase with time due to thixotropy and other factors (excess pore water dissipation and increased the horizontal normal effective stress) (Andersen & Jostad, 2002). The shear strength of the soil will recover and increase with time by more than 100% for some cases (Andersen et al., 2008). Figure 4.2 shows data plotted by Andersen and Jostad (2002) using data from (Skemption & Northey, 1952) and NGI files. Thixotropy issues are not limited to field.

Most laboratory model tests use remolded soil, so it is important to understand the strength recovers with time to properly interpret model test data.

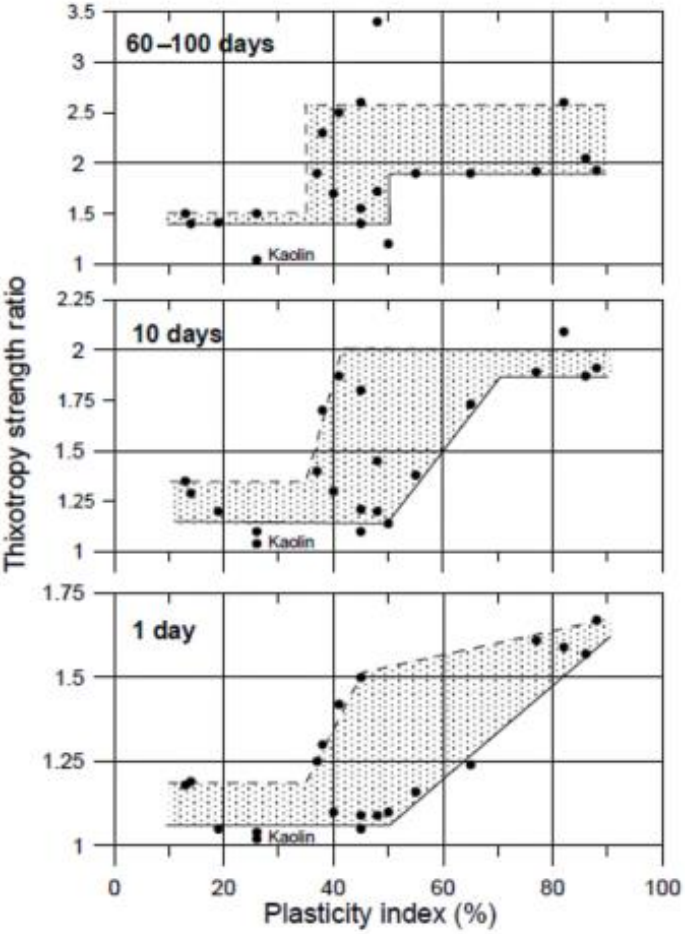

Figure 4.2 Thixotropy strength ratio vs. plasticity (reprinted from Andersen & Jostad, 2002).

Thixotropy increases in soil with increasing sensitivity of the soil (Yang & Andersen, 2015). According to Terzaghi (1944), sensitivity of the clay can be defined as the ratio between the undisturbed (intact) strength $s_{u(undisturbed)}$ and remolded strength (s_{ur}).

It is not an easy number to measure, especially since inadvertent drying during curing can lead to an increase in soil strength due to consolidation, as opposed to thixotropic strength gain at constant water content. Furthermore, the equipment used and method of calculation may affect the estimates. Therefore, the acquired sensitivity after time (AS_t) is predicted instead of the sensitivity as presented by Skemption and Northey (1952).

4.2. Background

Skemption and Northey (1952) presented data for several minerals and natural clays, using the laboratory vane. They concluded that thixotropy of natural clays is likely to depend strongly on their mineral composition. Kaolin exhibited almost no thixotropy, illite showed a moderate strength increase, and bentonite showed a large strength gain after a very short time period and continued to gain strength even after a year.

Santos Soage (2011) did a study on thixotropy of marine soft clays. The study showed that there is a good correlation between plasticity index and thixotropy strength ratio. The study indicated that a construction of a three axis plot formed by liquidity index, plasticity index, and thixotropy strength ratio containing data of three reference single mineral clays should provide a good framework for selection of thixotropy strength ratios for geotechnical design. However, no firm conclusion can be drawn because of the limited testing program.

Andersen and Jostad (2002, 2004) and Lunne and Andersen (2007) showed thixotropy strength ratios after 1 day, 10 days, and 60–90 days for a number of natural clays. They observed that there is some relationship between thixotropy strength ratio and activity, and between thixotropy strength ratio and plasticity; however, the data showed a considerable scatter (Figure 4.2).

Yang and Anderson (2016) In this study, the thixotropy strength ratio of marine clays were studied based on marine clays from 15 offshore sites in Norway, Ghana, Angola, Egypt, India, and Malaysia. The thixotropy strength ratio has been correlated with the following parameters: activity, plasticity index, liquidity index, sensitivity, and water content. The best correlations seem to be between thixotropy strength ratio and liquidity index and between thixotropy strength ratio and water content. Further study is needed for high-sensitivity marine clays.

4.3. Research Objective and Scope

This research presents the results of single gravity displacement-controlled laboratory model tests, which are used to perform the cyclic T-bar and miniature vane shear tests. In this study, monotonic T-bar tests, cyclic T-bar tests, as well as vane shear tests were conducted to find:

6) The gain in undrained shear strength with time using cyclic T-bar tests (s_{u_t}),
7) The gain in undrained shear strength with time using vane shear tests ($s_{u\_t(MVT)}$),
8) Acquired sensitivity of soil using cyclic T- bar ($AS_{t(T\text{-}bar)}$) and how it is affected over time,
9) Soil sensitivity using vane shear tests ($A_{St(MVT)}$) and how it is affected over a prolonged period of time, and
10) Cyclic T-bar and vane shear results compared with other existing results.

4.4. Test Program

The test program consists of four series of tests. The first series is the monotonic T-bar tests, which is performed to find the undrained shear strength profile for GoM clay with different moisture water content as presented in Table 4.1. The second series of tests is the cyclic T-bar tests as shown in Table 4.1. The third series of tests is miniature vane shear tests (MVTs), which are conducted to find a relationship between the undrained shear strengths and the moisture water contents (Table 4.1). Table 4.1 presents the fourth series of miniature vane shear tests, which consisted of a total of 12 tests. A total of 37 tests are conducted in this study.

Table 4.1 Summary of the second thrust area test program.

Series No.	Test No.	Loading rate	Test description
1	1-8	20 mm/sec	Monotonic T-bar tests with different water contents
2	9		Cyclic T-bar test at time period of 0 hours
	10		Cyclic T-bar test at time period of 100 minutes
	11		Cyclic T-bar test at time period of 1 day
	12		Cyclic T-bar test at time period of 2 days
	13		Cyclic T-bar test at time period of 4 days
	14		Cyclic T-bar test at time period of 6 days
	15		Cyclic T-bar test at time period of 8 days

Table 4.1 Continued.

Series No.	**Test No.**	**Loading rate**	**Test description**
	16	20 mm/sec	Cyclic T-bar test at time period of 10 days
	17		Cyclic T-bar test at time period of 20 days
	18		Cyclic T-bar test at time period of 114 days
3	19-25	ASTM	Miniature vane shear Tests with different water contents
4	26		MVT at time period of 0 hour
	27		MVT at time period of 1 hour
	28		MVT at time period of 3 hours
	29		MVT at time period of 1 day
	30		MVT at time period of 2 days
	31		MVT at time period of 4 days
	32		MVT at time period of 6 days
	33		MVT at time period of 8 days
	34		MVT at time period of 10 days
	35		MVT at time period of 20 days
	36		MVT at time period of 31 days
	37		MVT at time period of 112 days

4.5. Full-Flow Penetrometer, T-bar Penetrometer

Full-flow penetrometers in use today are either spherical (ball) or cylindrical (T-bar) as a part of offshore geotechnical site investigations. A T-bar with a diameter of 12.7 mm (0.5 inches) and length of 50.8 mm (2 inches) used for this study to predict the undrained shear strength of the Gulf of Mexico clay with time (see chapter 2 for more details). It is fabricated to be connected to a load cell. The T-bar rod is connected to the robotic actuator and to the data acquisition system. The penetration rate is 20 mm/sec (0.787 in/sec) to present undrained loading condition (Langford & Aubeny, 2008; Yafrate el al., 2009). Furthermore, some previous empirical studies to estimate $N_{T\text{-}bar}$ after using field vane shear tests (FVTs) as reference have reported that for soils of low to moderate sensitivity (S_t), the $N_{T\text{-}bar}$ ranges 10.9-12.7 (M. Randolph, 2004). All undrained shear strengths are interpreted by using a T- bar bearing factor of 10.5. Accurate measurement of test soils is essential to properly interpret thixotropy effect with time. T-bar tests are conducted directly on test bed soils to provide independent measurements of the undrained shear strength of the soil. Figure 2.11 shows the setup of the T-bar model.

Miniature vane shear test apparatus and clay preparation can be found in Chapter 2, and Chapter 3, respectively.

4.5.1. Full-Flow Penetrometer Penetration Resistance

During penetration the T-bar penetrometer into the soil, there is a secondary factor affecting the measured resistance of the full-flow penetrometer (T-bar penetrometer). This factor is the difference in overburden pressure, which acts above and below the T-bar penetrometer. This factor relates directly to the penetrometer area ratio (A_s/A_p) (Yafrate et al., 2009). The penetrometer area ratio is the ratio between the projected area of the T- bar rod (A_R) and the projected area of the T-bar probe (A_p). The A_s/A_p is used around 1:10 as recommended by DeJong et al. (2010). Randolph et al. (2007) used the following correction to find the net penetration of the penetrometer ($q_{T\text{-}bar(net)}$) as illustrated in Equation 4.1.

$$q_{T\text{-}bar(net)} = q_{T\text{-}bar(m)} - [\sigma_{v0} - u_0 (1 - a_0)]\, A_R/A_p$$ **Equation 4.1**

where: $q_{T\text{-}bar(m)}$ is the measured penetration resistance, σ_{v0} is the total overburden stress, u_0 is the pore water pressure, and a_0 is the area ratio (0.7-0.9) according to Randolph et al. (2007). The area ratio is used as 0.7 in this study. Figure 4.3 shows a comparison between the measured and the net penetration resistance. It can be seen from Figure 4.3 that there is a small correction between the measured and net penetration resistances. According to Yafrate et al. (2009), there are some advantages of using full-flow penetrometer in soft clays comparing with conventional piezocone penetration test (CPTu) due to the large projected penetrometer area which leads to improve the accuracy of measurements in a very soft clay and the needed correction for overburden stress is small comparing with CPTu correction.

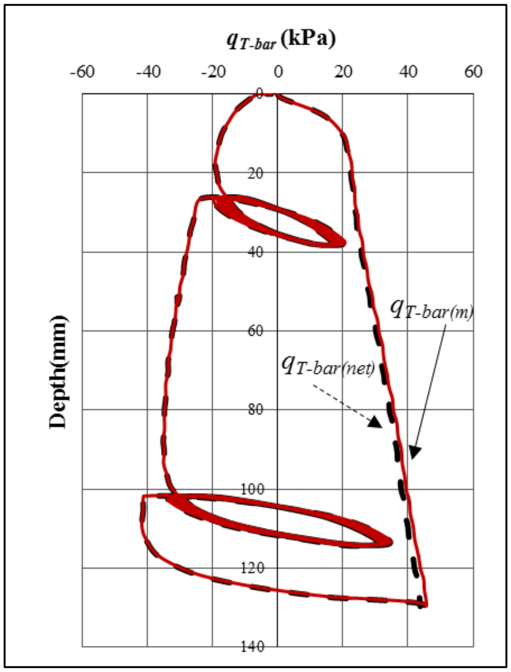

Figure 4.3 Net and measured penetration resistance.

4.6. Undrained Shear Strength of The Soil

Two series in total are performed at the geotechnical laboratory at Texas A&M University for the second thrust area. The first series consists of cyclic T-bar penetrometer tests are carried out to predict the thixotropy effect during different periods of time (prolonged period of time) and to find the degradation in the penetration resistance while increasing the number of cycles. After reaching the steady state, the remolded undrained shear strength can be estimated. Two locations are chosen to apply the cyclic loading along penetrating the T-bar penetrometer; the first location is at a penetration depth of 8 T-bar diameter (*D*) (deep penetration), and the second location is at a shallow penetration of 1.4 *D* (see Figure 4.3).

The second series is the vane shear test at a specific depth and constant water content. The vane has a diameter (D_v) of 25.4 mm (1.0 in) and height (H_v) of 50.8 mm (2.0 in) (see Figure 2.9). This series is aimed to predict the undrained shear strength and the remolded undrained shear strength during a prolonged period of time of about 4.0 months. In addition, they aim to find the sensitivity during the aging period.

4.6.1. Undrained Shear Strength Using Full-Flow Penetrometer

The undrained shear strength of the full-flow, T-bar, s_u defines as the net penetration resistance $q_{T\text{-}bar(net)}$ divided by the T-bar bearing factor ($N_{T\text{-}bar}$) as shown in Equation 4.2. The suggested $N_{T\text{-}bar}$ value is 10.5 (Langford & Aubeny, 2008; Yafrate et al., 2009). Since this research aims to measure the gain in the undrained shear strength due to thixotropy strength recovery with time, Equation 4.3 is used.

$$s_u = q_{T\text{-}bar(net)} / N_{T\text{-}bar} \qquad \textbf{Equation 4.2}$$

$$s_{u\_t} = q_{T\text{-}bar(net)} / N_{T\text{-}bar} \qquad \textbf{Equation 4.3}$$

where: s_u is the undrained shear strength for undisturbed clay, and s_{u_t} is the gain in the undrained shear strength with time.

4.7. Cyclic Full-Flow Penetrometer

Full-flow penetrometers (T-bar and ball penetrometers) are increasingly used to assess the geotechnical offshore undrained shear strength. According to Yafrate et al. (2009), full-flow penetrometers are nowadays widely used in soft clays due to the following advantages: 1) penetrometers have a large projected penetrometer area which leads to improving the accuracy of measurements in a very soft clay and 2) the needed correction for overburden stress is small comparing with CPTu correction.

This section shows some of the second series of the test program. Equation 4.3 uses to find the gain undrained shear strength with time. It is clear from Figure 4.4 to Figure 4.12 that there are some variations in the net penetration resistance and the extraction resistance due to the thixotropy effect. By looking closely at Figure 4.5 to Figure 4.12 for the shallow and the deep cycles, it can be seen that the degradation in the resistance increases while increasing the number of cycles. Furthermore, the greatest degradation in resistance is observed during the first cycle, and it continued to slightly degrade for a few cycles (around 5-10 cycles) to reach the steady-state. This pattern of degradation has also been observed by Hodder et al. (2008) and Yafrate et al. (2009).

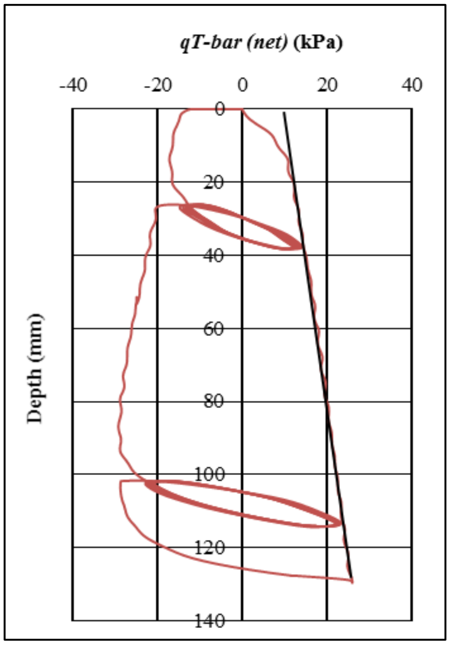

Figure 4.4 Directly after mixing.

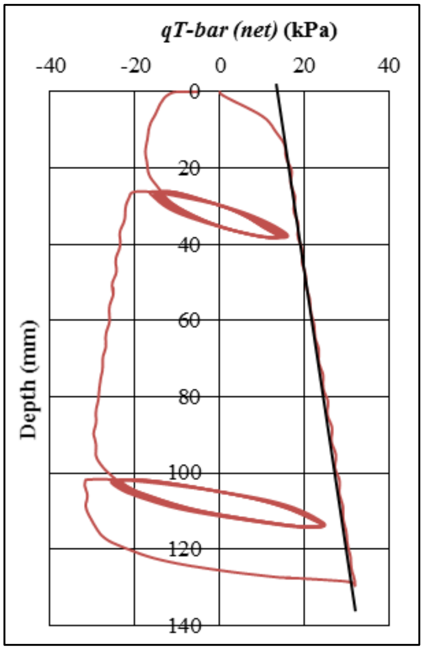

Figure 4.5 Two days after mixing the soil.

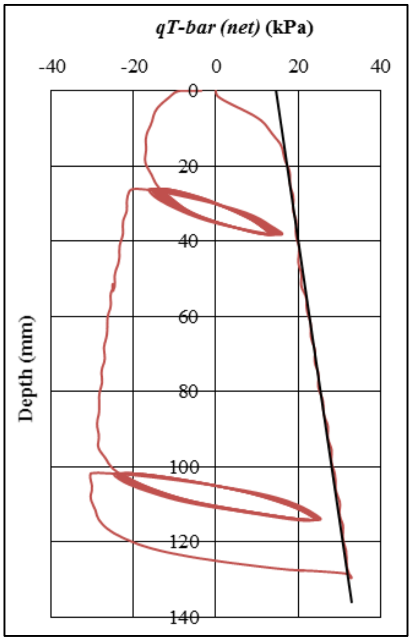

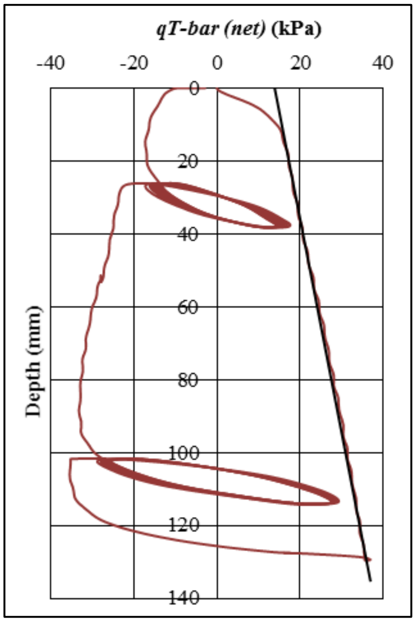

Figure 4.6 Four days after mixing the soil.

Figure 4.7 Six days after mixing the soil.

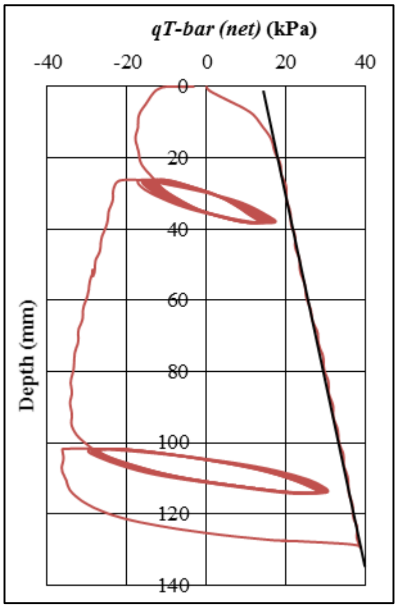

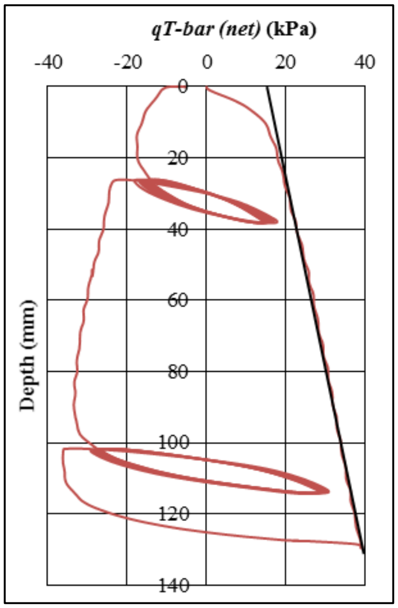

Figure 4.8 Eight days after mixing the soil.

Figure 4.9 Ten days after mixing the soil.

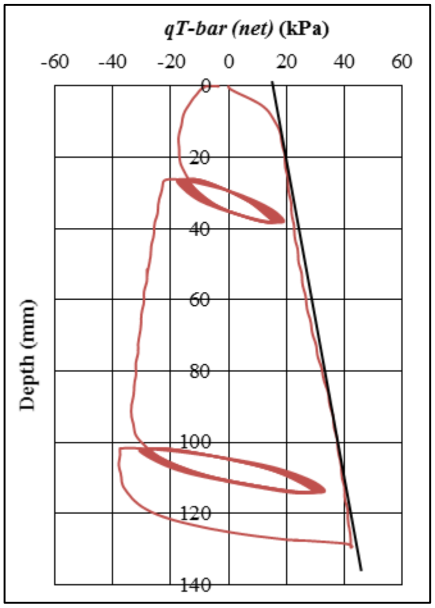

Figure 4.10 22 days after mixing the soil. **Figure 4.11 31 days after mixing the soil.**

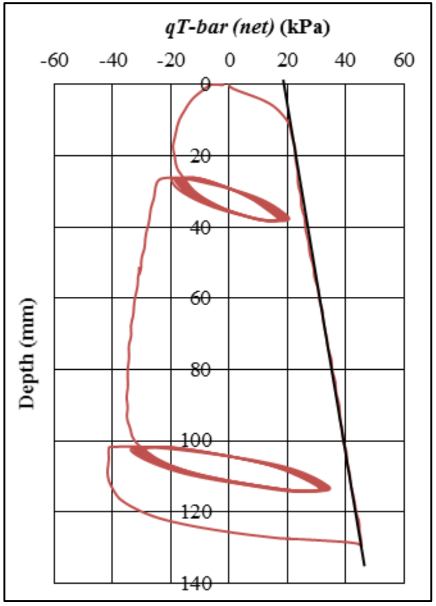

Figure 4.12 114 days after mixing the soil.

4.7.1. Undrained Shear Strength Using Miniature Vane Shear Tests

Since the vane shear test is widely used in geotechnical laboratory and in situ investigations to measure the undisturbed strength ($s_{u(undisturbed)}$), the remolded strength

($s_{u(MVT)r}$), and the sensitivity of soil (S_t) which is the ratio between the undisturbed strength and the remolded strength. In addition, vane shear tests are used as a reference to estimate the sensitivity of the soil. Yafrate et al. (2009) used field vane shear tests (FVTs) data as a reference to estimate the sensitivity of soil and then to evaluate the T-bar remolded bearing factor (see Equation 4.8). Therefore, miniature vane shear tests data are used in this study to provide an alternative measurement of undrained shear strength for comparison with the T-bar results. Series two of MVTs are performed to evaluate thixotropic effects under prolonged time periods, including acquired sensitivity and the percent thixotropic strength regain. The second series consists of 12 tests are all conducted on the same soil under a constant moisture water content of (~76%). Equation 4.4 and Equation 4.5 are used to find the undrained shear strength ($s_{u\_t(MVT)}$) according to the ASTM D4648/D4648M-16 (2016).

Vane tests applies a torque at a constant rate of rotation as explained in ASTM D4648/D4648M-16 (2016).

$$s_{u\_t(MVT)} = T / K \qquad \textbf{Equation 4.4}$$

$$K = \frac{\pi D_V{}^2 H_V}{2 * 10^9}\left[1 + \frac{D_V}{3H_V}\right] \qquad \textbf{Equation 4.5}$$

Figure 4.13 to Figure 4.23 show some of the MVT results during curing periods of the soil. It can be seen that the undrained shear strength increased during the soil curing due to thixotropy effect. Furthermore, the remolded strength, $s_{u(MVT)r}$, increases slightly while increasing the curing period as shown in Figure 4.23 and Figure 4.14. DeGroot et al. (2010) captured some differences between using two different methods to remold the soil which are remolding the soil using by hand only and both by hand and vane shear test together. In addition, the results show that the undrained shear strength increases immediately after mixing the soil (Figure 4.23).

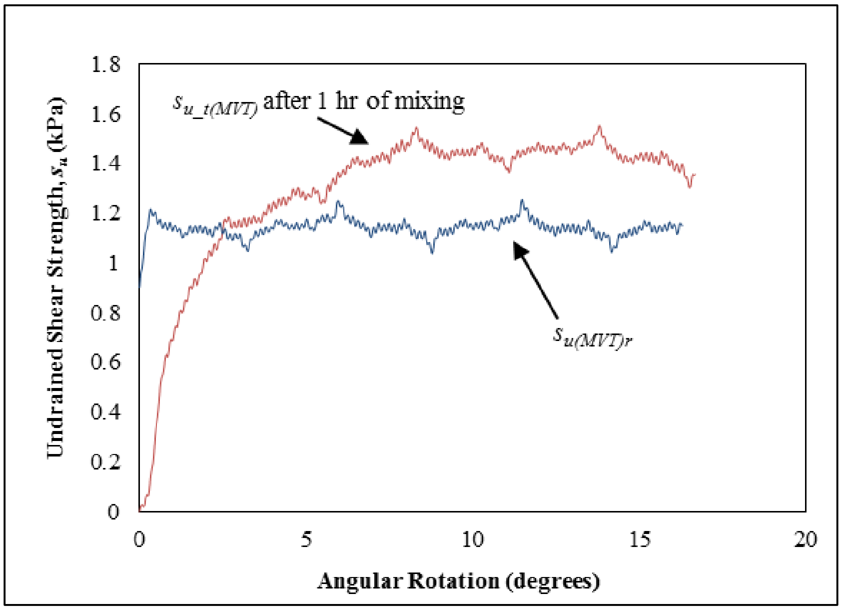

Figure 4.13 Vane shear tests MVTs (1 hour after mixing).

Figure 4.14 Vane shear tests MVTs (3 hours after mixing).

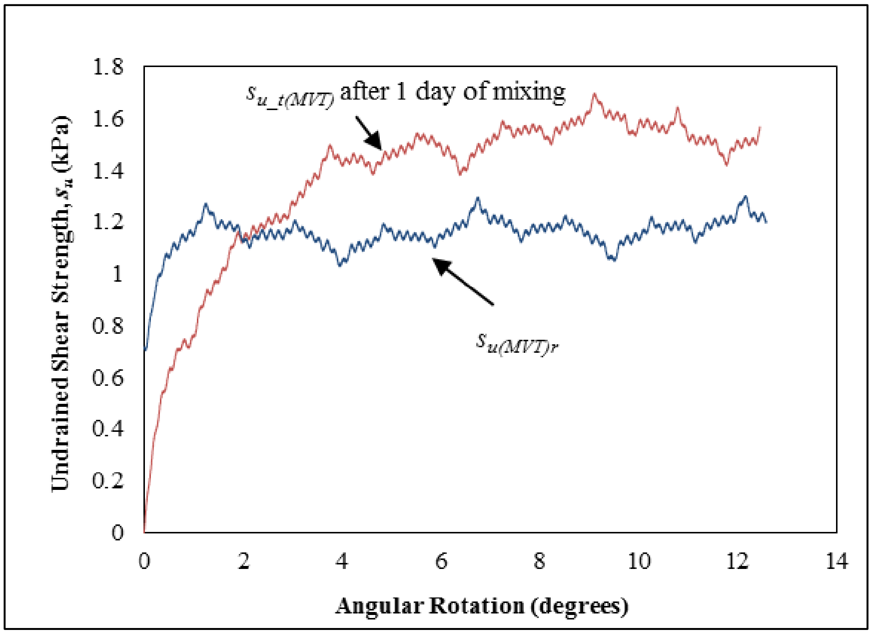

Figure 4.15 Vane shear tests MVTs (1 day after mixing).

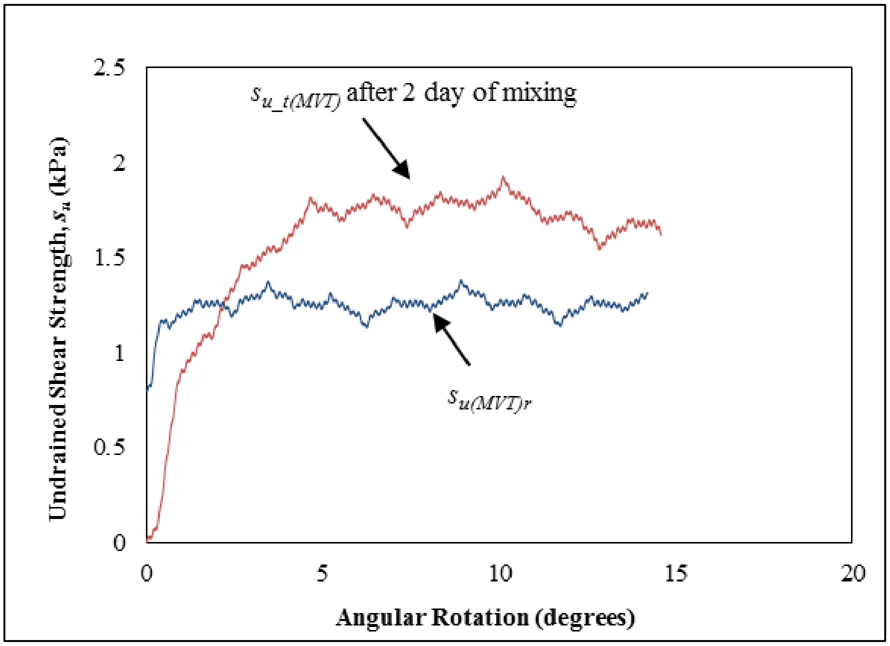

Figure 4.16 Vane shear tests MVTs (2 days after mixing).

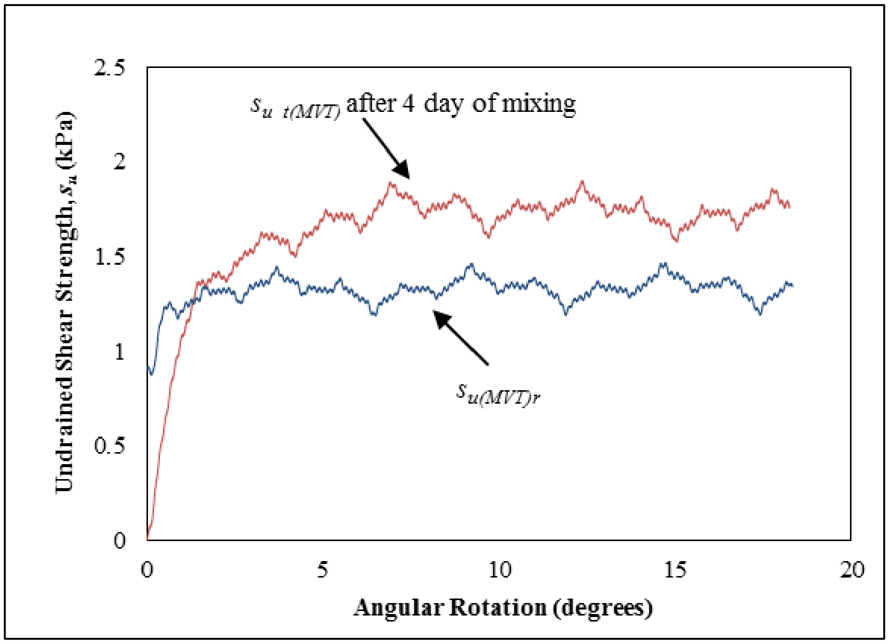

Figure 4.17 Vane shear tests MVTs (4 days after mixing).

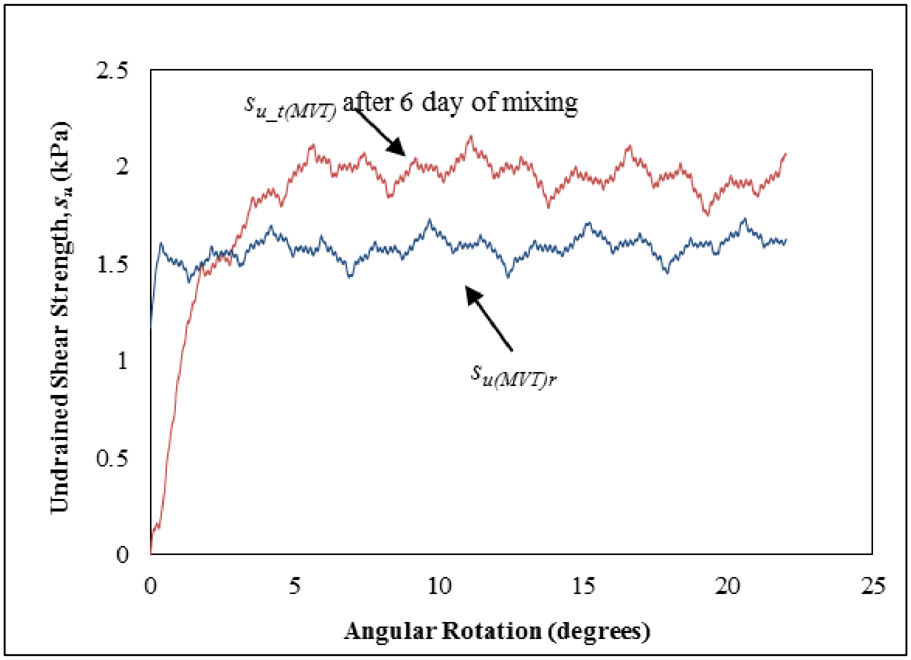

Figure 4.18 Vane shear tests MVTs (6 days after mixing).

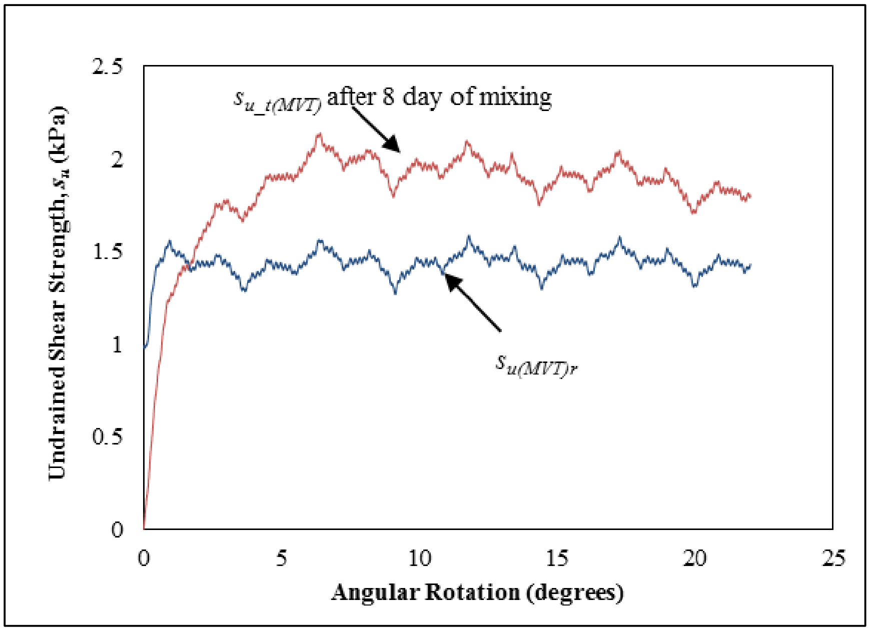

Figure 4.19 Vane shear tests MVTs (8 days after mixing).

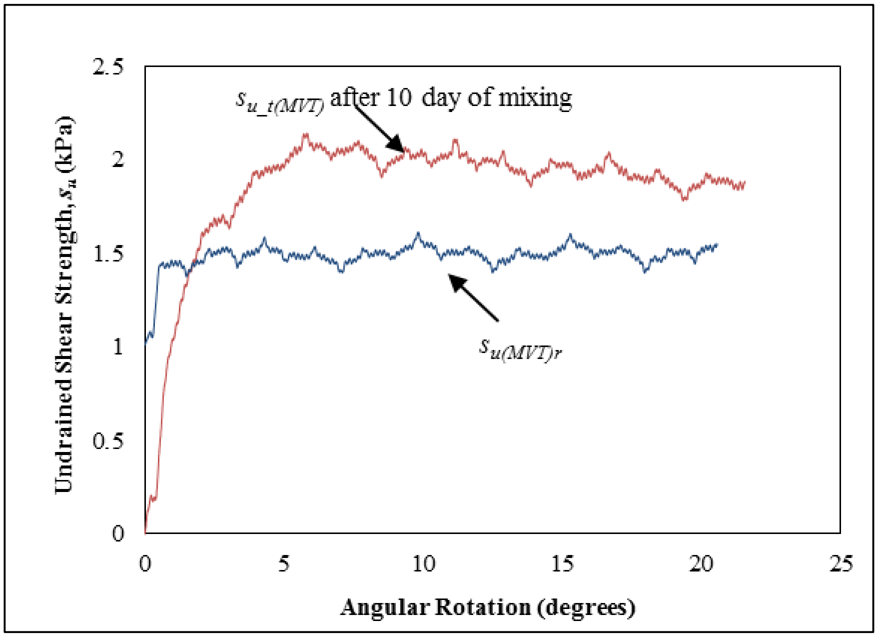

Figure 4.20 Vane shear tests MVTs (10 days after mixing).

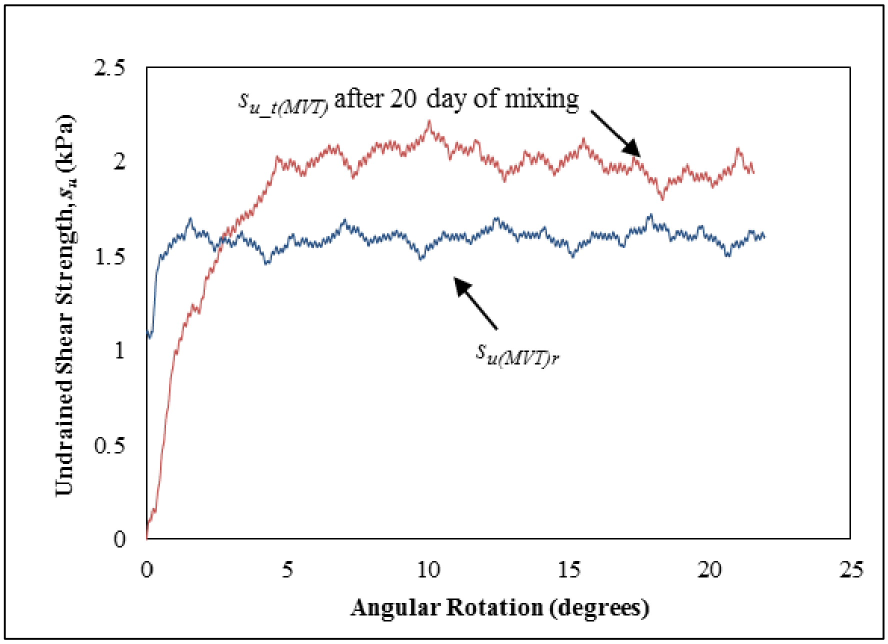

Figure 4.21 Vane shear tests MVTs (20 days after mixing).

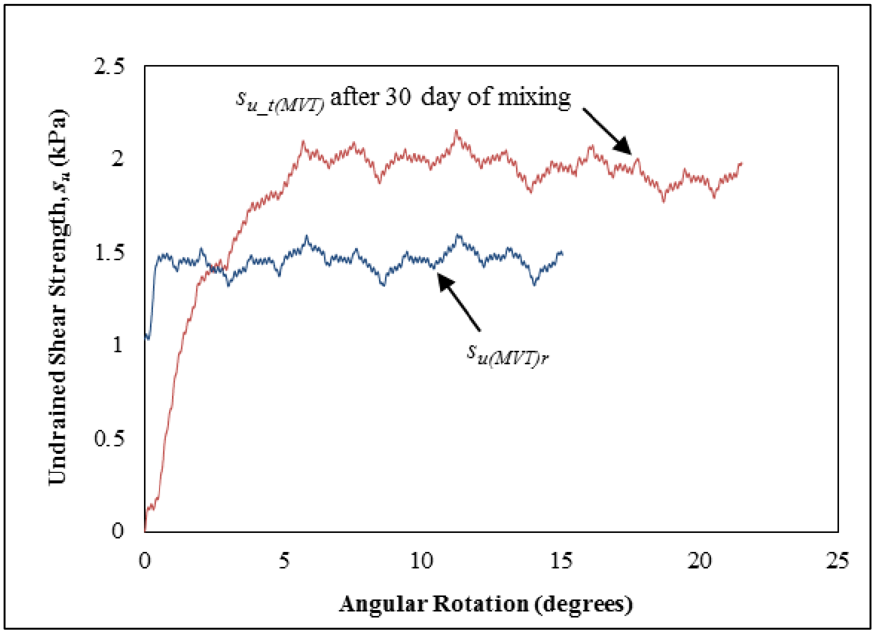

Figure 4.22 Vane shear tests MVTs (30 days after mixing).

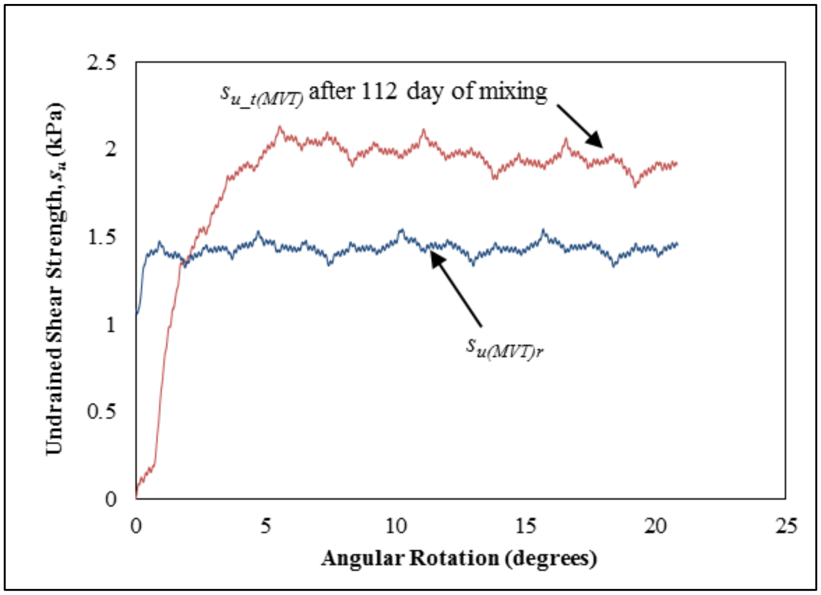

Figure 4.23 Vane shear tests MVTs (112 days after mixing).

5.2.3. Remolded Undrained Shear Strength Using MVTs

According to ASTM D4648/D4648M-16, (2016), the undrained shear strength for the miniature vane test should be measured by rotating the vane rapidly for a minimum of

5 to 10 complete revolutions. Thereafter, a vane test needs to be performed within 1 minute after remolding the soil to find the maximum remolded torque (T_r). In this study, about seven complete revolutions are conducted to estimate the remolded undrained shear strength ($s_{u(MVT)r}$). Equation 4.6 is used to predict the remolded undrained shear strength, $s_{u(MVT)r}$.

$$s_{u(MVT)r} = T_r / K \qquad \textbf{Equation 4.6}$$

4.8. Remolded Undrained Shear Strength

Two methods are followed to measure the remolded undrained shear strength; the first one is from using cyclic full-flow penetrometer test (s_{ur}), and the second one is from using the MVTs, $s_{u(MVT)r}$.

4.8.1. Remolded Undrained Shear Strength Using T-Bar Tests

The remolded undrained shear strength is the ratio between the remolded penetration resistance (usually obtained after reaching the steady state ~ 5-10 cycles as shown in Figure 4.4 to Figure 4.12 and Figure 4.24 a-b) and the remolded shear strength factor ($N_{T\text{-}bar(r)}$) (Equation 4.7). Figure 4.24 shows normalized penetration resistance (penetration resistance at cycle number (n) ($q_{T\text{-}bar(n)}$) divided by the initial net penetration $q_{T\text{-}bar(net)}$) versus the number of cycles. According to Yafrate et al. (2009) and DeJong, et al. (2010), the remolded shear strength factor $N_{T\text{-}bar(r)}$ is different from the initial T-bar shear strength factor, $N_{T\text{-}bar}$, and it must be evaluated differently form the $N_{T\text{-}bar}$ where the $N_{T\text{-}bar(r)}$ increases as the soil sensitivity increases. Yafrate et al. (2009) presented two empirical equations to predict the $N_{T\text{-}bar(r)}$. The first equation is by using the sensitivity from FVTs ($S_{t(FVT)}$) data as shown in Equation 4.8. The second equation is by using the extraction ratio ($q_{T\text{-}bar(net)}/q_{T\text{-}bar(ext)}$).

where: $q_{T\text{-}bar(ext)}$ is the extraction resistance at the same depth of the $q_{T\text{-}bar(net)}$ as presented in Equation 4.9.

$$s_{ur} = q_{T\text{-}bar(r)} / N_{T\text{-}bar(r)}$$ **Equation 4.7**

$$N_{T-bar(r)} = 12 + \frac{5.5}{1+\left(\frac{S_{t(FVT)}}{6}\right)^{-3}}$$ **Equation 4.8**

$$N_{T-bar(r)} = 12 + \frac{5.5}{1+\left(\frac{q_{T-bar(net)}/q_{T-bar(ext)}}{1.8}\right)^{-20}}$$ **Equation 4.9**

In this study, two methods are used to estimate the $N_{T\text{-}bar\ (r)}$. In the first method, the T-bar bearing factor will assume to be equaled to ($N_{T\text{-}bar}$ = 10.5). The second method is to use Equation 4.8 to predict the $N_{T\text{-}bar\ (r)}$. The Equation 4.9 will not be used in this study. The sensitivity that is used in Equation 4.8, it is taken from the MVTs data that are conducted in this study. A comparison is made to compare these two different methods, and how that affects the remolded undrained shear strength and the acquired sensitivity of clay with time.

4.8.2. Remolded Undrained Shear Strength Using MVTs

According to ASTM D4648/D4648M-16, (2016), the undrained shear strength for the miniature vane test should be measured by rotating the vane rapidly for a minimum of 5 to 10 complete revolutions. Thereafter, a vane test needs to be performed within 1 minute after remolding the soil to find the maximum remolded torque (T_r). In this study, about seven complete revolutions are conducted to estimate the remolded undrained shear strength ($s_{u(MVT)r}$). Equation 4.10 is used to predict the remolded undrained shear strength, $s_{u(MVT)r}$.

$s_{u(MVT)r} = T_r / K$ **Equation 4.10**

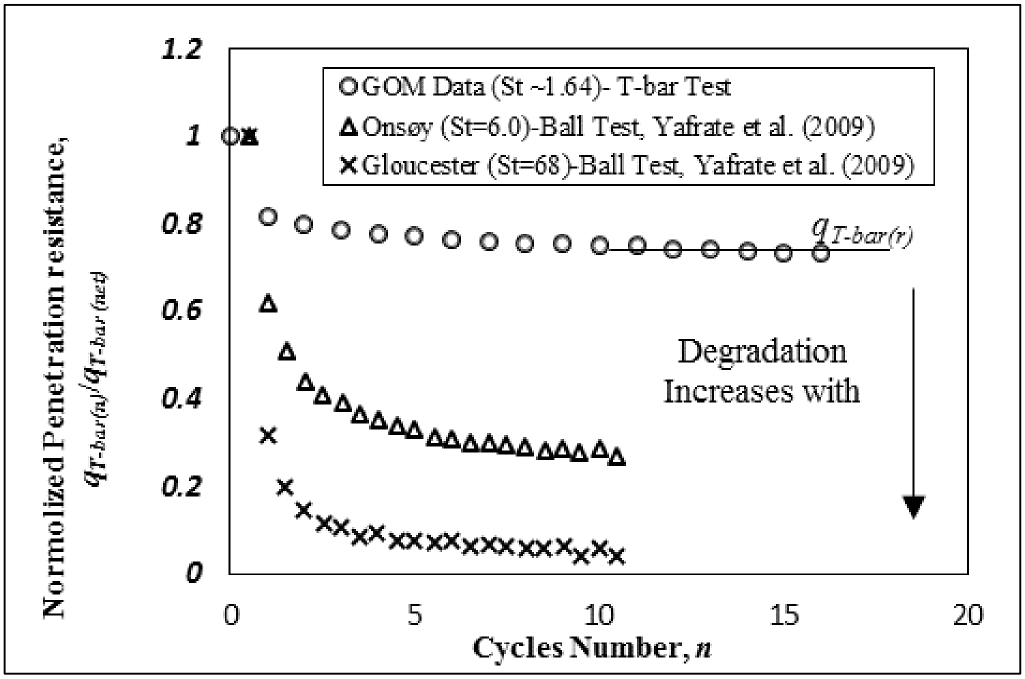

a) Comparison with previous studies.

Figure 4.24 Normalized penetration resistance vs. the number of cycles.

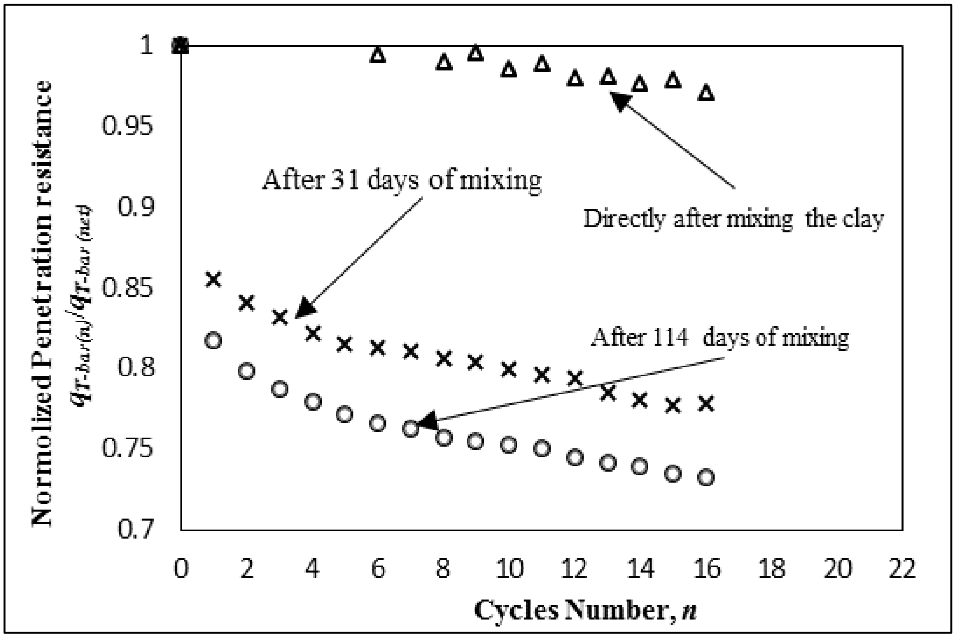

b) Some of the T-bar results for different time of curing.

Figure 4.24 Continued.

4.9. Penetration Resistance Degradation

The cyclic T-bar penetrometer tests aim to find the remolded undrained shear strength of the GOM clay. Figure 4.24 a shows normalized penetration resistance (penetration resistance at cycle number (n) ($q_{T\text{-}bar(n)}$) divided by the initial net penetration $q_{T\text{-}bar(net)}$) versus the number of cycles of one of the T-bar data and some other studies conducted using full-flow penetrometers at different sites. Moreover, Figure 4.24a presents how the undrained shear strength of the full-flow (T-bar and ball) penetrometers decreases with increasing the sensitivity. Figure 4.24b presents a comparison between normalized penetration resistances versus the number of cycles under different periods of time. It shows how the normalized penetration resistance decreased with an increase in the curing period. In other words, when the sensitivity of soil increases due to thixotropy, the normalized penetration resistance decreases. In addition, Figure 4.24b shows how the sensitivity increases as the time of curing increases. Referring to plot (b) of Figure 4.24, it is clear that almost no degradation occurs for the cyclic test at time 0 hours due to remolding the soil directly before conducting the test. This test is conducted directly after remolding the soil by the drill mixer; therefore, there is no degradation in strength. Proceeding with the curing period, the degradation is captured to be high at the first cycle and it continued to slightly degrade to reach the steady state at about ~5-10 cycles as shown in plot (b) of Figure 4.24.

4.10. Sensitivity And Acquired Sensitivity

According to Terzaghi (1944), sensitivity of the clay can be defined as the ratio between the undisturbed strength $s_{u(undisturbed)}$ and remolded strength (s_{ur}). It is not an easy number to predict, especially after remolding the soil and waiting for the curing period to occur. Furthermore, it can be estimated differently depending on the used equipment and the used methods of calculations. Since this research uses remolded GoM clay (disturbed soil), the acquired sensitivity with time (A_{St}) is evaluated instead of the sensitivity as presented by Skemption and Northey (1952) and as shown in Equation 4.11 (for MVTs) and Equation 4.12 (for T-bar tests), which is essentially the same as the thixotropy strength ratio definition. Therefore, a relationship between these two methods is presented to find a good way to estimate the acquired sensitivities with time.

$A_{St(MVT)} = s_{u\_t(MVT)} / s_{u(MVT)r}$ **Equation 4.11**

$A_{St(T\text{-}bar)} = s_{u\_t} / s_{ur}$ **Equation 4.12** where: $AS_{t(MVT)}$ is the estimated acquired sensitivity from MVTs, and $AS_{t(T\text{-}bar)}$ is the estimated acquired sensitivity using from T-bar penetrometer tests.

4.10.1. Acquired Sensitivity Using MVTs

Since the vane shear tests are widely used in the geotechnical investigations in clay and silt soil, the miniature vane shear apparatus is used to estimate the acquired sensitivity of the clay soil in this research. For miniature vane shear tests, the ASTM D4648/D4648M-16, (2016) procedure is followed to measure the undrained shear strength $s_{u\_t(MVT)}$ and the remolded undrained shear strength $s_{u(MVT)r}$ as explained in the previous sections. Equation 4.11 is used to measure the acquired sensitivity $AS_{t(MVT)}$ with time.

The $s_{u(MVT)r}$ is used as constant number, which is found after remolding the soil and conducting the test at time of 0.0 hour. Equation 4.10 shows the variations in the acquired sensitivities with time. It can be seen that there is a large increase in the acquired sensitivity during the first few hours ~3 hours where the increase in the acquired sensitivities is around 23%. The strength continues to sharply increase to be around 69% after 10 days of the mixing. After 20 days to 112 days of mixing clay, the acquired sensitivities continues to slightly increase to be at around 81%. A sensitivity of 1.81 is used in Equation 4.8 to find the remolded T-bar factor $N_{T\text{-}bar(r)}$.

4.10.2. Acquired Sensitivity Using Full-Flow Penetrometer

As explained in the sensitivity section, the acquired sensitivity of the clay using a full-flow penetrometer is the ratio of the undrained shear strength s_{u_t} to the remolded undrained shear strength s_{ur} with time. The procedure that is followed to evaluate the remolded strength for the T-bar tests is from the degradation profile of the remolded strength after reaching the steady-state ~ 5-10 cycles as shown in Figure 4.24b. The T- bar remolded bearing factor is firstly used as ($N_{T\text{-}bar(r)}$= $N_{T\text{-}bar}$ =10.5), and then it is secondly used from Equation 4.8 (Yafrate et al., 2009). Therefore, there is ambiguity in the determination of s_{ur}. The Acquired sensitivity from MVTs data after 112 days of curing is used to find $N_{T\text{-}bar(r)}$ in Equation 4.8. The $N_{T\text{-}bar(r)}$ from Equation 4.8 is found to be (12.15). Figure 4.25 shows a comparison of the acquired sensitivities using $N_{T\text{-}bar(r)}$ equals to 10.5 and 12.15. It is clear from Equation 4.10 that the results from the MVTs and T-bar (for $N_{T\text{-}bar(r)}$ =12.15) gave a very good matching, especially for the first 30 days. The results of the acquired sensitivities using the $N_{T\text{-}bar(r)}$ = 10.5 are a little underestimated comparing with the MVTs results and T-bar results using $N_{T\text{-}bar(r)}$ corrected (Equation 4.8). Therefore, the remolded T-bar bearing factor $N_{T\text{-}bar(r)}$ needs to be corrected to estimate the remolded undrained shear strength for penetrometers. Equation 4.8 might be adjusted in the future based on additional after obtaining additional data. Furthermore, Figure 4.25 shows a direct relationship between the acquired sensitivity and the time. When the curing period increases, the acquired sensitivity increases.

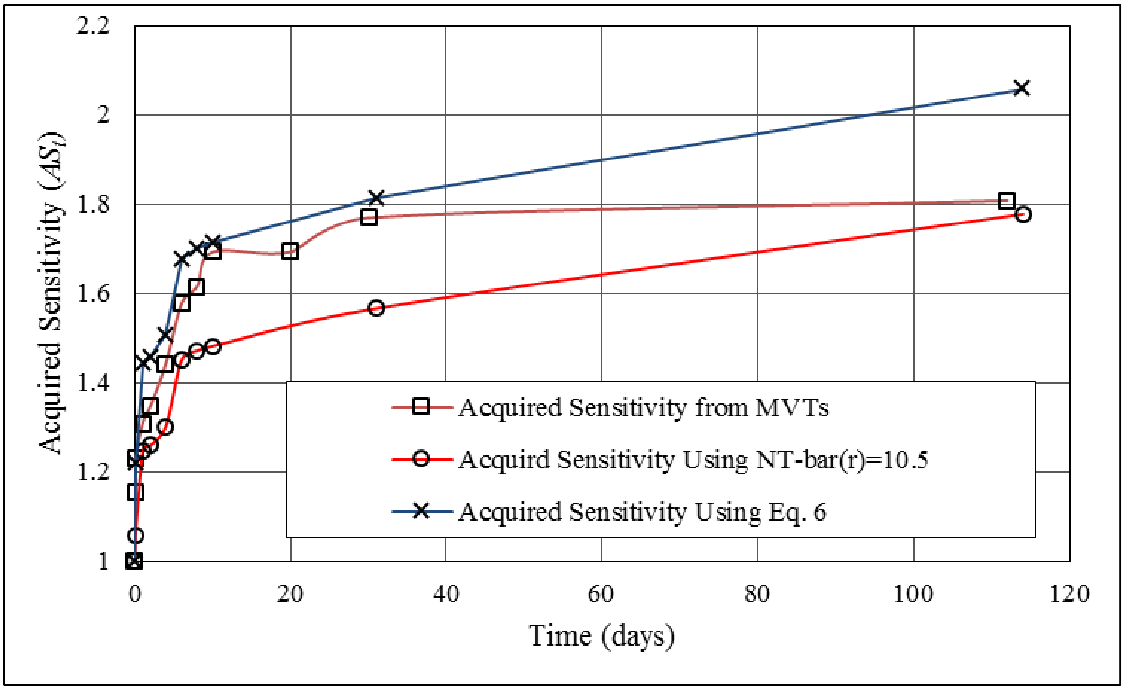

Figure 4.25 Comparison of Acquired sensitivity for different studies vs. time.

4.11. The Percentage Of Thixotropy Strength Regain

The percentage thixotropy regain defined as the difference between the gain in shear strength and the remolded shear strength divided by the remolded shear strength, and all times 100 ($(\frac{s_{u\_t(MVT)} - s_{u(MVT)r}}{s_{u(MVT)r}})*100$ for MVTs, and $(\frac{s_{u\_t} - s_{ur}}{s_{ur}})*100$ for T-bar tests).

Most of the data from previous studies are limited to 60 days. In this paper, the testing program lasted to 114 days. From Figure 4.26, the results show that the undrained shear strength for both cyclic T- bar tests for different embedment depths and MVTs increases immediately after mixing (remolding) the soil. For both tests, the gain in strength ranges from about 0 to 30% during the first day and it continues to increase sharply to about 45% (for T-bar tests) and about 57% (for MVT) over the first 6 days. This gain in strength continues to increase gradually to about 78% after 114 days for the T-bar tests and to about 81% after 112 days for vane share test. In addition, Figure 4.26 shows a comparison between the T-bar tests, MVTs, and previous studies. These results show a very good agreement with the existing results for the first 60 days as they are limited (Andersen & Jostad, 2002; Jeanjean, 2006). As can be seen, there is a very good agreement between the results (the T-bar and miniature vane shear tests) and the previous results, especially for the first 30 days. It is worth mentioning that the gain in strength continues to increase after the prolonged periods of time as can be seen from Figure 4.26. Therefore, a future study should be conducted to cover more than 114 days of curing time to better understand the prolonged time effect on the thixotropy.

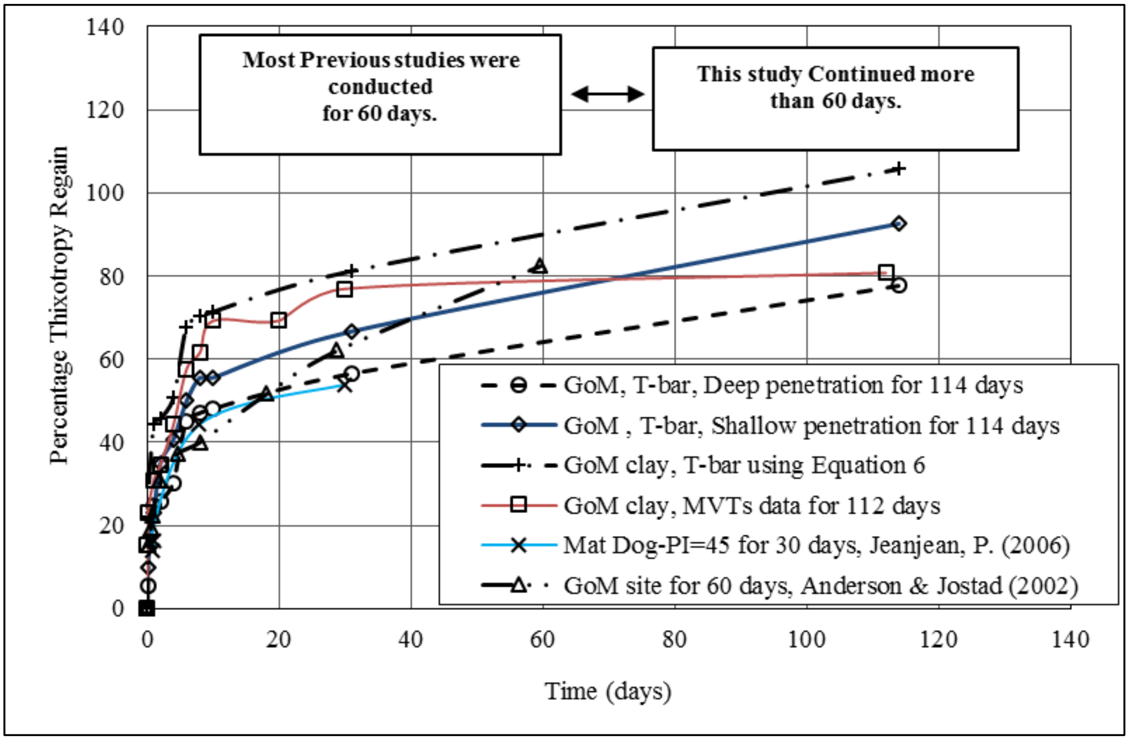

Figure 4.26 Percentage thixotropy regain vs. time.

4.12. Nomenclature

a_0	Area Ratio
A_c	Activity of Soil
A_p	Projected Area Of The T-Bar Probe
A_R	Projected Area Of The T- Bar Rod
AS_t	Acquired Sensitivity
$AS_{t(MVT)}$	Acquired Soil Sensitivity Using Vane Shear Tests
$AS_{t(T\text{-}bar)}$	Acquired Sensitivity Of Soil Using Cyclic T-bar
CPTu	Conventional Piezocone Penetration Test
D	T-bar Diameter
D_v	Vane Diameter
FVTs	Field Vane Shear Tests
GoM clay	Gulf of Mexico clay
H_v	Measured Height of The Vane Blade
I_P	Plasticity Index
K	Vane Blade Constant
MVT	Miniature Vane Test
MVTs	Miniature Vane Tests
$N_{T\text{-}bar}$	T-bar Bearing Factor
$N_{T\text{-}bar(r)}$	Remolded T-bar Bearing Factor
N	Number of Cycles
$q_{T\text{-}bar(ext)}$	Extraction Resistance

$q_{T\text{-}bar(m)}$	Measured Penetration Resistance
$q_{T\text{-}bar(n)}$	Penetration Resistance At Cycle Number (n)
$q_{T\text{-}bar(net)}$	Net Penetration Resistance
S_t	Sensitivity of Soil
$S_{t(FVT)}$	Sensitivity From Field Vane Shear Tests
s_u	Undrained Shear Strength
$s_{u(MVT)}$	Undrained Shear Strength Using Miniature Vane Test
$s_{u(MVT)r}$	Remolded Undrained Shear Strength Using Miniature Vane Test
$s_{u(undisturbed)}$	Undisturbed (Intact) Strength
$s_{u\_t(MVT)}$	The Gain In Undrained Shear Strength With Time Using Vane Shear Tests
s_{u0}	Undrained Shear Strength at the surface
s_{ur}	Remolded Undrained Shear Strength
s_{u_t}	Thixotropy Strength Ratio (The Gain In Undrained Shear Strength With Time)
T	Maximum Torque
TDZ	Touch Down Zone
Tr	Maximum Remolded Torque
TRT	Tourqe Transducer
u_0	Pore Water Pressure
w	Embedment depth
$w\%$	Water Moisture Content

σ_{v0} total overburden stress

4.13. References

Al-janabi, H. A., Shlash, K. T., and Fattah, M. Y. (2014). “The Behavior of Bounded Foundations on Sandy Soil Bounded Shallow Foundations on Iraqi Sandy Soil with Different Densities,” In. Saarbrücken: LAP LAMBERT Academic Publishing.

Andersen, K. H., and Jostad, H. P. (2002). “Shear strength along outside wall of suction anchors in clay after installation,” Paper presented at The Twelfth International Offshore and Polar Engineering Conference.

Andersen, K. H., Lunne, T., Kvalstad, T. J., and Forsberg, C. F. (2008). “Deep water geotechnical engineering,” Paper presented at the Proceedings of the 24th National Conference of the Mexican Society of Soil Mechanics, Aguascalientes, Mexico City, Mexico.

ASTM D4318-17e1, A. I. (2017). “Standard Test Methods for Liquid Limit, Plastic Limit, and Plasticity Index of Soils,” West Conshohocken, PA.

ASTM D4648/D4648M-16, A. I. (2016). “Standard Test Methods for Laboratory Miniature Vane Shear Test for Saturated Fine-Grained Clayey Soil,” West Conshohocken, PA.

Beemer, R. D. (2016). “Experimental studies of squat gravity caissons and monopiles for offshore applications,” (Ph.D.), Texas A&M University.

DeGroot, D., Lunne, T., and Tjelta, T. (2010). “Recommended best practice for geotechnical site characterisation of cohesive offshore sediments,” Frontiers in Offshore Geotechnics II, Perth, Australia.

Dejong, J., Yafrate, N., Degroot, D., Low, H. E., and Randolph, M. (2010). “Recommended practice for full-flow penetrometer testing and analysis,” Geotechnical Testing Journal, 33(2), 137-149.

Fattah, M. Y., Shlash, K. T., and Mohammed, H. A. (2014). “Bearing capacity of rectangular footing on sandy soil bounded by a wall,” Arabian Journal for Science and Engineering, 39(11), 7621-7633.

Fattah, M. Y., Shlash, K. T., and Mohammed, H. A. (2014a). “Experimental Study on the Behavior of Bounded Square Footing on Sandy Soil,” Engineering and Technology Journal, 32(5 Part (A) Engineering), 1083-1105.

Fattah, M. Y., Shlash, K. T., and Mohammed, H. A. (2015). “Experimental study on the behavior of strip footing on sandy soil bounded by a wall,” Arabian Journal of Geosciences, 8(7), 4779-4790.

Hodder, M., White, D., and Cassidy, M. (2008). “Centrifuge modelling of riser-soil stiffness degradation in the touchdown zone of a steel catenary riser,” Paper presented at the ASME 2008 27th International Conference on Offshore Mechanics and Arctic Engineering.

Jeanjean, P. (2006). “Setup characteristics of suction anchors for soft Gulf of Mexico clays: Experience from field installation and retrieval,” Paper presented at the Offshore Technology Conference.

Langford, T., and Aubeny, C. P. (2008). “Model Tests for Steel Catenary Riser in Marine Clay,” Paper presented at the Offshore Technology Conference, Houston, Texas, USA.

Lunne, T., & Andersen, K. H. (2007, January). Soft clay shear strength parameters for deepwater geotechnical design. In Offshore site investigation and geotechnics, confronting new challenges and sharing knowledge. Society of Underwater Technology.

Mohammed, H. A. (2013). “Experimental and Statistical Study on the Behavior of Bounded Foundation on Sandy Soil,” (M.Sc. M.Sc. thesis), University of Technology 2013.

Randolph, M. (2004). “Characterization of soft sediments for offshore applications,” Proc. ISC-2 on Geotechnical and Geophysical Site Characterization, 2004.

Randolph, M. F., Low, H. E., and Zhou, H. (2007). “In situ testing for design of pipeline and anchoring systems,” Paper presented at the OFFSHORE SITE INVESTIGATION AND GEOTECHNICS, Confronting New Challenges and Sharing Knowledge.

Santos Soage, R., 2011, “Study in Thixotropy of Marine Soft Clays,” M.S. thesis, Imperial College London, London.

Skemption, A., and Northey, R. (1952). “The Sensitivity of Clays,” Géotechnique, 3(1), 30-53.

Terzaghi. (1944). “Ends and means in soils mechanics,” Eng. Journ. (Canada), 27:608.

Yafrate, N., DeJong, J., DeGroot, D., and Randolph, M. (2009). “Evaluation of remolded shear strength and sensitivity of soft clay using full-flow penetrometers,” Journal of Geotechnical and Geoenvironmental Engineering, 135(9), 1179-1189.

Yang, S., and Andersen, K. H. (2015). “Thixotropy of marine clays,” Geotechnical Testing Journal, 39(2), 331-339.

Mitchell JK (1960). “Fundamental aspects of thixotropy in soils,” *Journal of the Soil Mechanics and Foundations Division*, ASCE, 86(SM3), pp. 19-52.

5. EXPERIMENTAL AND NUMERICAL INVESTIGATION OF THE PERFORMANCE OF PILES AND SUCTION CAISSONS SUBJECTED TO INCLINED CYCLIC LOADING IN COHESIVE SOILS

5.1. Introduction

Suction caissons are often an attractive anchorage solution relative to alternatives such as drag anchors (Colliat et al. 1997). Advantages of suction caissons include: 1) relative ease of installation, 2) reliable predictive methods for load capacity avoid the need for proof load testing, and 3) precise horizontal and vertical positioning.

Suction anchors in moderate water depths can be used for catenary moorings with loading angles generally around 25° or less to provide primarily horizontal loading of the suction anchor (Randolph, 2012). In some cases, the loading angles can be varied depending on the location of the suction pile from the structure. Furthermore, suction piles in soft soils with a large length to diameter ratio can provide interesting solutions for conductor installation (Sparrevik, 2002).

A number of previous studies using scale model tests to evaluate the capacity of suction caissons have been performed (Clukey and Morrison, 1995; Fuglsang & Steensen-Bach, 1991). Numerical studies employing the finite element method and upper bound plastic limit analyses have also been used to evaluate the suction caisson ultimate load capacity (Aubeny & Murff, 2003; Sparrevik, 2002). A quasi-monotonic analysis is typically employed for suction caissons. In existing design methodologies, the caisson must resist a peak cyclic load when assessing the effect of cyclic loading on quantifying the reduction in shear strength. Winkler springs can be employed using *p-y* curves for lateral loads and *Q*-*z* and *t*-*z* for axial loads (API 2003; DNV 2014). Since the cumulative deformations significantly depend on the number of cycles and load amplitudes (Li et al. 2015), the cumulative deformation should be taken into consideration in the design methodologies.

This study involves two parts: 1) an experimental study; 2) a finite element investigation. For the experimental study, laboratory model tests imposed displacement-controlled cyclic loading. These experiments measured the degradation in vertical and lateral soil resistance while increasing the number of cycles. The finite element studies investigated caisson performance for aspect ratios L/D = 4, 5, and 6, and load inclination angles ψ = 20, 45, 60, and 75.

The load attachment for the anchoring chain is generally between 50 to 70% of the total suction caisson embedment, in order to maximize the lateral resistance and to promote primarily translational motions of the caisson rather than rotation (Randolph et al. 1998; Randolph, 2012) (Figure 5.1). Storms in offshore anchor and foundation applications are comprised of non-uniform load amplitudes. In this study, a storm loading sequence with non-uniform load amplitudes with zero load reversal was used (Figure 5.2a-b). These load distributions were given by Anderson (2015). For computational convenience, the load cycle amplitudes were reduced to smaller packets of load amplitudes.

The main focus of this study is to calibrate the FE model (nonlinear kinematic hardening model) using the experimental results and to investigate the permanent cumulative deformation using a parametric study.

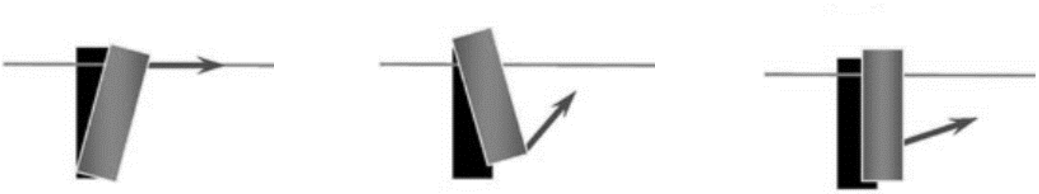

Figure 5.1 Effect of padeye depth on suction anchor response.

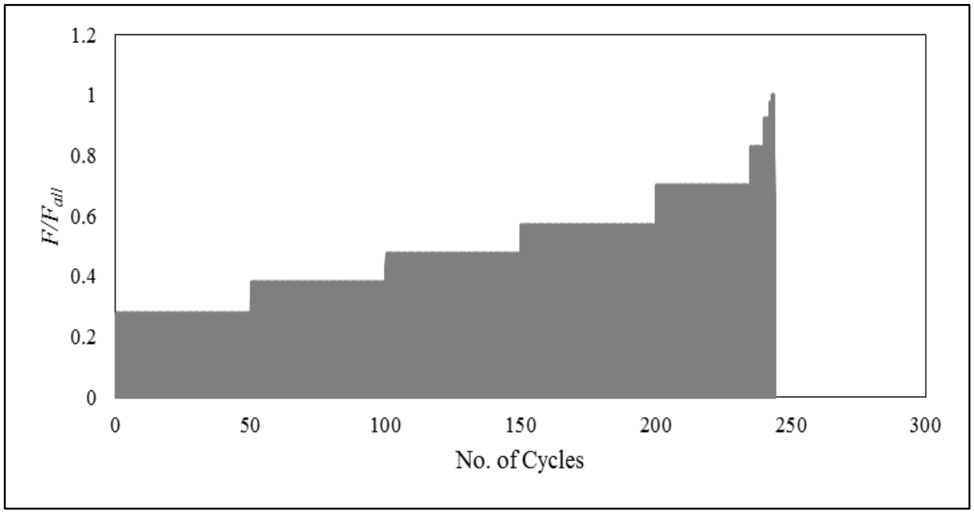

a) Increasing load amplitude history.

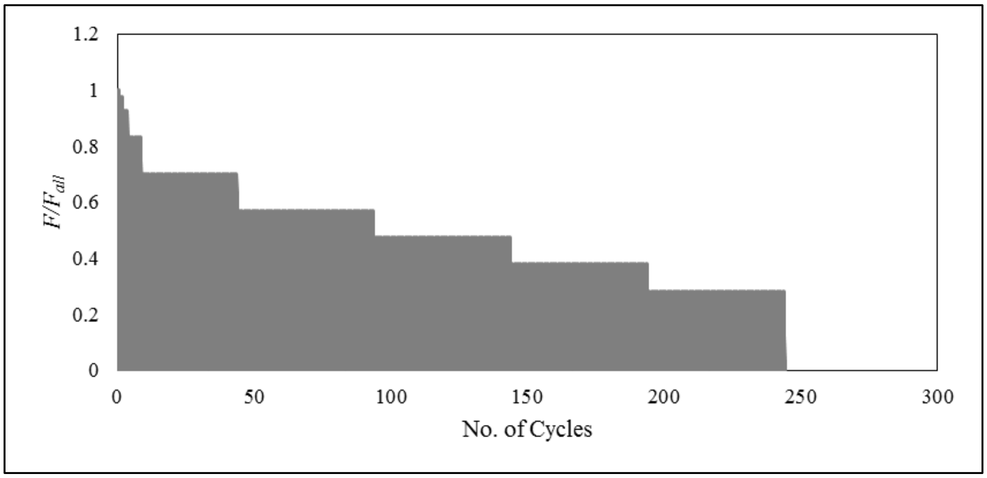

b) Decreasing load amplitude history.

Figure 5.2 Non-uniform load amplitude history.

5.2. Background

For more than two decades, suction caissons have been employed to support fixed offshore structures and to keep floating structures in station. Different studies were conducted to evaluate the performance of suction caissons for these applications. In the following sections, the common practice for installation, axial capacity, lateral capacity analysis, and the *p-y* curves will be presented.

5.2.1. Suction Caissons Analysis

In this section, the American Petroleum Institute (API) for installation (penetration), axial capacity, and lateral capacity analyses of suction caissons will be summarized. Some results and recommendations from research on suction caisson analysis are also presented.

5.2.3. Suction Caisson Installation

The installation of suction caissons usually starts with placing the caisson on the soil under its own weight. This creates a seal between the caisson wall and the soil. Following that, suction will be applied to the caisson to reach the designated penetration depth. According to Huang et al., (2003), installation steps should be predicted prior to the installation to prevent soil plug failure.

According to the American Petroleum Institute (API RP 2SK, A 2008), the adhesion factor method can be used to predict the penetration resistance during installation. Equation 5.1 shows the total estimated penetration resistance as the summation of two components, which are the side wall resistance and the tip resistance.

$$Q_t = Q_s + Q_{tip} \Rightarrow Q_t = A_{wall}\,(\alpha * s_u)_{ave} + (N_{c*}\, s_{u,tip} + \gamma' * w) * A_{tip} \qquad \textbf{Equation 5.1}$$

where: Q_t is the total suction caisson penetration resistance, Q_s is the side wall resistance, Q_{tip} is tip resistance, A_{wall} is the embedded area of the inside and outside wall, α is the adhesion factor, s_u is the undrained shear strength of the soil, N_c is the bearing capacity factor, $s_{u,tip}$ is the undrained shear strength at the tip, γ' is the submerged unit weight, w is the embedded depth of the suction caisson, and A_{tip} is the cross-sectional area at the tip. Figure 5.3 shows a sketch of a suction caisson subjected to axial compression.

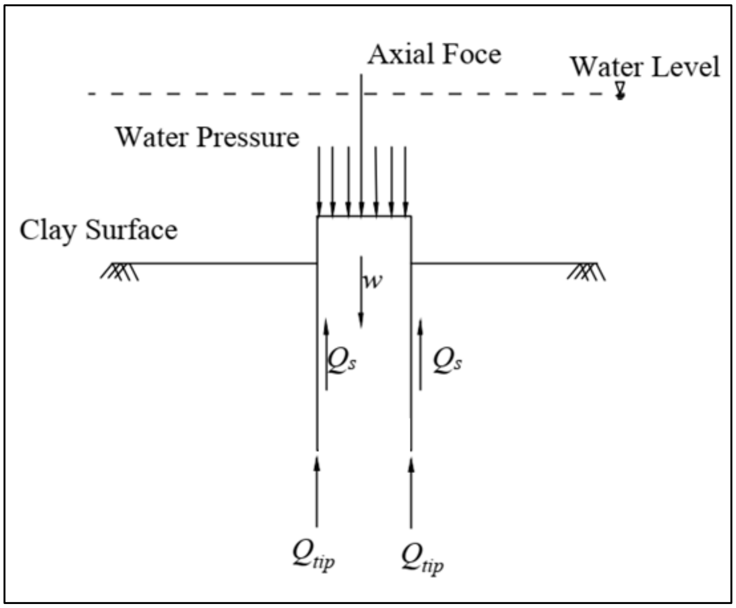

Figure 5.3 A sketch of a suction caisson with compression axial force.

5.2.3. Axial capacity of suction caisson

The pullout capacity for sealed caisson includes the bearing capacity of the caisson base and the external wall friction capacity. Unlike the sealed caisson, the vertical unsealed capacity is primarily due to the internal and external wall friction (Colliat et al. 1995, 1997).The axial capacity of the sealed caisson is assumed to be the sum of friction on the exterior side wall and end-bearing at the tip (or reverse end bearing depending whether the caisson is loaded in tension or compression). Equation 5.2-Equation 5.4 are used to predict the axial capacity (R) due to soil resistance (API RP 2GEO. 2011).

$$R = Q_f + Q_p = f(w) * A_s + q\ A_p \qquad \textbf{Equation 5.2}$$

$$f(w) = \alpha * s_u \qquad \textbf{Equation 5.3}$$

$$q = N_c * s_{u,tip} \qquad \textbf{Equation 5.4}$$

where: Q_f is the side friction resistance, Q_p is the end bearing, $f(w)$, is the unit side shear, w is the depth below mudline, A_s is the side surface area of the caisson, q is the unit end bearing, A_p is the gross end area of the caisson, α is the dimensionless side friction factor, s_u is the undrained shear strength of the soil at the required depth, N_c is the end bearing factor, and $s_{u,tip}$ is the undrained shear strength of the soil at the pile tip. Figure 5.4 shows a sketch of a suction caisson subjected to axial tension. For the tensile failure, the soil plug inside the suction will come out with the caisson.

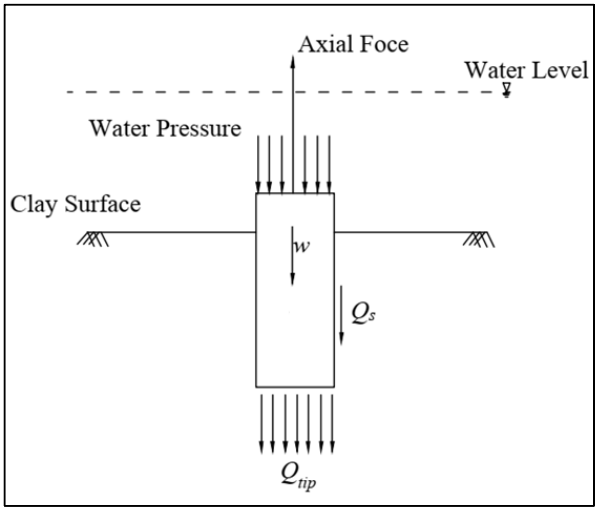

Figure 5.4 A sketch of a suction caisson with tension force.

5.2.3. Lateral capacity of suction caisson

Finite element method is a rigorous general approach to evaluate the lateral capacity of suction caissons. The API RP 2SK (A 2008) recommends using finite element method, plastic limit analysis, or limit equilibrium. The plastic limit analysis is one of the alternatives to finite element analysis, which is comparatively less computationally expensive and easier to use. An upper-bound plasticity model for laterally loaded piles was developed by Murff and Hamilton, (1993) by assuming a combined three-dimensional failure mechanism: a conical soil wedge moving upward near the surface and a plane strain flow-around failure at depth as shown in Figure 5.5a This model was simplified further by Aubeny et al. (2001). The lateral bearing (N_p) factor varies with depth (Figure 5.5b). Namely, it has lower values at shallow depths on account of the reduced soil resistance due to the failure wedge that develops near the ground surface (mudline).

This model was later generalized by Aubeny et al. (2003) to predict ultimate load capacity under inclined loads. For the case of purely axial loading, the formulation of the model reduces to the α- method for side friction in addition to the reverse end bearng contribution. For the case of pure lateral loading, the formulation reduces to the lateral loaded caisson analysis discussed above. The interaction between the axial and lateral resistance for inclined loading was estimated based on finite element simulations (Aubeny et al., 2003).

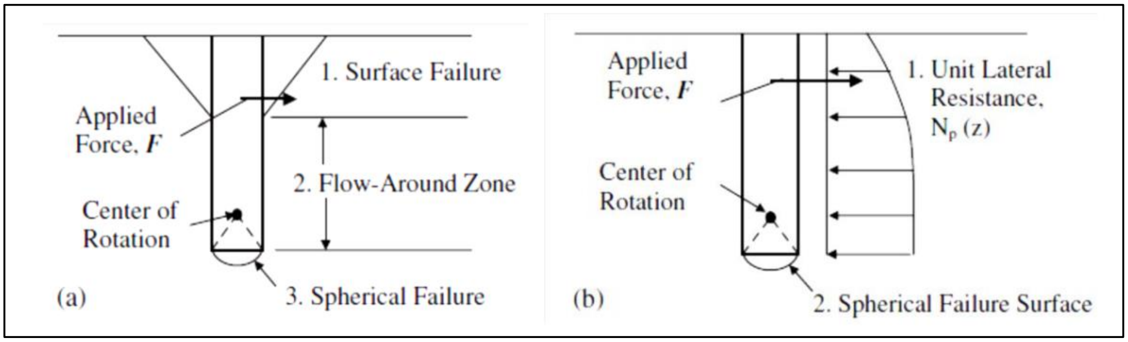

Figure 5.5 Failure Mechanisms of Suction Caissons: (a) three-dimensional failure mechanism proposed by Murff and Hamilton (1993), and (b) simplified analysis (reprinted from Aubeny et al., 2001).

5.2.2. P-Y Curves for Flexible Piles in Clay

P-y analyses can be modified for the larger caisson diameter to be used for suction caissons which are primarily subjected to lateral loads (API RP 2A). The behavior of a laterally loaded flexible pile can be expressed in the form of the differential equation, as shown in

Equation 5.5. This equation can be solved by discretizing the pile using finite difference method with discrete translational springs to represent the soil resistance as a foundation of y (Reese et al., 1975).

$$EI\frac{d^4y}{dz^4} = p$$ **Equation 5.5**

where: p is the soil resistance per unit length, y is the pile deflection, z is the depth, EI is the flexural stiffness of the pile.

Matlock (1970) developed *p-y* curves for static and cyclic conditions based on field tests of laterally loaded ~ 0.32 m diameter piles along with laboratory tests in soft clay. Equation 5.6 was suggested by Matlock to predict the ultimate soil resistance (p_u).

$$p_u = N_p\, s_u\, D$$ **Equation 5.6**

where: p_u is the ultimate soil resistance, N_p is the bearing capacity factor for laterally loaded pile, s_u is the undrained shear strength of the soil, and D is the pile diameter.

The ultimate soil resistance is assumed to be 9 at depths sufficiently deep for plane-strain (flow-around) conditions to prevail, and can be calculated using Equation 5.7 for shallower depths.

$$N_p = 3 + \frac{\gamma' z}{s_u} + J\frac{z}{D}$$ **Equation 5.7**

where: γ' is the submerged unit weight of the soil, z the depth, J is the dimensionless constant ranges from 0.25 to 0.5.

Equation 5.8 is used to predict the pile deflection (y_{50}).

$$y_{50} = 2.5\varepsilon_{50} D$$ **Equation 5.8**

where: ε_{50} is the axial strain, ranges from 0.005 to 0.02.

The non-dimensional expression of the *p*-*y* curves by Matlock (1970) can be found in Equation 5.9 and Equation 5.10 for static and cyclic conditions, respectively.

$$\frac{p}{p_u} = 0.5\left(\frac{y}{y_{50}}\right)^{\frac{1}{3}}$$ **Equation 5.9**

$$\frac{p}{p_u} = 0.72\left(\frac{z}{z_R}\right)$$ **Equation 5.10**

5.3. Finite Element Analysis

In this study, a nonlinear kinematic hardening model was used to simulate the cyclic response of piles/caissons along with the experimental tests. This model is available in commercial FE (ABAQUS), and it is based on a simple kinematic hardening constitutive model with Von Mises failure criterion. The model will be calibrated using the experimental data results to predict the cumulative plastic deformations.

5.3.1. Mesh and Boundary Conditions

A three-dimensional mesh (using ABAQUS) was used in this study. A cylindrical mesh soil with a distance of 7 *D* from the centerline to the far end of the cylinder as shown in Figure 5.6. The bottom edges were restrained to move in all directions. The pile was simulated as a hollow body sealed from the top. An 8-noded linear brick, fully integrated, hourglass control (C3D8) was used to model the soil, and (C3D8I) to model the pile. Dimensions of the soil elements at the soil-caisson boundary were on the order of ??*D*. Nodes at the soil-caisson boundary were tied together to model full adhesion, $\alpha = 1$. To model less than full adhesion, $\alpha < 1$, the nodes at the interface were still tied together, but the soil strength in the elements at the soil-caisson boundary was reduced by a factor α.

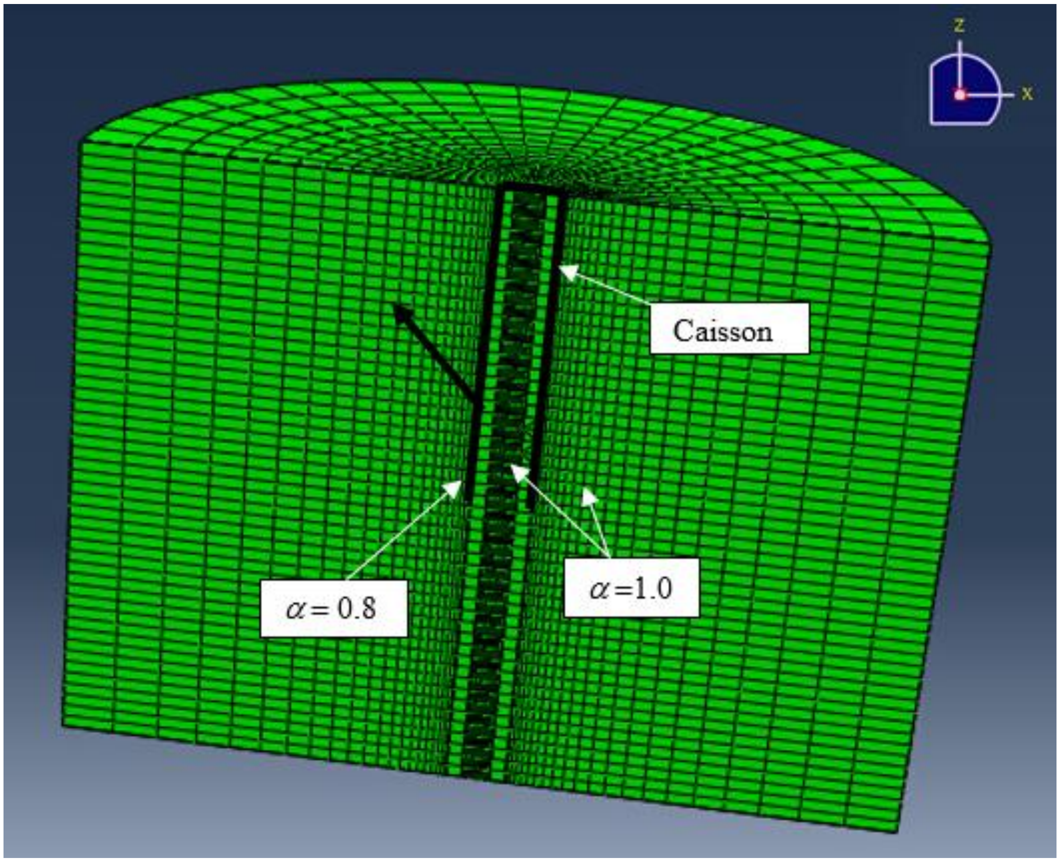

Figure 5.6 Finite element mesh.

5.3.2. Constitutive Model

As previously discussed, a nonlinear kinematic hardening model was used in this study. The undrained shear strength s_u characterizes the fine-grained soil strength. This model aims only to model purely undrained behavior; as such, pore-pressure buildup and dissipation are not simulated. However, undrained behavior is considered a reasonable simplification first approximation for fine-grained soil subjected to rapid cyclic loading. Uniaxial strength relates to the undrained shear strength for a von Mises yield criterion as follows:

$$\sigma_{max} = \sqrt{3}\, s_u$$ **Equation 5.11**

According to the Abaqus Analysis user's manual (6.13), the evolution law of this model consists of two hardening components: kinematic and isotropic. The nonlinear kinematic hardening component describes the translation of the yield surface in stress space through the backstress parameter α_b. The isotropic hardening component describes the change of the equivalent stress defining the size of the yield surface, σ_o, as a function of plastic deformation as shown in Figure 5.7a-b. The evolution of stresses is defined as

$$\sigma = \sigma_0 + \alpha_b$$ **Equation 5.12**

where σ_0 is the stress at zero plastic strain and α is the backstress, which determines the kinematic evolution of the yield surface in the stress space. Figure 5.8a-b shows force and strain-controlled loading, respectively.

The yield surface of the kinematic hardening model is defined as

$$F = f(\sigma - \alpha_b) - \sigma_0 = 0$$ **Equation 5.13**

where = $f(\sigma - \alpha_b)$ is the equivalent Mises stress with respect to the backstress α_b.

The kinematic hardening models assume associated plastic flow:

$$\dot{\varepsilon}^{pl} = \dot{\bar{\varepsilon}}^{pl} \frac{\partial F}{\partial \sigma}$$ **Equation 5.14**

where $\varepsilon^{\dot{p}l}$ is the rate of plastic flow and $\varepsilon^{-\dot{p}l}$ is the equivalent plastic strain rate.

The evolution of the kinematic component of the yield stress is described by the expression

$$\dot{\alpha}_b = C\frac{1}{\sigma_\circ}(\sigma-\alpha_b)\dot{\bar{\varepsilon}}^{pl} - \gamma\alpha_b\dot{\bar{\varepsilon}}^{pl}$$ **Equation 5.15**

where C = initial kinematic hardening modulus [$C = \sigma_{max}\,\varepsilon_{\max} = E$] and γ is a parameter determining the rate of decrease of the kinematic hardening with increasing plastic deformation. Since $\sigma_{max} = C/\gamma + \sigma_o$, the γ can be found using Equation 5.6 (Gerolymos et al. 2005; Anastasopoulos et al. 2011).

$$\gamma = \frac{C}{\sqrt{3}s_u - \sigma_\circ}$$ **Equation 5.16**

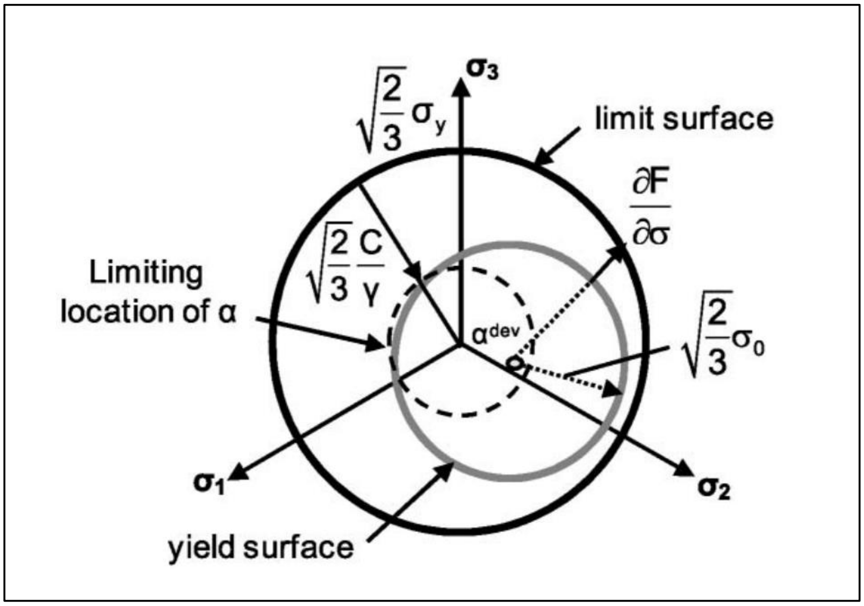

a) Three-dimensional representation of the hardening in the nonlinear isotropic/kinematic model.

Figure 5.7 Hardening model (reprinted from Simulia, 2014).

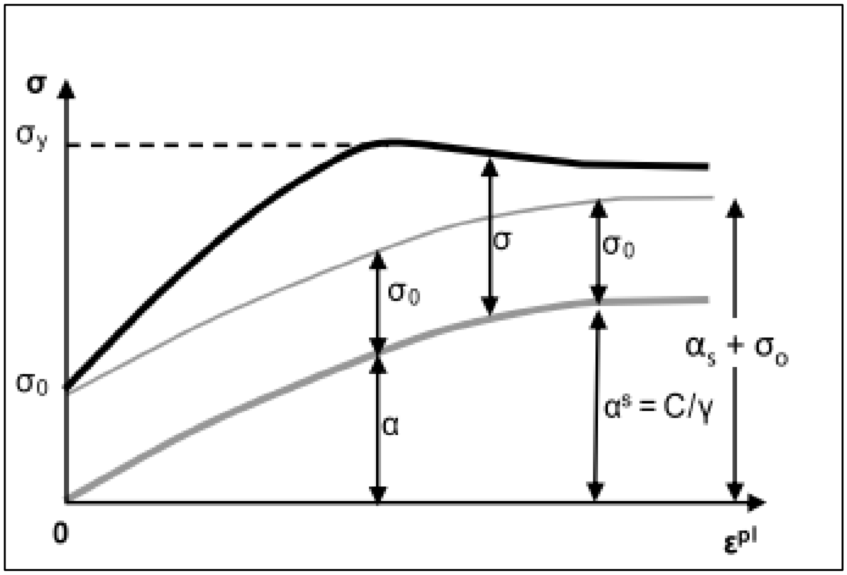

b) One-dimensional representation of the hardening in the nonlinear isotropic/kinematic model.

Figure 5.7 Continued.

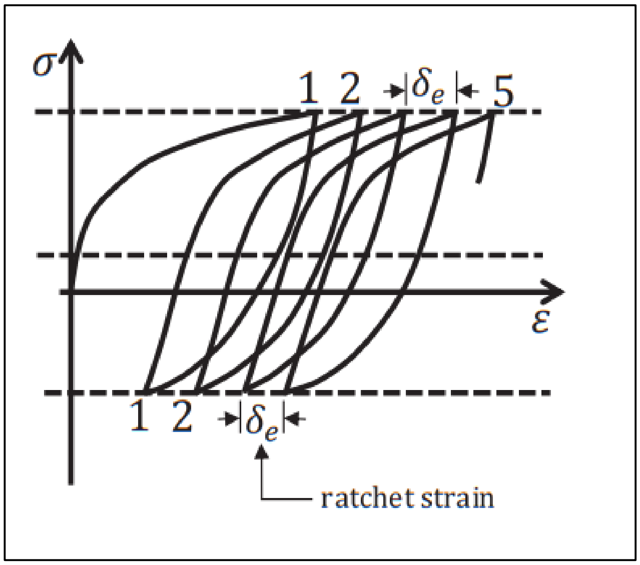

a) Force-controlled loading.

Figure 5.8 Force and strain controlled loading (reprinted from Simulia, 2014).

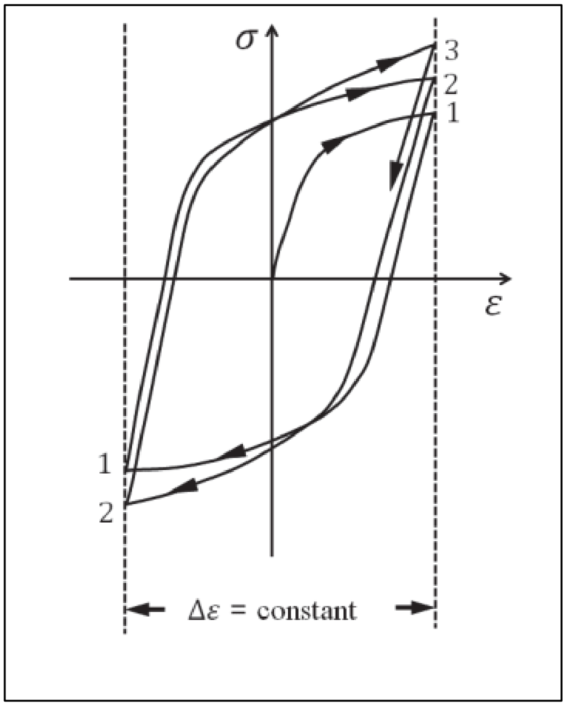

b) Strain-controlled loading

Figure 5.8 Continued.

5.3.3. Model Validation (Comparison to Existing Monotonic Solutions)

The FE model described above was validated by: (1) comparison of predicted ultimate load capacity to plastic limit analysis (PLA; Aubeny et al. 2001; Aubeny et al. 2003) and (2) comparison to the load-displacement curve for monotonic loading (backbone curve) predicted from previous FE studies (Al-Ramthan and Aubeny, 2019). All comparisons were made for the following condition: (1) a strength profile $s_u = 2 + 1.6z$, (2) a caisson with aspect ratio for $L/D = 5$, and (3) a load attachment depth located at a depth equal to two-thirds of the total length of the caisson. Figure 5.9 shows an acceptable level of agreement to about 1% of the load capacity predicted by PLA.

Figure 5.9 shows a reasonable match to the previous FE prediction. Additional validation of the FE model is presented subsequently in this chapter, based on comparisons to experimental backbone curve measurements made in this study.

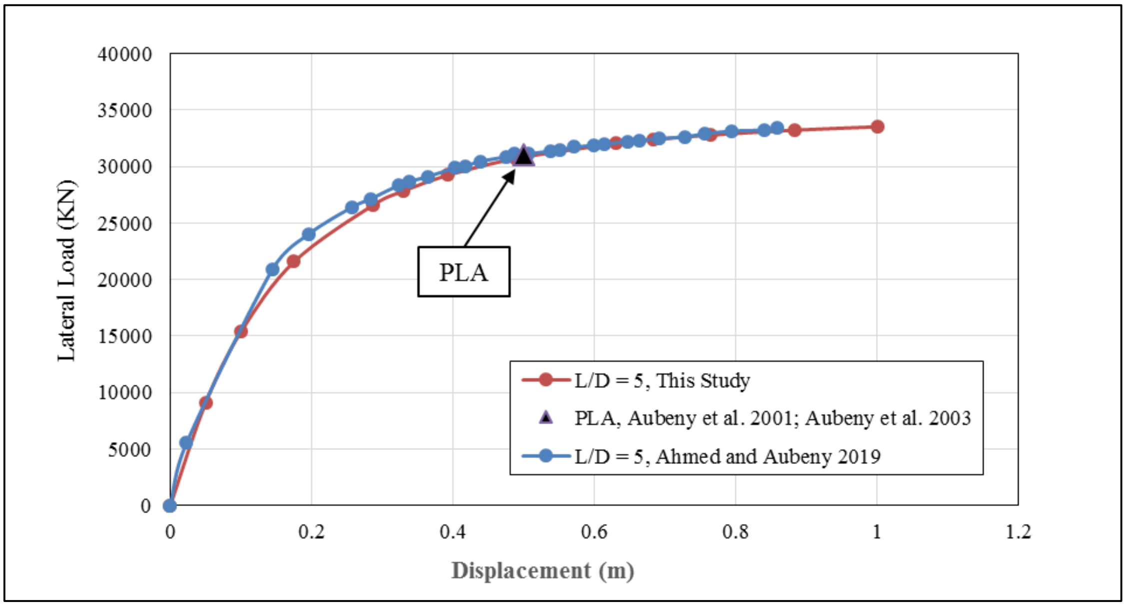

Figure 5.9 Comparisons between FEA and previous studies.

5.4. Experimental Program

This sub-chapter introduces the experimental results. The experimental results include vertical and lateral monotonic and cyclic loading tests for suction caissons with an aspect ratio (*L/D*) of 2 for different cyclic amplitudes.

5.4.1. Caisson Models

Eight suction caisson models were used in this study. The caisson models are comprised of aluminum. The properties of the suction caissons can be found in Table 5.1. Figure 5.10 shows sketches of the used caissons with other fabrications.

Table 5.1 Caisson models.

Pile #	Outer Diameter (D)	Inner Diameter (D_{in})	Embedded Length (L)	Total Length (L_t)
1-2, &8	49.4 (1.945 in)	47.5 (1.87 in)	99 (3.9 in)	111.3 (4.38 in)
2-7	50.8 (2 in)	50 (1.97 in)	99 (3.9 in)	111.3 (4.38 in)

a) Caisson installation (open vent)

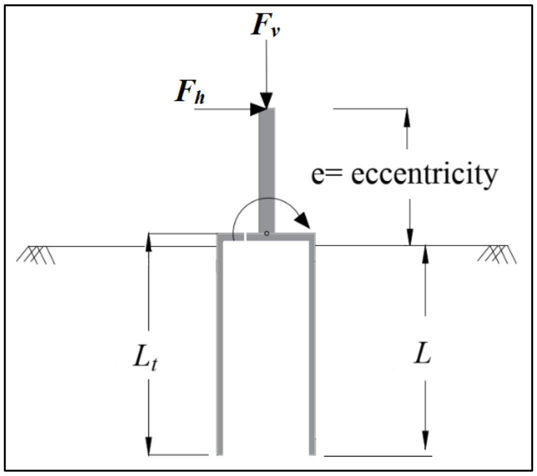

b) A sketch shows the vertical, horizontal forces and the moment for L/D = 2.

Figure 5.10 Suction caisson models.

5.4.2. Test Program

The test program comprised four tests series. Series 1 (Table 5.2) involved caisson installation at different penetration rates. Series 2 (Table 5.3) involved vertical cyclic loading tests at different cyclic amplitudes ranging from 0.002- 0.02 *D*. Series 3 (Table 5.4) introduced lateral monotonic and cyclic loading at different tilts ranging from

0.5° - 1.5° and different eccentricities. Series 4 (Table 5.5) introduced pullout tests with open and sealed vents. Series 5 studied a parametric study of a 3-D finite element method. In addition, multiple T-bar and miniature vane shear tests were conducted to establish the undrained shear strength profile as well as the relationship between the water content and the undrained shear strength.

Table 5.2 Series 1: Installation at different penetration rate effects.

Test No.	**Loading rate**
1	0.5 mm/sec
2	1 mm/sec
3	2 mm/sec
4	5 mm/sec

Table 5.3 Series 2: Summary of the vertical cyclic loading tests.

Test	**Velocity mm/sec**	**Test Description**	**No. of cycles**
5	1	1-way cyclic load amplitudes of 0.002 *D*.	1000
6		1-way cyclic load amplitudes of 0.0045 *D*.	1000
7		1-way cyclic load amplitudes of 0.0095 *D*.	1000
8		1-way cyclic load amplitudes of 0.02 *D*.	1000

Table 5.4 Series 3: Summary of the lateral monotonic and cyclic tests.

Test	Velocity mm/sec	Test Description	Eccentricities *e*	No. of cycles
9	1	Monotonic lateral tests, 0.3 *D*	1.58 *D*	-
10		1-way cyclic load amplitudes, tilt of ~ 0.5	1.6 *D*	150
11		1-way cyclic load amplitudes, tilt of ~ 1.5	2.38 *D*	150
12		1-way cyclic load amplitudes, tilt of ~ 1.5	0.74 *D*	150

Table 5.5 Series 4: Pullout tests

Test No.	Loading rate	Test description
13	1	Open vent
14		Sealed vent
15		Sealed vent
16		Sealed vent
17		Sealed vent

5.4.3. Test Bed Strength Profile

Information on the test bed strength profile was explained in Chapter 3. T-bar tests were conducted directly on test bed soils to provide independent measurements of the undrained shear strength. The dimensions of the T-bar as explained before are 1.27 cm (0.5 inches) in diameter by 5.08 cm (2 inches) in length. The penetration rate was 20 mm/sec (0.787 in/sec) to achieve undrained loading conditions (Langford and Aubeny

2008; Yafrate el al. 2009). All undrained shear strengths were interpreted by using a T-bar bearing factor of 10.5. Multiple undrained shear strength profiles were calculated depending on moisture water content of the soil bed. All the profiles show that the shear strength increases linearly with depth. Figure 5.11 depicts the undrained shear strength profiles using T-bar tests.

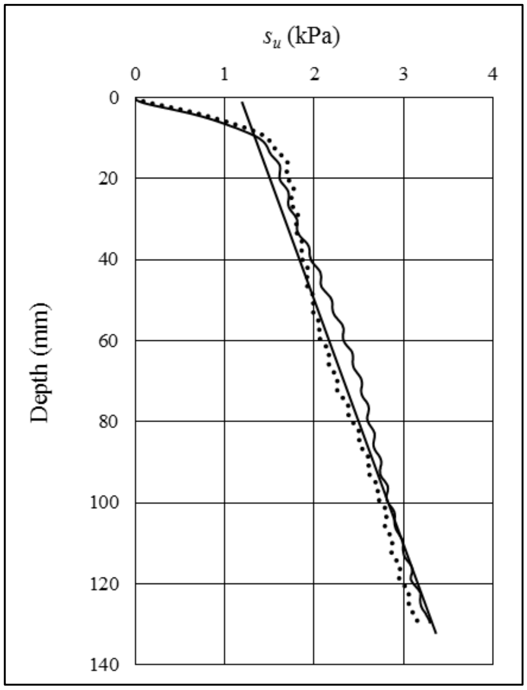

Figure 5.11 Undrained shear strength profiles selected from T-bar tests.

5.5. Experimental Measurements of Uplift Loading

5.5.1. Pullout Resistance

To investigate pullout resistance, multiple tests were conducted after applying the vertical and lateral cyclic tests. Two tests were vented (unsealed), and four were completely sealed. Figure 5.12 shows the normalized pullout resistance for the vented and sealed tests. The soil resistance for the vented test tends to rapidly reach peak resistance and then drop abruptly. In the absence of suction, the caisson separates from the soil as shown in Figure 16 a. Peak resistance occurs at a displacement of about 5% *D*.

Under sealed caisson conditions uplift resistance reaches an ultimate value at relatively large displacements, with only a very minor tendency for softening at large displacements, as shown in Figure 5.12a-b. The observed failure mechanism involves the entire soil plug pulling out with the caissons (see photographs in Figure 5.13). The gap between the soil and the inside top of the caissons was filled with water as noticed when the soil layer was removed. Peak resistance occurred at a displacement of about 20-25% *D*.

Figure 5.12 shows no large difference between the vented and the sealed uplift resistance. This is likely due to the fact that the caisson with the open vent was not subjected to cyclic loading before monotonic pullout to failure. By contrast, the sealed caissons were subjected to vertical and/or lateral cyclic loading tests before the pullout tests. Equation 5.2 was adapted to predict the adhesion factor α. The adhesion factor was about 0.75-0.8 and 0.45-0.55 for the vented and sealed caissons, respectively.

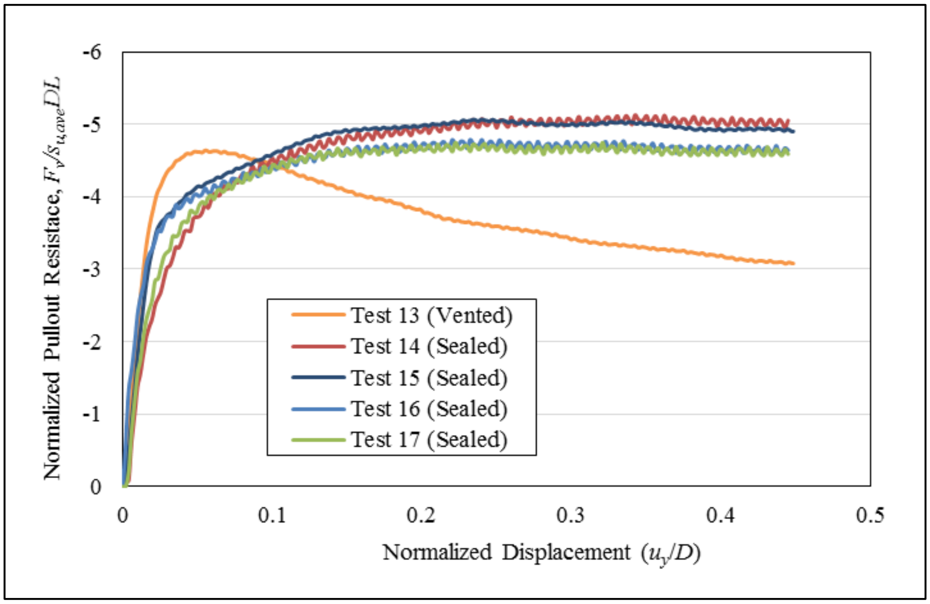

a) Vented and sealed caissons.

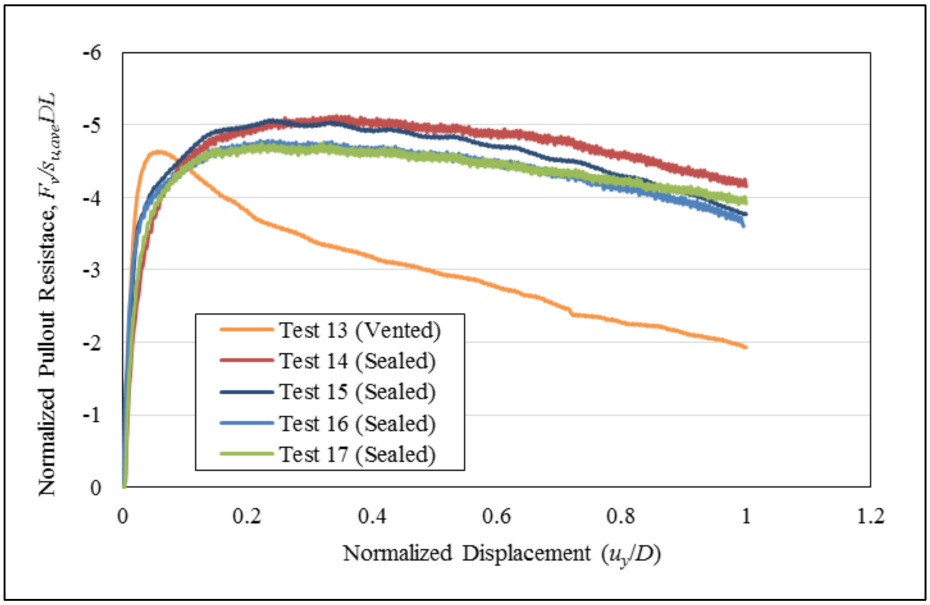

b) After pulling out the caissons for 1.0 *D*.

Figure 5.12 Normalized pullout resistance vs. time.

a) Soil with vented caisson

b) Soil after pulling out a sealed caisson. **c) Soil plug.**

d) Removing soil plug (sealed caisson).

Figure 5.13 photographs with vented and sealed caissons.

5.5.2. Cyclic Amplitudes of 0.2% *D*

Test 5 of the second series was penetrated to a depth (*L*) of 99 as explained above and then a 1000 load cycles were applied into the caisson. Figure 5.14a-b shows the degradation in the resistance while increasing the number of cycles for the very small cyclic amplitude. The vertical resistance approaches the steady-state after about 20 cycles. This reduction in resistance is due to multiple reasons, 1) softening and remolding the soil with increasing the number of cyclic, that causes the reduction in the undrained shear strength (Al-Janabi and Aubeny 2019; Al-Janabi el. al., 2019). Figure 5.14c presents the displacement versus time.

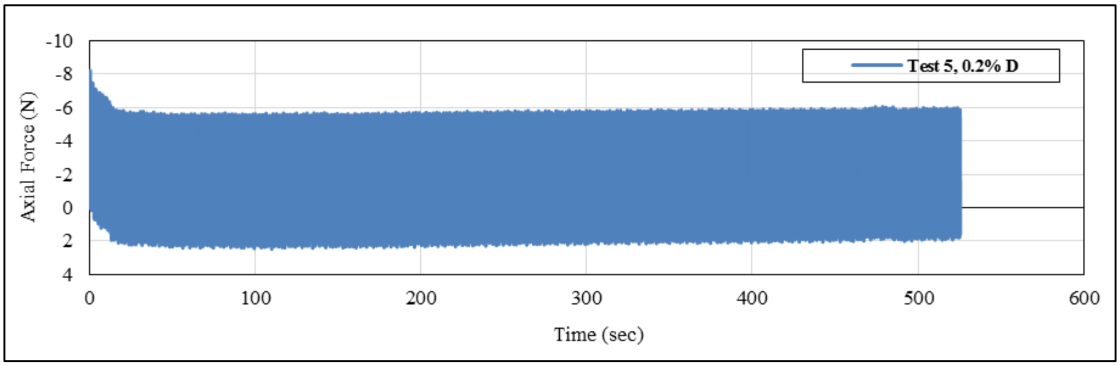

a) Axial force vs. time.

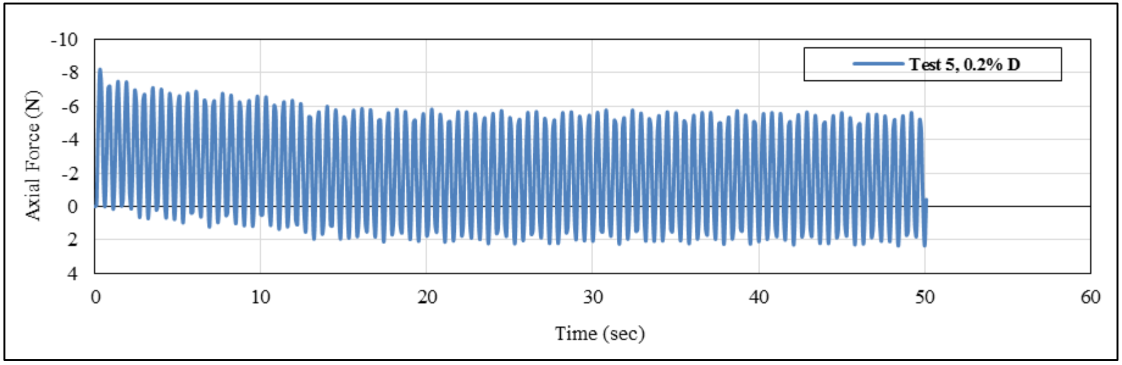

b) First 100 load cycles.

Figure 5.14 Vertical cyclic test with cyclic amplitude ~ 0.002 *D*.

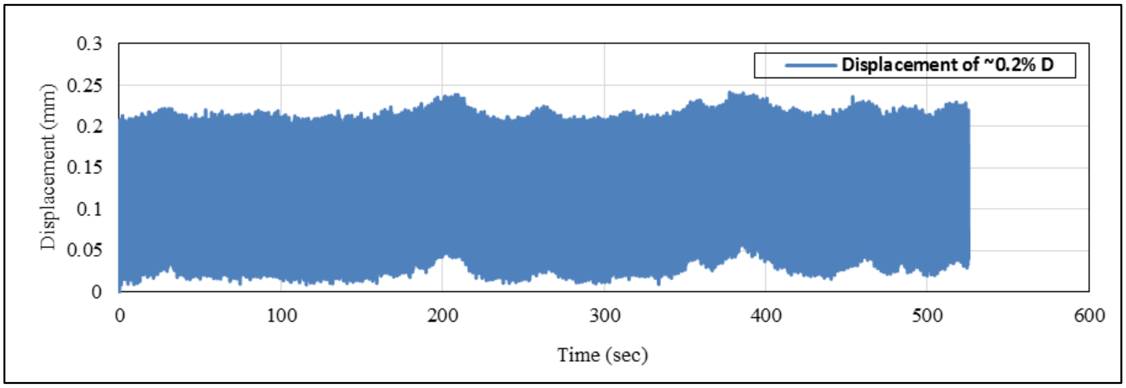

c) Displacement vs. time.

Figure 5.14 Continued.

5.5.3. Cyclic Amplitude of 0.45% *D*

For the small cyclic amplitude (Test 6), Figure 5.15a shows the soil resistance degrades rapidly during the first few cycles, around 5-10 cycles (Al-Janabi & Aubeny 2019), with a reduced rate of degradation as cyclic loading continues to an apparent steady-state after about 20 cycles. The resistance drops to about 35% for the first 100 load cycles.

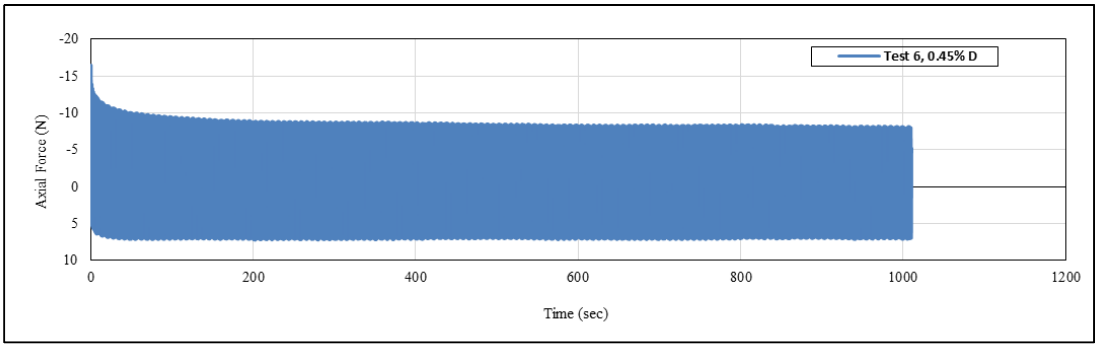

a) Axial force vs. time.

Figure 5.15 Vertical cyclic test with cyclic amplitude ~ 0.0045 *D*.

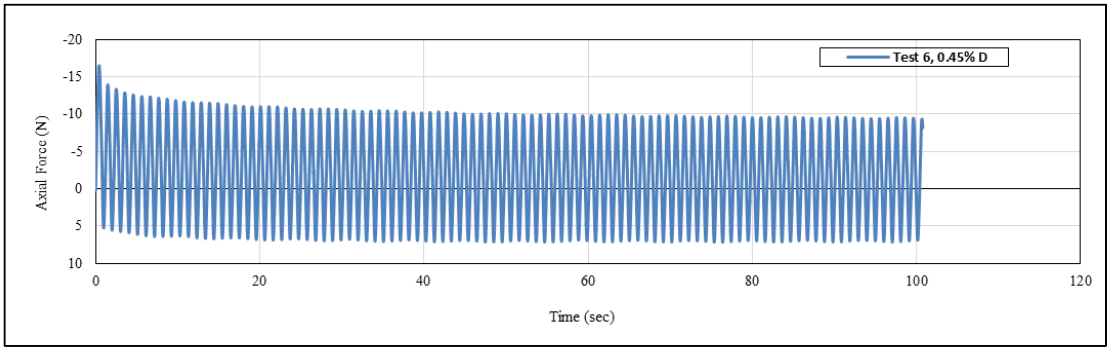

b) First 100 load cycles.

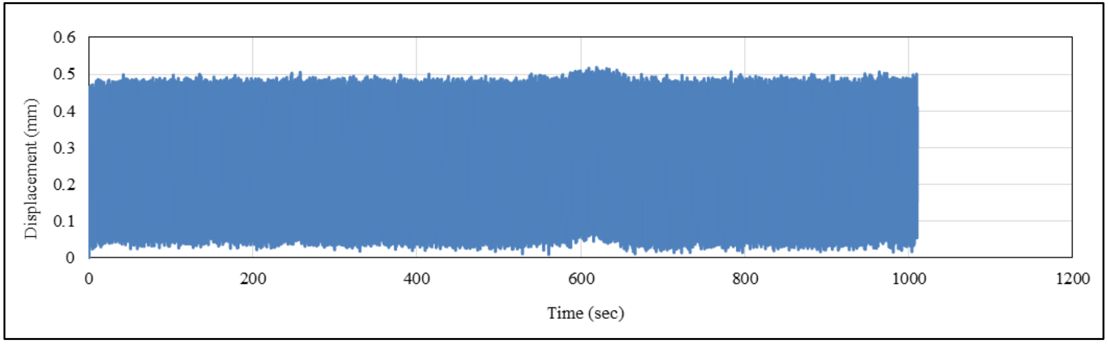

c) Displacement vs. time.

Figure 5.15 Continued.

5.5.4. Cyclic Amplitudes of 0.95% and 2% *D*

In a manner similar to the behavior during small cyclic amplitude tests(Test 6), the soil resistance degrades by about 30% after 5-10 cycles, with a reduced rate of degradation to an apparent steady-state after about 100 cycles. Figure 5.16 and Figure 5.17 show that the resistance declines to a steady state of about 57% of its original value after about 200 cycles. However, soil erosion was observed as well. That leads to the same behavior as noticed in the small cyclic amplitude. Therefore, there was no need to conduct more tests with larger cyclic amplitude.

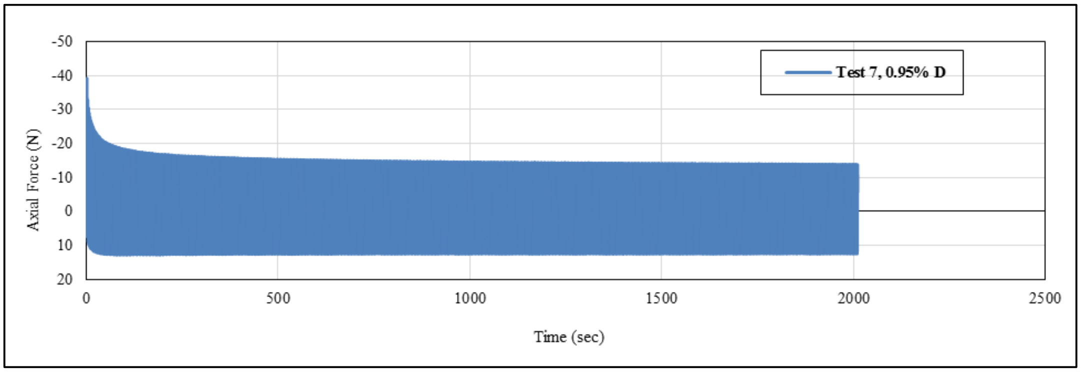

a) Axial force vs. time.

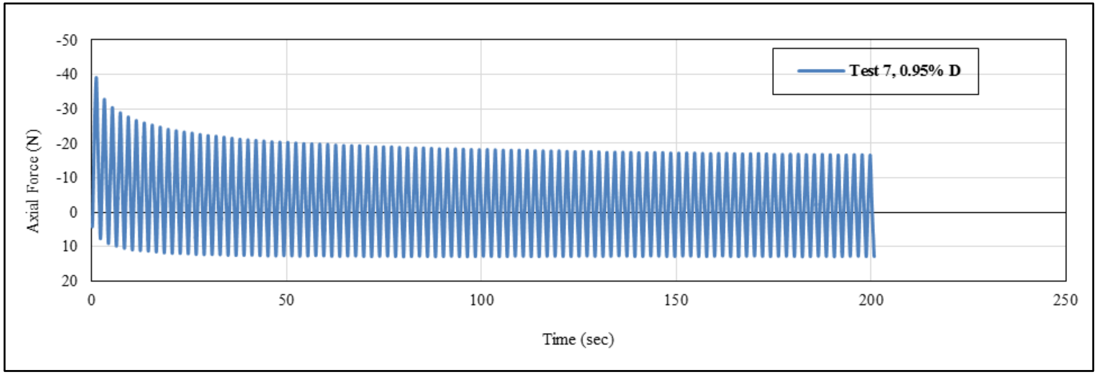

b) Axial force vs. time for the first 100 load cycles.

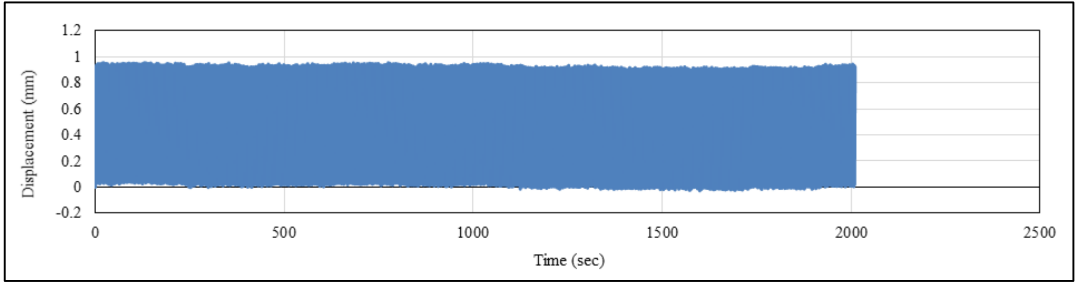

c) Displacement vs. time.

Figure 5.16 Vertical cyclic test with cyclic amplitude ~ 0.0095 *D*.

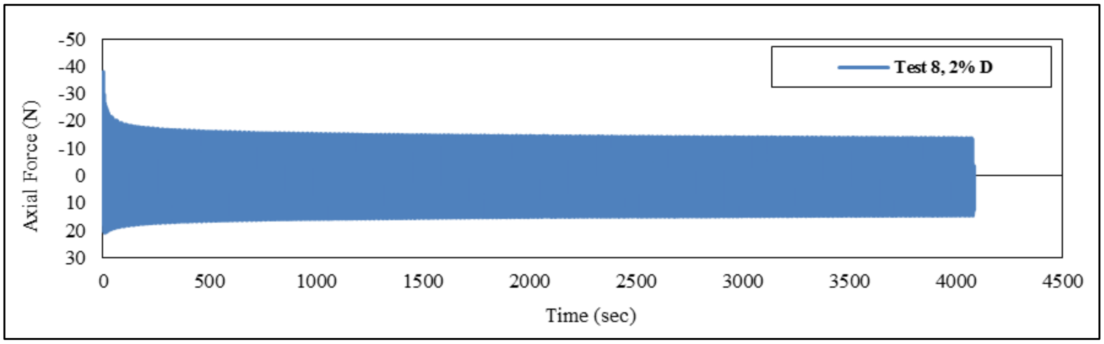

a) Axial force vs. time.

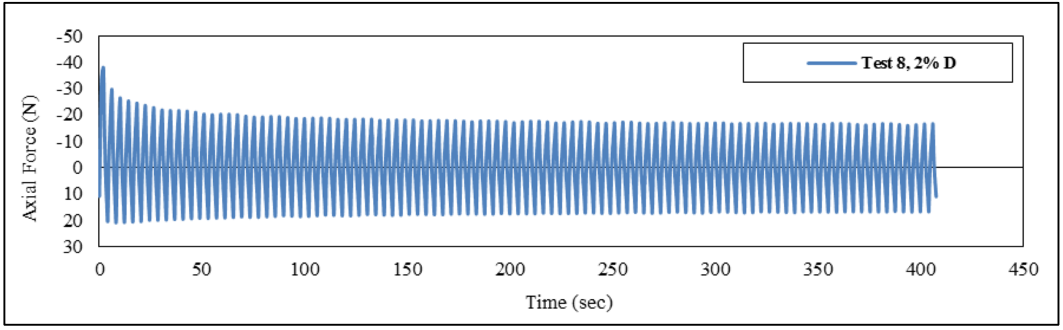

b) Axial force vs. time for the first 100 load cycles.

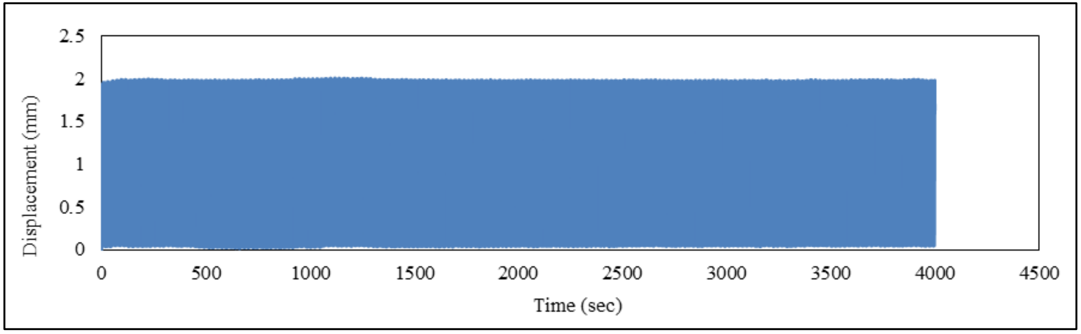

c) Displacement vs. time.

Figure 5.17 Vertical cyclic test with cyclic amplitude ~ 0.02 *D*.

5.6. Results for Lateral Load Tests

5.6.1. Lateral Monotonic Resistance

Test 9 was conducted by laterally moving the pile to about 0.3 *D* at an eccentricity (*e*) of 1.58 *D* (from the mudline) to predict the lateral resistance, F_h. Figure 5.18 shows the lateral resistance versus the displacement. It shows a comparison with previous experimental and numerical analysis but at different eccentricities and different soil types. These previous studies used the same foundation dimension but different soil type and different eccentricities. However, this difference in the predicted resistance is likely because of the different eccentricities.

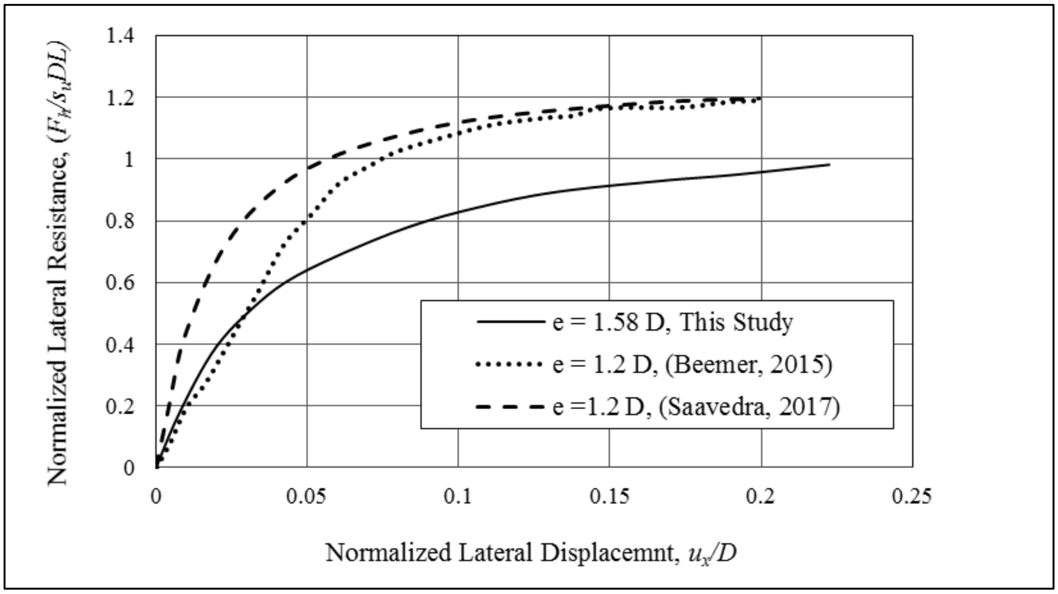

Figure 5.18 Lateral monotonic resistance with previous studies.

5.6.2. Lateral Cyclic Loading Test, Tilt ~ 0.5° and 1.5°

Three lateral cyclic tests were carried out by imposing target tilts of ~ 0.5°-1.5° for 150 cycles of 1-way cyclic amplitudes (with zero reversal). The aim of these tests was to capture the behavior of soil degradation while increasing the number of cycles.

Figure 5.19a (Test 10) shows the degradation in the soil resistance by increasing the number of cycles for a tilt of 0.5°. The reduction in soil resistance between the 1st cycle and the 10st cycle is about 40%. The reduction in the lateral resistance continues to decrease, but at a reduced rate to reach a point when the reduction in resistance is very small when increasing the number of cycles at about 40 cycles. This reduction in resistance is due to softening and remolding the soil by increasing the number of cycles (i.e. that causes the reduction in the undrained shear strength) (Al-Janabi et al. 2019).

Figure 5.20a and Figure 5.21a depicts lateral forces versus time for a tilt of 1.5°. The same trend of degradation (Test 10) was observed for Test 11 and 12. The reduction in soil resistance between the 1st cycle and the 10st cycle is about 41%. Figure 5.19b to Figure 5.21b show the displacement versus time. Figure 5.19c to Figure 5.21c show tilt versus the time.

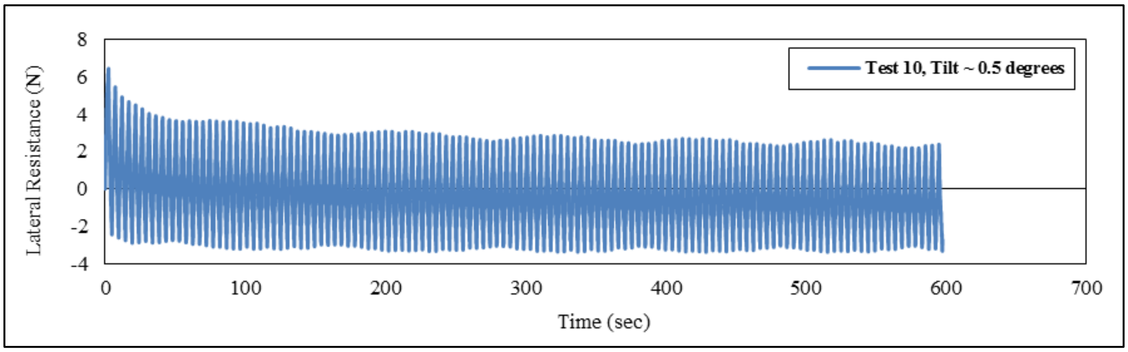

a) Lateral force vs. time.

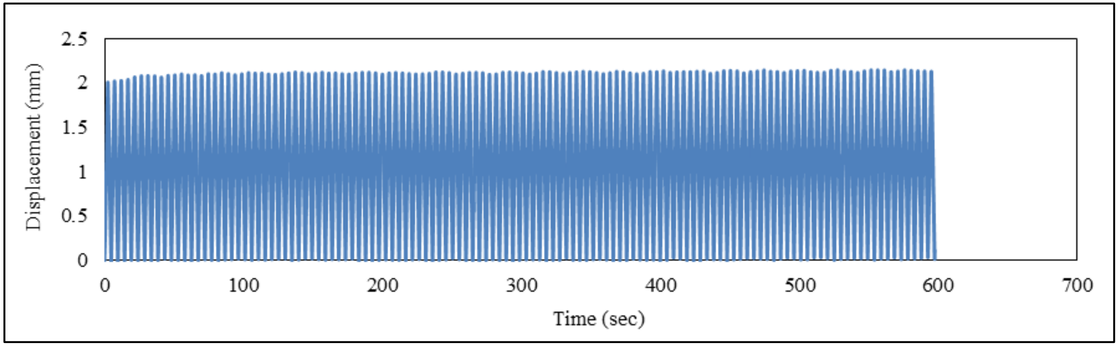

b) Displacement vs. time.

Figure 5.19 Lateral cyclic test with a tilt of ~ 0.5°.

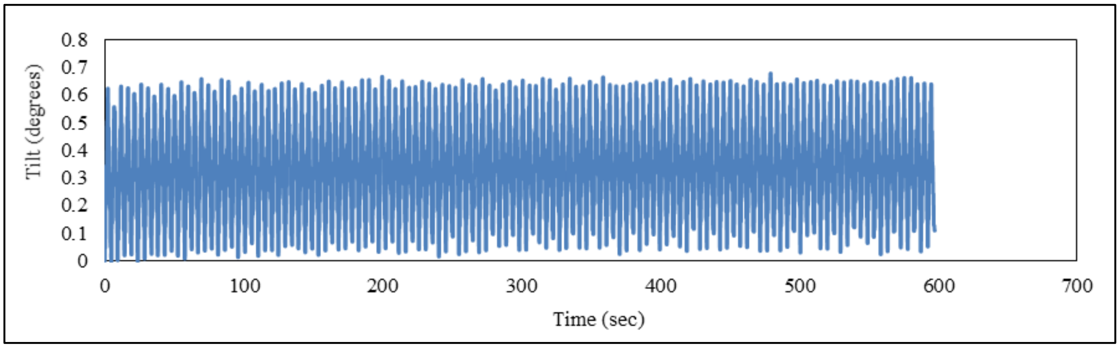

c) Tilt vs. time.

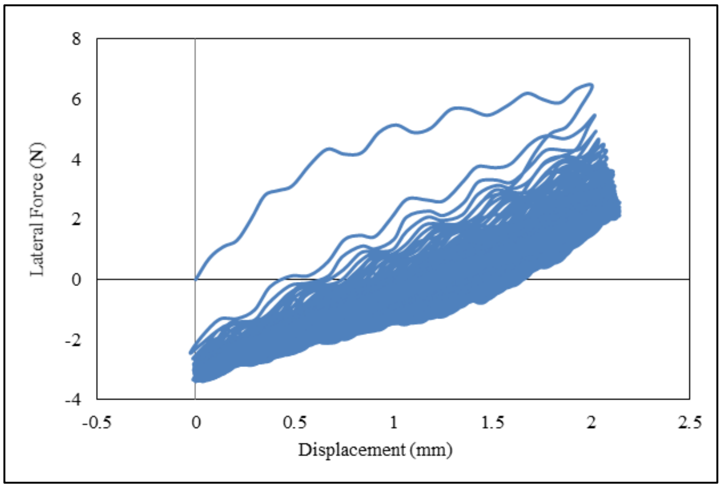

d) Lateral Force vs. Displacement.

Figure 5.19 Continued.

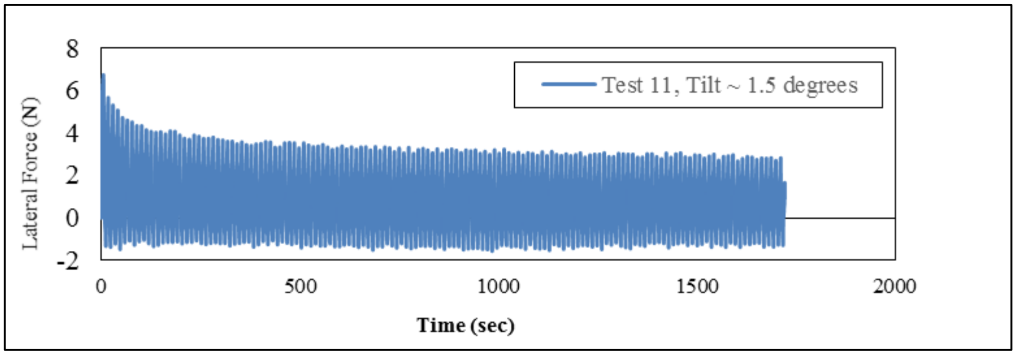

a) Lateral force vs. time.

Figure 5.20 Lateral cyclic test with a tilt of ~1.5°.

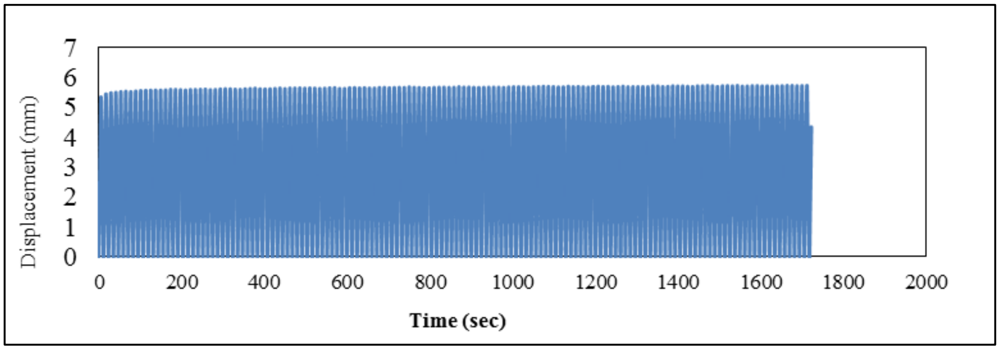

b) Displacement vs. time.

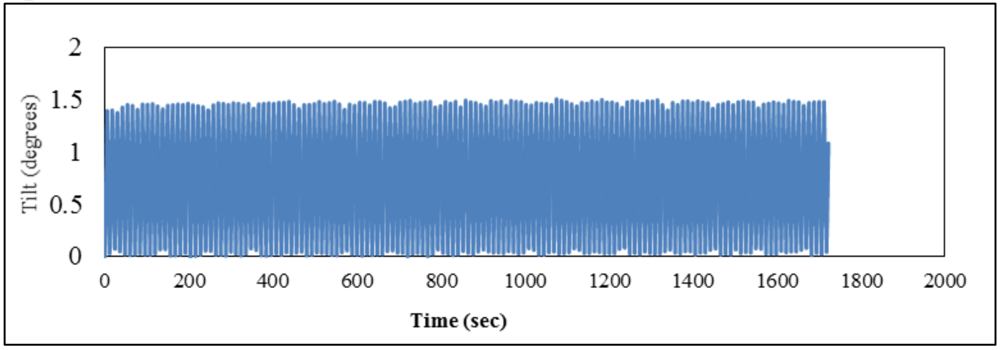

c) Tilt vs. time.

Figure 5.20 Continued.

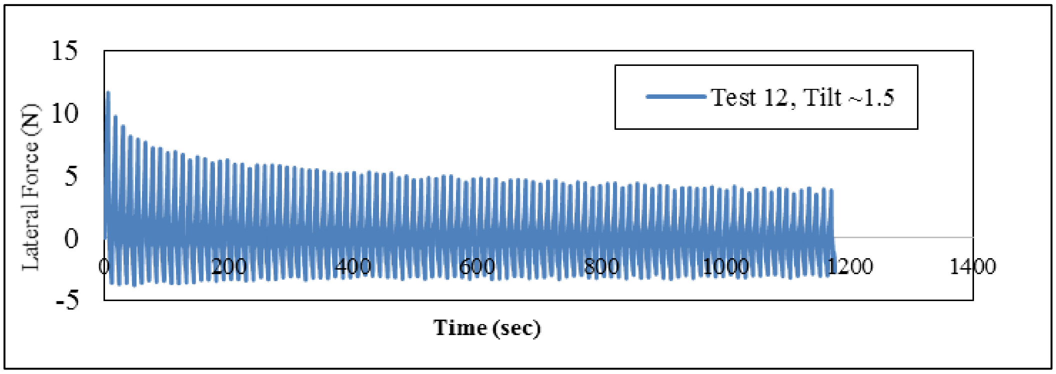

a) Lateral force vs. time.

Figure 5.21 Lateral cyclic test with a tilt of ~1.5°.

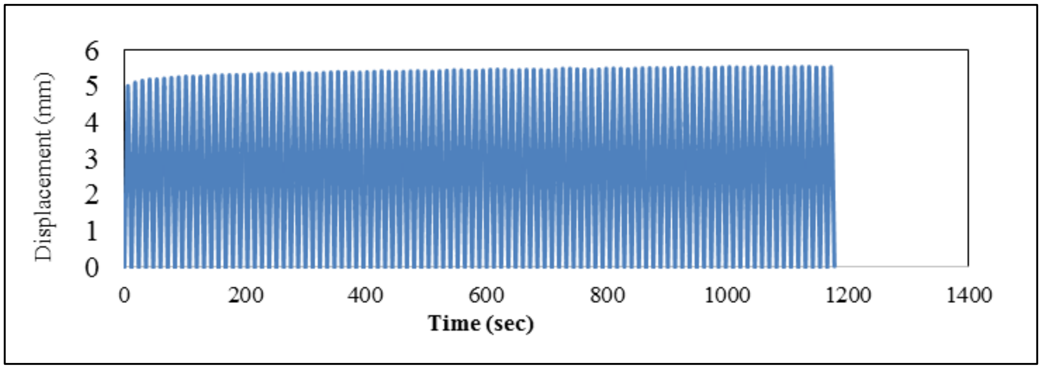

b) Displacement vs. time.

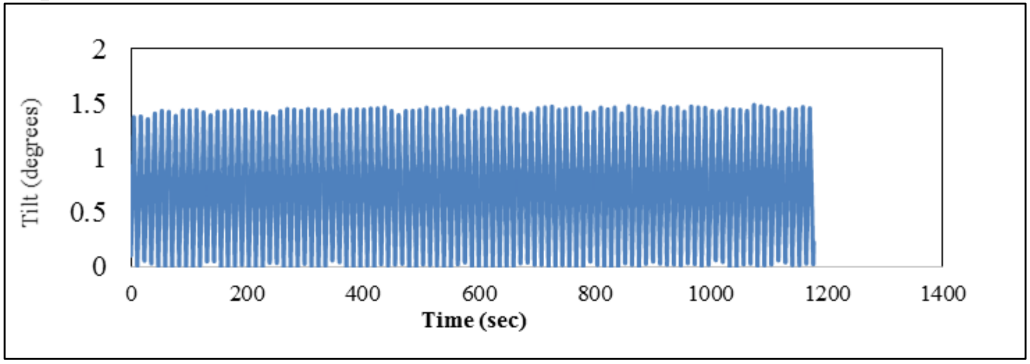

c) Tilt vs. time.

Figure 5.21 Continued.

5.7. Calibrate the Constitutive Model Using the Experimental Results

Three-dimensional analyses were performed using ABAQUS (Simulia 2014) to calibrate the kinematic hardening model with the experimental results. A cylindrical mesh soil with a distance of 7*D* from the centerline to the far end of the cylinder was used as shown in Figure 5.6. For the pure lateral and vertical tests, the depths of the meshes were set to 2 *L* and 3 *L*, respectively. The pile was simulated as a hollow body sealed from the top. An 8-noded linear brick, fully integrated, hourglass control (C3D8) was used to model the soil, and (C3D8I) to model the pile. In the analyses presented herein, the soil properties from the laboratory results were fed into the model. The undrained shear strength was varied with depth (see Figure 7a-b) along with all the input parameters (e.g. the stress at zero plastic strain (0.1 σ_{max}) (Anastasopoulos et al. 2011; Ahmed and Aubeny 2019), the modulus of elasticity (E), the stress at zero strain, the initial kinematic hardening modulus (C), and the rate of decrease of the kinematic hardening with increasing plastic deformation parameter (γ)). Poisson's ratio was assumed to be constant (ν=0.45).

The modulus of elasticity was taken as 300 s_u. The initial kinematic hardening modulus C was $E = C = 300\ s_u$. The rate of decrease of the kinematic hardening with increasing plastic deformation parameter (γ) was found from Equation 5.6 A strength reduction equal to the adhesion factor ($\alpha = 0.8$) was assigned to the elements adjacent to the pile (Figure 5.6) to model the interface effect.

5.8. Numerical Analysis Methodology

In this study, the model was calibrated for all of the lateral and vertical monotonic and cyclic loading tests. For lateral resistance, Figure 5.22 shows a good correlation between the experimental and numerical results.

For the lateral and vertical cyclic amplitudes, the analysis applied the same lateral and vertical displacements that were used in the experimental results. Figure 5.23a-b shows a comparison between the lateral cyclic resistance versus time for the experimental and numerical results. Good agreement between the numerical model and experimental results was obtained for both compression and tension resistance. Figure 5.23b shows good agreement between the FE predictions and experimental results for the maximum and minimum load intensity (Peak and trough). Figure 5.24a-b depicts that the FE predictions slightly overestimated the results for both the peak and trough. The FE predicted trends of degradation in soil resistance was generally validated by the experimental results.

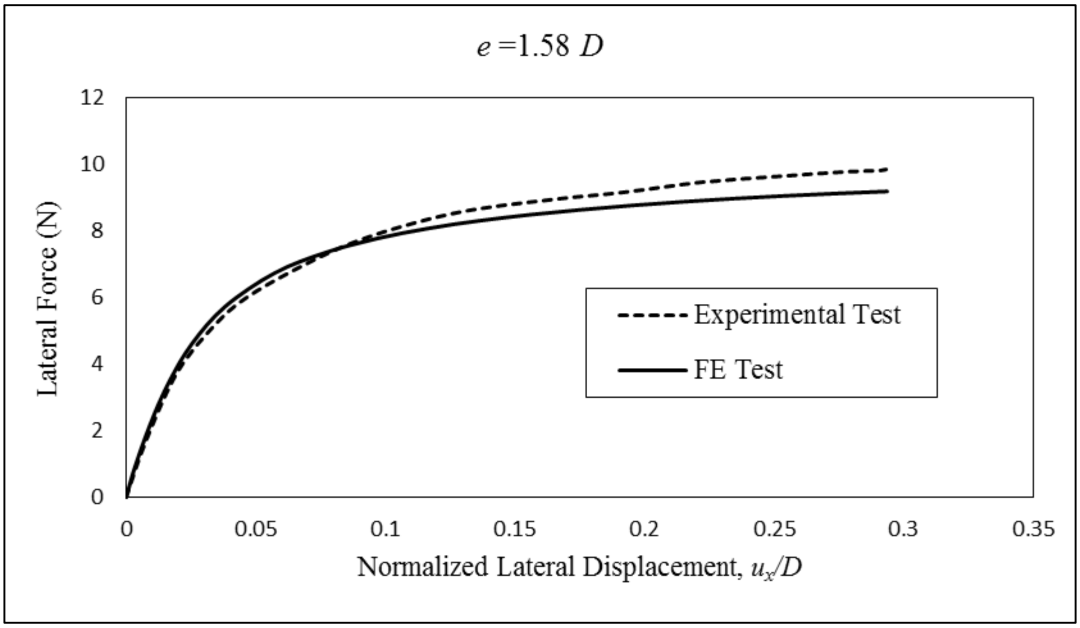

Figure 5.22 Comparison between the experimental results and FE results.

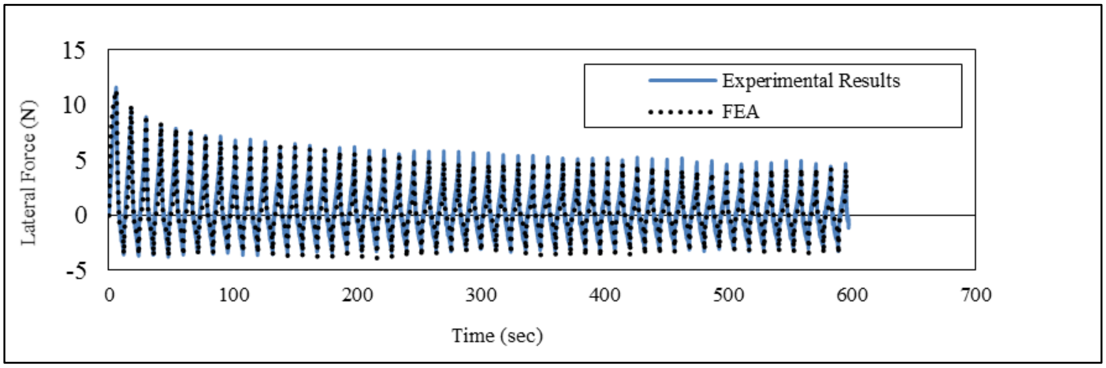

a) Experimental results vs. finite element results.

Figure 5.23 Lateral load vs. time (experimental and numerical results).

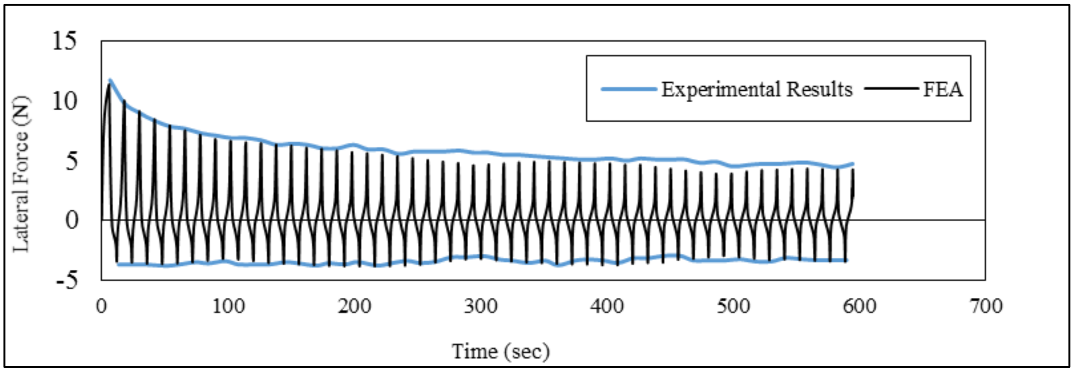

b) Experimental trend vs. finite element results.

Figure 5.23 Continued.

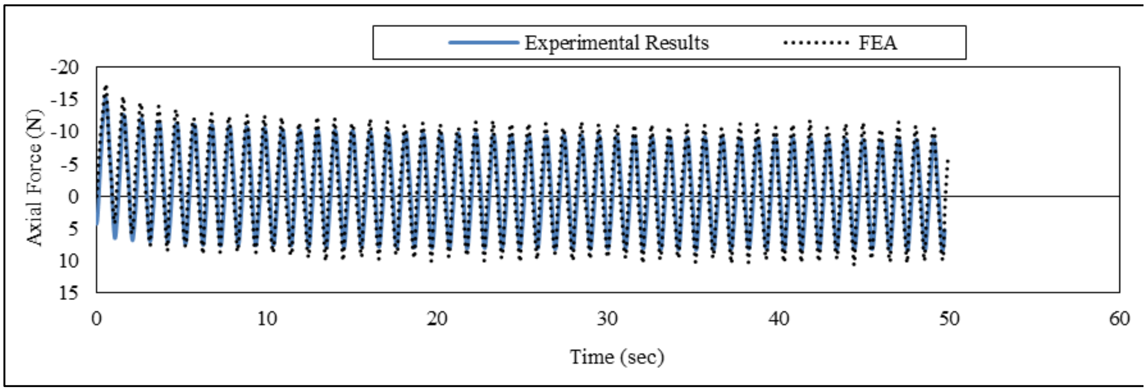

a) Experimental results vs. finite element results.

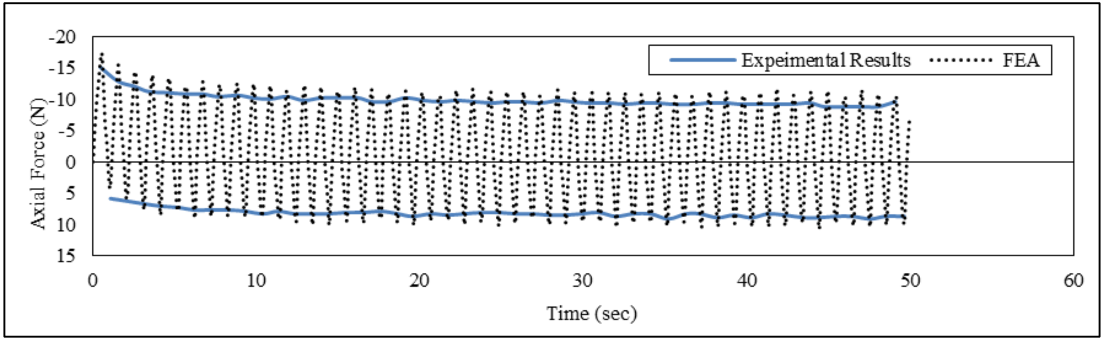

b) Experimental trend vs. finite element results.

Figure 5.24 Vertical load vs. time (experimental and numerical results).

5.9. Comparisons to Previous Measurements

A comparison to a previously published centrifuge test data is made to evaluate the validity of the calibrated model. In the centrifuge test described by Randolph et al. (1998), a suction caisson model with a diameter of 45 mm, a length of 106 mm, an anchor chain attached at depth of 67 mm with a scaling factor of (1:120). These tests were conducted to simulate an actual prototype suction caisson with a diameter of 5.4 m, a maximum embedment depth of 12.7 m, and an anchor chain attached at depth of 8.1 m with a load angle of 11°. In the normally consolidated clay, monotonic tests were conducted to predict the ultimate load capacity (F_{ult}) and then the design load capacity (F_{all}). The ultimate load capacity was 8800 kN with a normalized lateral displacement u_x/D = 0.36. The suction caisson was subjected to three packets of cyclic load amplitudes (100 cycles for $F=F_{all}$, 200 cycles for F= 1.3 F_{all}, and 16 cycles for F=1.6 F_{all}). The comparison in this study is made for the prototype dimensions, which are 5.4 m in diameter, 12.75 (~12.7) m in embedment depth, and an anchor chain attached at depth of 8.1 m with a load angle of 11°. The

Figure 5.25 shows essentially full agreement with the lateral displacement curve from the previous centrifuge test. The cumulative lateral displacement of the caisson for the increased markedly as the peak load was increased.

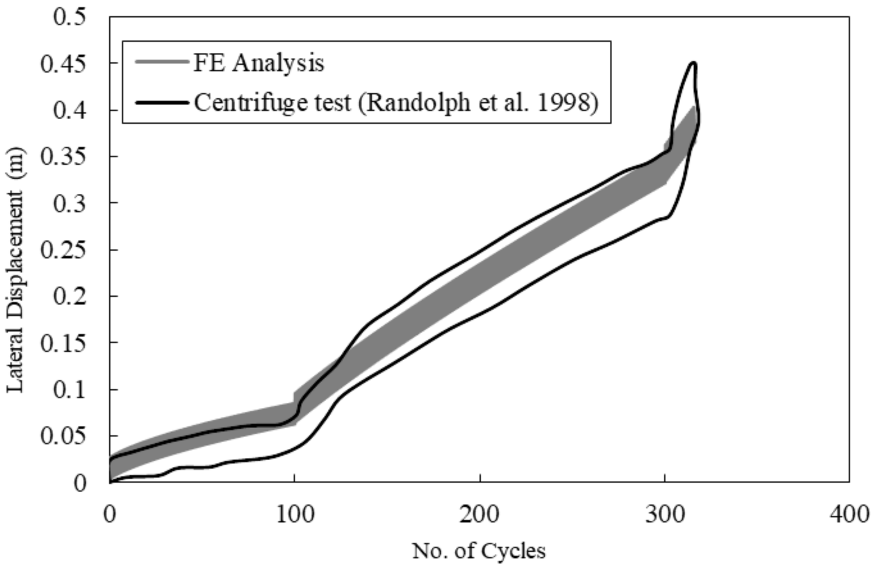

Figure 5.25 Experimental and numerical results.

5.10. Parametric Study

Using the calibrated FE model, a parametric study was conducted to predict cumulative deformations during force-controlled cyclic loading. Storm load on offshore anchors and foundations comprise non-uniform load amplitudes. All simulations in this study involved non-uniform load amplitudes with zero load reversal. The study utilized load distribution packets given by Anderson (2015). The number of load cycle amplitudes of these load packets were reduced for computational efficiency (Figure 5.2a-b). In this study, 5 m in diameter caisson with different aspect ratios of *L/D*= 4, 5, and 6 with different load inclination $\psi = 20^{\circ}, 45^{\circ}, 60^{\circ}$, and 75° were examined.

A clay profile for a normally consolidated clay was used, with a shear strength of 2 kPa at the mudline and increasing with depth at a rate of 1.6 kPa/m. All analyses were considered to be undrained, implying a Poisson's ratio $\nu = 0.45$. The pile was assumed a rigid body with a large modulus of elasticity of $1*10^{12}$ kPa and Poisson's ratio of 0.3. The adhesion factor (α =0.8) was assigned into the elements around the pile, and $\alpha = 1.0$ for the elements far from the pile wall (Figure 5.6) to simulate the reality.

The initial yield stress was set to 0.1 of the maximum stress (Anastasopoulos et al. 2011). All the piles were loaded at the padeye which was located at the two-third point along to the pile depth (optimal depth of the maximum load capacity). To evaluate the cumulative deformations under inclined cyclic loading, a realistic estimate of the working loads to be applied to the caisson should be estimated.

In this study, PLA was used to estimate the ultimate load capacity (F_{ult}) of the pile (Aubeny et al. 2003; Aubeny et al. 2001). A typical safety factor reduction *FS* of 2 was applied to compute an applied operational load (F_{all}) as shown in Table 5.6.

For the base case conditions described above a parametric study was conducted to investigate the effect of (a): aspect ratio *L/D*, (b) load inclination angle ψ, and (c) the effects of non-uniform load amplitudes F/F_{all}. where *F* is a load various from zero to the applied operational load.

Table 5.6 Ultimate and allowable load cases.

L/D	**ψ (degree)**	**F_{ult} (kN)**	**F_{all} (kN)**	**F/F_{all}**
4	20	19075	9523	Figure 5.2a
	45	15845	7923	
	60	12957	6479	
	75	11617	5809	
5	20	28765	14383	Figure 5.2b
	45	21471	10736	
	60	17550	8775	
	75	15736	7868	

Table 5.6 Continued.

L/D	ψ (degree)	F_{ult} (kN)	F_{all} (kN)	F/F_{all}
6	20	42255	21128	Figure 5.2a
	45	27825	13913	
	60	22734	11367	
	75	20381	10191	

5.10.1. Effect of Soil Properties and Adhesion Factor

In a previous study reported by Ahmed and Aubeny (2019), a parametric study of the soil properties, as well as the adhesion factor, was investigated. They concluded that the cumulative displacements under-uniform cyclic loading are highly sensitive to the soil initial stiffness. In addition, they recommended using the initial yield stress $\sigma_0/\sigma_{max} = 0.1$, which falls in the same range (0.1-0.3) that was recommended by Anastasopoulos et al. (2011). This parameter was not further studied in this paper and all predictions proceeded on a basis of $\sigma_0/\sigma_{max} = 0.1$. The focus of this study is to predict the cumulative displacements for various aspect ratios and inclination loads subjected to non-uniform packets of load amplitudes.

As explained earlier, the undrained shear strength was varied with depth (see Figure 5.11) along with all the input parameters. The modulus of elasticity was taken as 300 s_u. The initial kinematic hardening modulus C was E= C= 300 s_u. The rate of decrease of the kinematic hardening with increasing plastic deformation parameter (γ) was found from Equation 5.6 The adhesion factor, $\alpha = 0.8$ was assigned into the first elements adjacent to the inner and outer pile wall (Figure 5.6).

For the aspect ratio of $L/D = 5$, two load distributional packets were used as shown in Figure 5.2a-b. Case 1 (Figure 5.2a) begins with packets of the small load amplitudes (50 cycles at $F = 0.28\ F_{all}$), and Case2 (Figure 5.2b) begins with packets of the large load amplitudes $N = 1$ (1 cycles at $F = F_{all}$), which equals to the applied operational load (F_{all}) and then decreases to smaller packets.

5.10.2. Effect of Variable Load Amplitudes

In this study, two cases will be examined to investigate which case provides the larger cumulative displacement. These cases were tested for the aspect ratio of 5 for various load inclination as follows:

Case 1: applying small non-uniform load amplitudes (50 cycles at $F = 0.28\ F_{all}$) to large load amplitudes ($F = F_{all}$) as shown in Figure 5.2a.

Case 2: Progressively increasing cyclic load amplitudes, large load amplitudes ($F = F_{all}$) to small load amplitudes ($F = 0.28\ F_{all}$) as shown in Figure 5.2b.

Figure 5.26 to Figure 5.30 show that Case 1 generates larger cumulative displacement for all load inclinations ψ = (20°-75°). This was observed in a previous study (Randolph et al. 1998), although, they used different load amplitude sequences as explained earlier. For ψ = 20°, 45, 60, and 75°, the displacements from Case 1 were about 30%, 37%, 40% and 40% of Case 2, respectively. However, Case 1 will be used in this study to investigate the cumulative deformation of the suction caissons. Furthermore, these figures show that the normalized lateral cumulative displacements jumped for the first cycle ($N = 1$, and $F = F_{all}$) and then reduces when reducing the load amplitudes ($F < F_{all}$) (case 2). Figure 5.26a to Figure 5.29a illustrate the lateral force versus the cumulative lateral displacements for Case 1 and Case 2. Figure 5.26b, Figure 5.29b, and Figure 5.30a-b show the lateral cumulative displacement versus the number of cycles. It shows that for the first load packets (Case 1), there is a slight increase in the displacement and reaches a steady-state after about 10 cycles. For the second and third load packets (Case 1), there is a noticeable increase in the displacement and there is no steady-state reached. For the other load packets (up to $F = F_{all}$) of Case 1, there is a sharp increase in the cumulative displacements. This sharp increase was noticed as well in some previous studies reported by Randolph et al. (1998); Li et al. (2015).

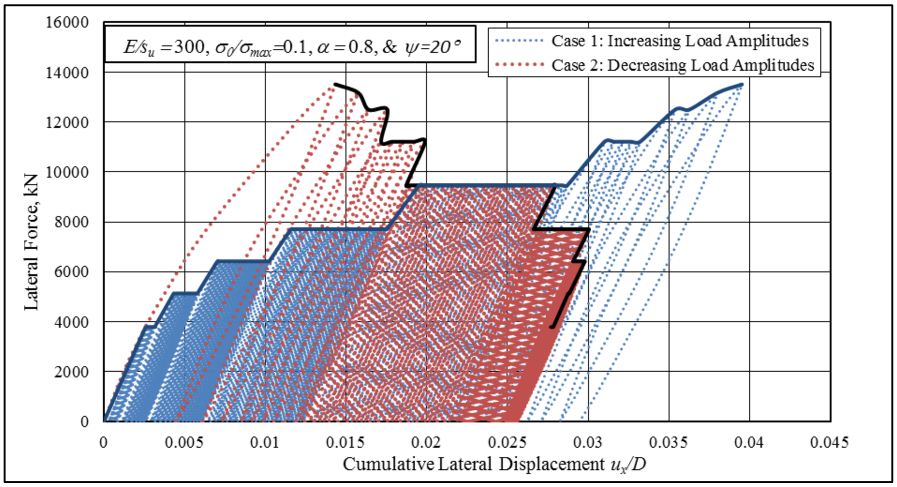

a) The influence of increasing and decreasing the non-uniform load amplitudes on the lateral displacements.

Figure 5.26 Cumulative lateral displacement for *L/D* = 5 and ψ = 20°.

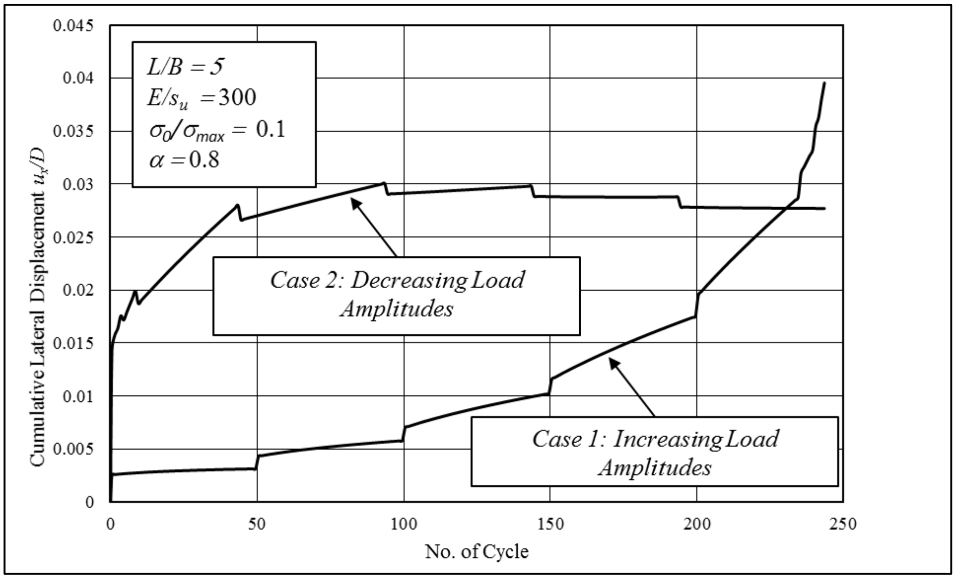

b) The influence of no-uniform load amplitude packets on the lateral displacement.

Figure 5.26 Continued.

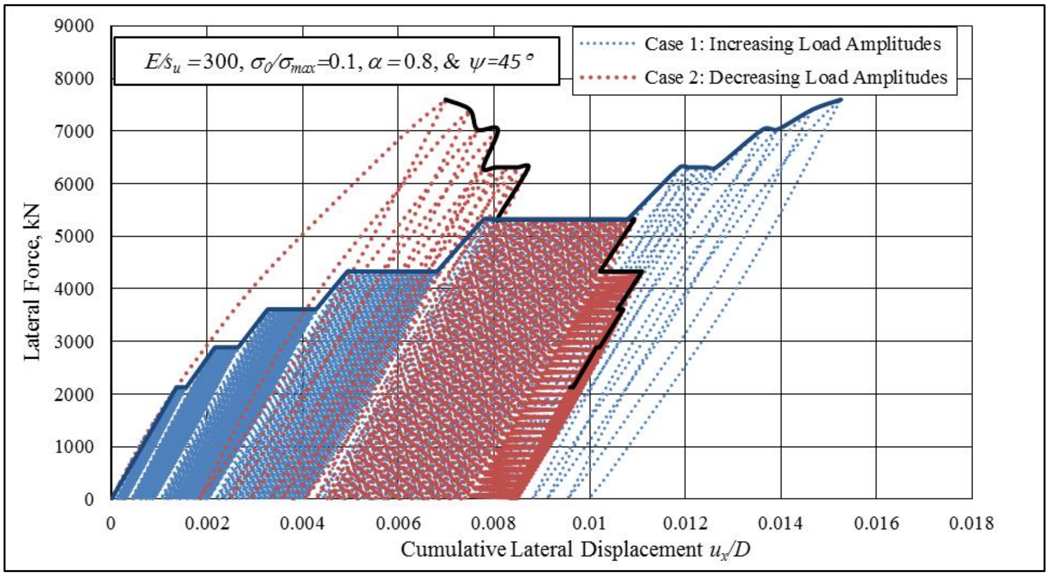

a) The influence of increasing and decreasing the non-uniform load amplitudes on the lateral displacements.

Figure 5.27 Cumulative lateral displacement for *L/D* = 5 and ψ = 45°.

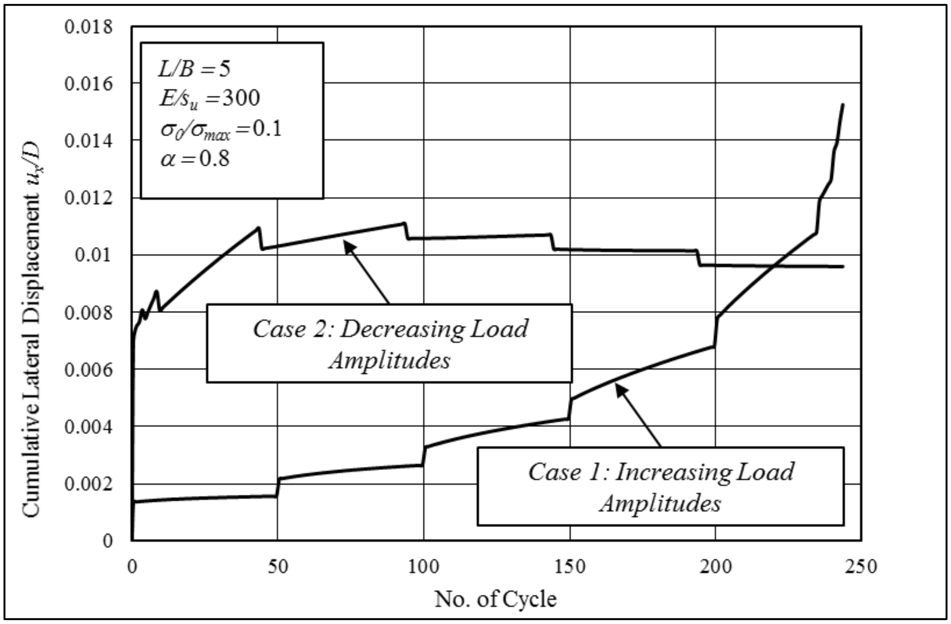

b) The influence of no-uniform load amplitude packets on the lateral displacement.

Figure 5.27 Continued.

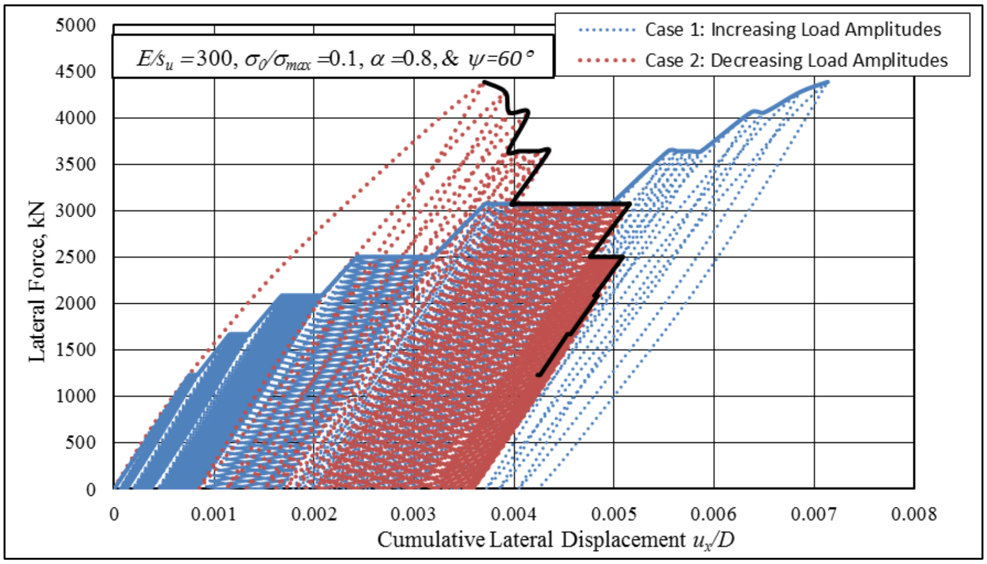

a) The influence of increasing and decreasing the non-uniform load amplitudes on the lateral displacements.

Figure 5.28 Cumulative lateral displacement for *L/D* = 5 and ψ = 60°.

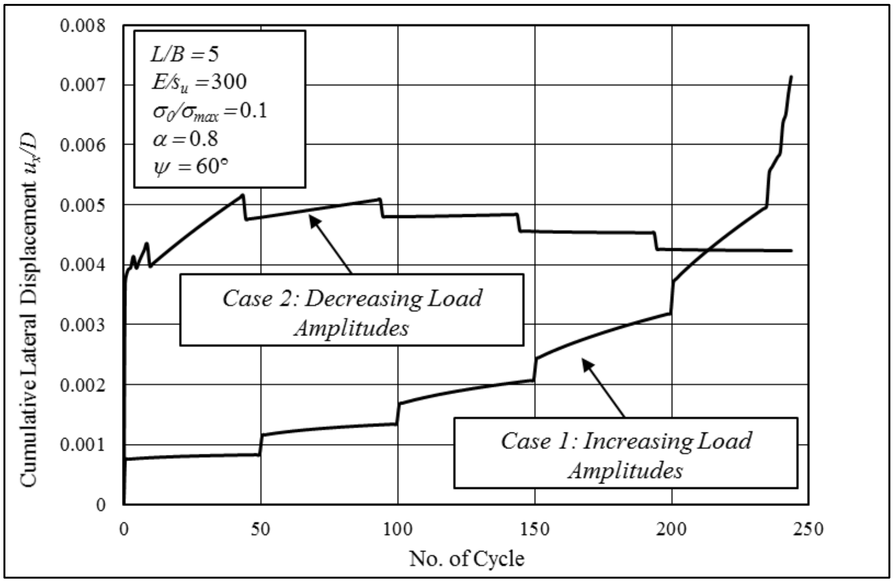

b) The influence of no-uniform load amplitude packets on the lateral displacement.

Figure 5.28 Continued.

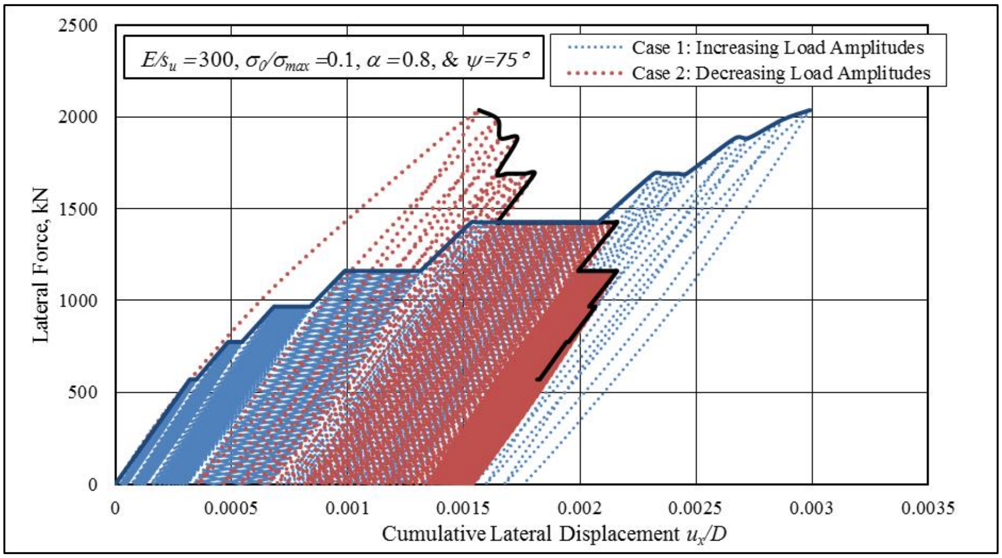

a) The influence of increasing and decreasing the non-uniform load amplitudes on the lateral displacements.

Figure 5.29 Cumulative lateral displacement for *L/D* = 5 and ψ = 75°.

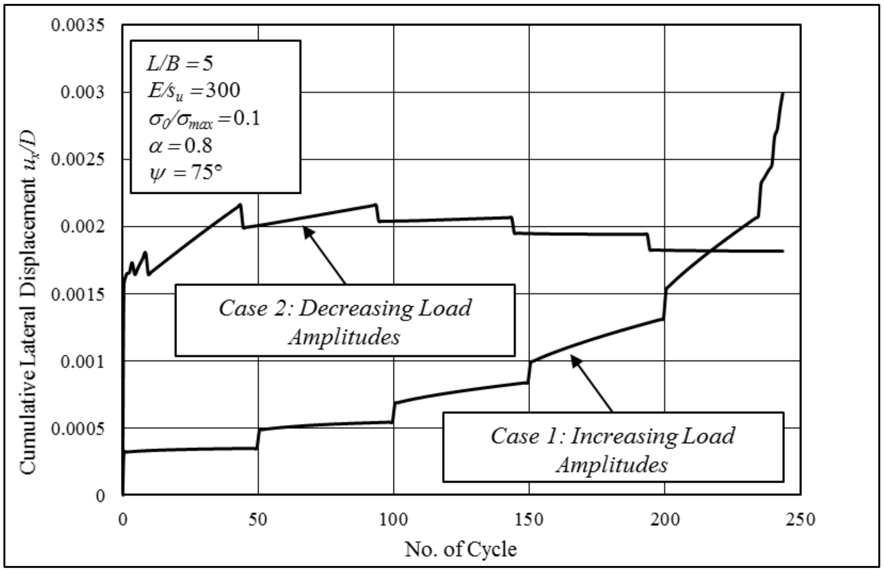

b) The influence of no-uniform load amplitude packets on the lateral displacement.

Figure 5.29 Continued.

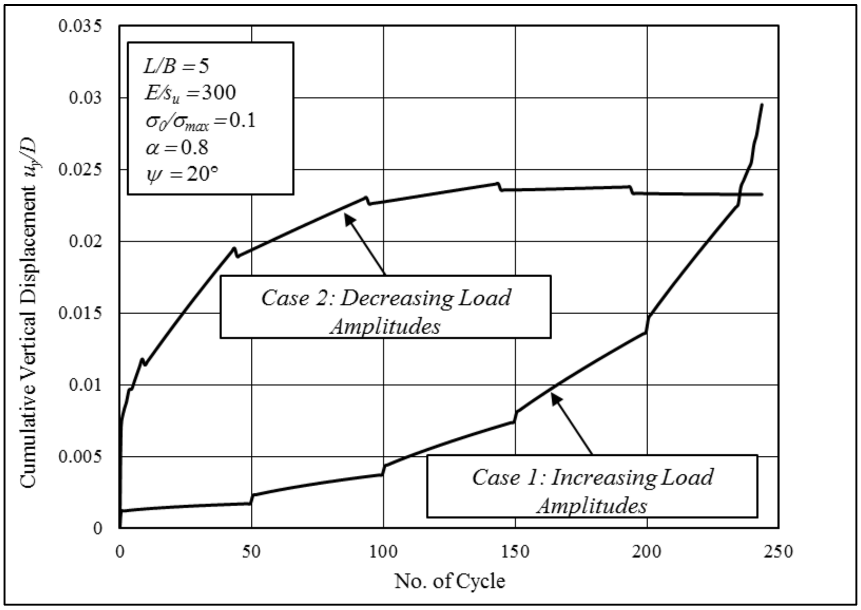

a) Cumulative vertical displacement for *L/D* = 5 and ψ = 20°.

Figure 5.30 Cumulative vertical and resultant displacement for *L/D* = 5 and ψ = 20°.

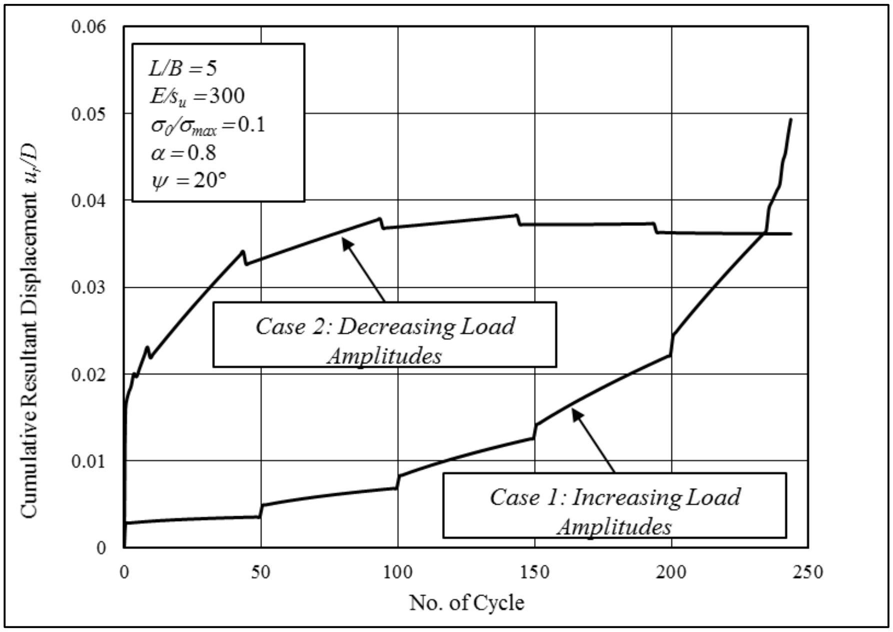

b) Cumulative resultant displacement for *L/D* = 5 and ψ = 20°.

Figure 5.30 Continued.

5.10.3. Effect of Aspect Ratio, L/D = 4, 5, & 6

Figure 5.31a shows the normalized lateral cumulative displacements for different aspect ratios for ψ of 45°, E/s_u of 300, σ_0/σ_{max} of 0.1, α of 0.8 for the inner and outer elements which touch the caisson wall, and α of 1.0 for element far from the wall. The normalized permanent cumulative displacement for the aspect ratio, *L/D*, of 4 is larger than 5 and 6. For the first load packet (50 cycles at $F = 0.28\ F_{all}$), there is a slight difference in the cumulative displacement for the different aspect ratios. That increases while increasing the amplitude loads ($F = 0.38$ to $1.0\ F_{all}$).

Figure 5.31b-c shows the normalized vertical and resultant cumulative displacements. The pile has more tendency to move upwards rather than laterally. There is about 60% difference between the vertical and lateral movements for all the aspect ratios. The curves are slightly nonlinear for a number of cycles about 15-20 cycles and nearly linear after 20 cycles.

Figure 5.32a-e shows the normalized lateral and vertical cumulative displacements for load angles of 20° and different aspect ratios. The trend of the lateral cumulative displacements seemed to be different from other inclination loads. Different aspect ratios have the same lateral cumulative displacement with a small difference for the aspect ratio of 6 as shown in Figure 5.32a. This behavior occurs only for the inclination load of 20°, since it is nearly pure lateral loading (Figure 5.1). For the load angle of 20°, the lateral cumulative displacements for all the aspect ratios are higher than the vertical cumulative displacements due to the large lateral load amplitudes, which were applied at two-thirds of the pile length. In contrast, the vertical cumulative displacements tend to increase while increasing the inclination load (Figure 5.31c and Figure 5.32c,d) for the same reason cited above.

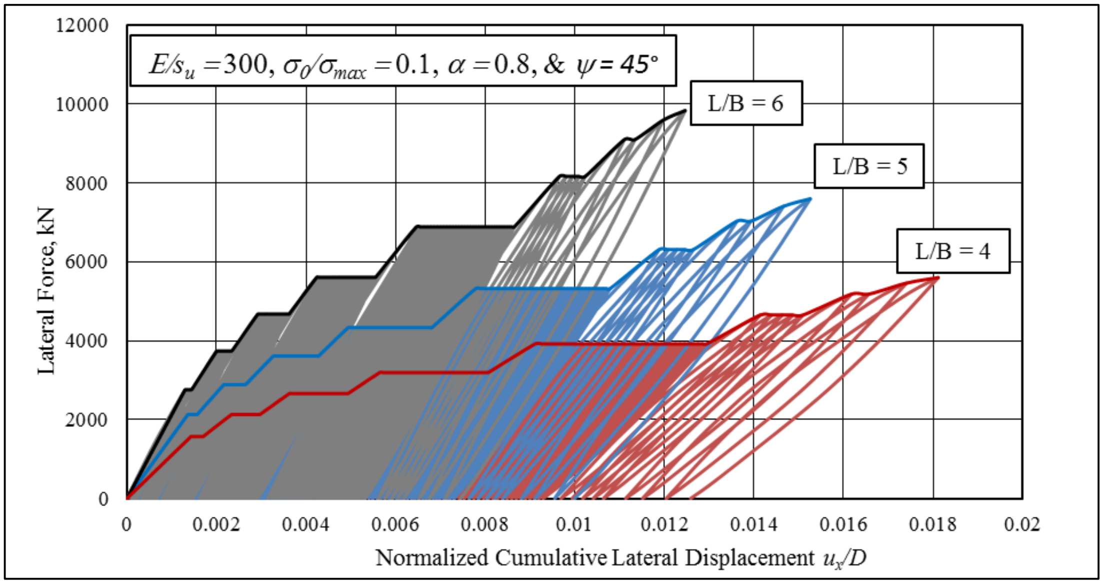

a) Lateral force vs. normalized lateral displacements.

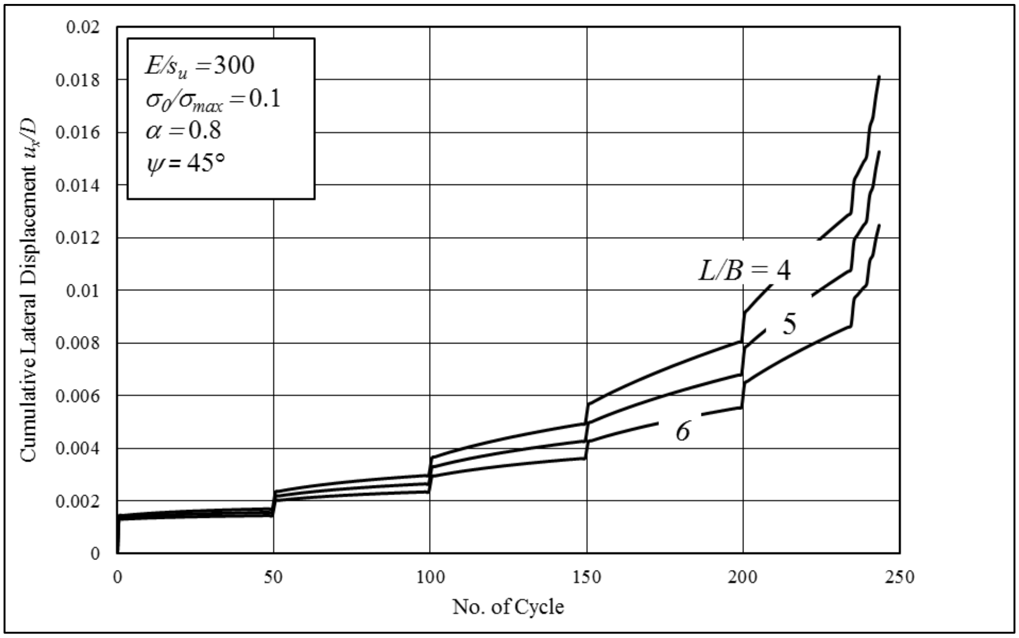

b) Normalized lateral displacements vs. no. of load cycles

Figure 5.31 Cumulative displacements for different aspect ratios.

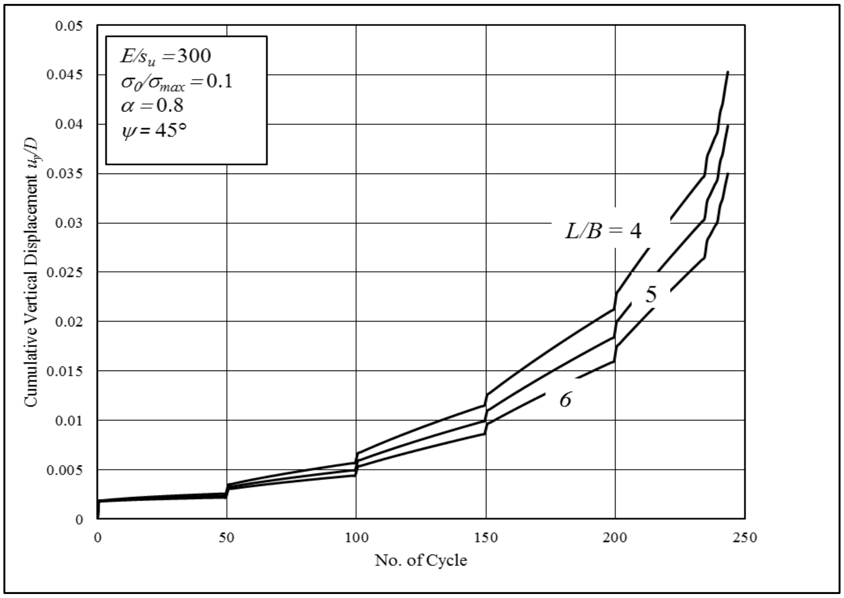

c) Cumulative vertical displacements vs. no. of load cycles.

Figure 5.31 Continued.

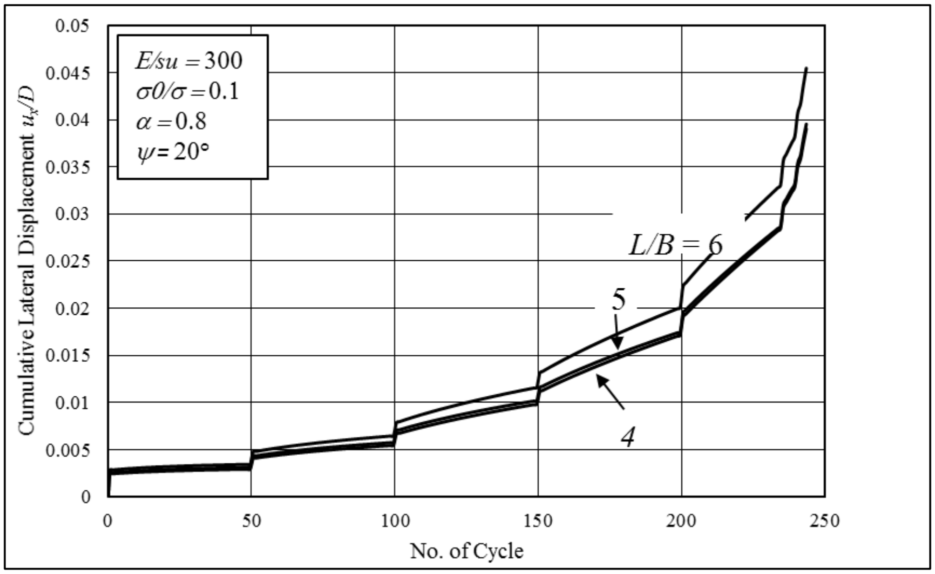

a) Normalized lateral displacements vs. no. of load cycles, ψ of 20°.

Figure 5.32 Cumulative displacements for different aspect ratios.

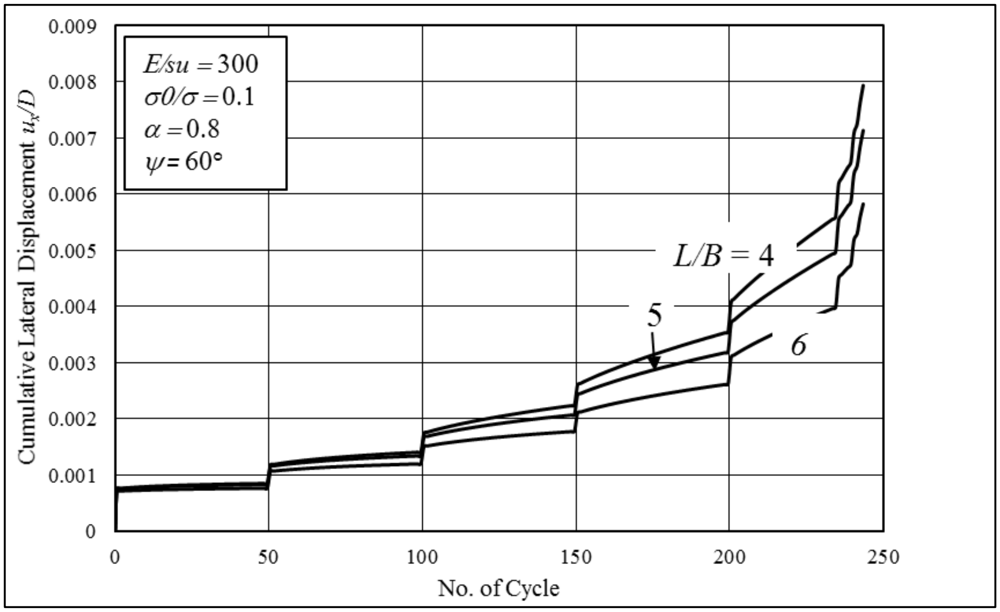

b) Normalized lateral displacements vs. no. of load cycles, ψ of 60°.

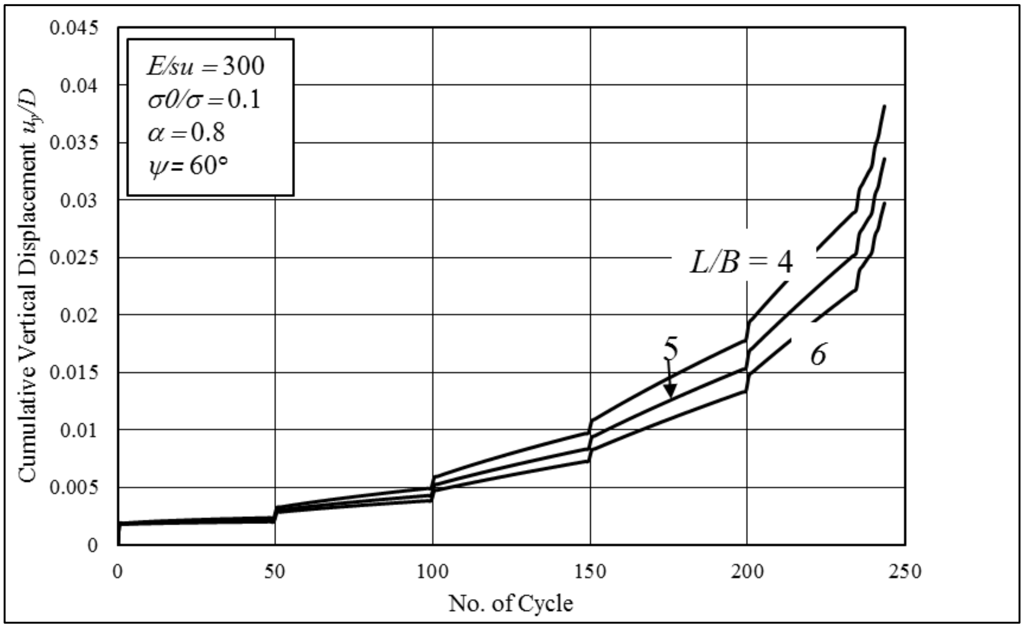

c) Normalized vertical displacements vs. no. of load cycles, ψ of 60°.

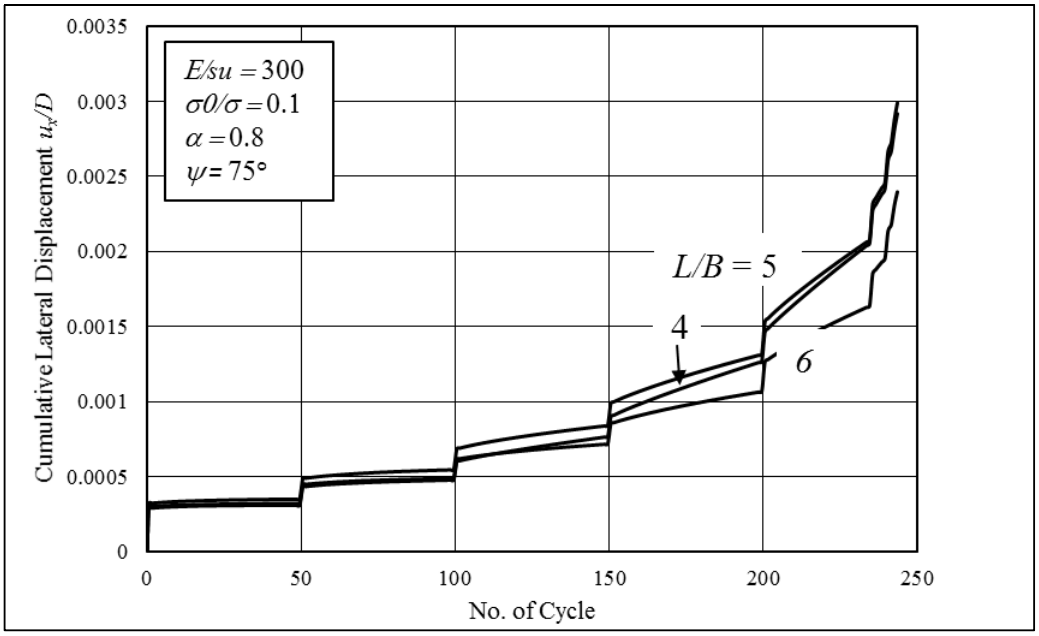

d) **Normalized lateral displacements vs. no. of load cycles, ψ of 75°.**

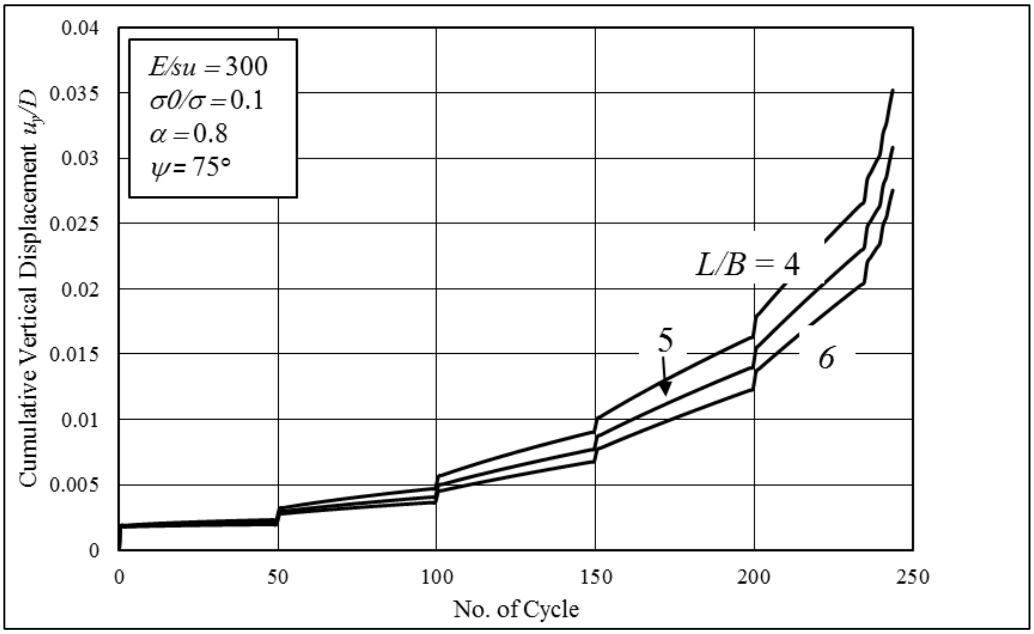

e) **Normalized vertical displacements vs. no. of load cycles, ψ of 75°.**

Figure 5.32 Continued.

5.10.4. Effect of Load Inclination for Different Aspect Ratios

Suction anchors may be used as catenary moorings in moderate water depths. The load attachment for the anchoring chain is generally between 50 to 70% of the total suction caisson embedment to maximize lateral resistance by minimizing rotation (Figure 5.1). However, the chain of the anchor subtends an angle ψ of 10° to 20° (Randolph, 2012; Randolph et al. 1998). In some cases (e.g. artificial seabed), the loading angles can be varied depending on the location of the suction pile from the structure. However, the load angles of 20° to 75° will be investigated.

Figure 5.33 shows the effect of the load inclination on the tilt. A higher tilt was predicted for the inclination load of 20° and the lowest tilt was for an inclination of 75°. When increasing the load angle (increasing the vertical load and decreasing the lateral load), the pile tends to move upward, resulting in reduced tilt as shown in Figure 5.33. Although very small tilt occurred for all load inclinations because the load attachment was at two-thirds the embedment depth (i.e. there is kind of pure translation as shown in Figure 5.1) and discussed by Randolph (2012). It is worth mentioning that the tilt trend is similar to the displacement trend where it increases while increasing the load amplitude packets as shown in Figure 5.33.

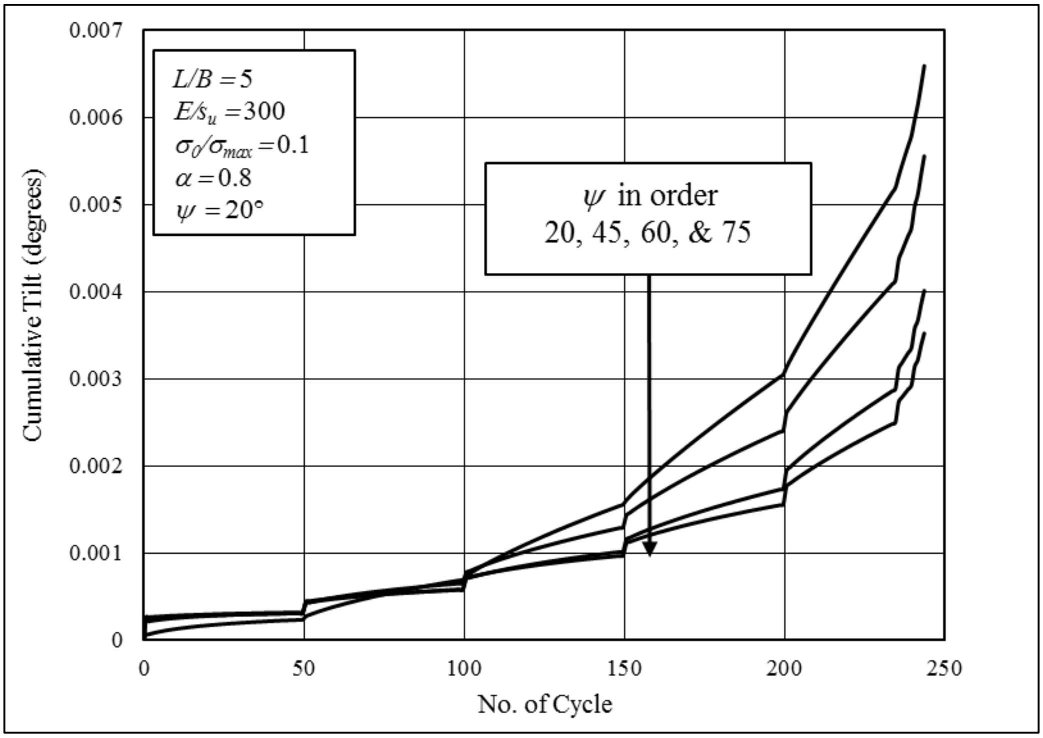

Figure 5.33 Effect of load inclination on tilt.

Figure 5.34a-d summarizes all the effects of different inclination loads and aspect ratios on deformations. The cumulative displacements for ψ = 20° for all aspect ratios are larger than all the other load angles because the lateral load is higher when the ψ = 20°.

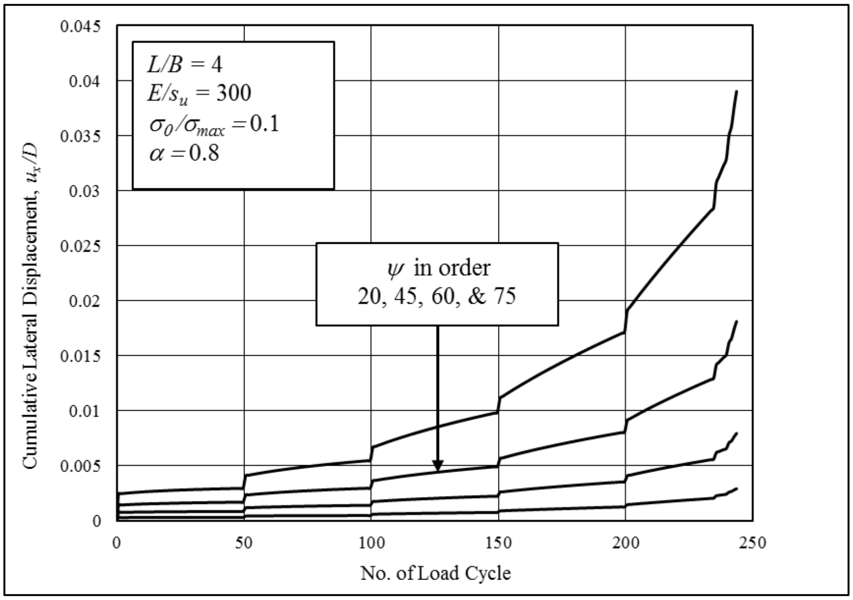

a) Lateral displacement vs no. of load cycles for *L/B* = 4.

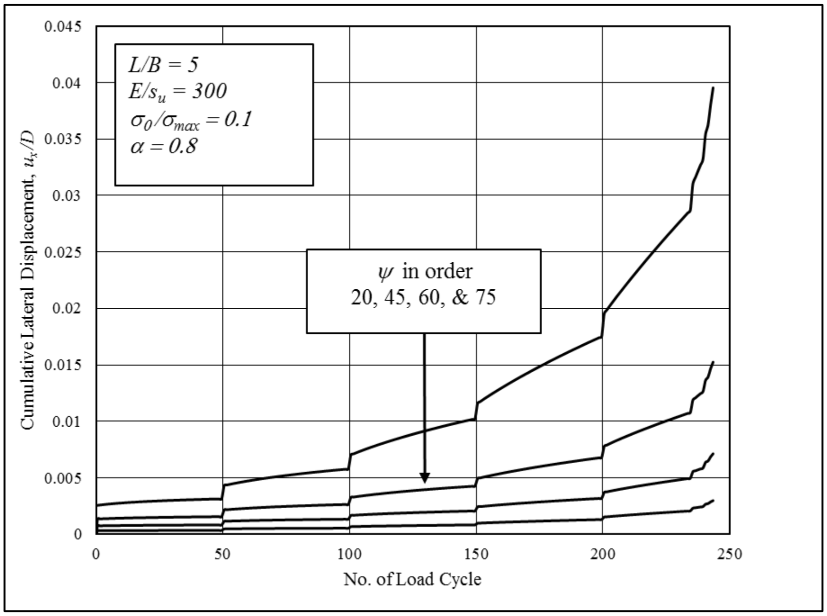

b) Lateral displacement vs no. of load cycles for *L/B* = 5.

Figure 5.34 Effect of load inclination on cumulative displacement for different aspect ratios.

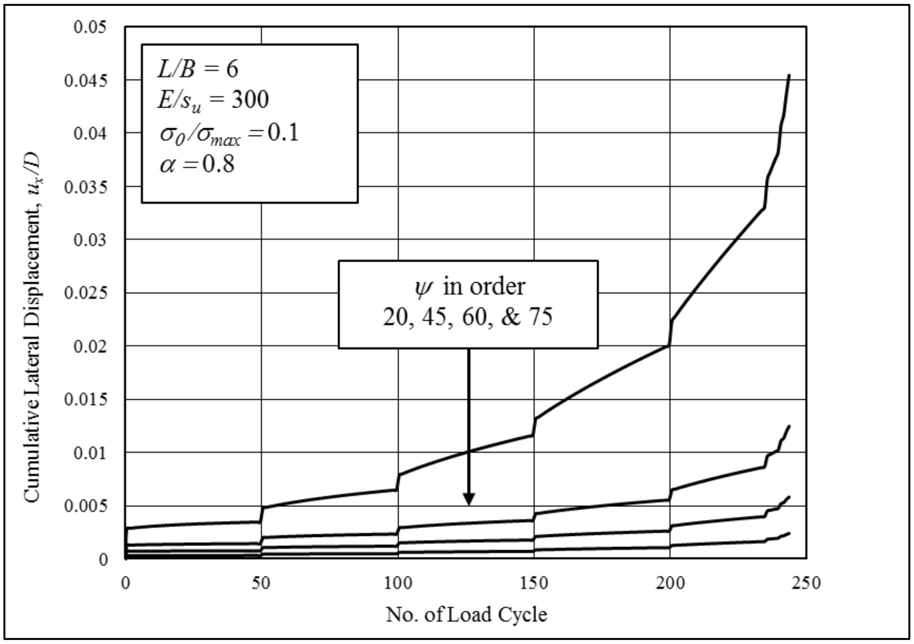

c) Lateral displacement vs no. of load cycles for *L/B* = 6.

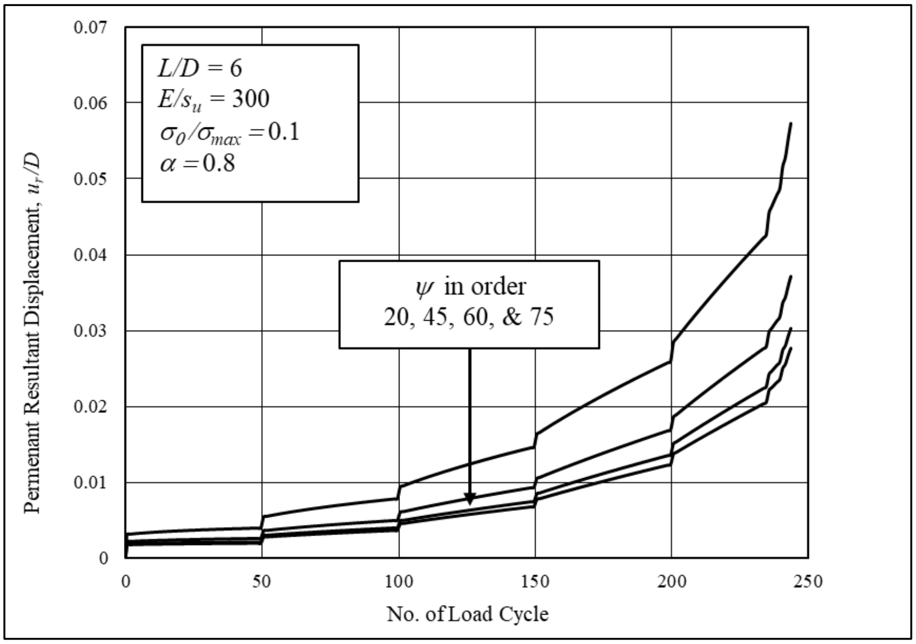

d) Resultant cumulative displacement vs no. of load cycles for *L/B* = 6.

Figure 5.34 Continued.

5.11. Nomenclature

API	American Petroleum Institute
A_s	Side Surface Area of The Caisson
A_{tip}	Cross-Sectional Area at The Tip
A_{wall}	Embedded Area of The Inside And Outside Wall
C	Initial Kinematic Hardening Modulus
D	Pile Outer Diameter
D_{in}	Pile Inner Diameter
e	Eccentricity
E	Modulus of Elasticity
EI	Flexural Stiffness of The Pile
$f(\sigma - \alpha_b)$	Equivalent Mises Stress With Respect To The Backstress
F	Yield Surface of The Kinematic Hardening Model
$f_{(w)}$	Unit Side Shear
F_{all}	Allowable Load Capacity (Applied Operational Load)
FE, FEA	Finite Element, Finite Element Analysis
F_h	Lateral Force
F_r	Resultant Force
F_{ult}	Ultimate Load Capacity
F_v	Axial Load
GoM	Gulf of Mexico

J	Dimensionless Constant Ranges From 0.25 to 0.5
L	Length of Embedded Pile/Caisson
L_t	Total length of the caisson with the lid
N	Number of Cycles
N_c	Bearing Capacity Factor
N_p	Bearing Capacity Factor For Laterally Loaded Pile
p	Soil Resistance Per Unit Length
PLA	Plastic Limit Analysis
p_u	Ultimate Soil Resistance
q	Unit End Bearing
Q_f	Side Friction Resistance
Q_p	End Bearing
Q_s	Side Wall Resistance
Q_t	Total Penetration Resistance
Q_{tip}	Tip Resistance
R	Axial Capacity
s_u	Undrained Shear Strength
$s_{u(ave)}$	Average Undrained Shear Strength
$s_{u,tip}$	Undrained Shear Strength at the pile tip
s_{u0}	Undrained Shear Strength at the surface
u_r	Cumulative Resultant displacement
u_x	Cumulative Lateral displacement

u_y	Cumulative Vertical displacement
w	Embedment Depth
y	Pile Deflection
y_{50}	Pile Deflection at (y_{50})
z	Depth
$\dot{\bar{\varepsilon}}^{pl}$	Equivalent Plastic Strain Rate
α	Adhesion Factor
α_b	Backstress
$\dot{\varepsilon}^{pl}$	Rate of Plastic Flow
ε_{50}	Axial Strain
γ	Parameter Determining The Rate of Decrease of The Kinematic Hardening With Increasing Plastic Deformation
γ'	Submerged Unit Weight
σ_0	Stress at Zero Plastic Strain
σ_{max}	Maximum Stress
ψ	Inclination angle

5.12. References

Al-Janabi, H. A., & Aubeny, C. P. (2019, July). Experimental Measurement of Thixotropy and Sensitivity in Gulf of Mexico Clay. In The 29th International Ocean and Polar Engineering Conference. International Society of Offshore and Polar Engineers.

Al-Janabi, H. A., Aubeny, C. P., Chen, J., & Luo, M. (2019, April). Experimental Measurement of Touchdown Zone Stiffness for SCR in Gulf of Mexico Clay. In Offshore Technology Conference. Offshore Technology Conference.

Al-Ramthan, A. Q. & Aubeny C. P., (2019). Numerical Investigation of the Performance of Caissons in Cohesive Soils under Cyclic Loading. ASCE (Submitted).

Anastasopoulos, I., Gelagoti, F., Kourkoulis, R., & Gazetas, G. (2011). Simplified constitutive model for simulation of cyclic response of shallow foundations: validation against laboratory tests. Journal of Geotechnical and Geoenvironmental Engineering, 137(12), 1154-1168.

Andersen, K. H. (2015). Cyclic soil parameters for offshore foundation design. Frontiers in offshore geotechnics III, 5.

API (2003). Recommended practice for planning, designing and constructing fixed offshore platforms–working stress design (RP 2A-WSD), American Petroleum Institute.

ASTM Committee D-18 on Soil and Rock. (2018). *Standard test methods for liquid limit, plastic limit, and plasticity index of soils*. ASTM international.

ASTM. (2016). Standard test method for laboratory miniature vane shear test for saturated fine-grained clayey soil.

Aubeny, C. P., Han, S. W., & Murff, J. D. (2003). Inclined load capacity of suction caissons. International Journal for Numerical and Analytical Methods in Geomechanics, 27(14), 1235-1254.

Aubeny, C. P., Murf, J. D., & Moon, S. K. (2001). Lateral undrained resistance of suction caisson anchors. International Journal of Offshore and Polar Engineering, 11(03).

Aubeny, C., & Murff, J. D. (2003). Simplified limit solutions for undrained capacity of suction anchors. In Deepwater Mooring Systems: Concepts, Design, Analysis, and Materials (pp. 76-90).

Clukey, E. C., Morrison, M. J., Gamier, J., & Corté, J. F. (1995, January). The response of suction caissons in normally consolidated TLP loading conditions. In Offshore Technology Conference. Offshore Technology Conference.

Colliat, J. L., Boisard, P., Andersen, K., & Schroeder, K. (1995, January). Caisson foundations as alternative anchors for permanent mooring of a process barge offshore Congo. In Offshore Technology Conference. Offshore Technology Conference.

Colliat, J. L., Boisard, P., Gramet, J. C., & Sparrevik, P. (1997, December). Geotechnical design and installation behaviour of suction anchor piles-comparison with drag anchors. In Proc., 7th Int. Conf. on Behaviour of Offshore Struct., Pergamon, Delft, The Netherlands (Vol. 1, p. 133).

Colliat, J. L., Dendani, H., Puech, A., & Nauroy, J. F. (2011). Gulf of Guinea deepwater sediments: Geotechnical properties, design issues and installation experiences. In *Proceedings of the 2nd International Symposium on Frontiers in Offshore Geotechnics (ISFOG), Perth, Australia* (pp. 59-86).

Dejong, J., Yafrate, N., Degroot, D., Low, H. E., & Randolph, M. (2010). Recommended practice for full-flow penetrometer testing and analysis. Geotechnical Testing Journal, 33(2), 137-149.

Fattah, M. Y., Shlash, K. T., & Mohammed, H. A. (2014). Bearing capacity of rectangular footing on sandy soil bounded by a wall. Arabian Journal for Science and Engineering, 39(11), 7621-7633.

Fattah, M. Y., Shlash, K. T., & Mohammed, H. A. (2014a). Experimental Study on the Behavior of Bounded Square Footing on Sandy Soil. Engineering and Technology Journal, 32(5 Part (A) Engineering), 1083-1105.

Fattah, M. Y., Shlash, K. T., & Mohammed, H. A. (2015). Experimental study on the behavior of strip footing on sandy soil bounded by a wall. Arabian Journal of Geosciences, 8(7), 4779-4790.

Fuglsang, L.D., and Steensen-Bach, J.O. (1991). "Breakout Resistance of Suction Piles in Clay," Proceedings of the International Conference on Centrifuge 1991, Boulder, Colorado, pp.153–159.

Gerolymos, N., Gazetas, G., and Tazoh, T. "Seismic response of yielding pile in non-linear soil." Proc., Proc. 1st Greece–Japan workshop, seismic design, observation, and retrofit of foundations, Athens, 11-12.

Gerolymos, N., Gazetas, G., and Tazoh, T. (2005). “Seismic response of yielding pile in non-linear soil.” Proc. 1st Greece-Japan Workshop, Seismic Design, Observation, and Retrofit of Foundations, National Technical Univ. of Athens, Athens, Greece, 25–36.

Langford, T., & Aubeny, C. P. (2008, January). Model tests for steel catenary riser in marine clay. In *Offshore Technology Conference*. Offshore Technology Conference.

Li, W., Igoe, D., & Gavin, K. (2015). Field tests to investigate the cyclic response of monopiles in sand. Proceedings of the Institution of Civil Engineers-Geotechnical Engineering, 168(5), 407-421.

Randolph, M. F. (2012). Offshore design approaches and model tests for sub-failure cyclic loading of foundations. In Mechanical behaviour of soils under environmentally induced cyclic loads (pp. 441-480). Springer, Vienna.

Randolph, M. F., Low, H. E., & Zhou, H. (2007, January). In situ testing for design of pipeline and anchoring systems. In OFFSHORE SITE INVESTIGATION AND GEOTECHNICS, Confronting New Challenges and Sharing Knowledge. Society of Underwater Technology.

Randolph, M. F., O'neill, M. P., Stewart, D. P., & Erbrich, C. (1998, January). Performance of suction anchors in fine-grained calcareous soils. In Offshore technology conference. Offshore Technology Conference.

Simulia (2014). "ABAQUS Documentation." Dassault Systèmes, Providence, RI, USA.

Sparrevik, P. (2002, January). Suction pile technology and installation in deep waters. In *Offshore technology conference*. Offshore Technology Conference.

Yafrate, N., DeJong, J., DeGroot, D., & Randolph, M. (2009). Evaluation of remolded shear strength and sensitivity of soft clay using full-flow penetrometers. *Journal of Geotechnical and Geoenvironmental Engineering*, *135*(9), 1179-1189.

Huang, J., Cao, J., & Audibert, J. M. (2003, January). Geotechnical design of suction caisson in clay. In *The Thirteenth International Offshore and Polar Engineering Conference*. International Society of Offshore and Polar Engineers.

API RP 2SK. (A 2008). “Design and Analysis of Stationkeeping Systems for Floating Structures,” API Recommended Practice 2SK, Third Edition, American Petroleum Institute, Addendum May 2008.

API RP 2GEO. (2011). “Geotechnical and Foundation Design Considerations,” ANSI/API Recommended Practice 2GEO, First Edition, American Petroleum Institute, April 2011.

Murff, J. D. and Hamilton, J. M. (1993). “P-ultimate for Undrained Analysis of Laterally Loaded Piles.” J. Geotechnical Engineering, ASCE, 119(1), 95-107.

Reese, L. C., Cox, W. R., & Koop, F. D. (1975, January). Field testing and analysis of laterally loaded piles om stiff clay. In Offshore Technology Conference. Offshore Technology Conference.

Matlock, H. (1970). Correlations for design of laterally loaded piles in soft clay. Offshore technology in civil engineering’s hall of fame papers from the early years, 77-94.

DNV (2014). "Design of Offshore Wind Turbine Structures, DET NORSKE VERITAS AS."

6. EXPERIMENTAL MEASUREMENT OF TOUCHDOWN ZONE STIFFNESS FOR SCR IN GULF OF MEXICO CLAY[*]

6.1. Introduction

Steel Catenary Risers (SCRs) are long steel pipes that hang freely between the seabed and floating production facilities (Figure 6.1a). A critical location for SCR fatigue damage is at the TDZ, with the intensity of fatigue stresses being highly dependent on seabed stiffness, which is commonly modeled using equivalent soil springs (Figure 6.1b) characterized by soil resistance P (kN/m) and displacement y (m). The SCR tends to self-embed to depth h within the TDZ. Since soil strength s_u commonly (but not always) increases with soil depth, greater trench depth usually leads to greater soil resistance P.

Figure 6.2 illustrates typical P-y behavior. The "backbone curve" corresponds to initial penetration of the SCR into the seabed. An uplift half cycle of loading may involve large displacements that fully separate the riser from the seabed or smaller displacements are the soil and riser remain in contact. Upon re-penetration, the riser depth may exceed the earlier reversal depth y_1, which corresponds to a condition of trench formation. Alternatively, if $y \leq y_1$ after re-penetration, the resulting soil resistance P will be less than P_1, producing a relaxation or "stiffness degradation" effect.

---

[*] Reprinted with permission from "Experimental Measurement of Touchdown Zone Stiffness for SCR in Gulf of Mexico Clay" by Authors' Husham A. Al-Janabi, Charles P. Aubeny, Jinbo Chen, and Meng Luo, 2019. Offshore Technology Conference (OTC 2019), Volume Number, 1-20, Copyright [2019] by the Offshore Technology Conference (OTC 2019).

Both monotonic and cyclic *P*-*y* curves are commonly derived from single-gravity laboratory model tests, where a short segment of pipe is pushed into the soil testbed and subjected a history of uplift and re-penetration cycles of interest. Although random loading sequences occur in the field, laboratory model tests usually impose either displacement-controlled cyclic loading, where the pipe is repeatedly re-penetrated to a depth y_1, or force-controlled cyclic loading, where the pipe is repeatedly re-penetrated to the point at which a soil resistance P_1 mobilizes. Since the movement of the SCR close to the seabed is mainly imposed from the global motion of the platform, the displacement-controlled tests are appropriate to a fatigue life study after a large number of load cycles, while the force-controlled cyclic loading may be more relevant in predicting the trench formation, in particular, in the early life of an SCR.

An additional consideration in developing a laboratory model test program for investigating *P*-*y* behavior is the possibility of stiffness recovery due to reconsolidation and possibly thixotropic strength gain during rest periods during storm events. Previous investigators have actually included rest periods in the imposed load histories on SCRs during model tests (Clukey et al., 2017; Langford and Aubeny, 2008). These studies report noticeable increases in soil resistance following the rest period, but they appeared to be short-lived; i.e. within less than 10 cycles after the resumption of loading the soil resistance reduces to roughly the same level that existed prior to the rest period. As will be discussed subsequently in this chapter, the extent and duration of soil stiffness recovery can be significantly influenced by the details of the test method.

This chapter presents the findings of a series of single-gravity laboratory model tests on a “rigid” pipe investigating *P*-*y* behavior for SCRs in high plasticity Gulf of Mexico (GOM) clay. Three monotonic and 21 cyclic tests are conducted under displacement-controlled loading. The objective is to acquire data on soil resistance during monotonic and cyclic loading and to assess the effect of recovery during rest periods. In contrast to the procedure utilized in a previous study on the effects of setup during rest periods (Langford and Aubeny, 2008), where the riser was held at a fixed elevation during the rest period, the riser in this study is subjected to a constant (self-weight) vertical load. Thus, further embedment of the riser is possible as consolidation occurred during the rest period. The riser model is fabricated to be a rigid steel pipe section with a diameter D of 50.8 mm (2 inches) and a length L of 304.8 mm (12 inches). A high plasticity GOM clay with undrained shear strength corresponding to typical normally consolidated conditions is used in this study to represent the seabed at TDZ. The monotonic tests are conducted at the beginning of the program to obtain the vertical loading resistance with depth at different rate effects. These results compared to existing models before proceeding with vertical cyclic loading tests. The study investigated the following aspects of soil-riser interaction: (1) the effect of riser embedment depth h over a range h/D = 0.25-2, (2) the effect of loading rate during monotonic penetration, with load rates varying from 1 to 15 mm/sec, (3) vertical stiffness degradation as a function of load cycle under cyclic displacement amplitudes in the range $\Delta y_{cyc}/D$ = 0.02-0.05, and (4) stiffness recovery during rest (pause) periods ranging from 1 to 13 hours. Cyclic displacement motion Δy_{cyc} refers to the peak-to-trough displacements.

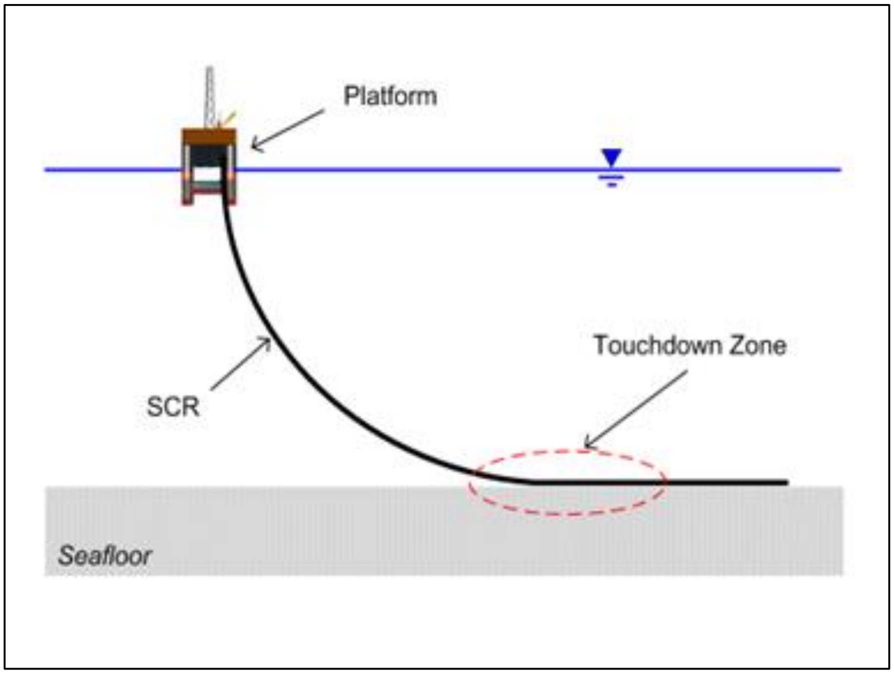

a) SCR Configuration.

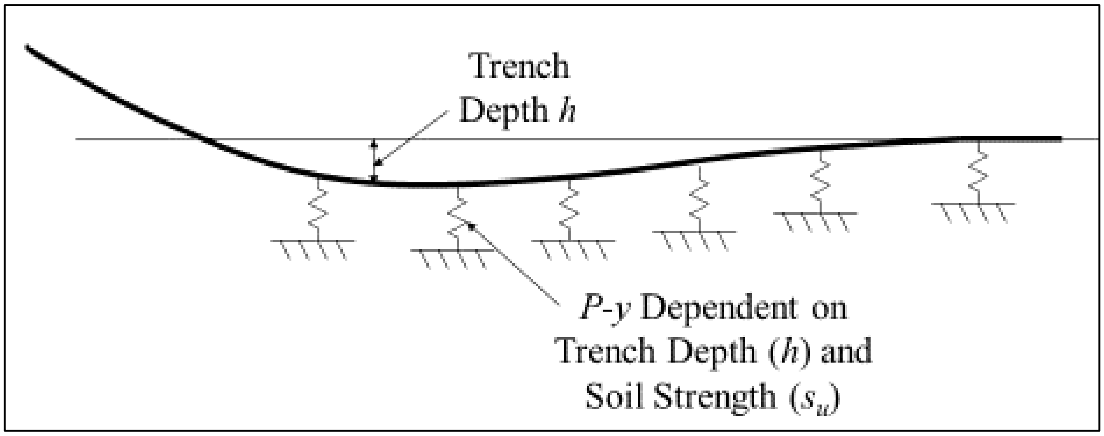

b) Equivalent Spring Model.

Figure 6.1 Steel catenary risers in the touchdown zone.

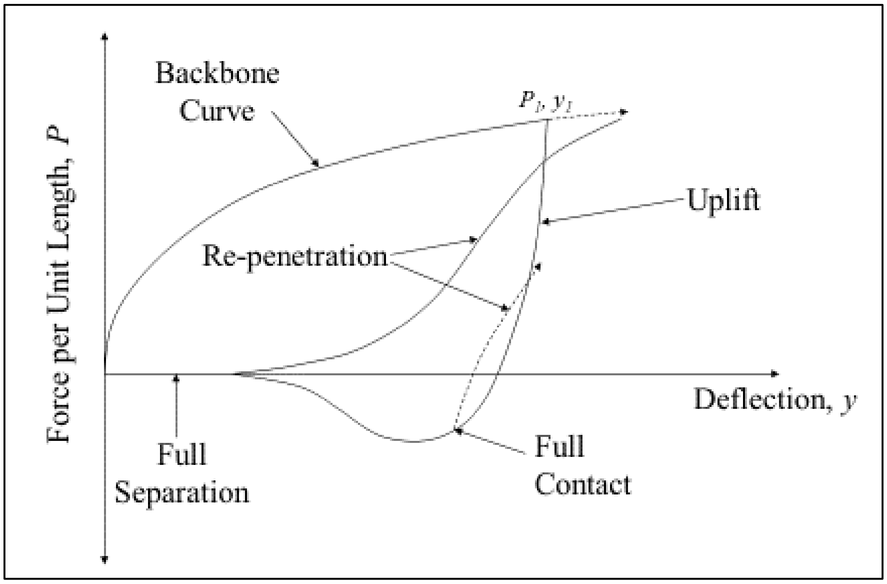

Figure 6.2 Typical *P-y* Behavior.

6.2. Background

6.2.1. Load-Deflection (P-y) Curves

In previous studies, most numerical models have been developed to describe the seabed-riser interaction based on load-deflection (P-y) curves. For laterally loaded piles, *P-y* curves are used, which are essentially Winkler springs. In this section, some previous experimental and numerical studies will be discussed.

Matlock (1970) developed design procedures for constructing P-y relationships for saturated soft clays subjected to either short-term static loading or cyclic loading based on full-size instrumented piles (results of field measurements).

Al-Janbai el al., (2019) presented the findings of a series of single-gravity laboratory model tests on a “rigid” pipe investigating *P-y* behavior for SCRs in high plasticity Gulf of Mexico (GOM) clay. Authors described the reconsolidation following the rest periods, which led to a short-term increase the soil secant stiffness and soil resistance that rapidly declines upon resumed cyclic loading; however, the degraded resistance was slightly greater than the pre-rest period levels. With continued sequences of cyclic loading followed by rest periods, the soil stiffness gradually trends upward. This behavior was believed to be due to the fact that settlement of the pipe was permitted to occur during the rest periods.

Bridge & Willis (2002) presented a test setup, which is part of the STRIDE JIP project to predict the soil-riser interaction. The soil properties were similar to the properties of GOM soil. Vertical and horizontal movements were simulated to model the waves and the vessels motions. A nonlinear model of the soil-riser interaction at the touch down zone was developed as a results of the test data.

Hu et al. (2011) conducted a centrifuge test with applying a dynamic vertical motion to investigate the steel catenary riser's movement at the touchdown zone. It was observed that soil degradation increases while increasing the number of load cycles.

Aubeny et al. (2005) developed an empirical equation for predicting the collapse load for a cylinder embedded in a cohesive clay in open trench at different embedment depths. The empirical equation was developed using a finite element analysis. In addition, the authors considered the soil strength variations with depth.

Clukey et al. (2008) showed the soil-riser-fluid interaction at the TDZ by using coupled Eulerian-Lagrangian capability. The effects of cyclic loading were ignored in the study.

6.3. Objectives

Monotonic and cyclic model tests using single gravity, displacement-controlled laboratory model tests of soil stiffness are conducted. All tests used high plasticity Gulf of Mexico clay with undrained shear strength corresponding to typical normally consolidated conditions. A test program is developed to evaluate:

- rate effects for monotonic and cyclic loading,
- vertical stiffness for displacement amplitudes ranging from 0.02-0.05 D (where D = riser outer diameter),
- soil stiffness degradation with increasing in the number of cycles,
- stiffness recovery during rest periods, and
- stiffness recovery under prolonged cyclic loading.

A high plasticity GOM clay with undrained shear strength corresponding to typical normally consolidated conditions is used in this study to represent the seabed at TDZ. The monotonic tests are conducted at the beginning of the program to obtain the vertical loading resistance with depth at different rate effects. These results compared to existing models before proceeding with vertical cyclic loading tests. The study investigated the following aspects of soil-riser interaction:

(1) the effect of riser embedment depth h over a range h/D = 0.25-2,

(2) the effect of loading rate during monotonic penetration, with load rates varying from 1 to 15 mm/sec,

(3) vertical stiffness degradation as a function of load cycle under cyclic displacement amplitudes in the range $\Delta y_{cyc}/D$ = 0.02-0.05, and

(4) stiffness recovery during rest (pause) periods ranging from 1 to 16 hours for $\Delta y_{cyc}/D = 0.02$ and 1 to 13 hours for $\Delta y_{cyc}/D = 0.05$.

6.4. Test Program

The test program comprises four test series. Series 1 (Table 6.1) involved monotonic loading at different penetration rates. Series 2 in Table 6.2 involved initial penetration to different embedment depths and penetration rates followed by cyclic loading, with one exception, at a cyclic amplitude $\Delta y_{cyc}/D = 0.05$. The exception is Test 10, which is loaded at a cyclic amplitude $\Delta y_{cyc}/D = 0.02$. Series 3 (Table 6.3) introduced rest periods between packets of cyclic loading, with a "large amplitude" cyclic amplitude $\Delta y_{cyc}/D = 0.05$. Tests 11a to test 11j denote individual packets of cyclic loading within a single test. Series 4 (Table 6.4) similarly involved packets of load cycles interspersed with rest periods, but with small amplitude loading, a cyclic amplitude $\Delta y_{cyc}/D = 0.02$. In addition, multiple T-bar and miniature vane shear tests are conducted to establish the undrained shear strength profile as well as the relationship between the water content and the undrained shear strength.

Table 6.1 Series 1: Monotonic Penetration at Different Loading Rates.

Test No.	**Velocity (mm/sec)**	**Test description**
1	1 mm/sec	Penetrated into 1.0 *D*
2	10 mm/sec	Penetrated into 1.0 *D*
3	15 mm/sec	Penetrated into 1.3 *D*

Table 6.2 Series 2: Cyclic Testing with No Rest Periods.

Test No.	Load/Disp. Control	Velocity mm/sec	Test Description	No. of cycles
4		1	h=0.5 D and then $\Delta y_{cyc}/D$ =0.05 D, 2-way displacement.	1000
5		5	h =0.5 D and then $\Delta y_{cyc}/D$ =0.05 D, 2-way displacement.	1000
6		1.5	h =0.25D and then $\Delta y_{cyc}/D$ =0.05 D, 2-way displacement.	1000
7			h =0.5 D and then $\Delta y_{cyc}/D$ =0.05 D, 2-way displacement.	200
8			h =1.0 D and then $\Delta y_{cyc}/D$ =0.05 D, 2-way displacement.	1000
9		1	h =2.0 D and then $\Delta y_{cyc}/D$ =0.05 D, 2-way displacement.	1000
10		1.5	h =0.5D and then $\Delta y_{cyc}/D$ =0.02 D, 2-way displacement.	535

Table 6.3 Series 3: Large Amplitude Cyclic Loading with Rest Periods.

Test No.	Load/Disp. Control	Velocity mm/sec	Test Description	No. of cycles
11a	Displacement control	1.5	h=0.5 D and then $\Delta y_{cyc}/D$ =0.05D, 2-way displacement.	100
11b to 11i			After the pause period (1-2 hrs.), $\Delta y_{cyc}/D$ =0.05 D, 2-way disp.	100
11j			After the pause period about (13 hrs.), $\Delta y_{cyc}/D$ =0.05 D, 2-way disp.	100

Table 6.4 Series 4: Small Amplitude Loading with Rest Periods.

Test	Load/Disp. Control	Velocity mm/sec	Test Description	No. of cycles
12 a	Displacement control	1.5	h =0.5 D and then $\Delta y_{cyc}/D$ =0.02 D, 2-way displacement.	300
12 b to 12 c			After the pause period (3-4 hrs.), $\Delta y_{cyc}/D$ =0.02 D, 2-way displacement.	300

Table 6.4 Continued.

Test	Load/Disp. Control	Velocity mm/sec	Test Description	No. of cycles
12 d			After the pause period about (16 hrs.), $\Delta y_{cyc}/D$ =0.02 D, 2-way displacement.	300

6.5. Test Equipment

The test equipment used in the experiments, including the test basin for conducting the tests, the model riser pipe segment, the loading frame, the smart motors, the sensors, the data acquisition system, etc. (see Chapter 1 for more details).

6.6. Model Seabed Properties

Gulf of Mexico clay is used in this investigation. The soil model is prepared as explained in (Chapter 2). After finishing a given riser load test, the affected soil is removed and replaced by new soil using the same placement procedure as described above.

The index properties of the clayey soil are determined by using standard tests ASTM D4318-00, (2018).

6.7. Undrained Shear Strength of the Soil

This section is explained in details in (Chapter 3). T-bar tests are conducted directly on test bed soils to provide independent measurements of the undrained shear strength of the soil supporting the riser pipe. The dimensions of the T-bar as explained before are 1.27 cm (0.5 inches) in diameter by 5.08 cm (2 inches) in length. T-bar measurements are connected to the robotic actuator and directed to the data acquisition system in a manner similar to that described above for the model test pipe measurements. The penetration rate is 20 mm/sec (0.787 in/sec) to achieve undrained loading conditions (Langford and Aubeny 2008; Yafrate el al. 2009). All undrained shear strengths are interpreted by using a T- bar bearing factor of 10.5. Multiple undrained shear strength profiles are calculated depending on moisture water content of the soil bed. All the profiles show that the shear strength increases linearly with depth. Table 6.5 shows the strength gradient for all tests. The miniature vane shear test apparatus in this thrust area is used to establish relationships between water content and undrained shear strength. The undrained shear strength is computed from vane measurements in accordance ASTM D4648/D4648M-16, (2016).

6.7.1. Penetration Resistance of T- bar Penetrometer

T-bar penetrometer measurements require a correction for the T-bar rod, since there is no cancellation of overburden pressure within the footprint of the rod. The correction factor relates directly to the penetrometer area ratio (A_R/A_p) (Al-Janabi and Aubeny, 2019; Yafrate et al., 2009). The penetrometer area ratio is the ratio between the projected area of the T- bar rod (A_R) and the projected area of the T-bar probe (A_p). The A_R/A_p is used around 1:10 as recommended by DeJong et al., (2010). Randolph et al., (2007) used the following correction to find the net penetration of the penetrometer ($q_{T\text{-}bar\,(net)}$) as shown in Equation 6.1.

$$q_{T\text{-}bar\,(net)} = q_{T\text{-}bar\,(m)} - [\sigma_{v0} - u_0(1 - a_0)]\, A_R/A_p$$ **Equation 6.1**

where: $q_{T\text{-}bar(m)}$ is the measured penetration resistance, σ_{v0} is the total overburden stress, u_0 is the pore water pressure, and a_0 is the area ratio (0.7-0.9) according to Randolph et al., (2007). A penetration ratio of 0.7 is selected for this study.

Figure 6.3 shows the corrected penetration resistance. Figure 6.4 presents some of the T-bars test results that have been determined with different water contents. Figure 6.5 illustrates the relationship between undrained shear strength and moisture water content using a miniature vane shear test. Table 6.5 shows the undrained shear strength equations for different moisture water contents.

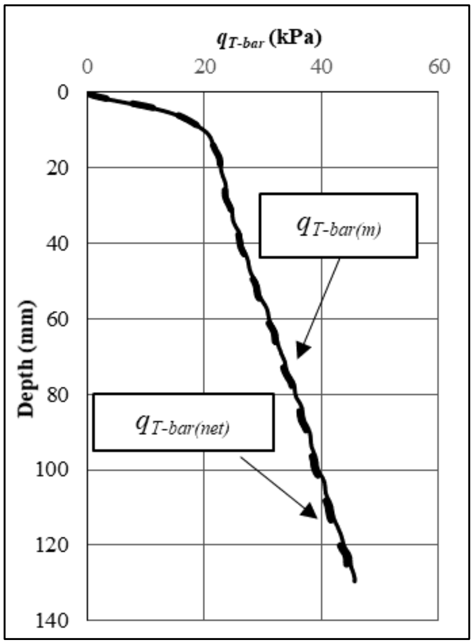

Figure 6.3 Measured vs. corrected penetration resistance.

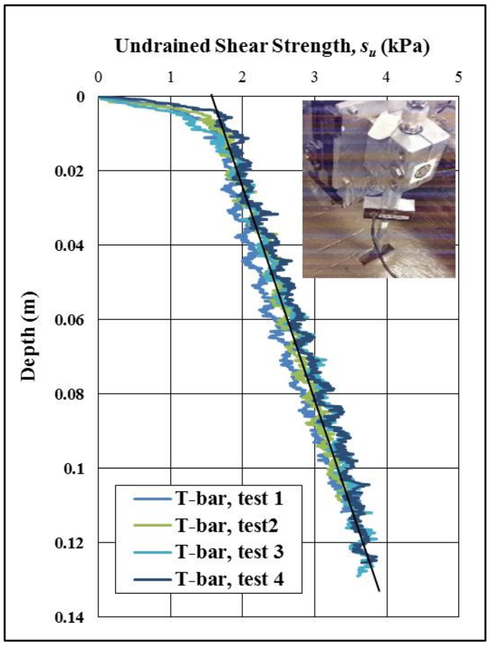

Figure 6.4 Some of the T-bars test results.

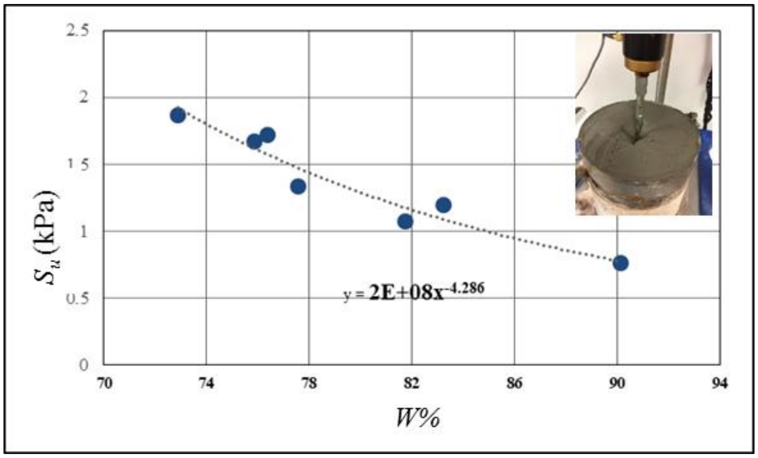

Figure 6.5 Undrained shear strength s_u vs. water content w%.

Table 6.5 Undrained Shear Strength Using (T-bars Test).

Test no.	**s_{u0} (kPa)**	**Strength gradient (kPa /m)**	**Undrained Shear Strength, s_u (kPa)**
1-4	1.0	16.7	$1.0+16.7h$
8&9	1.4	18.8	$1.4+18.8h$
7	1.3	14	$1.3+14h$
6, 10, &11-a -11-j	1.5	16.3	$1.3+16.3h$
12-a -12-d	1.4	12.3	$1.4+12.3h$

6.8. Buoyancy Effect

The total soil resistance consists of two components: the soil strength resistance and the buoyancy resistance. Figure 6.6a shows a general sketch with the total force per unit length P_t and the buoyancy force of soil per unit length P_b. Equation 6.2 shows the total resistance of the soil, q_t, the strength resistance of the soil, q_s, and the buoyancy resistance of the soil, q_b.

$$q_t = q_s + q_b \Rightarrow P_t/D = P/D + P_b/D \qquad \textbf{Equation 6.2}$$

Assuming that the trench does not collapse, Aubeny and Dunlap (2003) express the buoyancy resistance as shown in Equation 3.

$$q_b = \begin{cases} \dfrac{\gamma' D^2}{D}\left[\dfrac{1}{4}\cos^{-1}\left(1-\dfrac{2h}{D}\right)-\left(\dfrac{1}{2}-\dfrac{h}{D}\right)\sqrt{\dfrac{h}{D}-\left(\dfrac{h}{D}\right)^2}\right]\cdots\cdots\cdots 0\le\dfrac{h}{D}\le 0.5 \\ \dfrac{\gamma' D^2}{D}\left[\dfrac{\pi}{8}+\dfrac{h}{D}-\dfrac{1}{2}\right]\cdots\cdots\cdots\cdots\cdots\cdots\cdots\cdots\cdots\cdots\cdots\cdots\dfrac{h}{D}>0.5 \end{cases} \qquad \textbf{Equation 6.3}$$

Figure 6.6b-h and Figure 6.7 show the surface heave that generated from pushing the pipe into the soil and the trench. The surface heave considers a factor that affects the seabed resistance. In addition to the surface heave, another factor contributes with the effect of the seabed resistance is remolding the soil close to the pipe (Langford and Aubeny 2008a; Hodder, White et al., 2009). Hodder et al., (2009) presented a heave factor, f_b, ranging from 1.5 for shallow penetration to 1 for deep penetration. Equation 4 shows the heave factor in the buoyancy resistance equation.

$$q_b = (f_b A_s \gamma')/D \qquad \textbf{Equation 6.4}$$

where A_s is the submerged cross-sectional area of the riser. Therefore, f_b is added to Equation 6.3 to be as shown below in Equation 6.5.

$$q_b = \begin{cases} \frac{\gamma' D^2 f_b}{D}\left[\frac{1}{4}\cos^{-1}\left(1-\frac{2h}{D}\right)-\left(\frac{1}{2}-\frac{h}{D}\right)\sqrt{\frac{h}{D}-\left(\frac{h}{D}\right)^2}\right]\cdots\cdots\cdots 0 \le \frac{h}{D} \le 0.5 \\ \frac{\gamma' D^2 f_b}{D}\left[\frac{\pi}{8}+\frac{h}{D}-\frac{1}{2}\right]\cdots\cdots\cdots\cdots\cdots\cdots\cdots\cdots\cdots\cdots \frac{h}{D}>0.5 \end{cases}$$

Equation 6.5

Since the entire test program is conducted using displacement controlled loading, the buoyancy effect is considered only in the first 20 cycles, because there is no displaced soil after reaching the target depth except Tests 9 and 12a to 12d.

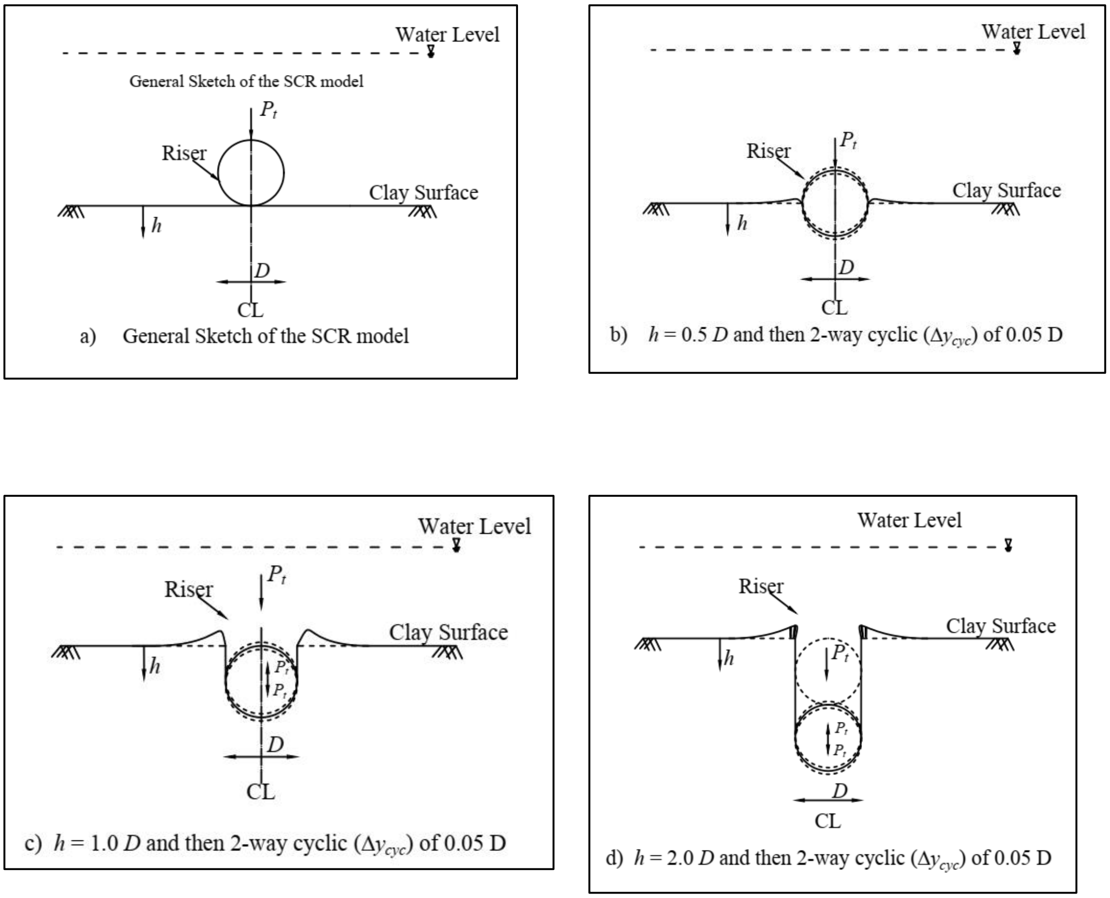

a) General Sketch of the SCR model

b) $h = 0.5\,D$ and then 2-way cyclic (Δy_{cyc}) of 0.05 D

c) $h = 1.0\,D$ and then 2-way cyclic (Δy_{cyc}) of 0.05 D

d) $h = 2.0\,D$ and then 2-way cyclic (Δy_{cyc}) of 0.05 D

Figure 6.6 Some sketches illustrate the steps of penetrating and cycling the riser.

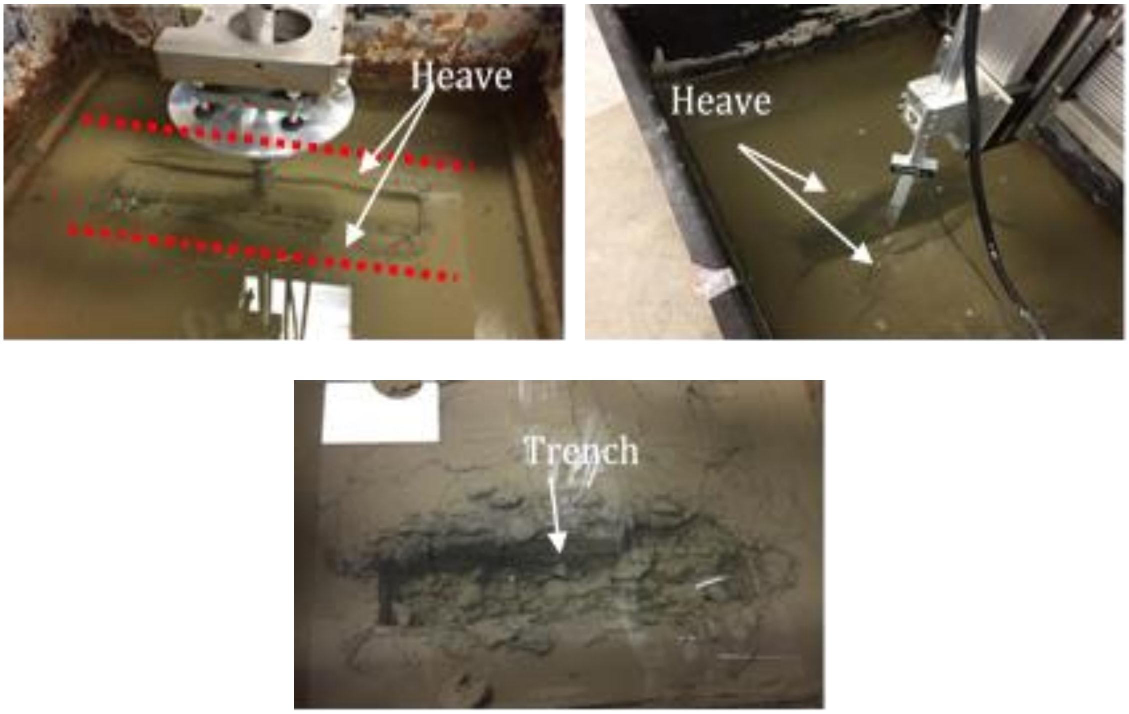

Figure 6.7 Some photos show the heave and the formed trenches.

6.9. Rate Effect Results and the Comparison With Existing Results

Three monotonic tests and two vertical cyclic loading tests are carried out to evaluate the rate effect.

6.9.1. Monotonic Tests

The first two tests penetrated to a depth of 1*D* (50.8 mm) at different penetration rates of 1mm/sec, and 10 mm/sec, respectively. The riser in Test 3 is pushed into about 1.3*D* about 66.04 mm with different velocity of 15 mm/sec as shown in Table 6.1. To compare the results with existing results, the bearing factor is needed, and Equation 6.6 shows the bearing factor calculation.

$$N_p = P/s_u D$$ **Equation 6.6**

where N_p is bearing factor, P is the soil resisting force per unit length arising from soil shearing resistance, D is riser diameter, and s_u is undrained shear strength. Figure 6.8 shows the bearing factor of the monotonic tests on y-axes and the normalized displacement, y/D on x-axes. The variation in the bearing factor between Test 1 and Test 2 is around 11%. This percentage increases to about 27% between Tests 1 and 3. The larger bearing factor measured in Test 3 is an apparent consequence of a higher motion rate. Similar trends are reported by Langford and Aubeny (2008).

The first test is compared to an empirical equation developed by Aubeny et al., (2005) and finite element results by Merifield et al., (2008) as shown in Figure 6.9. Equation 6.7 shows the Aubeny et al., equation.

$$N_p = a\,[h/D]^b \qquad \textbf{Equation 6.7}$$

where N_p is bearing factor, a varies from 4.97 to 6.93 depending on the adhesion factor α, h is penetration depth, D is pipe diameter, and the exponent b varying from 0.23 to 0.29 depending on a. For the purpose of comparing Equation 6.7 to laboratory measurements, an adhesion factor $a = 0.5$ is assumed, or $a = 5.95$ and $b = 0.26$. Figure 6.9 shows very good agreement between the test measurements produced in this study, the Aubeny et al. equation and the Merifield et al. finite element solutions.

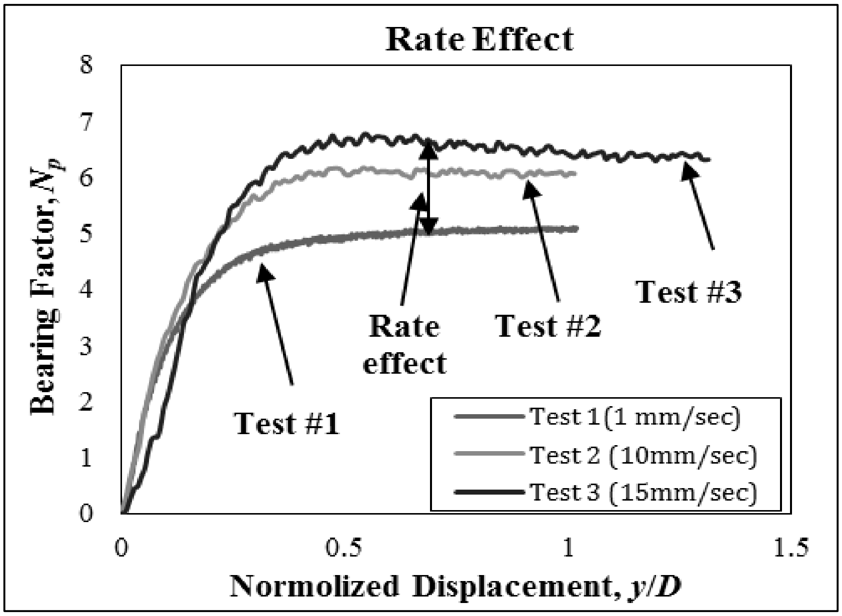

Figure 6.8 Different loading rates for monotonic loading tests.

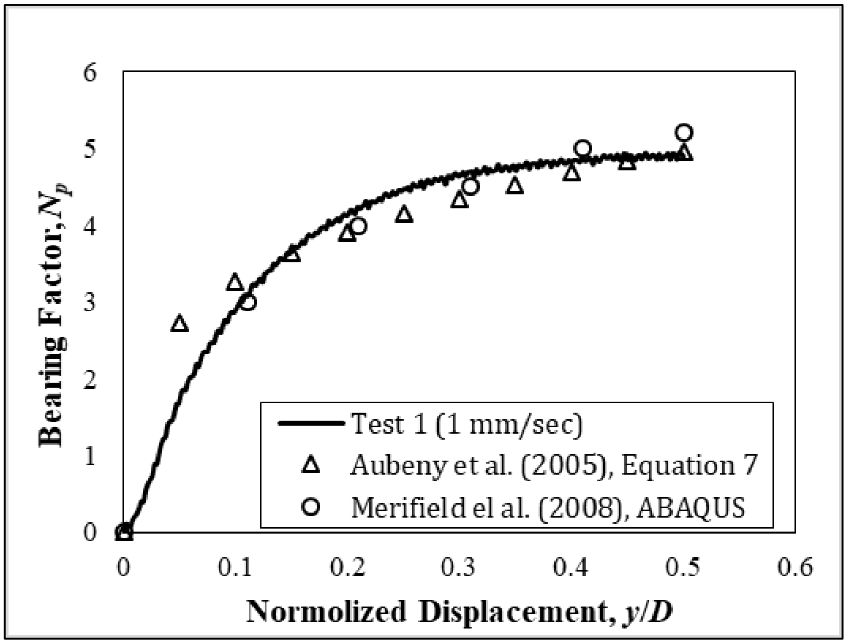

Figure 6.9 Comparison with previous studies for monotonic tests.

6.9.2. Cyclic Tests

To investigate rate effects during cyclic loading, two additional cyclic tests, Tests 4 and 5, are conducted at velocities 1mm/sec and 5 mm/sec, respectively. The pipe in the both tests penetrated to a depth of 0.5*D* and are then cyclically loaded (2-way) with an amplitude 0.05 *D*. Figure 6.10 compares *P-y* curves from the two tests. For the first cycle of both tests, the reduction in soil resistance is about 19%. The rate of degradation decreases with increasing numbers of cycles, and eventually approaches a state of zero resistance irrespective of loading rate. Figure 6.10 also illustrates the effect of loading rate on uplift (suction) resistance. In the first load cycle a 5-fold reduction in loading rate leads to about a 50% reduction in suction.

Soil erosion is also observed during cyclic loading for both loading rates, as evidenced by the cloudy water shown in Figure 6.11. Erosion, along with remolding and possibly water entrainment, likely contributed to the measured extreme reductions in soil resistance (essentially zero resistance) shown in Figure 6.10 after 1,000 cycles.

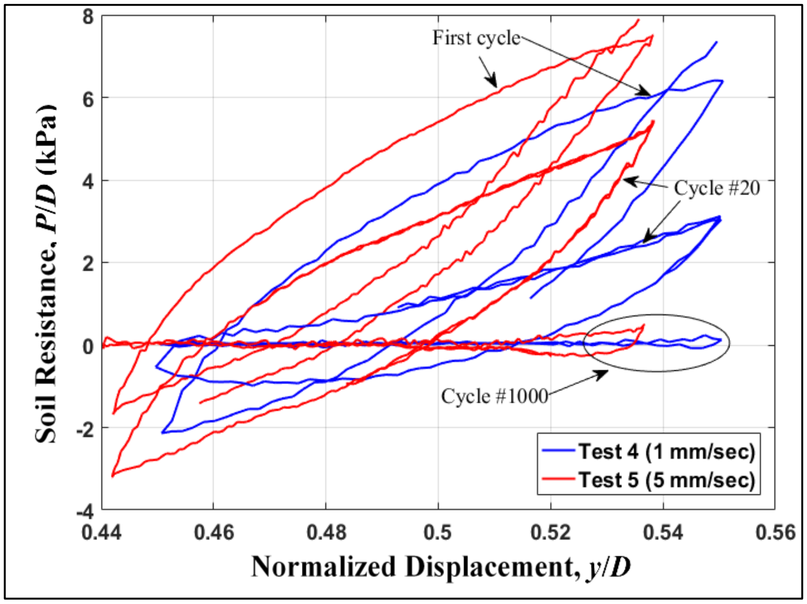

Figure 6.10 Cyclic tests with different loading rates.

6.10. Erosion (Scour)

Erosion, along with remolding and possibly water entrainment, likely contributed to the measured extreme reductions in soil resistance (essentially zero resistance) shown in Figure 6.10 after 1,000 cycles. Figure 6.11 shows photographs indicating erosion during testing.

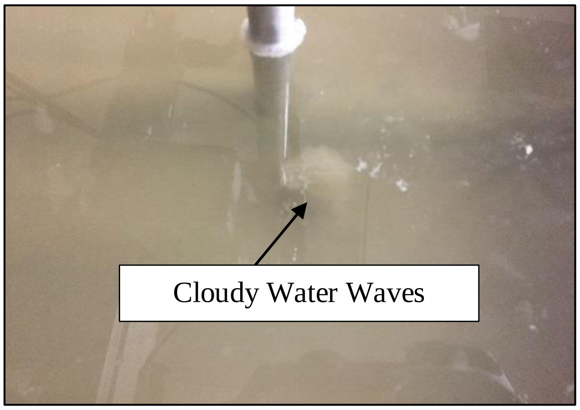

Figure 6.11 Cloudy water wave (scour).

6.11. Stiffness Degradation Under Cyclic Loading

This section presents and interprets the results from Test Series 2 to 4 (Test 6 to Test 12 a-d).

6.11.1. Large Cyclic Amplitude (2-way 5% *D*)

Displacement controlled loading is used for all tests. Tests 6-9 are subjected to parcels of 1000 cycles, except Test 7, which is subjected to a parcel of 200 cycles. Tests 6-9 penetrated to a different depth as shown in Table 6.2 and then cycled to approximately 5.08 mm (5% D).

6.11.2. Shallow Penetration Depth, *h/D*= 0.25 to 1.0

For the shallow penetration depths, (0.25 *D*, 0.5 *D*, and 1.0 *D*), three tests are carried out (see Table 6.2 for more details). The results from Tests 6-8 are presented in Figure 6.12a-12c, respectively. Plot (a) to plot (c) of Figure 6.12 present the variation in the vertical resistance of the soil with the vertical penetration for the shallow penetration depths. Figure 6.13 shows the degradation in the resistance while increasing the number of cycles for the shallow and deep penetrations. From plot (a) to plot (c) of Figure 6.12 and Figure 6.13, it is clear that the reduction in soil resistance during cyclic loading is greatest at shallow depths and decreases somewhat with increasing penetration. For example, the resistance reduces by about 50%, 42%, and 40% for penetration depths 0.25*D*, 0.5*D*, and 1*D*, respectively during the first 10 cycles. After the first 10 load cycles, the resistance continues to decrease, but at a reduced rate. For shallow penetration depths, the vertical resistance approaches zero after a large number of cycles ranging from 600-1000 cycles for both the penetration and the extraction resistance. For *h/D* =1.0 *D*, Test 8, the steady state is reached at about 200 cycles. This reduction in resistance is due to multiple reasons, 1) softening and remolding the soil with increasing the number of cyclic, that causes the reduction in the undrained shear strength, and 2) trench formation, it is noticed that for the shallow penetration there is clouded waves coming out from beneath the pipe, in other words, the soil erosion (scour) occurs during the cyclic loading as shown in the Figure 6.11. Since the resistance reaches numbers close to zero, this indicates to trench formation.

6.11.3. Deep penetration, *h/D*= 2.0 *D*

For the deep penetration, Test 9, it can be seen from plot (d) of Figure 6.12 that the soil resistance degrades rapidly during the first few cycles, around 5-10 cycles, with a reduced rate of degradation as cyclic loading continues to an apparent steady state. This behavior also is captured by Hodder et al. (2009). Figure 6.12d shows that the resistance drops to about 33% in the first 10 cycles. Figure 6.13 shows that a large portion of the soil resistance degradation occurs after about 60 cycles. In contrast to what is observed for the cases of shallow penetration, the soil resistance on a deeply penetrated pipe subjected to cyclic loading degrades to a steady state value that is well above zero. In this test no soil erosion is evident and the water stayed clear. This can be explained as the pipe is totally covered by a large block of soil, which prevented soil erosion. Figure 6.13 also shows a comparison between all of the different penetration depths and how that affects the resistance.

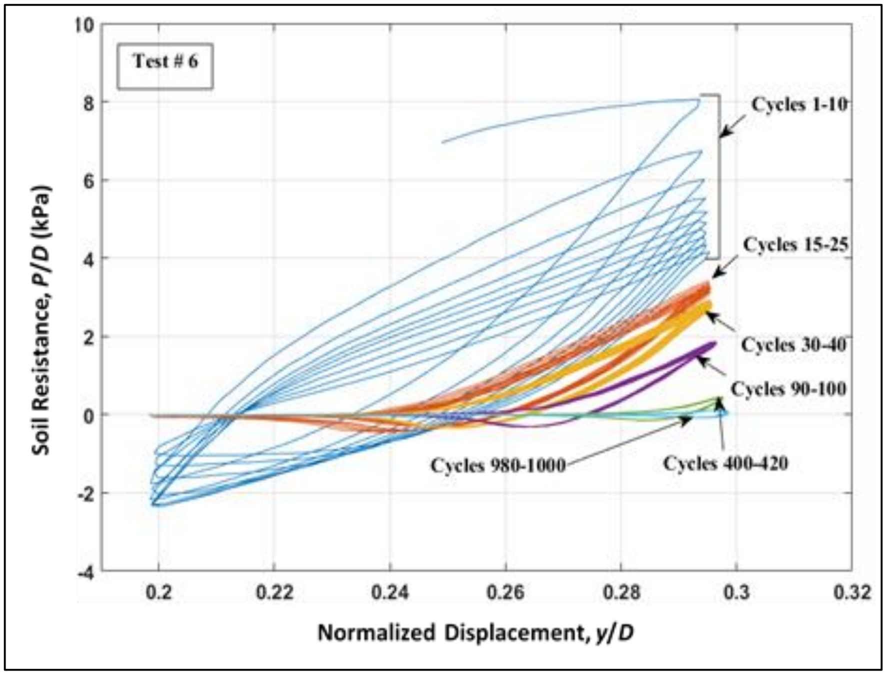

a) ***h*/*D* = 0.25.**

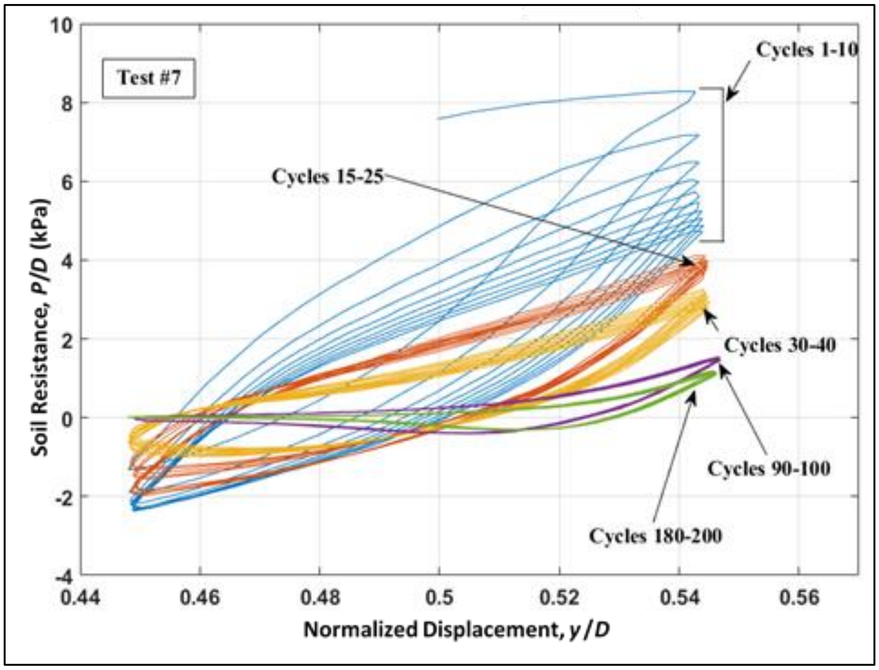

b) ***h*/*D* = 0.5.**

Figure 6.12 Cyclic tests with different penetration depths, *h/D*.

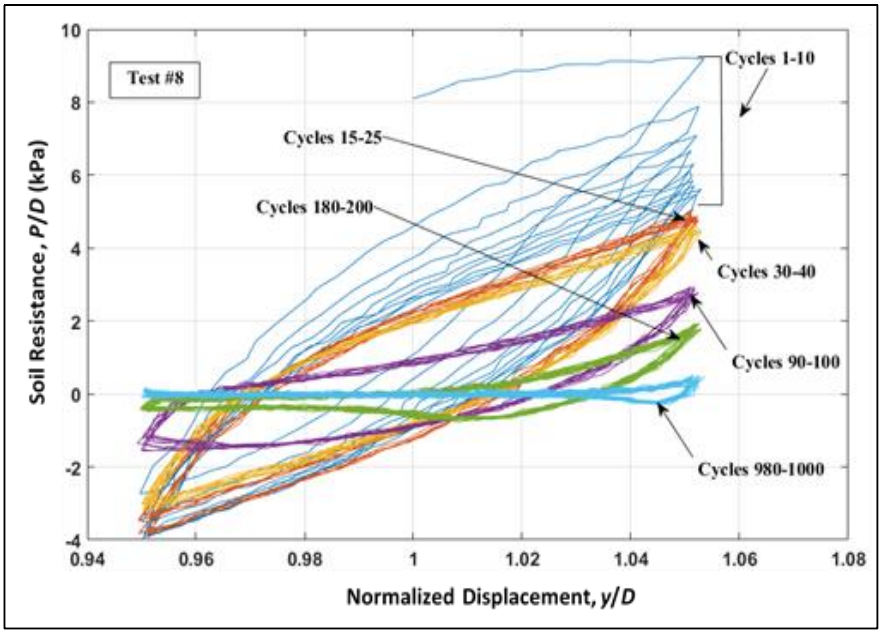

c) *h*/*D* = 1.0.

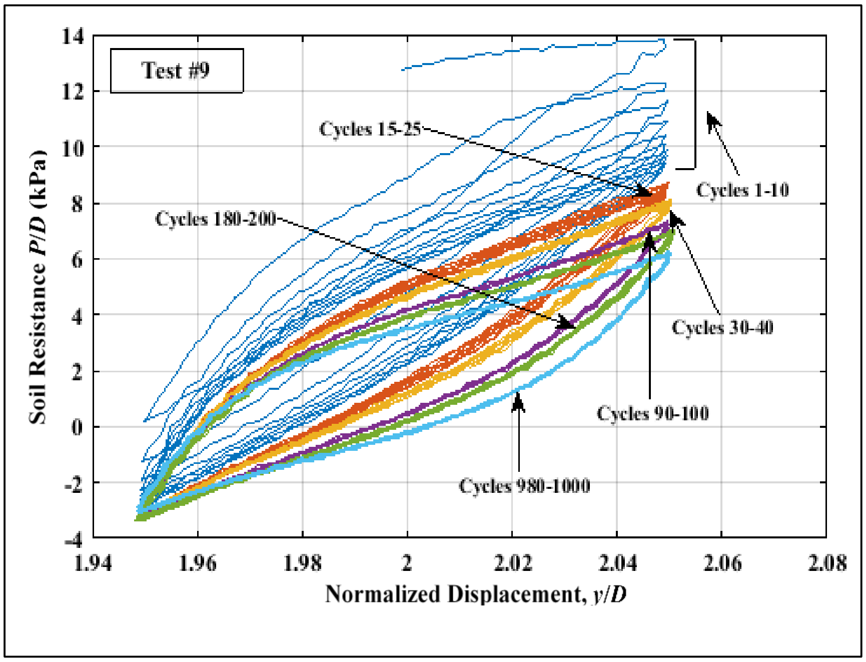

d) *h*/*D* = 2.0

Figure 6.12 Continued.

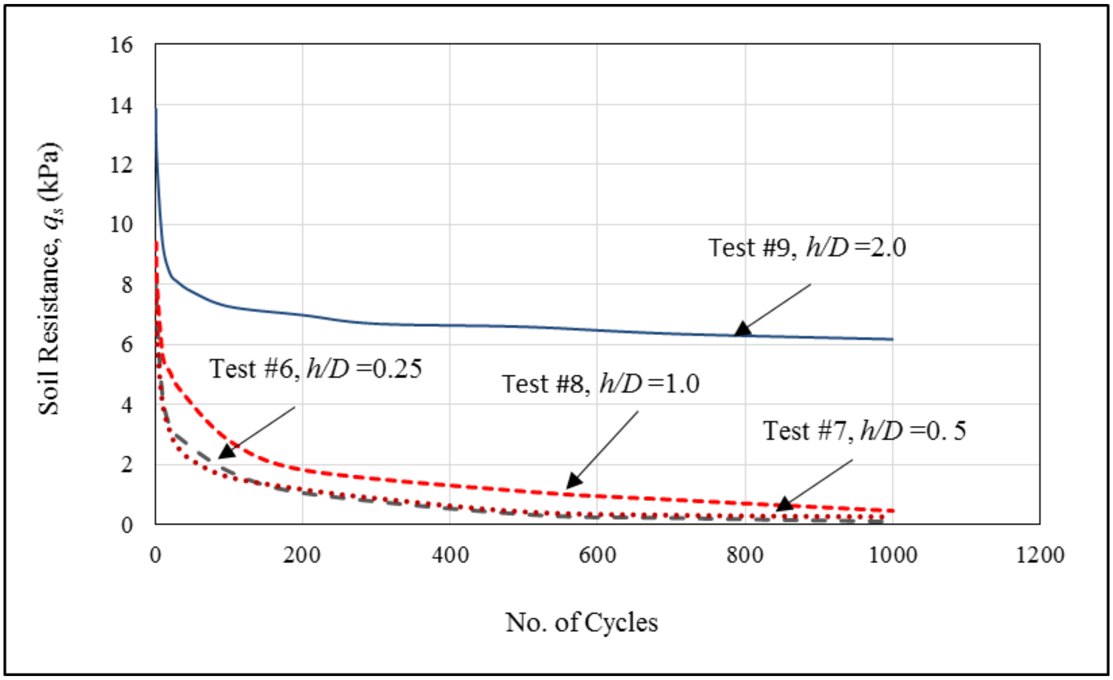

Figure 6.13 Soil resistance degradation while increasing the number of cycles for different penetration depths.

6.11.4. Small Cyclic Amplitude (2-way 2% *D*)

Test 10 from the second series is performed with a small cyclic amplitude for a shallow penetration depth *h/D*= 0.5 to capture the behavior of the soil degradation with increasing numbers of load cycles, and to compare it with other results for a different cyclic amplitude and penetration depth (Figure 6.14). The measured vertical resistance in this case is similar to that measured for deep penetration *h/D*= 2.0 with the large cyclic amplitude of 5% *D*, Test 9, as shown in Figure 6.15. It can be seen from Figure 6.15 that the soil resistance degrades rapidly during the first few cycles, around 5-10 cycles, but reaches an apparent steady state after about 60 cycles. Furthermore, it is worth mentioning that no erosion is noticed for the small cyclic amplitude as it is not noticed in Test 9.

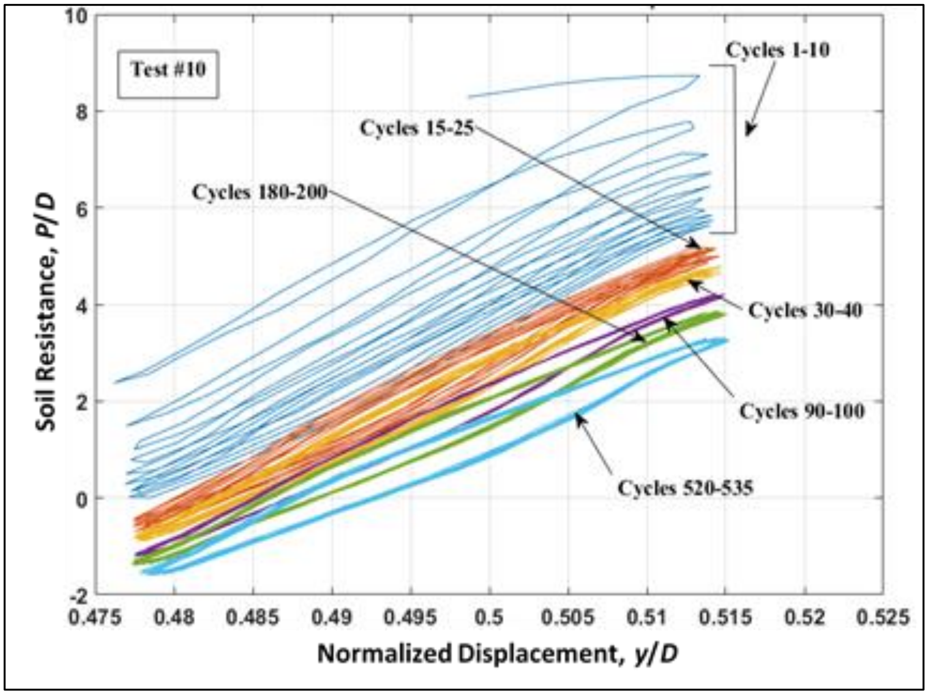

Figure 6.14 Soil resistance, *P*/*D* vs. normalized displacement for *h*/*D* = 0.5.

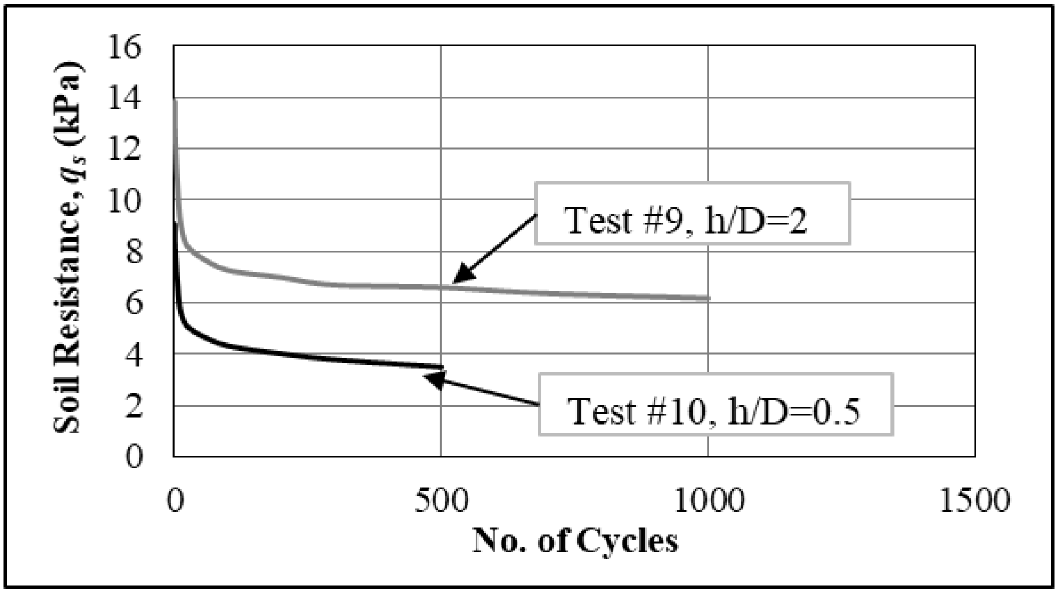

Figure 6.15 soil resistance, *P*/*D* vs. No. of cycles.

6.12. Pause period

Two series of testing, series 3 (Test 11a to 11j) and series 4 (Test 12a to 12d), are conducted to observe the reconsolidation effect and its influence on stiffness recovery by allowing the pipe to rest in the trench for different periods of time. The following sections present test results for large and small amplitude cyclic loading.

6.12.1. Large Cyclic Amplitude (2-way 5% *D*), Test 11a -11j

The riser initially penetrated to a depth of 0.5D under a constant penetration rate of 1.5 mm/sec and then are subjected to a series of ten 100 cycle load parcels (Tests 11a to 11j). At the end of each sequence, the vertical restriction is unlocked to allow the pipe to rest on the soil bed (the trench formed by the initial penetration) for time periods ranging from 1 to 2.5 hrs for Tests 11b through 11i, and around 13 hrs. for Test 11j. The purpose of this test procedure is to measure the stiffness recovery due to reconsolidation and the longevity of the recovery after the resumption of cyclic loading. Noting that the pipe is free to settle under its own weight during the pause period, the vertical settlement is recorded for each pause. After completion of each pause, the pipe is re-connected to the actuator rod, and another 100-cycle packet of displacement controlled loading is performed. This procedure is followed through all of series 3. Equation 6.8 is used to find the normalized secant stiffness.

$$K_{norm} = K_{secant}/P_1 \quad = (\Delta P/\Delta y)/P_1 \qquad \textbf{Equation 6.8}$$

where K_{norm} is the normalized secant stiffness, K_{secant} is the secant stiffness, ΔP is the change in soil resistance, Δy is the change in vertical displacement, and P_1 is the maximum prior soil resistance. Figure 6.2 shows the P_1 location.

The K_{norm}-$\Delta y/D$ plot in Figure 6.16 shows selected unload secant stiffness curves derived from Test 11a. The overall magnitude of the normalized stiffness decreased with increasing numbers of load cycles. This also is found by (Langford and Aubeny 2008). After conducting test 11a, the vertical restriction is unlocked and the pipe is left to rest inside the formed trench for about an hour. At the end of each rest period, the pipe is re-attached to the actuator rod, and the second sequence of parcels is applied as described in the previous section. The pause period for the Test 11i series is 2.5 hours and 13 hours for Test 11j.

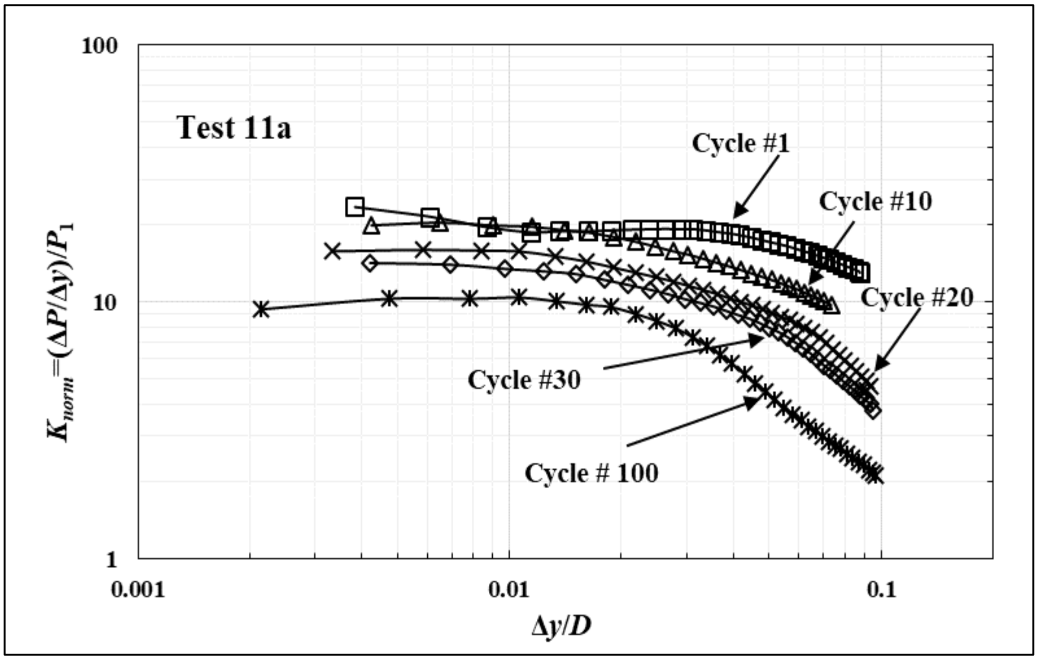

Figure 6.16 Test 11-a: normalized secant stiffness vs. Normalized cyclic displacement (unloading stage).

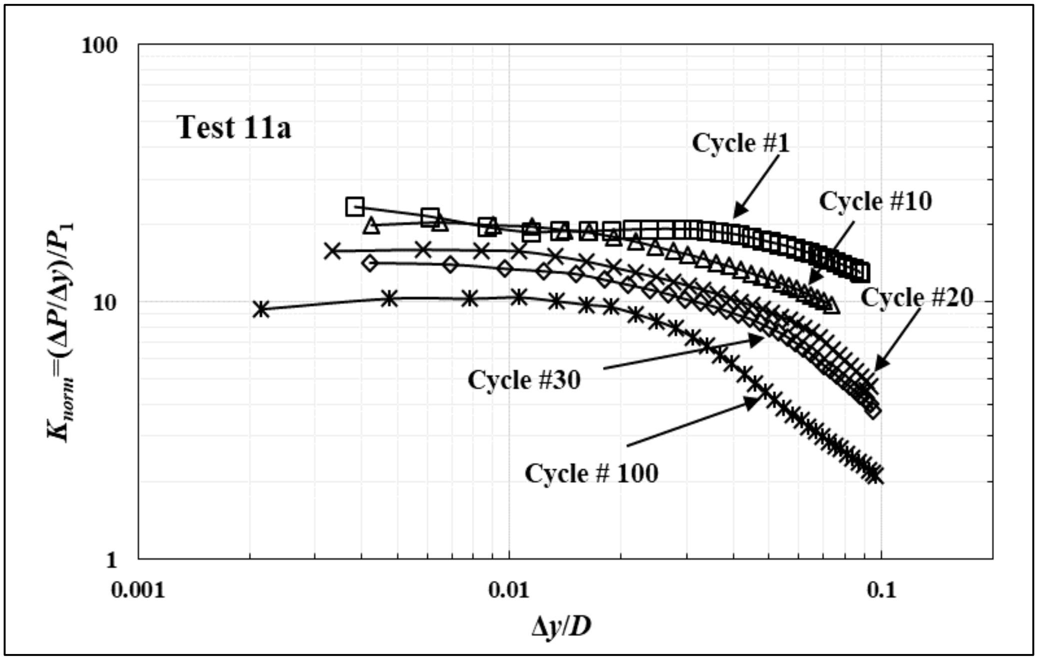

Figure 6.16 Test 11-a: normalized secant stiffness vs. Normalized cyclic displacement (unloading stage).

6.13. Reconsolidation Effects During Test 11a to Test 11j

To illustrate the reconsolidation effect, Figure 6.17 shows some sequences of Test 11a -11j that captures the reconsolidation effects. Figure 6.17 shows unload secant stiffness for the first load cycle, and cycle 100 before and after the rest period. These results capture the stiffness recovery after the pause period. Figure 6.18 shows the degradation in the resistance with increasing numbers of cycles and the gain in resistance during the pause periods. From plot (a) and plot (b) of Figure 6.17, it is observed that the consolidation following rest periods leads to a short-term increase the soil stiffness, which quickly declines, but the resistance stays a bit larger than the pre-rest period levels after the resumption of cyclic loading as shown in Figure 6.18. However, under prolonged cyclic loading, the soil stiffness gradually trends upward. In other words, the secant stiffness keeps increasing and becomes stiffer than the previous parcels. Recalling plot (b) of Figure 6.17, the increment in resistance between point A and B ranges around 140%, and 265% for A and C. These increments in the soil stiffness can be explained with the following reasons: 1) reconsolidation effects, 2) thixotropy, and 3) the incremental increase of undrained shear strength with increasing pipe embedment depth. The stiffness increases while increasing the depth as presented in Figure 6.4a-b.

In a previous study Langford and Aubeny, (2008), the pause period sequences are conducted, but the pipe is kept locked in place during the pause period. In other words, the recovery is the significant factor in that study. The findings are that the resistance tends to increase around 20% and quickly vanish after cycling the pipe to be less than the previous parcels. Therefore, the findings of this study on stiffness recovery because of the reconsolidation effect are particularly important, as this has been a major source of uncertainty in prior investigations.

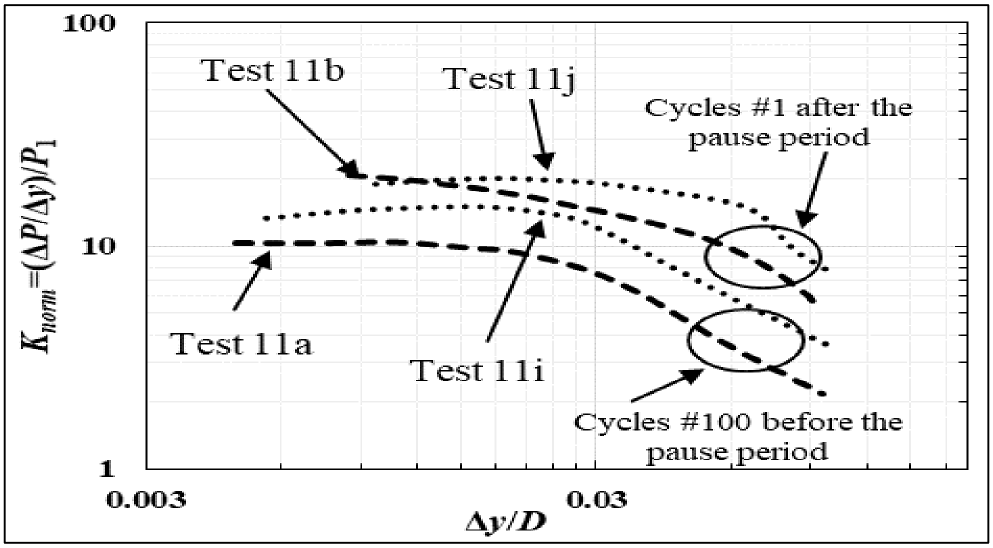

Figure 6.17 Normalized stiffness during pause periods.

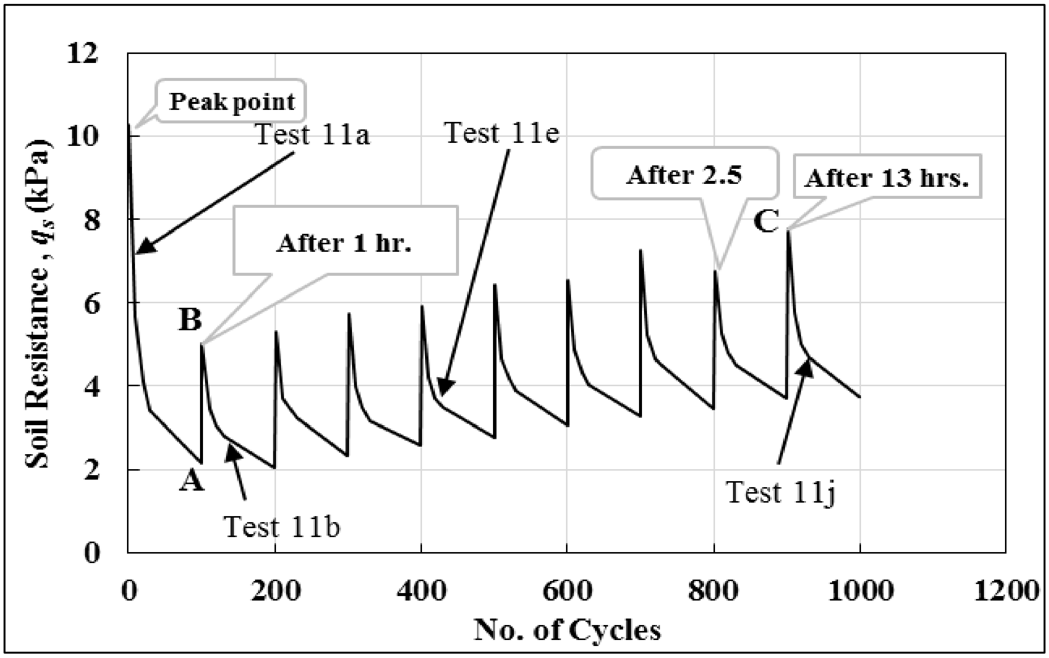

Figure 6.18 Soil Resistance vs. number of cycles.

6.13.1. Small Cyclic Amplitude (2% *D*), *h/D*=0.5

Pause period has been applied to a small cyclic amplitude, Test 12a to Test 12d, as well to find the reconsolidation effects on the soil stiffness. The reconsolidation effects for Gulf of Mexico needs to be found to better understand the regain in the soil stiffness during the rest periods of the riser. Four sequences of 300 cycle load parcels are conducted with three rest period which are 3, 3.5, and 16 hours for Test 12b, Test 12c, and Test 12d, respectively. It is difficult to plot the normalized secant stiffness versus the normalized displacement since these tests are conducted with a small cyclic amplitude. Therefore, the vertical soil resistance versus the number of cycles is plotted as shown in Figure 6.19.

6.13.2. Reconsolidation Effects During Test 12a to test 12d

Figure 6.19 shows the behavior of the resistance during the pause period and how the resistance degrades with an increasing the cyclic number. For the first rest period, after 3 hours, the regain in resistance is negligible, and the small recovery that does occur vanishes almost immediately after the resumption of cyclic loading. Soil resistance approaches an apparent steady state at about 200 cycles. It is important to mention that after unlocking the actuator rod from the pipe at the end of cyclic loading in Test 12a, the pipe displaced upwards for a small distance. This could be because the small cyclic amplitude is applied. Oliphant et al. (2009) state that “in the shallow trench, the vertical force increases with lateral movement but in a deep trench the net vertical force variation is not significant”. It is noted that, after finishing Test 12b and unlocking, the pipe displaced upward for a small distance (less than the previous test) as captured by the laser sensors. Furthermore, the third sequence of releasing the pipe did not record any upward displacement of the pipe. This suggests that the soil tends to be softened with increasing the number of cycles and the cyclic amplitude $\Delta y_{cyc}/D$. Recalling Figure 6.19, the regain in resistance during the rest periods ranges between point A and B around 18% and for A and C around 30%. Those results give a good agreement with Hodder et al. (2009).

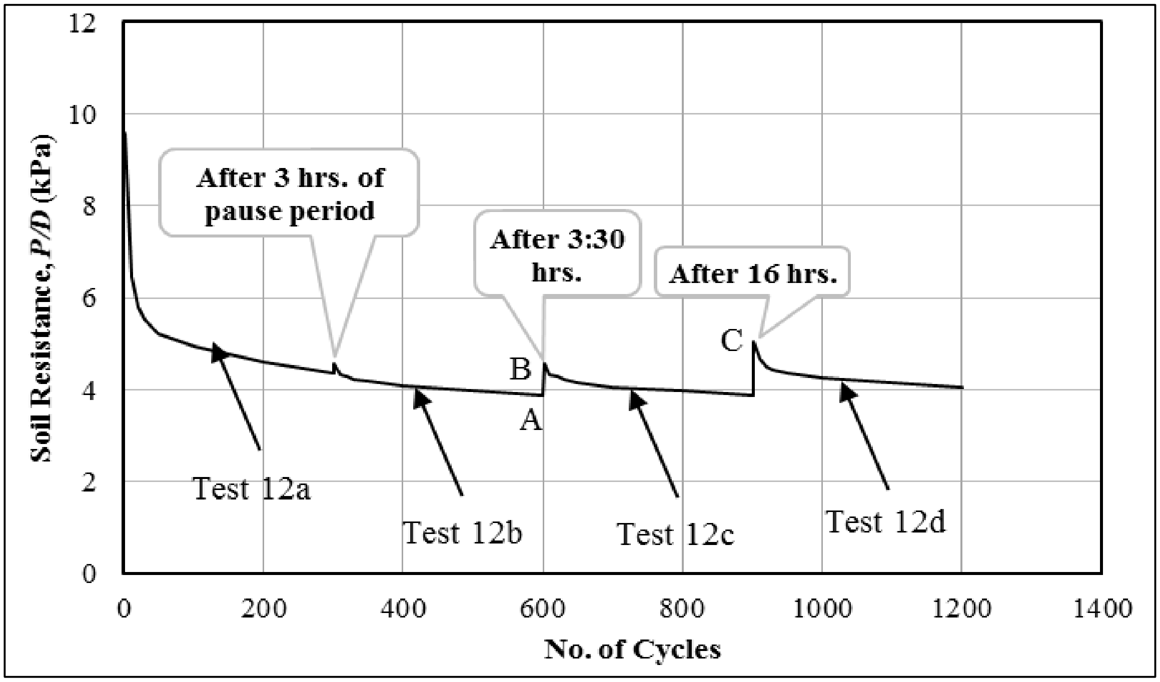

Figure 6.19 Test 12: Soil resistance vs. number of cycles.

6.14. Recommendations

Future tests are recommended to evaluate:

1. Reconsolidation and thixotropy effects at different depths and cyclic amplitudes.
2. Lateral cyclic loading tests are needed to better understand the fatigue life of SCR and the trench formation.

6.15. Nomenclature

a	Factor Varies From 4.97 to 6.93 Depending on Adhesion Factor
a_0	Area Ratio
A_p	Projected Area Of The T-Bar Probe

A_R	Projected Area Of The T- Bar Rod
A_s	Submerged Cross-Sectional Area of Riser
b	Factor Varying From 0.23 to 0.29 Depending on a
D	Pipe Diameter
GoM	Gulf of Mexico
h	Embedment Depth
K_{norm}	Normalized Secant Stiffness
K_{secant}	Secant Stiffness
L	Pipe Length
N	Number of Cycles
N_p	Bearing Factor
P	Soil Resistance Per Unit Length
$P1$	Maximum Soil Resistance at Maximum Depth
P_b	Buoyancy Force of Soil Per Unit Length
PLA	Plastic Limit Analysis
P_t	Total Force Per Unit Length
q_b	Buoyancy Resistance of Soil
q_s	Strength Resistance of Soil
q_t	Total Resistance of Soil
$q_{t\text{-}bat(m)}$	Measured Penetration Resistance
$q_{t\text{-}bat(net)}$	Net Penetration Resistance
SCR	Steel Catenary Riser

s_u	Undrained Shear Strength
s_{u0}	Undrained Shear Strength at the surface
s_{u0}	Undrained Shear Strength at the surface
TDZ	Touch Down Zone
$w\%$	Water Moisture Content
y	Vertical Displacement
$y1$	Maximum Vertical Displacement
ΔP	Change In Soil Resistance
Δy	Change In Vertical Displacement
Δy_{cyc}	Cyclic Displacement Amplitude
γ'	Submerged Unit Weight
σ_{v0}	Total Overburden Stress

6.16. References

Al-Janabi, H. A. & Aubeny, C. P. (2019). Experimental Measurement of Thixotropy and Sensitivity in Gulf of Mexico Clay. In The International Society of Offshore and Polar Engineers Conference. Submitted for Review.

Al-janabi, H. A., Shlash, K. T., & Fattah, M. Y. (2014). The Behavior of Bounded Foundations on Sandy Soil Bounded Shallow Foundations on Iraqi Sandy Soil with Different Densities. *In. Saarbrücken: LAP LAMBERT Academic Publishing.*

ASTM Committee D-18 on Soil and Rock. (2018). *Standard test methods for liquid limit, plastic limit, and plasticity index of soils*. ASTM international.

ASTM. (2016). Standard test method for laboratory miniature vane shear test for saturated fine-grained clayey soil.

Aubeny, C. P., Shi, H., & Murff, J. D. (2005). Collapse loads for a cylinder embedded in trench in cohesive soil. *International Journal of Geomechanics*, *5*(4), 320-325.

Aubeny, C., & Dunlap, W. (2003, September). Penetration of cylindrical objects in soft mud. In *OCEANS 2003. Proceedings* (Vol. 4, pp. 2068-2073). IEEE.

Beemer, R. D. (2016). *Experimental studies of squat gravity caissons and monopiles for offshore applications* (Doctoral dissertation).

Chen JB, Newlin J, Luo M, Zhang H, Hadley C and Hu S. (2019) Practice of Riser-Soil Interactions at Touch Down Zones for Steel Catenary Risers. Offshore Technology Conference, OTC-29553-MS. Houston, TX, USA.

Chen JB, Xu FB, Newlin J, Zhang H, Shuang H and Luo M. (2019a) Large Deformation Finite Element Analysis of Riser-Soil Interactions With Strain-Softening Soils. Offshore Technology Conference, OTC-29376-MS. Houston, TX, USA.

Clukey, E. C., Aubeny, C. P., Zakeri, A., Randolph, M. F., Sharma, P. P., White, D. J., ... & Cerkovnik, M. (2017, May). A Perspective on the State of Knowledge Regarding Soil-Pipe Interaction for SCR Fatigue Assessments. In *Offshore Technology Conference*. Offshore Technology Conference.

Dejong, J., Yafrate, N., Degroot, D., Low, H. E., & Randolph, M. (2010). Recommended practice for full-flow penetrometer testing and analysis. *Geotechnical Testing Journal*, *33*(2), 137-149.

Fattah, M. Y., Shlash, K. T., & Mohammed, H. A. (2014). Bearing capacity of rectangular footing on sandy soil bounded by a wall. *Arabian Journal for Science and Engineering*, *39*(11), 7621-7633.

Fattah, M. Y., Shlash, K. T., & Mohammed, H. A. (2014a). Experimental Study on the Behavior of Bounded Square Footing on Sandy Soil. *Engineering and Technology Journal*, *32*(5 Part (A) Engineering), 1083-1105.

Fattah, M. Y., Shlash, K. T., & Mohammed, H. A. (2015). Experimental study on the behavior of strip footing on sandy soil bounded by a wall. *Arabian Journal of Geosciences*, *8*(7), 4779-4790.

Hodder, M., White, D., & Cassidy, M. J. (2009, January). Effect of Remodling and Reconsolidation on the Touchdown Stiffness of a Steel Catenary Riser: Guidance from Centrifuge Modelling. In *Offshore Technology Conference*. Offshore Technology Conference.

Langford, T. E., & Aubeny, C. P. (2008a, January). Large scale soil-riser model testing on high plasticity clay. In *The Eighteenth International Offshore and Polar Engineering Conference*. International Society of Offshore and Polar Engineers.

Langford, T., & Aubeny, C. P. (2008, January). Model tests for steel catenary riser in marine clay. In *Offshore Technology Conference*. Offshore Technology Conference.

Merifield, R., White, D. J., & Randolph, M. F. (2008). The ultimate undrained resistance of partially embedded pipelines. *Géotechnique*, *58*(6), 461-470.

Mohammed, H. A. (2013). *Experimental and Statistical Study on the Behavior of Bounded Foundation on Sandy Soil*. (M.Sc. M.Sc. thesis), University of Technology 2013.

Oliphant, J., Maconochie, A., White, D., & Bolton, M. (2009). Trench interaction forces during lateral SCR movement in deepwater clays. Offshore Technology Conference.

Randolph, M. F., Low, H. E., & Zhou, H. (2007, January). In situ testing for design of pipeline and anchoring systems. In *OFFSHORE SITE INVESTIGATION AND GEOTECHNICS, Confronting New Challenges and Sharing Knowledge*. Society of Underwater Technology.

White, D. J., & Randolph, M. F. (2007). Seabed characterisation and models for pipeline-soil interaction. *International Journal of Offshore and Polar Engineering*, *17*(03).

Yafrate, N., DeJong, J., DeGroot, D., & Randolph, M. (2009). Evaluation of remolded shear strength and sensitivity of soft clay using full-flow penetrometers. *Journal of Geotechnical and Geoenvironmental Engineering*, *135*(9), 1179-1189.

Bridge, C., & Willis, N. (2002, May). Steel catenary risers–results and conclusions from large scale simulations of seabed interaction. In *Proc. of the Int. Conf. on Deep Offshore Technology* (pp. 40-60).

Clukey, E., Jacob, P., & Sharma, P. P. (2008, January). Investigation of riser seafloor interaction using explicit finite element methods. In *Offshore Technology Conference*. Offshore Technology Conference.

Matlock, H. (1970). Correlations for design of laterally loaded piles in soft clay. *Offshore technology in civil engineering's hall of fame papers from the early years*, 77-94.

Hu, H. J. E., Leung, C. F., Chow, Y. K., & Palmer, A. C. (2011). Centrifuge modelling of SCR vertical motion at touchdown zone. *Ocean Engineering*, *38*(7), 888-899.

You, J. H. (2012). Numerical Modeling of Seafloor Interaction With Steel Catenary Riser. Texas A&M University, College Station, USA. Doctor of Philosophy.

7. EXPERIMENTAL MEASUREMENT OF MONOTONIC AND CYCLIC LATERAL RESISTANCE OF RISERS AND PIPELINES IN GULF OF MEXICO CLAYS[*]

7.1. Introduction

Steel Catenary Risers (Figure 7.1a) that connect floating platforms with seabed facilities are routinely used in offshore oil and gas developments. One of the key design challenges of SCRs is to ensure an adequate fatigue life of an SCR to be consistent with the platform design life. For the fatigue damage to an SCR, one of the critical locations is the point close where the SCR touches the seabed, called "touchdown zone" (TDZ). During operation of SCRs, trenches will form in the TDZ, and the SCR can sweep several diameters in the horizontal and the vertical directions (Bridge & Howells, 2007).

Pipelines laid on the seabed experience external hydrodynamic loading and other forces from the internal temperature and pressure. The external hydrodynamic loading is minimal in deep water but can be significant in shallow water. Episodes of heating and cooling lead to longitudinal expansion cycles in the pipe, with pipe buckling occurring during the former. Excessive buckle amplitude may lead to high bending strains in the pipe section, and the accumulation of fatigue damage through the pipeline operating life. There is a significant issue related to excessive buckling, which is high bending strain in the pipe section and the accumulation of fatigue through the pipeline operating life (Chatterjee et al. 2012). Figure 7.1b illustrates a typical *H-u* behavior (where *H* is lateral

---

[*] Reprinted with permission from "Experimental Measurement of Touchdown Zone Stiffness for SCR in Gulf of Mexico Clay" by Authors' Husham A. Al-Janabi, Charles P. Aubeny, Jinbo Chen, and Meng Luo, 2019. Canadian Geotechnical Journal, Copyright [2019] by the Canadian Geotechnical Journal.

resistance and u is lateral displacement). The "backbone curve" corresponds to the initial lateral movement of the pipe into the soil. Both monotonic and cyclic H-u curves are commonly derived from single-gravity laboratory model tests, where a short segment of pipe is pushed into the soil testbed and subjected to a history of lateral movement cycles of interest. Although random loading sequences occur in the field, laboratory model tests usually impose either displacement-controlled cyclic loading, where the pipe is repeatedly re-swept to a lateral distance of u_1, or force-controlled cyclic loading, where the pipe is repeatedly re-swept to the point at which a soil resistance H_1 mobilizes. Since the movement of the SCR close to the seabed is mainly imposed from the global motion of the platform, displacement-controlled tests are more appropriate for the fatigue assessment after a large number of load cycles (Chen et al. 2019, 2019a).

This chapter presents the findings of a series of single-gravity laboratory model tests on a "rigid" pipe investigating H-u behavior for SCRs in high plasticity Gulf of Mexico (GOM) clay. Four series of tests, as well as multiple T-bar and miniature vane shear tests are performed in this study. All monotonic and cyclic tests are conducted under displacement-controlled loading. The objective of the program is to acquire data on soil resistance during horizontal monotonic and cyclic loading and to assess the effect of recovery during rest periods. In contrast to the procedure utilized in previous studies on the effects of setup during rest periods (Al-Janabi el al. 2019), where the rest periods were applied after conducting the vertical cyclic loading, the riser in this study is subjected to a constant (self-weight) vertical load. Thus, further embedment of the riser is permissible from the consolidation during the rest period. A high plasticity GOM clay with undrained shear strength corresponding to typical normally consolidated conditions is used in this study to represent the seabed at TDZ. The vertical monotonic tests are conducted at the beginning of the program to obtain the vertical loading resistance with depth at different rates and to compare to other existing results. These results are compared to existing models before proceeding with lateral monotonic and cyclic loading tests. The study investigated the following aspects of riser/pipeline-soil interaction: (1) the effect of riser embedment depth h over a range w/D ~ 0.5-1.0, (2) the effect of loading rate during monotonic penetration, with load rates varying from 1 to 15 mm/sec, (3) lateral resistance degradation as a function of load cycle under cyclic displacement amplitudes in the range $\Delta u_{cyc}/D$ ~ 0.15-0.5, (4) resistance recovery during rest (pause) periods ranging from 2 to 23 hours for $\Delta u_{cyc}/D$ ~ 0.15-0.5, (5) better understanding of trench formation, (6) simulation of the riser initial vertical penetration by applying very small lateral cyclic amplitude motions, (7) the lateral resistance behavior after the rest period, and (8) the shape of trenches and berms that formed during the lateral movements with different embedment depths w/D of 0.5 and 1.0. Cyclic displacement amplitudes Δu_{cyc} refer to one-half of the difference between maximum and minimum displacements.

Figure 7.2a and Figure 7.2b show the catenary zone, TDZ, and surface zone, seven months after installation the riser (Bridge & Howells, 2007). Figure 7.2a-b shows the trenches formation due to the vertical and lateral movements at/near the TDZ. Figure 7.2b (photograph b) shows the deepest and the widest trench formation (in the buried zone). Most previous studies have focused on the vertical movements at the TDZ. This chapter will explain in general the cyclic lateral movements at the TDZ and at the surface zone (seabed).

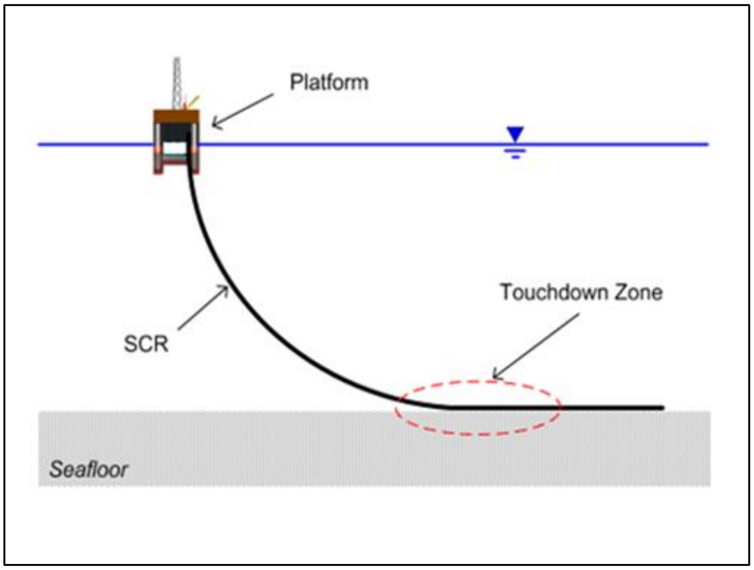

a) SCR Configuration.

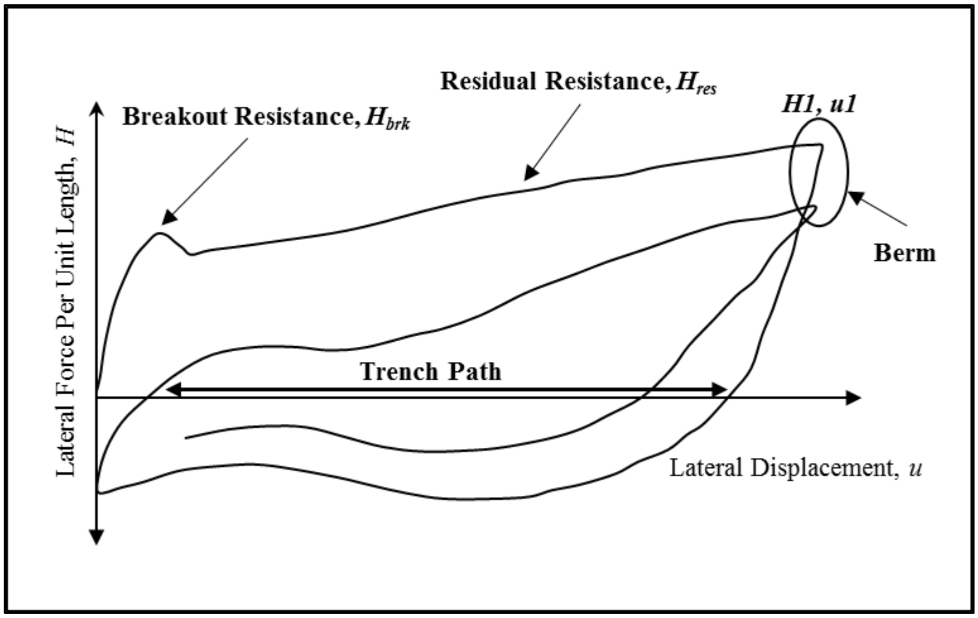

b) Typical *P-y* Behavior.

Figure 7.1 Steel Catenary Riser (SCR).

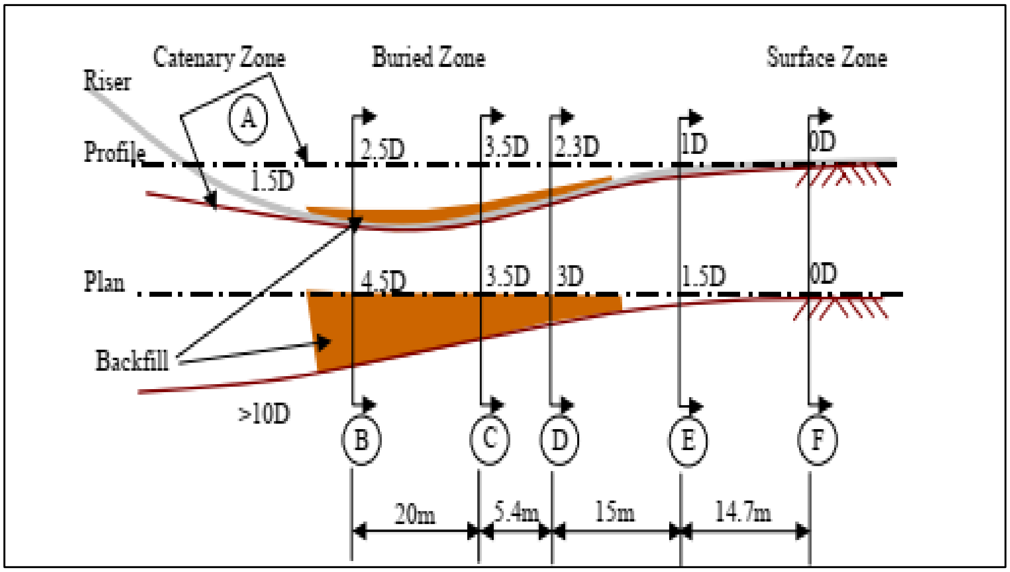

a) Sketch of Allegheny gas export SCR trench.

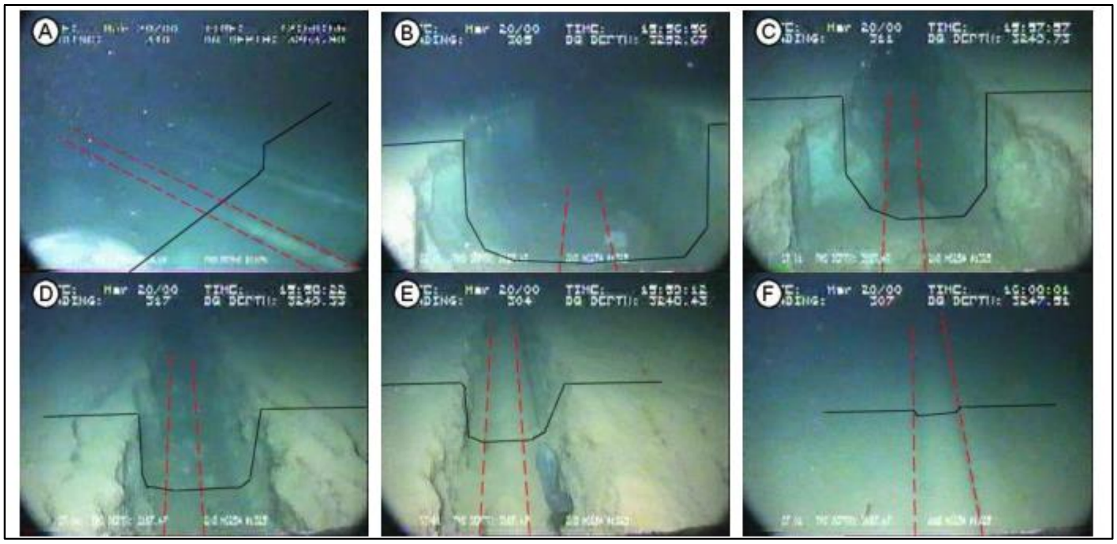

b) Multiple pictures of Allegheny trench, seven months after installation.

Figure 7.2 A sketch and Multiple pictures of Allegheny trench, seven months after instillation (reprinted from Bridge & Howells, 2007).

7.2. The Properties of Soil

The soil properties and preparations are explained in Chapter 2 in detail. The index properties of the clayey soil (Table 7.1) are determined by using standard tests ASTM D4318-00, (2018).

Table 7.1: The index properties of the soil.

Physical Properties	Values (%)
Liquid Limit (L.L)	59
Plastic Limit (P.L)	30
Plasticity Index (P.I)	29

7.3. Test Equipment

All test equipment is explained in Chapter 1 of this dissertation.

7.4. Test Program

The test program comprised four test series. Series 1 (Table 7.2) involved vertical monotonic loading at different penetration rates to provide comparisons to previous studies in the literature. Series 2 (Table 7.3) involved initial static penetration to a target depth then purely lateral monotonic loading at different penetration depths w/D of 0.5 and 1.0 as shown in Figure 7.3a-b. Series 3 (Table 7.4) introduced rest periods between packets of cyclic loading, with a “small lateral displacement amplitudes” $\Delta u_{cyc}/D \sim 0.15$. Tests 6a to Test 6d in Table 7.4 involved (1) initial penetration to $w/D = 0.5$, (2) applying 1000 very small cyclic amplitudes ($\Delta u_{cyc}/D$ = 1% - 2.5%) followed by a lateral monotonic displacement $u/D = 0.3$ (Figure 7.3c-d), (3) 200 cycles of lateral loading at $\Delta u_{cyc}/D = 0.15$

(Figure 7.3e), (4) a rest period of 2 - 23 hours, (5) lateral monotonic loading to $u/D \sim 1.0$ to evaluate strength recovery (Figure 7.3f), and (6) 100 additional load cycles of lateral loading at $\Delta u_{cyc}/D = 0.5$ (Figure 7.3g). Series 4 (Table 7.4) similarly involved packets of load cycles interspersed with rest periods, but with embedment depth w/D of 1.0. In addition, multiple T-bar (at different position across the test bin) and miniature vane shear tests are conducted to establish the undrained shear strength profile as well as the relationship between the water content and the undrained shear strength.

A total of 13 tests, three with vertical monotonic loading, six with lateral monotonic loading, and four with lateral cyclic loading are conducted in this study. The loading rate is fixed at 1.5 mm/sec for the entire test program except the tests are shown in Table (2). All tests, including the T-bar, are conducted with a dimensionless velocity vD/c_v exceeding 100s, where v is the pipe/T-bar velocity and c_v is the coefficient of consolidation. The loading rates satisfy the criterion of Chatterjee et al. (2013) for ensuring fully undrained conditions. Figure 7.3 shows sketches of the test program at a penetration depth of 0.5 *D*. The same procedure is followed for the penetration depth of 1.0 *D*.

Table 7.2 Series 1: Vertical Monotonic Penetration at Different Loading Rates.

Test No.	Velocity (mm/sec)	Test description
1	1 mm/sec	Penetrated into ~ 1.0 *D*
2	10 mm/sec	Penetrated into ~ 1.0 *D*
3	15 mm/sec	Penetrated into ~ 1.3 *D*

Table 7.3 Series 2: Summary of Pure Monotonic Tests.

Test No.	Loading rate	Test description
4	1.5 mm/sec	Penetrated into 0.5 *D*, & laterally displaced to ~ 3.0 *D*
5		Penetrated into 1.0 *D*, & laterally displaced to ~ 3.0 *D*

Table 7.4 Series 3 and Series 4: Summary of Monotonic and Cyclic Tests.

Test	Load/Displacement Control	Velocity	Test Description	No. of cycles
6a	Displacement Control	1.5 mm/sec	Penetrated into $w/D = 0.5$, then applied $\Delta u_{cyc}/D \sim$ 1-2.5%, and then $u/D \sim 0.3$.	
6b			After Test 6a, the pipe retained to its original position and lateral cyclic displacement amplitudes with zero reversal $\Delta u_{cyc}/D \sim 0.15$ has been applied. Finally, the vertical restriction is released and pipe settle for 2-23 hour.	200
6c			After Test 6b, the vertical displacement is locked in place and $u/D \sim 1.0$ is applied.	
6d			After Test 6c, the pipe is retained to the original position and then $\Delta u_{cyc}/D \sim 0.5$ is applied.	100

Table 7.4 Continued.

Test	Load/Displacement Control	Velocity	Test Description	No. of cycles
7a	Displacement Control	1.5 mm/sec	Penetrated into $w/D = 1.0$, then applied $\Delta u_{cyc}/D \sim 1\text{-}2.5\%$, and then $u/D \sim 0.3$.	
7b			After Test 7a, the pipe retained to its original position and lateral cyclic displacement amplitudes with zero reversal $\Delta u_{cyc}/D \sim 0.15$ has been applied. Finally, the vertical restriction is released and pipe settled for 2-23 hour.	150
7c			After Test 7b, the vertical displacement is locked in place and $u/D \sim 1.0$ is applied.	
7d			After Test 7c, the pipe is retained to original position and then $\Delta u_{cyc}/D \sim 0.5$ is applied.	100

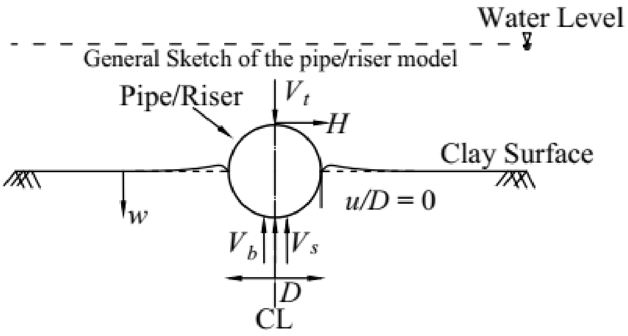

a) General sketch shows test program with nomenclature.

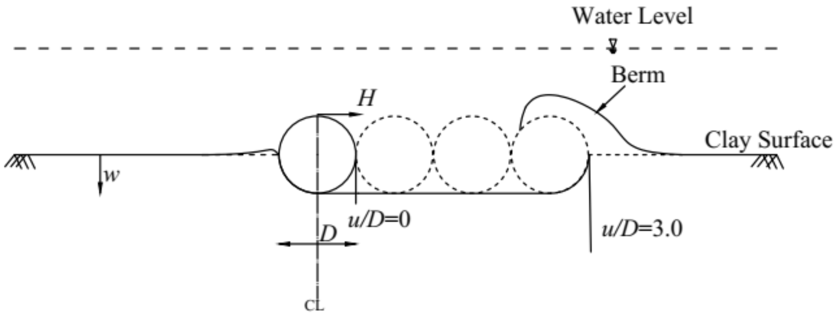

b) Test 4 *u/D* ~ 3.0 with embedment depth *w/D* = 0.5 *D*.

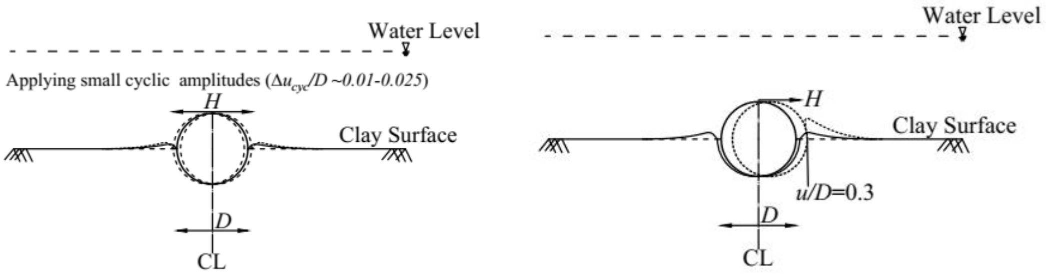

c) Test 6a, applying very small cyclic amplitudes. **d) Test 6a, lateral monotonic, *u/D* ~0.3.**

Figure 7.3 General sketches show the test program for *w/D* = 0.5 with nomenclature.

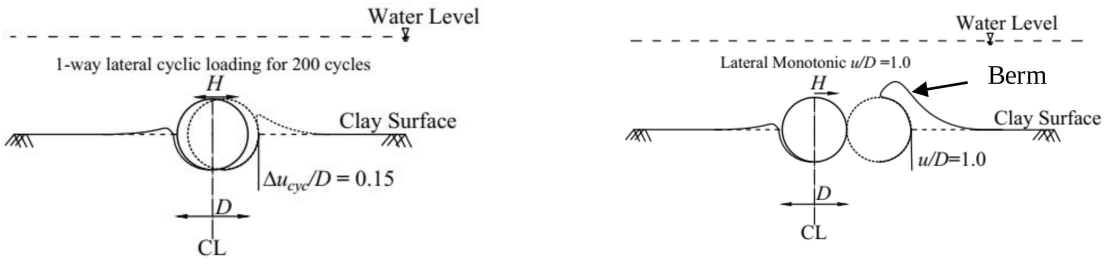

e) Test 6b, 200 lateral cycles for $\Delta u_{cyc}/D$ ~ 0.15.

f) Test 6c, lateral monotonic for *u/D* of 1.0 *D*.

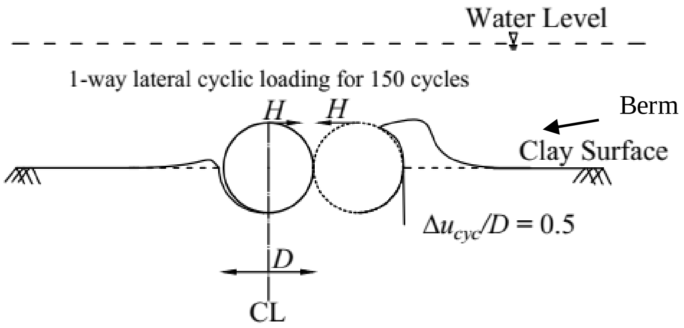

g) Test 6d, 100 lateral cycles (1-way) for $\Delta u_{cyc}/D$ ~ 0.5.

Figure 7.3 Continued.

From Figure 7.3h is embedment of the pipe from the original surface of the soil, H is the horizontal force per unit length, V is the vertical force per unit length, D is the pipe diameter, and u is the lateral movement from the front face of the pipe, as shown in Figure 7.3a.

7.5. Undrained Shear Strength of the Soil

The undrained shear strength is explained in details in Chapter 2. Figure 7.4a shows the corrected penetration resistance. Figure 7.4b presents some of the T-bars test results that have been determined with different water contents. Figure 7.4c illustrates the relationship between undrained shear strength and moisture water content using a miniature vane shear test. Table 7.5 shows the strength gradient for all tests.

Table 7.5 Undrained Shear Strength Using (T-bars Tests).

Test no.	s_{uo} (kPa)	Strength gradient (kPa/m)	Undrained Shear Strength, s_u (kPa)
1-3	1.1	16.7	s_u =1.1+16.7w
4 & 7a- 7d	1.3	14	s_u =1.3+14w
5	1.5	16.3	s_u =1.5+16.3w
6a to 6d	1.5	18.8	s_u =1.5+18.8w

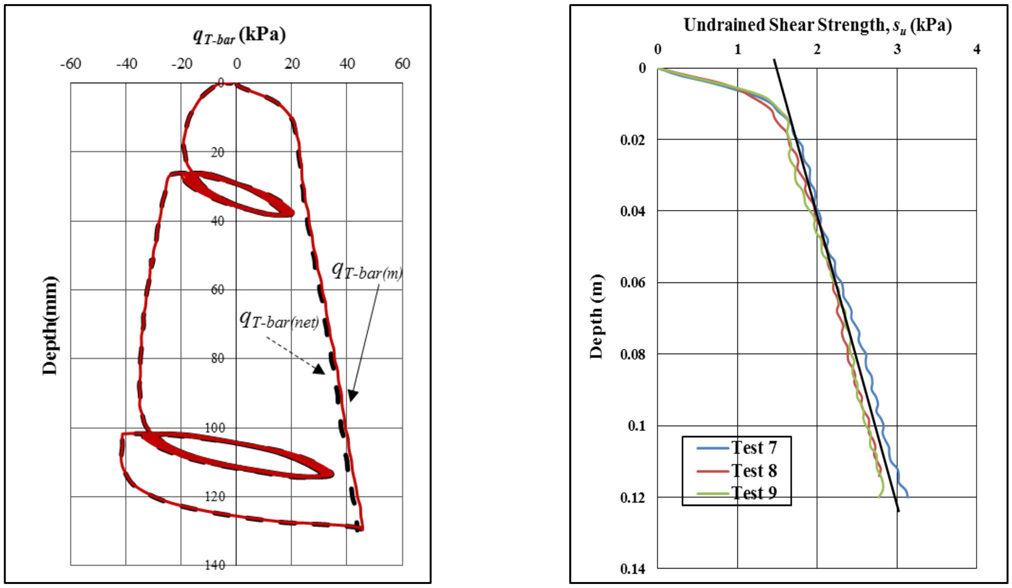

a) Measured vs. corrected penetration resistance. **b) Selected T-bar tests.**

Figure 7.4 Undrained shear strength profiles from different tests.

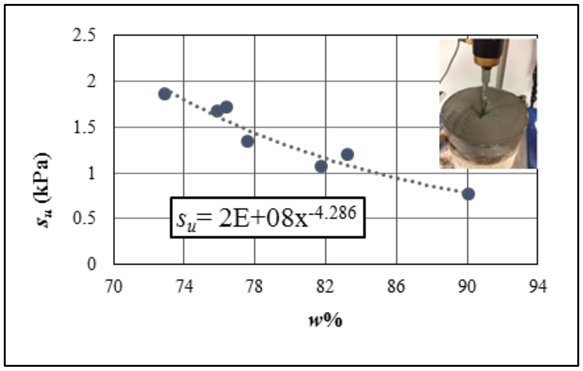

c) Undrained shear strength s_u vs. water content w%.

Figure 7.4 Continued.

7.6. Mechanism Response of The Lateral Resistance

A pipeline penetrates into the seabed during installation due to its own weight. In addition, the process of laying the pipe on the seabed leads to additional embedment depth. The pipe moves downward with any vessel motion which creates additional cyclic loads (White and Cheuk 2008). Risers/pipelines also experience lateral movements, which introduce a need to assess the lateral soil resistance to riser motions or to control buckling of pipelines. In the present study, a model pipe is cycled across a test bed of GoM clay under a fixed vertical penetration, whilst the horizontal soil resistance is measured. Fig. 1b shows the response involves (1) a steep rise in lateral resistance, (2) initial breakout of the pipe, (3) a gradual increase in lateral soil resistance with increased lateral penetration as berm forms ahead of the pipe, and (4) similar behavior with each subsequent cycle, but with lessened soil resistance across the trench and the berm.

A previous study by Bruton et al. (2009) investigated the lateral load-displacement response of “heavy” and “light” pipes. The vertical load is constant, in contrast to the present study, where the vertical position is fixed. Figure 7.5a shows the behavior of a light pipe which moves upward after the breakout resistance in subsequent cycles degrades to a residual value. This may be contrasted to the behavior of a heavy pipe (Figure 7.5b), which dives downward into stronger soil during lateral sweeps, resulting in accumulating passive resistance.

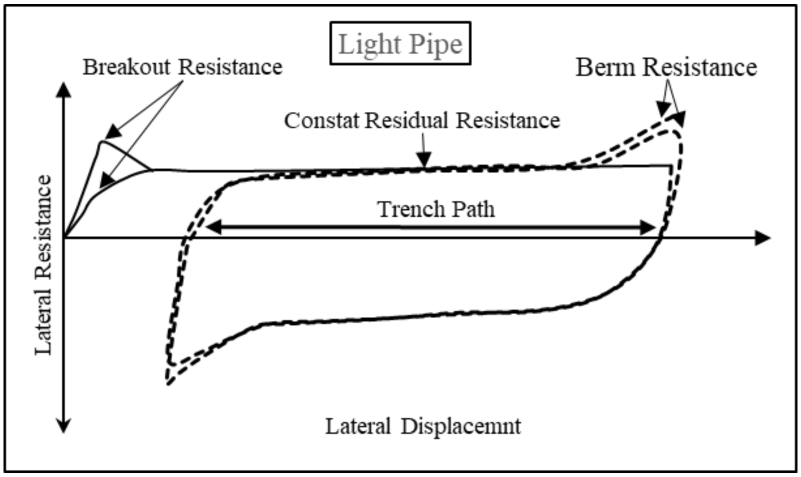

a-Light pipe

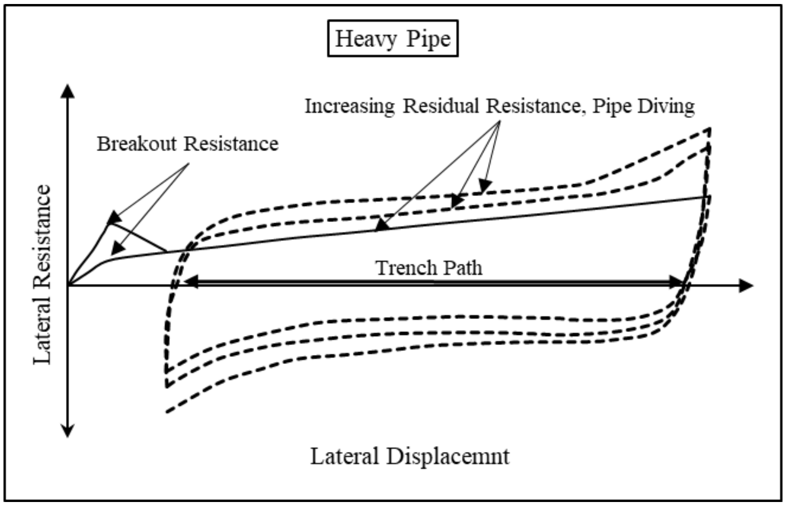

b- Heavy pipe.

Figure 7.5 Typical lateral response of pipelines.

7.7. Pipe Trajectory and Vertical Penetration

Wang et al. (2010) investigated the process of pipe penetration and lateral displacement using large deformation finite element method (LDFE), with a softening rate-dependent soil model. In the simulations, the pipe is penetrated to a depth of $w = 0.45$ D with ultimate resistance $V_{max} /Ds_{u0} = 6.2$. The load is then reduced to operating loads V_{op} /Ds_{u0} less than 1.5 to simulate light pipes and treater than 2.5 to simulate heavy pipes. Lateral sweeps are simulated at initial overpenetration ratios $R= V_{max}/ V_{op} = 1.25{\sim}10$. After initial penetration, the pipe is displaced horizontally to about $u/D = 3.0$. Figure 7.6a shows the results of pipe trajectories for different R=1.25~5.26 (Wang et al. 2010). Particularly noteworthy is that, at a vertical embedment of about one-half D, an overpenetration ratio $R = 2$ delineates the boundary between light-pipe and heavy-pipe behavior, where neither uplifting nor diving occur. The trajectory of the pipe in the current study (held constant at $w/D = 0.5$) is superimposed onto Fig 9a. The Wang et al. (2010) predictions for overpenetration ratio $R = 2$ are particularly relevant to the current study, since this condition corresponds to a nearly horizontal trajectory; i.e., the test condition imposed in the current study.

The breakout resistance is related directly to the pipe weight. Figure 7.6b shows the response of light and heavy pipes. For light pipes, the pipes tend to move upward (the breakout resistance), followed by a steady a steady-state, the pipe remains constant in the vertical position (the residual resistance) as shown in Figure 7.6b. Heavy pipes tend to move downward. Eventually, the pipe trajectory follows a constant elevation and the resistance approaches a steady-state condition (Figure 7.6b).

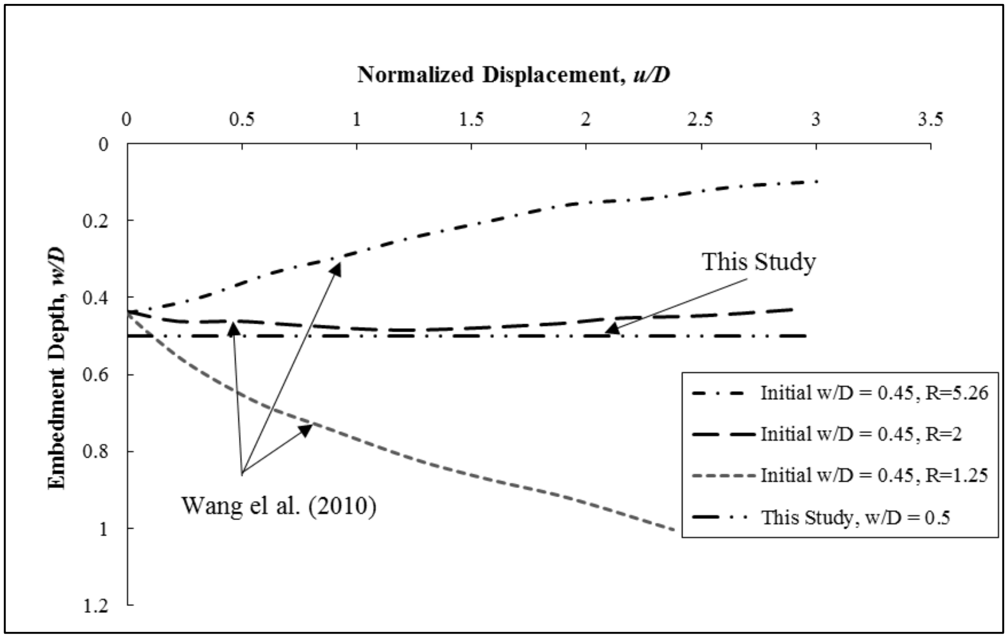

a) Pipe trajectory vs. embedment depth due to the effect of pipe weight (present study vs. previous studies).

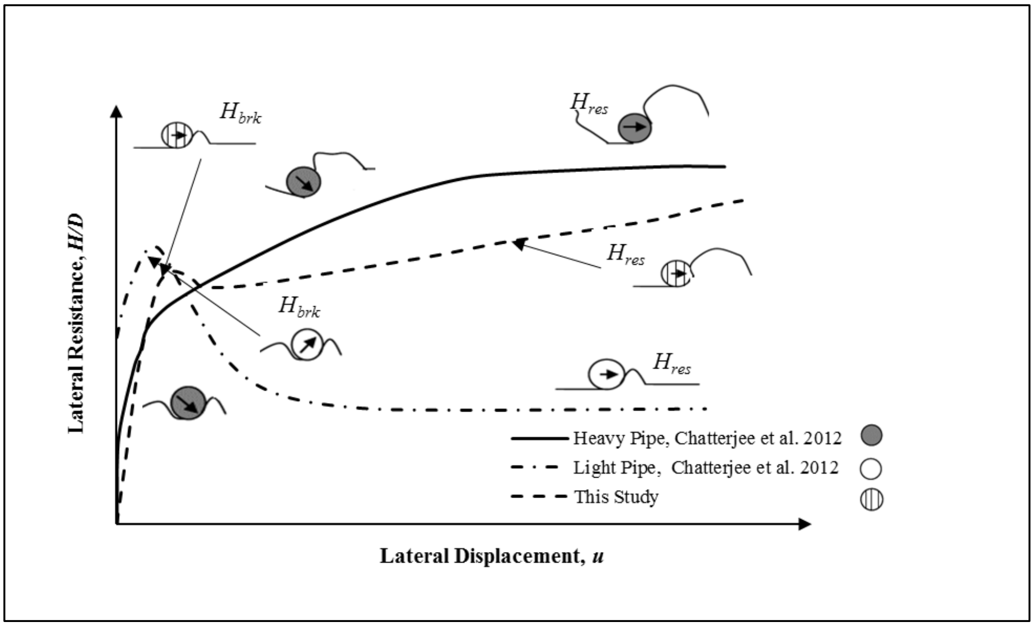

b) Effect of pipe weight on lateral resistance.

Figure 7.6 Effect of pipe weight.

7.8. Results and Data Interpretation

This section presents and interprets the test results described above in the earlier section.

7.8.1. Series 1: Vertical Monotonic Loading Tests With Different Penetration Rates and The Comparison With Existing Results

Three vertical monotonic tests are carried out to evaluate the rate effect (Table 7.2). The first two tests penetrated to a depth of 1.0 D (50.8 mm) at different penetration rates of 1mm/sec, and 10 mm/sec, respectively. The pipe in Test 3 is pushed in to a depth 1.3D (66.04 mm) at a velocity of 15 mm/sec (Table 7.2). These tests are carried out to be compared to data from other existing studies. Equation 7.1 shows the bearing factor which is used to compare with the previous published studies.

$$N_p = V/s_u D \qquad \textbf{Equation 7.1}$$

where N_p is bearing factor, V is the vertical soil resisting force per unit length from soil shearing resistance, D is riser diameter, and s_u is undrained shear strength. Figure 7.7a shows the bearing factor of the monotonic tests on y-axes and the normalized vertical displacement, y/D on x-axes. The variation in the bearing factor between Test 1 and Test 2 is around 11%. This percentage increases to about 27% between Tests 1 and 3. Similar trends are reported by Langford and Aubeny (2008).

The first test is compared to an empirical equation developed by Aubeny et al. (2005) and finite element results by Merifield et al. (2008) as shown in Figure 7.7b. Equation 7.2 shows the Aubeny et al. equation.

$$N_p = a\,[w/D]^b \qquad \textbf{Equation 7.2}$$

where N_p is bearing factor, a varies from 4.97 to 6.93 depending on the adhesion factor α, h is penetration depth, D is pipe diameter, and the exponent b varies from 0.23 to 0.29 depending on a. For the purpose of comparing Equation 7.2 to laboratory measurements, an adhesion factor $\alpha = 0.5$ is assumed, or $a = 5.95$ and $b = 0.26$. Figure 7.7b shows good agreement between the test measurements produced in this study, the Aubeny et al. equation and the Merifield et al. finite element solutions.

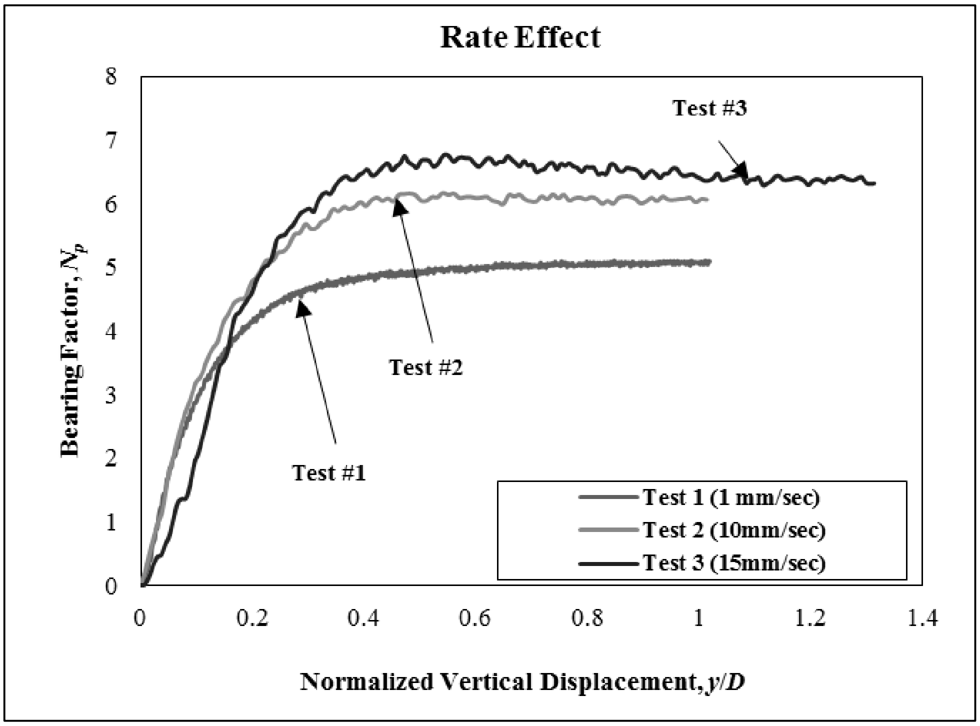

a) Different loading rates.

Figure 7.7 Vertical monotonic tests.

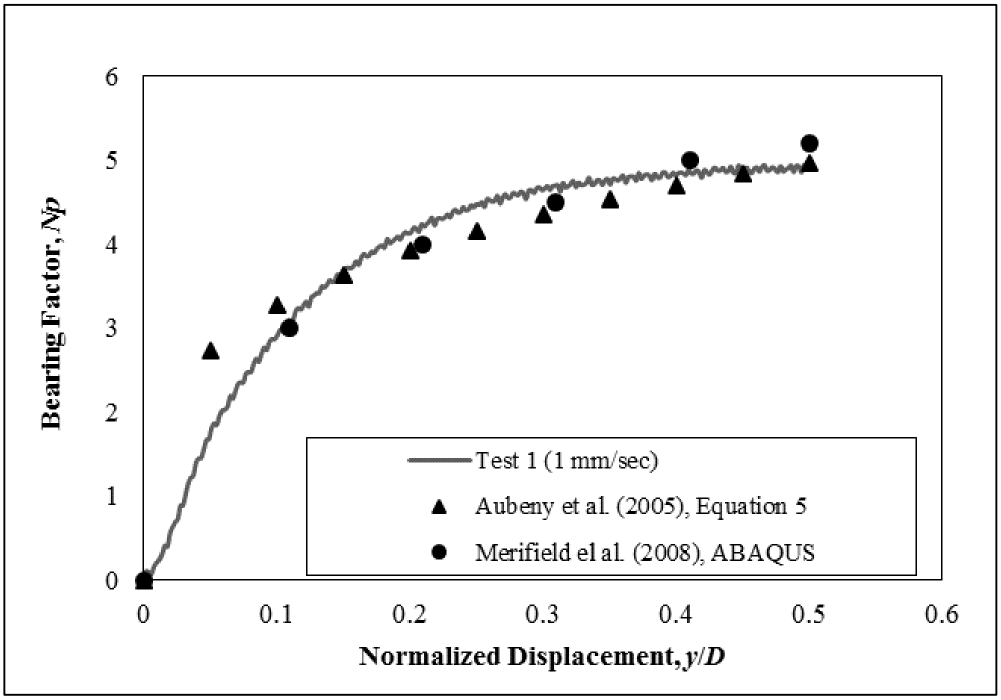

b) Comparison with previous studies.

Figure 7.7 Continued.

7.8.2. Series 2: Backbone Curve Resistance (*U/D* ~ 3.0) at Different Embedment Depths, *W/D* of 0.5 and 1.0

The purely monotonic lateral loading tests performed and summarized in Table 7.3. The first test is penetrated into a depth of 0.5 *D* and laterally moved to 3.0 *D* at a constant velocity of 1.5 mm/sec. Test 5 is penetrated into 1.0 *D* from the soil surface and is horizontally moved to 3.0 *D*. The objective of these tests is to evaluate horizontal resistance, evolving trench configuration and berm formation during horizontal loading at different embedment depths, *w/D*. Figure 7.8a shows the lateral resistance increasing by about 40% for the deeper penetration. A peak non-dimensional breakout lateral resistance,

H_{brk}/Ds_u, is reached at a small pipe displacement of ~ 0.15 D for (w/D = 0.5 and 1.0). This is followed by a drop in resistance, taken as evidence of a tensile failure at the pipe-soil interface. The lateral resistance then gradually increases with further horizontal pipe displacement. The increase in lateral resistance is caused by the berm in front of the moving pipe, which grows in size with pipe displacement as shown in Figure 7.3b.

Figure 7.8a compares lateral breakout resistance from this study to that predicted in previous studies, including empirical, finite element analysis, and upper bound plasticity solutions (Merifield et al. 2008; Wang et al. 2010; Chatterjee et al. 2012). These predictions agree well with the present study, although, there is a slight deviation from the Wang et al. (2010) results. Differences in horizontal resistance between the current study and studies of others (Wang et al., 2010) may be due to differences in loading rate.

The differing forms of residual lateral resistance response are linked to the trajectory of the pipe as shown in Figure 7.6a-b. The breakout resistance is approximately the same (with slight difference due to the difference in the embedment depth and penetration rate) for all studies as the pipe movement is close to horizontal. Figure 7.8b shows a comparison between this study and previous studies for the lateral residual resistance. A model is explained in details by White and Cheuk, (2008) will be also compared to this study. The model is based on tri-linear lateral resistance. The normalized breakout resistance, $h_{brk}= H/Ds_u$ is suggested by Verley and Lund (1995) based on normalized vertical load, $v = V/Ds_u$, the initial embedment depth, w_{in}/D, and the dimensionless ratio of undrained shear strength to weight, $s_u/\gamma' D$. This model is recalibrated by Bruton et al. (2006), leading to

Equation 7.3 to predict the breakout resistance, h_{brk}. Equation 7.4 is to predict the residual resistance, h_{res}, according to the tri-linear model. The lateral residual resistance is constant after the breakout resistance. White and Cheuk (2008) added the effect plowing and berm resistance to the basic lateral response as shown in Equation 7.5.

$$h_{brk} = 0.2v + \frac{3}{\sqrt{s_u / \gamma' D}} \frac{w_{in}}{D}$$ **Equation 7.3**

$$\frac{h_{res}}{v} = 1 - 0.65\left[1 - \exp(-\frac{1}{2}\frac{s_u}{\gamma' D}\right]$$ **Equation 7.4**

$$h_{res} = (\alpha\lambda v^{\beta} \times \frac{u}{D})^{\delta}$$ **Equation 7.5**

where α and β are plowing depth parameters, δ and λ are berm parameters. As suggested, $\alpha = 0.015$, $\beta = 2\text{-}3$ (3 is used), $\delta = 0.5$, and $\lambda = 1$. Figure 7.8b shows that

Equation 7.3 to Equation 7.5 slightly underestimates the breakout and the residual lateral resistance for both penetration depth of 0.5 and 1.0 compared to this study.

Three failure mechanisms governing lateral resistance are possible:

1- For R >2 (light pipe) lateral resistance decreases with increasing displacement due to upward movement of the pipe.

2- For constant vertical position, the lateral resistance gradually increases with increasing horizontal displacement. The increase in lateral resistance is caused by the berm in front of the moving pipe, which grows in size with pipe displacement.

3- For R <2 (heavy pipe), Increased lateral resistance occurs as the pipe moves downward. The berm in front of the pipe grows in size with increasing displacement. After *u/D* = 2.4 the pipe moves at a constant vertical position (Figure 7.6b). The resistance will continue to slightly increase with moving the pipe laterally (Wang et al. 2010).

Figure 7.9 shows illustrative photographs of the trenches and berms formed during lateral loading.

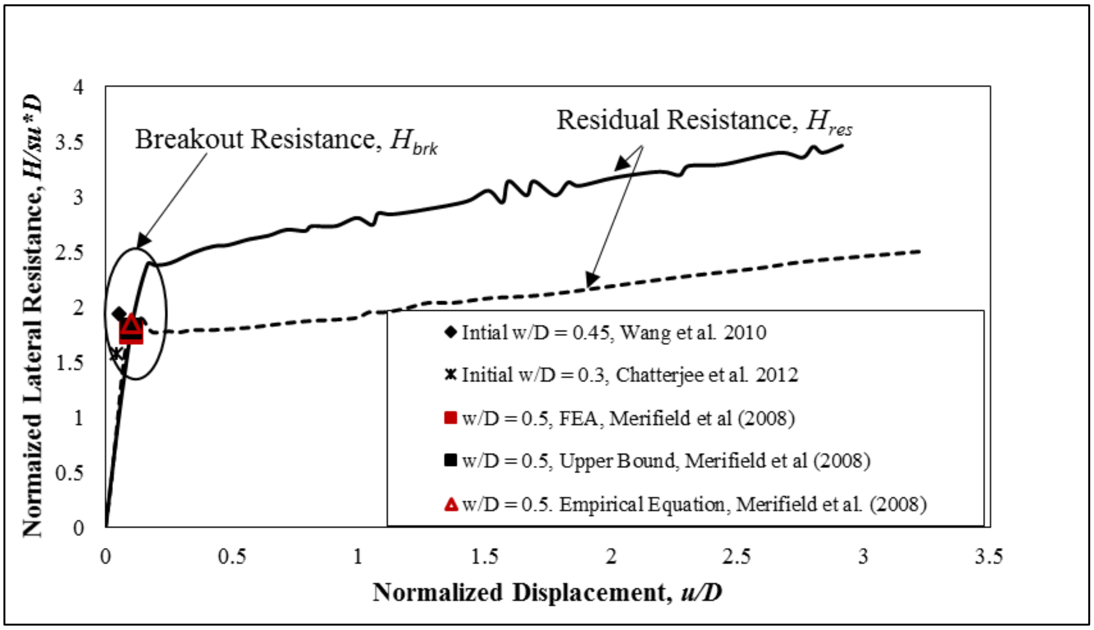

a) Lateral breakout resistance with previous studies.

Figure 7.8 Lateral resistance vs. normalized displacement.

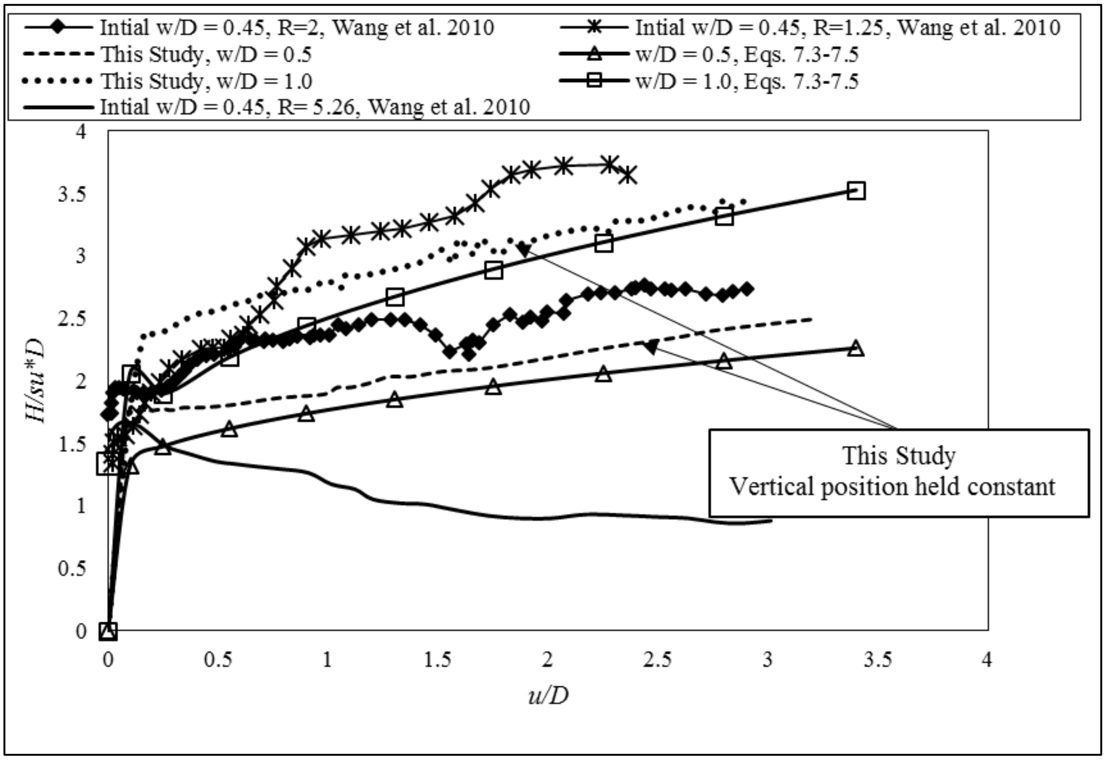

b) Lateral residual resistance with previous studies.

Figure 7.8 Continued.

a) Test 4 berm for *w/D* = 0.5. **b) Test 4 trench for *w/D* = 0.5.**

Figure 7.9 Photographs are taken during testing.

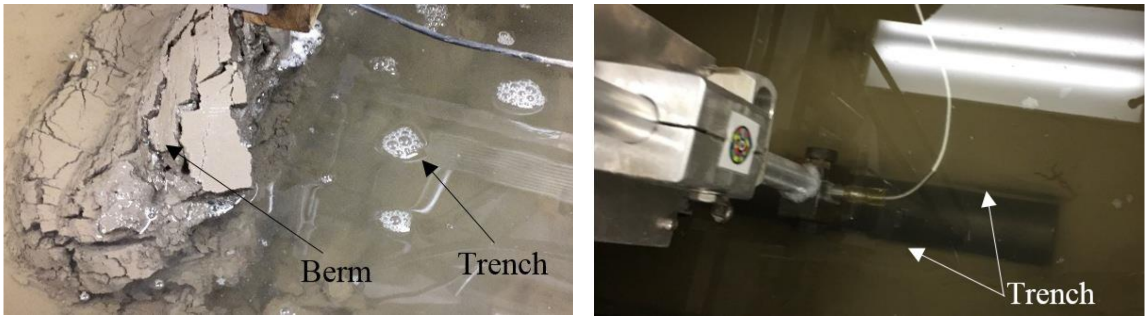

c) Test 5 for $w/D = 1$.

d) Test 6a for $\Delta u_{cyc}/D \sim 1\%\text{-}2.5\%$.

Figure 7.9 Continued.

7.8.3. Simulate the Riser Initial Vertical Penetration (and Then Apply Very Small Lateral Cyclic Amplitudes)

Series 3 and series 4 are identical except for the embedment depth. The embedment depth w/D of the third series is 0.5 and 1.0 for the fourth series. Table 7.4 shows a summary of these tests (Test 6a-d and Test 7a-d). To simulate the riser initial vertical penetration, the pipe is embedded to a depth of 0.5 D and 1.0 D (Test 6a and Test 7a), and then a series of very small lateral cyclic amplitudes, Δy_{cyc}, which ranged from (0.01 D to 0.025 D) is applied to the pipe. At the end of applying the small lateral cyclic amplitudes u_{cyc}/D, a small trench is formed (gaps both sides of the pipe) as shown in Figure 7.3c and Figure 7.10.

7.8.4. Monotonic Tests (Backbone Curve) With a Small Deformation, u/D ~ 0.3, for w/D = 0.5 and 1.0

Two monotonic loading tests (Test 6a and Test 7a) are conducted where ~ a 1000 of very small lateral movements ($\Delta u_{cyc}/D \sim$ 1%-2.5%) are applied at different embedment depths, $w/D = 0.5$ and 1.0, to simulate riser motions during initial vertical penetration as explained in the previous section. After applying the small lateral cyclic amplitudes, Test 6a, the pipe is laterally swept to 0.3 D, then is moved back to the centerline ($y = 0.0\ D$). Figure 7.10, comparing the results from Tests 6a and 7a, and shows the deeper penetration to increase lateral soil resistance by about 37%. Additionally, the effect of the small-amplitude cyclic loading ($\Delta u_{cyc}/D$ ~ 1%-2.5%) imposed prior to monotonic loading is apparent at low displacement levels. The vertical solid line in Figure 7.10 denotes the trench that is formed from the small cyclic loading.

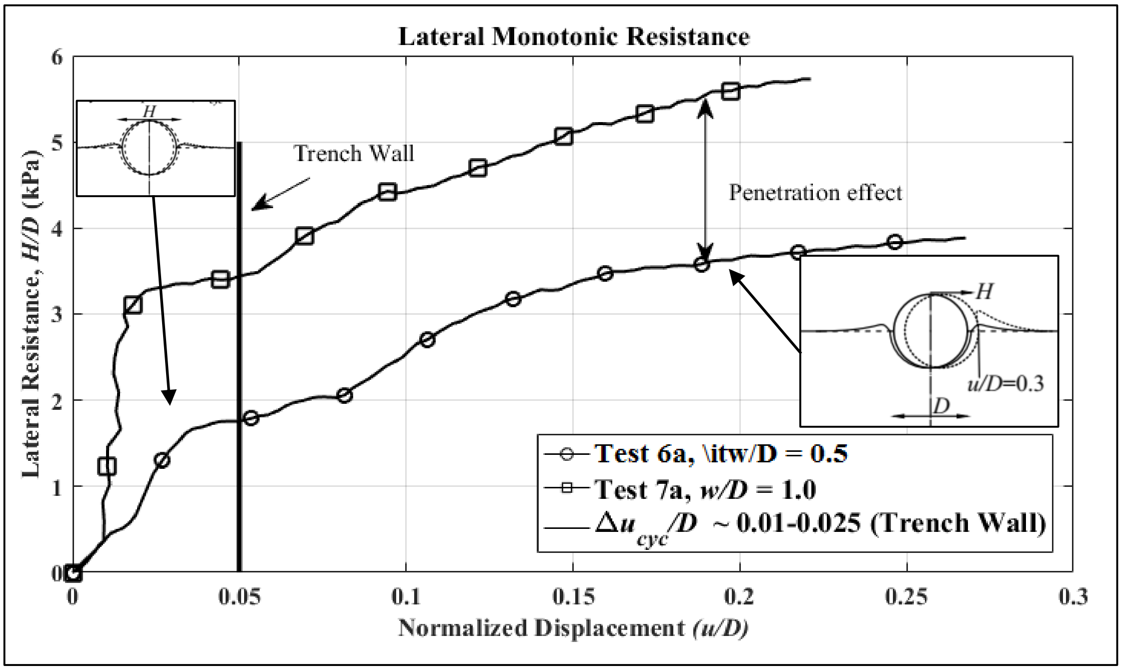

Figure 7.10 Normalized lateral resistance vs. normalized lateral displacement for *u/D* ~ 0.3 and *w/D* = 0.5 and 1.0.

7.8.5. Small Cyclic Amplitude $\Delta u/D$ of 0.15 D at w/D = 0.5 and 1.0

In Test 6b, the pipe is subjected to 1-way of 200 load cycles of a small cyclic amplitude of ~ 0.15 *D*, while in Test 7b, the pipe is subjected to 1-way of 150 load cycles as shown in Figure 7.11. Figure 7.11a shows lateral resistance dropping sharply after initial loading within the swept area (trench) and increasing as the pile approaches the berm formed by the sweeping motion (Figure 7.3d and Figure 7.3e). Figure 7.11b (Test 7b) shows the same behavior, but the decrease in soil resistance within swept area is more gradual under repeated cyclic loading. For example, the reduction in soil resistance from the backbone curve to the first load cycle at displacement *u/D* ~ 0.15 is about 70% for a shallowly embedded pipe (0.5*D* in Figure 7.11a). By contrast, the reduction in resistance is about 45% for a deeper embedment (1*D*, Figure 7.11b). This likely occurs for several reasons: 1) overall increased resistance at greater embedments and 2) the tendency of the berm to collapse into the trench and cover the pipe at greater embedment depths. The overall increased resistance at greater penetration is attributed to a combination of a greater undrained shear strength (Al-Janabi and Aubeny, 2019; Al-Janabi el. al. 2019; Oliphant et al. 2009) and increased constraint imposed by the soil above the pipe. The lateral resistance within the trench approaches zero after about 10 cycles for penetration depths 0.5*D* and 1*D*. Figure 7.12 shows the degradation in the lateral resistance while increasing the number of cycles for the shallow and deep penetrations. From plot (a) to plot (b) of Figure 7.10 and Figure 7.11, it is clear that the reduction in soil resistance during cyclic loading is greatest at shallow depths and decreases somewhat with increasing penetration. For example, the resistance at the berms reduces by about 46% and 41% for penetration depths 0.5*D* and 1*D*, respectively during the first 10 cycles. After the first 10 load cycles, the resistance continues to decrease, but at a reduced rate. For shallow penetration depths, the lateral resistance approaches zero after a large number of cycles ranging from 150-200 cycles for both the penetration and the extraction resistance. For *w/D* =1.0 *D*, Test 7b, the steady-state is reached at about 100 cycles with a lateral resistance of ~1.5 kPa. This reduction in resistance is due to multiple reasons, 1) softening and remolding the soil with increasing cycles, that causes the reduction in the undrained shear strength (Al-Janabi el al. 2019), and 2) it is noticed that there is clouded waves coming out when the pipe touching the soil berms, in other words, the soil erosion (scour) occurs during the cyclic loading. This erosion led to softening the soil and move it out of the berm as cloudy waves. This process led to reducing the size of the berm in front of the pipe; however, the reduction in lateral resistance occurred.

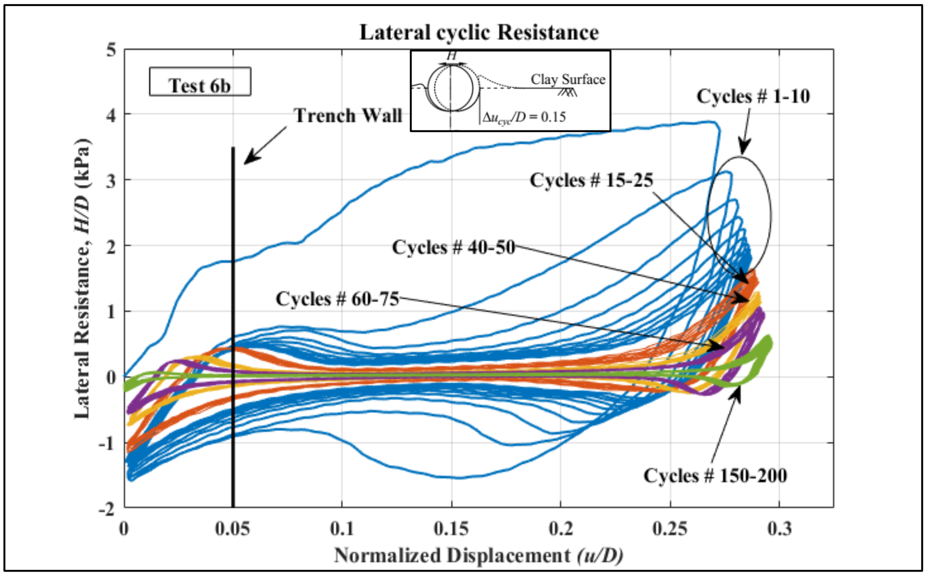

a) $\Delta u/D$ ~ 0.15 and w/D = 0.5.

Figure 7.11 Normalized lateral resistance vs. normalized lateral displacement.

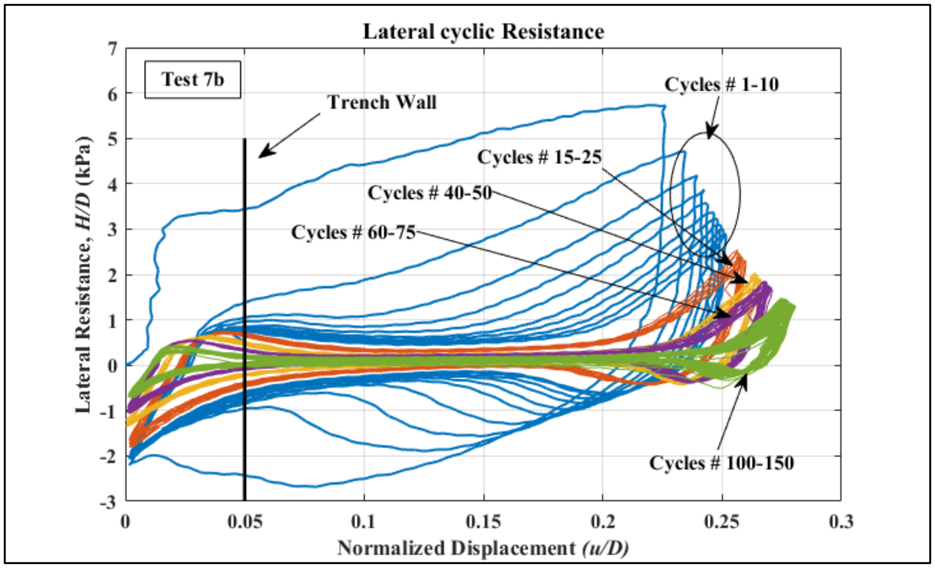

b) $\Delta u/D$ ~ 0.15 and w/D = 1.0.

Figure 7.11 Continued.

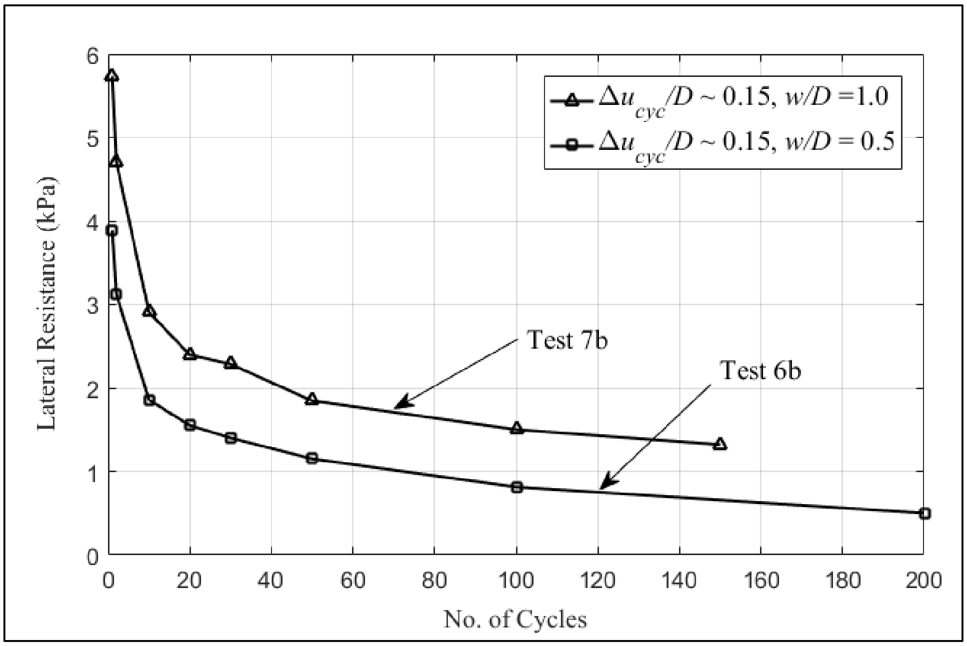

Figure 7.12 Lateral resistace vs. number of cycles for $\Delta u_{cyc}/D$ ~ 0.15 and w/D = 0.5 and 1.

7.9. Rest Period and Strength Recovery

In deep water, the seabed consolidates and gains strength over time during rest periods. In this study, the effect of consolidation on the pipe embedment of w/D = 0.5 is studied for a rest period of t = 23 hours.

The rest period is allowed to observe the strength recovery by allowing the pipe to rest in the trench for different periods of time. It is applied after conducting the lateral cyclic loading of Test 6b and Test 7b of series 3 and series 4. The pipe is free to settle under its own weight during the pause period. The vertical settlement is recorded for w/D = 0.5. This procedure is followed through all of series 3 and series 4 for the penetration depth of 0.5 D and 1.0 D. The rest period is followed by large lateral monotonic displacement u/D ~ 1.0.

The vertical displacement is captured during the rest period for Test 6b (w/D = 0.5). Therefore, it is believed that the consolidation occurs. In addition, thixotropy is a significant factor that affects strength recovery where the undrained shear strength increases to about 30% within 24 hours after remolding the soil (Al-Janabi and Aubeny 2019). Figure 7.12 shows the non-dimensional time factor (T) versus the normalized settlement ($\Delta w/D$). The time factor is calculated as ($T = c_v t/D^2$), where c_v is the coefficient of consolidation, which is taken as 0.0003 cm^2/sec as remolded GoM clay and t is the rest period time (NAVFAC, 1971). The pipe experienced immediate settlement to about 0.026 D due to soil softening during cyclic loading. Afterwards, an additional time-dependent settlement of 0.007 D occurred, as shown in Figure 7.12. The end of the primary consolidation occurs at a dimensionless T = 0.75.

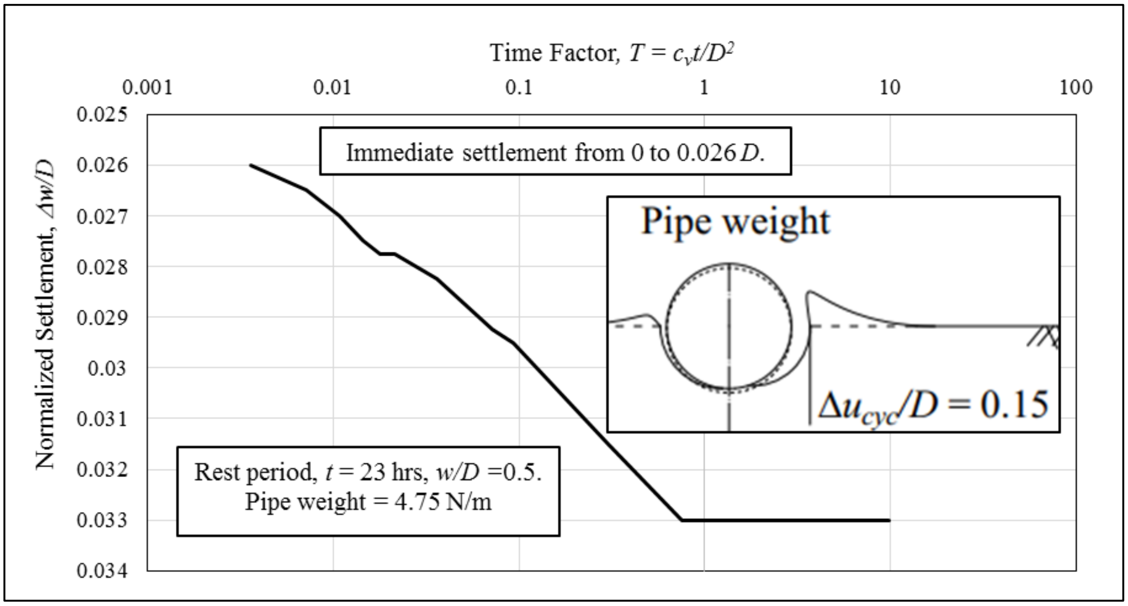

Figure 7.13 Pipe settlement with time.

7.9.1. Monotonic Tests (Backbone Curve) Large Deformation, u/D ~ 1.0 for w/D = 0.5 and 1.0 and Pause Period Effect

After imposing the rest period, the pipe is reconnected (locked) and another two lateral monotonic tests (Test 6c and Test 7c) with large displacement, *y*, are conducted. They are subjected to large lateral displacement of 1.0 to capture the lateral resistance degradation, trenches formation, and berms shapes. The pipe is horizontally pulled for a distance of 1.0 *D* as shown in Figure 7.3f. Figure 7.14a shows a comparison between Test 6c and Test 7c. This Fig. shows the horizontal resistance verses the lateral displacement after the pause period for both penetration depth *w/D* = 0.5 and *w/D* = 1.0. As shown on Figure 7.14a the resistance jumps up after the pause period and drops significantly during the pipe movement inside the trench. Therefore, there is a short-term increase in the soil resistance, which quickly declines to reach the point before the pause period because of the trench.

Figure 17 b shows a comparison between Tests 4 and 5 versus Tests 6c and 7c. This Fig. shows that the residual resistance increases after the rest period. The increase in the soil resistance after the rest period can be explained with the following reasons: (1) reconsolidation, (2) thixotropy, and (3) the increase in undrained shear strength due to the increased pipe embedment. Figure 7.14a shows that there is about a 28% difference in the lateral resistance due to embedment depths.

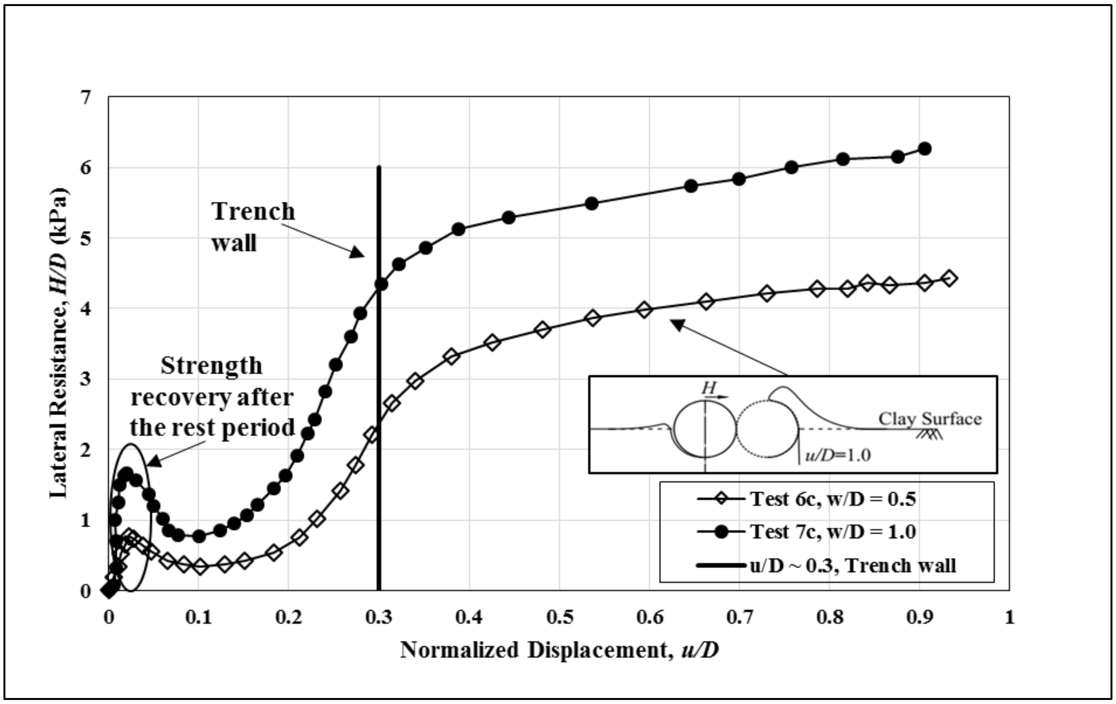

a) Normalized lateral resistance vs. normalized lateral displacement for *u/D* ~ 1.0 and *w/D* = 0.5 and 1.0.

Figure 7.14 Normalized lateral resistance vs. normalized lateral displacement.

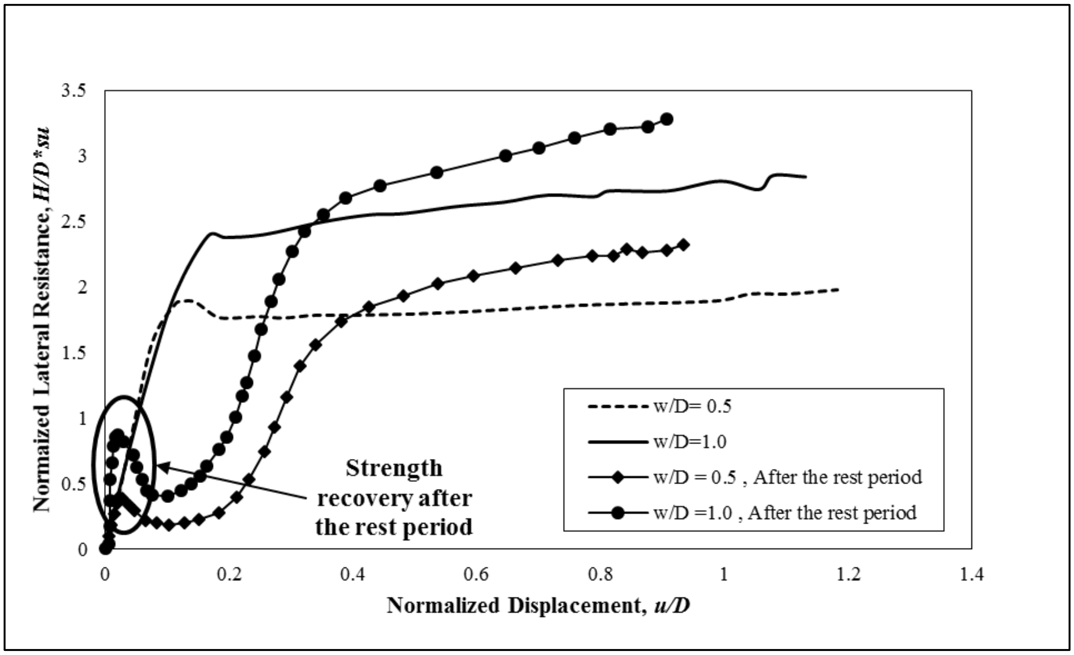

b) Normalized lateral resistance vs. normalized lateral displacement for *u/D* ~ 1.0 and *w/D* = 0.5 and 1.0 before and after the rest period.

Figure 7.14 Continued.

7.9.2. Large Cyclic Amplitude, $\Delta u_{cyc}/D$ ~ 0.5, w/D = 0.5 and 1.0

For the large cyclic displacement (shallow embedment depth, *w/D* = 0.5), Test 6d is conducted after forming the trench from Test 6c. 100 load cycles of $\Delta u_{cyc}/D$ ~ 0.5 are applied to the pipe. The aim of this test is to expand the currently limited database of measurements to better understand the degradation in lateral resistance under cyclic loading.

Figure 7.15a presents the variation in the lateral resistance at the trench path and the soil berm for the shallow vertical penetration depth. Figure 7.16 shows the degradation in the berm resistance with increasing numbers of cycles. From Figure 7.15a (Test 6d), it is clear that the reduction in soil resistance between the 1^{st} cycle and the 10^{st} cycle (at the berm) is about 51%. The reduction in the lateral resistance continues to decrease, but at a reduced rate to reach the steady state at about 45 cycles as shown in Figure 7.16. For the lateral resistance at the trench path (at $u/D = 0.5$), it is clear from plot (a) of Figure 7.15 that the reduction in resistance after forming the trench (Test 6c) drops by about 87% and approaches zero after about 10 cycles. This reduction in lateral resistance is believed to be due to the soil being swept all the way to the berm locations shown in Figure 7.3f and Figure 7.3g.

For the deep penetration (Test 7d), Figure 7.15b shows the reduced soil resistance as the pipe sweeps through the trench followed by the increase in resistance as the pipe approaches the berm. This behavior is similar to that observed at shallow penetration depth. From Figure 7.16, the steady-state occurs after about 45 cycles, as is the case for the shallow embedment depth. Close examination of Figure 7.15 shows a differing pattern of reduction of soil resistance within the trench under cycling loading at greater embedment depth (Figure 7.15b); namely, the rate of reduction is much more gradual. This is believed in part to be the result of the observed tendency of the soil to collapse back into the trench and sometimes cover the pipe at the greater embedment depth.

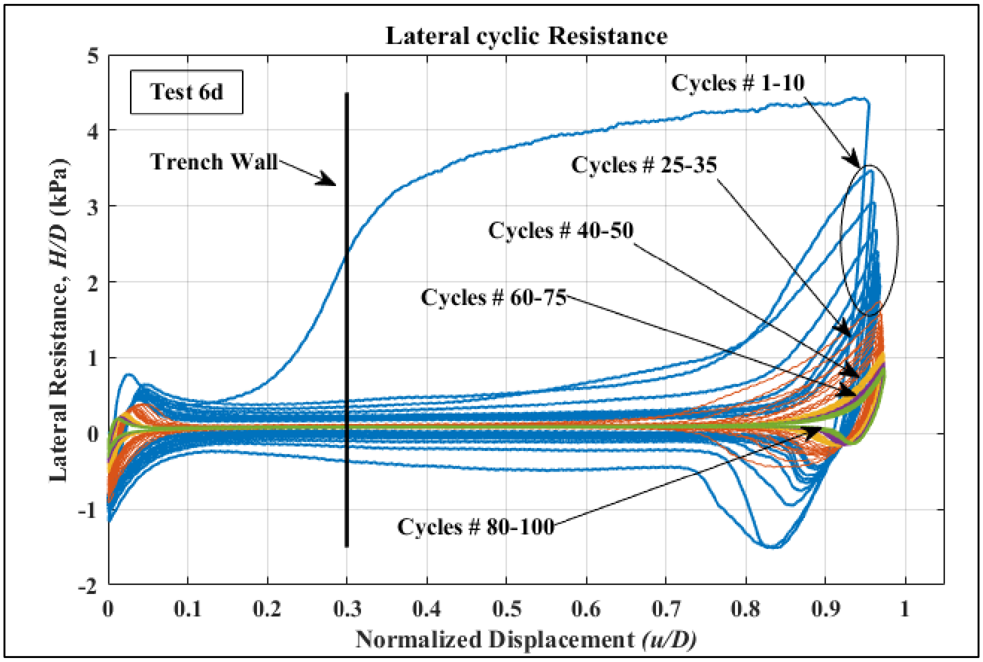

a) $\Delta u/D \sim 0.5$ and $w/D = 0.5$.

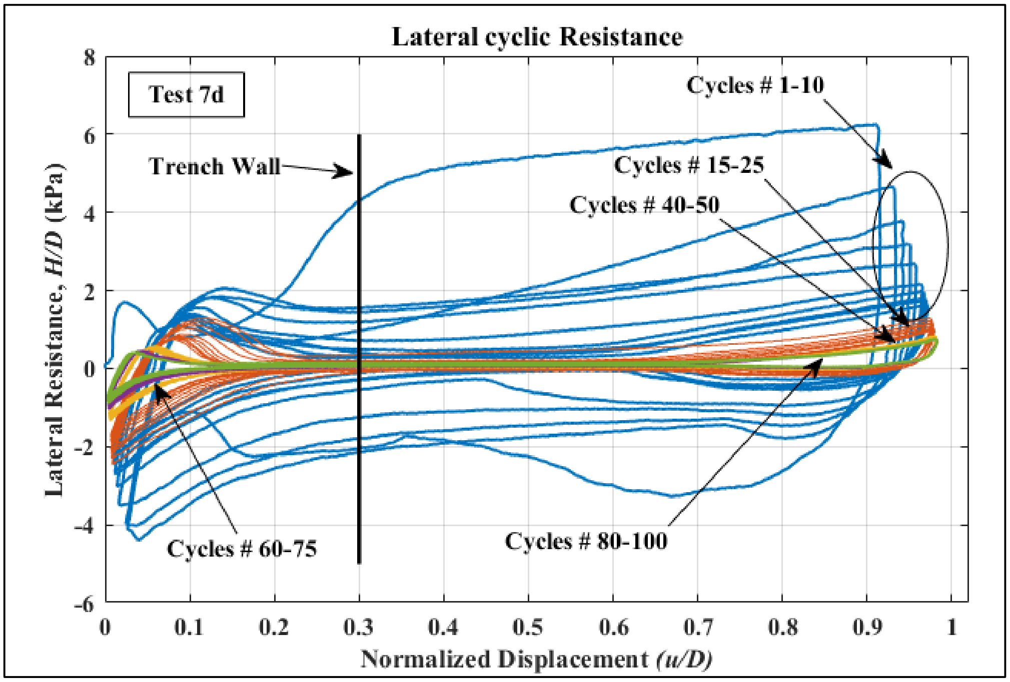

b) $\Delta u/D \sim 0.5$ and $w/D = 1.0$

Figure 7.15 Normalized lateral resistance vs. normalized lateral displacement.

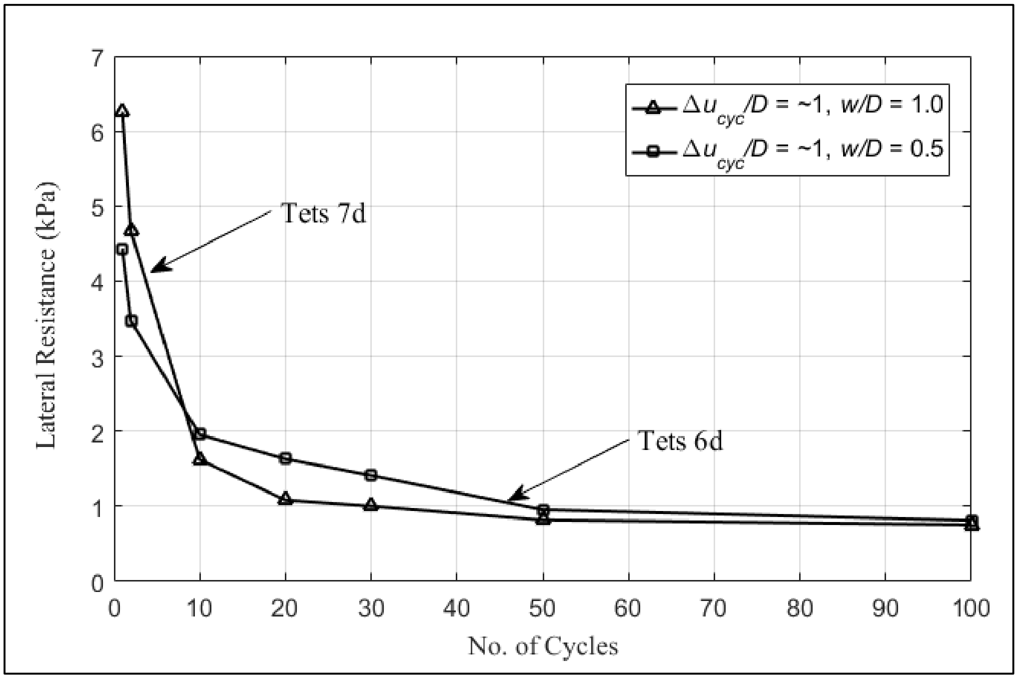

Figure 7.16 Lateral resistance vs. number of cycles for *u/D* ~1 and *w/D* = 0.5 and 1.

7.10. Trench Formation

The first step in examining trench formation involves pushing in the pipe to the required depth (either 0.5 *D* or 1 *D*) as shown in Figure 7.3a and Figure 7.9a-c. The rate of lateral motion for all trenches is 1.5 mm/sec. More than one trench is formed depending on the embedment depth, *w/D*, the horizontal movements, *u/D*, and cyclic displacement amplitudes, $\Delta u_{cyc}/D$. The first two trenches are formed after applying a large horizontal displacement *u/D* ~ 3.0. Different trench configurations develop depending on the pipe embedment depth for *w/D* = 0.5 and 1. The pipe is completely covered by the collapsing berm for *w/D* = 0.5 at a displacement *u/D* ~ 3.0 (Figure 7.9a-c). For *w/D* =1.0, the pipe is partially covered by the soil at the beginning of the movement and then is totally covered by a large block of soil. Tests 6b, 6c, 7b and 7c followed the same procedure, but with different penetration depth of 0.5 *D* and 1.0 *D*, respectively.

7.11. The Following Observations Can Be Made for the Entire Test Program:

1. For Tests 4 and Test 5 from Figure 7.8a, the lateral resistance increases rapidly when the pipe translates horizontally and then it increases slightly while increasing the lateral penetration.
2. For Test 6a and Test 7a, when applying small cyclic amplitudes $\Delta u_{cyc}/D$ ~ 1%-2.5% in the lateral direction, the backbone curve resistance at small displacements reduces due to the small gaps (trenches) that are formed as a result of this procedure.
3. For the rest period of 2-3 hours, Figure 7.14a shows that soil strength recovery following the rest periods leads to a short-term increase in the lateral resistance of the soil, which quickly declines after moving the pipe laterally.
4. At small-displacement amplitudes, the mechanism of berm formation initiates by a thin layer(s) rolling around the pipe. As the displacement amplitude increases, the soil completely covers the pipe, and ultimately collapses inside the trench in the wake of the pipe. This describes the $w/D = 0.5$ case with different displacement amplitude $\Delta u_{cyc}/D$.
5. For deep embedment $w/D = 1.0$, the pipe is nearly covered by the soil. When the pipe translates horizontally, the soil rolls over the pipe, cuts, and falls into the trench behind the pipe. In addition, the soil falls in front of the pipe when the pipe

pulls back to the centerline location. This behavior explains the higher lateral resistance for the deep penetration when the pipe moves inside the trench.

6. Figure 7.11a-b and Figure 7.12 show that the lateral soil resistance degradation is significant after the backbone curve. The reduction continues gradually until it reaches the steady state behavior after a few cycles. Furthermore, the behavior of the lateral resistance at the berms (Figure 7.11a-b) is similar, but the resistance is higher for $w/D = 1.0$ because of the embedment depth effect.
7. Figure 7.15a and Figure 7.16 ($w/D = 0.5$) show significant (~70%) drops in resistance when the pipe travels inside the trench.

7.12. Nomenclature

D	Pipe Diameter
GoM	Gulf of Mexico
H	Lateral Soil Resistance
H_1	Maximum Lateral Soil Resistance
H_{brk}	Breakout Lateral Resistance
h_{brk}	Non-Dimensional Breakout Lateral Resistance
h_{res}	Non-Dimensional Residual Lateral Resistance
H_{res}	Residual Lateral Resistance
L	Pipe Length
LDFE	Large Deformation Finite Element Method
N	Number of Cycles
N_p	Bearing Factor

PLA	Plastic Limit Analysis
$q_{T\text{-}bar(m)}$	Measured Penetration Resistance
$q_{T\text{-}bar(net)}$	Net Penetration Resistance
R	Overpenetration Ratios
SCR	Steel Catenary Riser
s_u	Undrained Shear Strength
s_{u0}	Undrained Shear Strength at the surface
t	Time
T	Time Factor
TDZ	Touch Down Zone
u	Lateral Displacement
u_1	Maximum Lateral Displacement
V_{max}	Ultimate Resistance
V_{op}	Operating Load
w	Embedment Depth
$w\%$	Water Moisture Content
w_{in}	Initial Embedment depth
Δu_{cyc}	Lateral Cyclic Displacement Amplitude
Δw	Settlement
α and β	Plowing Depth Parameters
δ and λ	Berm Parameters
γ'	Submerged Unit Weight

7.13. References

Al-Janabi, H. A. & Aubeny, C. P. (2019). Experimental Measurement of Thixotropy and Sensitivity in Gulf of Mexico Clay. In The International Society of Offshore and Polar Engineers Conference, 2019-TPC-0593. Honolulu, HI, USA.

Al-Janabi, H. A., Aubeny, C. P., Chen J., Luo M. (2019) Experimental Measurement of Touchdown Zone Stiffness for SCR in Gulf of Mexico Clay. Offshore Technology Conference, OTC-29504-MS. Houston, TX, USA.

Al-janabi, H. A., Shlash, K. T., & Fattah, M. Y. (2014). The Behavior of Bounded Foundations on Sandy Soil Bounded Shallow Foundations on Iraqi Sandy Soil with Different Densities. *In. Saarbrücken: LAP LAMBERT Academic Publishing.*

ASTM Committee D-18 on Soil and Rock. (2018). *Standard test methods for liquid limit, plastic limit, and plasticity index of soils*. ASTM international.

ASTM. (2016). Standard test method for laboratory miniature vane shear test for saturated fine-grained clayey soil.

Aubeny, C. P., Shi, H., & Murff, J. D. (2005). Collapse loads for a cylinder embedded in trench in cohesive soil. *International Journal of Geomechanics*, *5*(4), 320-325.

Aubeny, C., & Dunlap, W. (2003, September). Penetration of cylindrical objects in soft mud. In Oceans 2003. Celebrating the Past... Teaming Toward the Future (IEEE Cat. No. 03CH37492) (Vol. 4, pp. 2068-2073). IEEE.

Bridge, C. D., & Howells, H. A. (2007). Observations and modeling of steel catenary riser trenches. Paper presented at the The Seventeenth International Offshore and Polar Engineering Conference.

Bruton, D. A., White, D., Langford, T., & Hill, A. J. (2009, January). Techniques for the assessment of pipe-soil interaction forces for future deepwater developments. In *Offshore Technology Conference*. Offshore Technology Conference.Chatterjee, S., White, D. J., & Randolph, M. F. (2012). Numerical simulations of pipe-soil interaction during large lateral movements on clay. *Géotechnique*, *62*(8), 693.

Chatterjee, S., White, D. J., & Randolph, M. F. (2013). Coupled consolidation analysis of pipe–soil interactions. *Canadian Geotechnical Journal*, *50*(6), 609-619.

Chen JB, Newlin J, Luo M, Zhang H, Hadley C and Hu S. (2019) Practice of Riser-Soil Interactions at Touch Down Zones for Steel Catenary Risers. Offshore Technology Conference, OTC-29553-MS. Houston, TX, USA.

Chen JB, Xu FB, Newlin J, Zhang H, Shuang H and Luo M. (2019a) Large Deformation Finite Element Analysis of Riser-Soil Interactions With Strain-Softening Soils. Offshore Technology Conference, OTC-29376-MS. Houston, TX, USA.

Dejong, J., Yafrate, N., Degroot, D., Low, H. E., & Randolph, M. (2010). Recommended practice for full-flow penetrometer testing and analysis. Geotechnical Testing Journal, 33(2), 137-149.

Fattah, M. Y., Shlash, K. T., & Mohammed, H. A. (2014). Bearing capacity of rectangular footing on sandy soil bounded by a wall. *Arabian Journal for Science and Engineering*, *39*(11), 7621-7633.

Fattah, M. Y., Shlash, K. T., & Mohammed, H. A. (2014a). Experimental Study on the Behavior of Bounded Square Footing on Sandy Soil. *Engineering and Technology Journal*, *32*(5 Part (A) Engineering), 1083-1105.

Fattah, M. Y., Shlash, K. T., & Mohammed, H. A. (2015). Experimental study on the behavior of strip footing on sandy soil bounded by a wall. *Arabian Journal of Geosciences*, *8*(7), 4779-4790.

Langford, T., & Aubeny, C. P. (2008, January). Model tests for steel catenary riser in marine clay. In *Offshore Technology Conference*. Offshore Technology Conference.

Merifield, R., White, D. J., & Randolph, M. F. (2008). The ultimate undrained resistance of partially embedded pipelines. *Géotechnique*, *58*(6), 461-470.

Mohammed, H. A., Shlash, K. T., & Fattah, M. Y. (2014). The Behavior of Bounded Foundations on Sandy Soil. LAP LAMBERT Academic Publishing.

Naval Facilities Engineering Command (NAVFAC). (1971). Design manual 7.01: Soil mechanics, Alexandria, VA.Oliphant, J., Maconochie, A., White, D., & Bolton, M. (2009). Trench interaction forces during lateral SCR movement in deepwater clays.

Palmer, A. (2000). Catenary riser interaction with the seabed at the touchdown point. Paper presented at the Proceedings of the deepwater pipeline and riser technology conference.

Randolph, M. F., & White, D. (2008, May). Pipeline embedment in deep water: processes and quantitative assessment. In *Offshore Technology Conference*. Offshore Technology Conference.

Randolph, M. F., Low, H. E., & Zhou, H. (2007, January). In situ testing for design of pipeline and anchoring systems. In *OFFSHORE SITE INVESTIGATION AND GEOTECHNICS, Confronting New Challenges and Sharing Knowledge*. Society of Underwater Technology.

Verley, R., & Lund, K. M. (1995). *A soil resistance model for pipelines placed on clay soils* (No. CONF-950695-). American Society of Mechanical Engineers, New York, NY (United States).

Wang, D., White, D. J., & Randolph, M. F. (2010). Large-deformation finite element analysis of pipe penetration and large-amplitude lateral displacement. *Canadian Geotechnical Journal*, *47*(8), 842-856.

White, D. J., & Cheuk, C. Y. (2008). Modelling the soil resistance on seabed pipelines during large cycles of lateral movement. *Marine structures*, *21*(1), 59-79.White, D. J., & Randolph, M. F. (2007). Seabed characterisation and models for pipeline-soil interaction. International Journal of Offshore and Polar Engineering, 17(03).

Yafrate, N., DeJong, J., DeGroot, D., & Randolph, M. (2009). Evaluation of remolded shear strength and sensitivity of soft clay using full-flow penetrometers. *Journal of Geotechnical and Geoenvironmental Engineering*, *135*(9), 1179-1189.

8. CYCLIC LOADING OF PIPELINES/RISERS IN COHESIVE SOILS

8.1. Introduction

Pipelines that are laid on the seabed experience external hydrodynamic loading and other forces from the internal temperature and pressure. This external hydrodynamic loading is minimal in deep water, but can be significant in shallow water. Episodes of heating and cooling lead to longitudinal expansion-cycles in the pipe, with pipe buckling occurring during the former. Excessive buckle amplitude may lead to high bending strains in the pipe section and the accumulation of fatigue damage through the pipeline operating life. High bending strain in the pipe section and the accumulation of fatigue through the pipeline operating life is a significant issue related to excessive buckling (Chatterjee et al. 2012).

The pipe penetrates into the soil due to multiple factors (e.g. self-weight and dynamic movements) (Randolph and White, 2008). Due to the lateral movement, the pipe either rises or dives depending on its own weight relative to the current bearing capacity (Chatterjee et al. 2012; Zhang et al. 2002).

There are some empirical expressions for lateral resistance, and the subsequent steady residual resistance is a result of experimental investigations. These methods are commonly used in practice, but they are subject to significant scatter factors and uncertainty (Chatterjee et al, 2012). An expanded database can serve to reduce the level of uncertainty.

In the past several years, the industry has been pushing the limit of steel catenary risers (SCRs) applicability to relatively shallow regions, where the out-of-plane fatigue damage experiences an increase that requires more sophisticated modeling of the SCR-soil interaction in the lateral direction.

Figure 8.1 illustrates a typical *H-u* behavior (where *H* is lateral resistance and *u* is lateral displacement). The “backbone curve” corresponds to the initial lateral movement of the pipe into the soil. Both monotonic and cyclic *H-u* curves are commonly derived from single-gravity laboratory model tests, where a short segment of pipe is pushed into the soil testbed and subjected to a series of lateral movement cycles of interest. Although random loading sequences occur in the field, laboratory model tests usually impose either displacement-controlled cyclic loading, where the pipe is repeatedly re-swept to a lateral distance of u_1, or force-controlled cyclic loading, where the pipe is repeatedly re-swept to the point at which a soil resistance H_1 mobilizes. Since the movement of the SCR close to the seabed is mainly imposed from the global motion of the platform, displacement-controlled tests are more appropriate for the fatigue assessment after a large number of load cycles (Chen et al. 2019, 2019a).

This study presents the findings of a series of single-gravity laboratory model tests on a “rigid” pipe, and investigates *H-u* behavior for pipelines/SCRs in high plasticity Gulf of Mexico (GOM) clay. Two series of tests, as well as multiple T-bar and miniature vane shear tests, are performed in this study. Monotonic and cyclic tests are conducted under displacement-controlled loading for the first and second series of tests. The displacement-controlled loading is applied to the horizontal direction, and the pipe is released (constant vertical load) from the vertical direction.

The pipe model is fabricated to be a rigid steel pipe section with a diameter of D of 50.8 mm (2 inches) and a length of L of 304.8 mm (12 inches). A high plasticity GOM clay, with undrained shear strength corresponding to normally consolidated conditions, is used in this study to represent the seabed at TDZ. The vertical monotonic tests are conducted at the beginning of the program to obtain the vertical loading resistance with depth at different rate effects and to compare it with other existing results. These results are compared to existing models before proceeding with lateral monotonic and cyclic loading tests. The study investigated the following aspects of soil-riser interaction: (1) the effect of riser embedment depth w over a range of lateral cyclic amplitudes $\Delta u_{cyc}/D \sim 0.15\text{-}0.5$, (2) lateral resistance degradations as a function of load cycle under cyclic displacement amplitudes in the range $\Delta u_{cyc}/D = 0.15\text{-}0.5$, and (3) the shape of trenches and berms, which formed during the lateral (zig-zag) movement with different embedment depths. Cyclic displacement amplitudes Δu_{cyc} refer to one-half of the difference between maximum and minimum displacements.

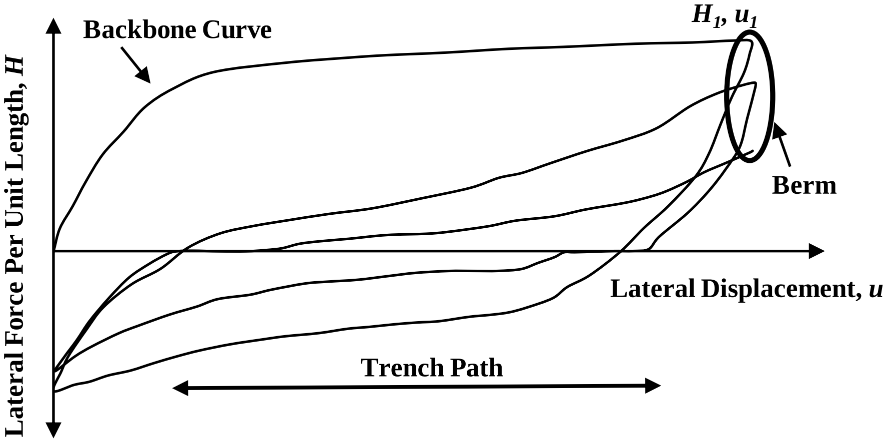

Figure 8.1 *H-u* Behavior of Steel Catenary Riser (SCR).

8.2. The Properties of The Seabed Model

A discussion of the soil test bed properties is explained in detail in Chapter 2.

8.3. Test Equipment

The following discussion describes the test equipment that is used in the experiments, which includes the test basin for conducting the tests, the model riser pipe segment, the loading frame, the motor, the sensors, and the data acquisition system. Further details can be found in Chapter 1.

8.4. Test Program

Two series of tests in total are carried out. Series 1 (Table 8.1) introduced small, medium, and large zig-zag monotonic tests and cyclic displacement amplitude tests (displacement amplitudes ($\Delta u_{cyc}/D$) refer to half of the range from peak to trough). Test 1a in Table 8.1 involved initial penetration w/D of 0.3, then released the vertical restriction, and followed by lateral monotonic movement u/D of 0.3. After that, Test 2b is conducted, which included 50 lateral cyclic loading amplitudes of $\Delta u_{cyc}/D$ ~ 0.15. Subsequently, Test 2c is conducted by moving the pipe laterally into u/D ~ 0.5. Afterward, another set of 50 cycles of $\Delta u_{cyc}/D$ ~ 0.25 (Test 2d) is applied into the pipe. After finishing Test 2d, Test 2e is carried out by moving the pipe horizontally into u/D ~ 1.0. Finally, Test 2f is performed by applying 50 load cycles in the pipe for displacement amplitudes of $\Delta u_{cyc}/D$ ~ 0.5. The vertical restriction of the pipe is freed (unlocked) after penetrating the pipe to a depth of 0.3D (Test 1a) to allow the pipe to sink, while moving laterally for the entire series 1. After reaching the new embedment depth, series 2 is conducted. The same exact procedure of series 1 is followed, but the movements are in the opposite direction as shown in Figure 8.2. In addition, multiple T-bar and miniature vane shear tests are conducted to establish the undrained shear strength profile, as well as the relationship between the water content and the undrained shear strength.

The motion rate is fixed at 1.5 mm/sec for the entire test program. Figure 8.2 shows sketches of the series 1 and series 2 of the test program starting at penetration depth of 0.3 D and penetrating deeper.

Table 8.1 Series 1 and Series 2: Summary of Zig-Zag Loading Tests.

Test	Velocity	Test Description	No. of cycles	Notes
1a	1.5 mm/sec	Penetrated into w/D=0.3 and laterally swept for u/D= 0.3 with free vertical restriction.		Constant vertical load
1b		After Test 1a, the pipe returned to its original position and 1-way lateral displacement $\Delta u_{cyc}/D$ of ~ 0.15 for 50 cycles is applied.	50	
1c		After Test 1b, monotonic lateral displacement y of ~ 1.0 D is applied.		
1d		After Test 1c, the pipe is returned to original position and 50 lateral cyclic amplitudes $\Delta u_{cyc}/D$ of ~ 0.25 is applied	50	
1e		After Test 1d, monotonic lateral displacement of ~ 1.0 D is applied.		
1f		After Test 1e, the pipe is returned to original position and 50 lateral cyclic amplitudes $\Delta u_{cyc}/D$ of ~ 1.0 is applied.	50	

Table 8.1 Continued.

Test	Velocity	Test Description	No. of cycles	Notes
2a	1.5 mm/sec	After finishing Test 1f, the pipe is laterally swept in the opposite direction for $y = 0.3\ D$ with free vertical restriction.		Constant vertical load
2b		After Test 2a, the pipe returned to its original position and 1-way lateral displacement $\Delta u_{cyc}/D$ of ~ 0.15 for 50 cycles is applied.	50	
2c		After Test 2b, monotonic lateral displacement y of ~ 1.0 D is applied.		
2d		After Test 2c, the pipe is returned to original position and 50 lateral cyclic amplitudes $\Delta u_{cyc}/D$ of ~ 0.25 is applied	50	
2e		After Test 2d, monotonic lateral displacement of ~ 1.0 D is applied.		
2f		After Test 2e, the pipe is returned to original position and 50 lateral cyclic amplitudes $\Delta u_{cyc}/D$ of ~ 1.0 is applied.	50	

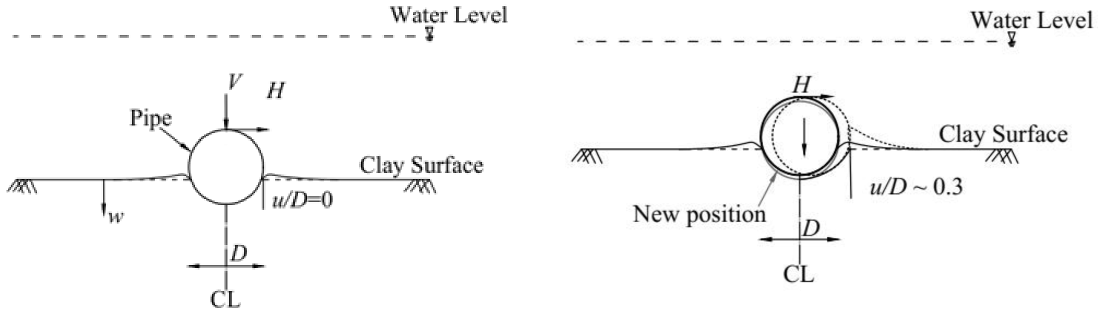

a) General sketch shows test program with nomenclature.

b) Test 1a, *u/D* ~ 0.3 with initial *w/D* = 0.3 *D*.

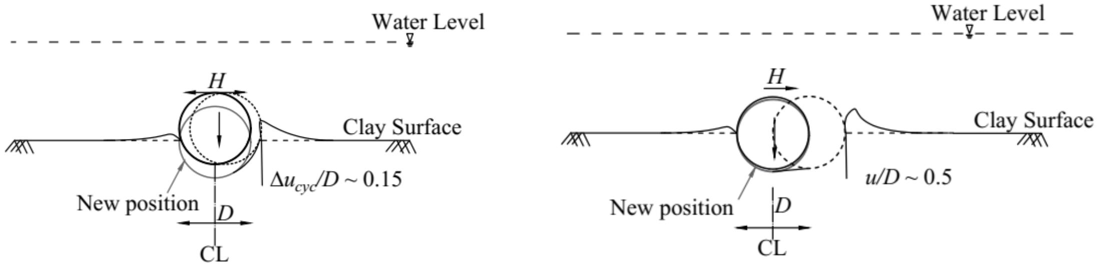

c) Test 1b, $\Delta u_{cyc}/D$ ~ 0.15, new *w/D* = 0.49.

d) Test 1c, *u/D* ~ 0.5.

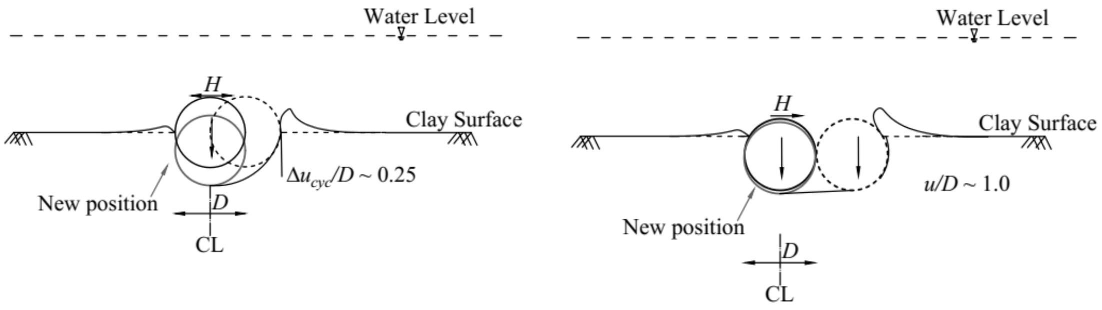

e) Test 1d, $\Delta u_{cyc}/D$ ~ 0.25, new *w/D* = 0.757.

f) Test 1e, *u/D* ~ *1.0.*

Figure 8.2 General sketch shows series 1 and series 2 with nomenclature.

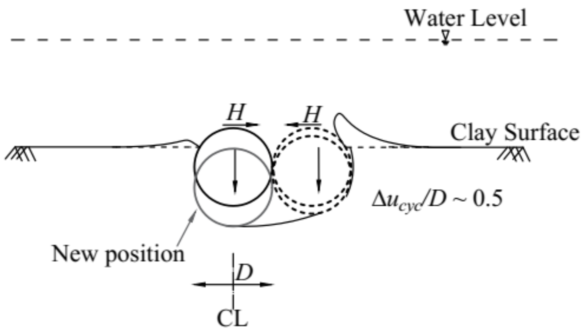

g) Test 1f, $\Delta u_{cyc}/D \sim 1.0$, new $w/D = 1.07$.

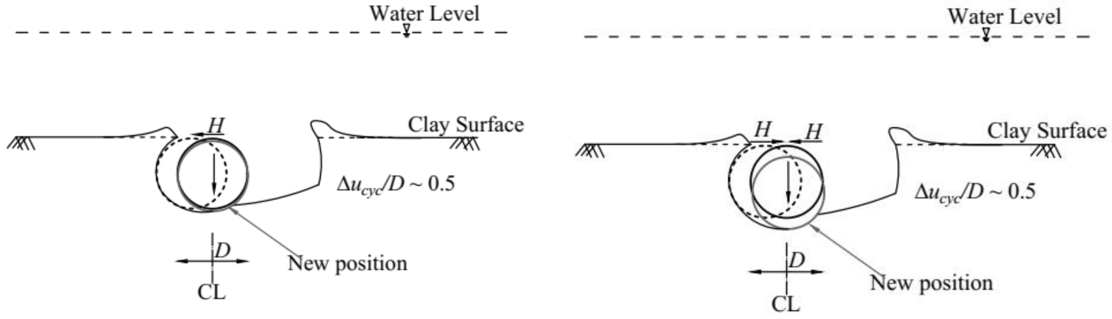

h) Test 2a, $u/D = 0.3$.

i) Test 2b, $\Delta u_{cyc}/D \sim 0.15$, new $w/D = 1.167$.

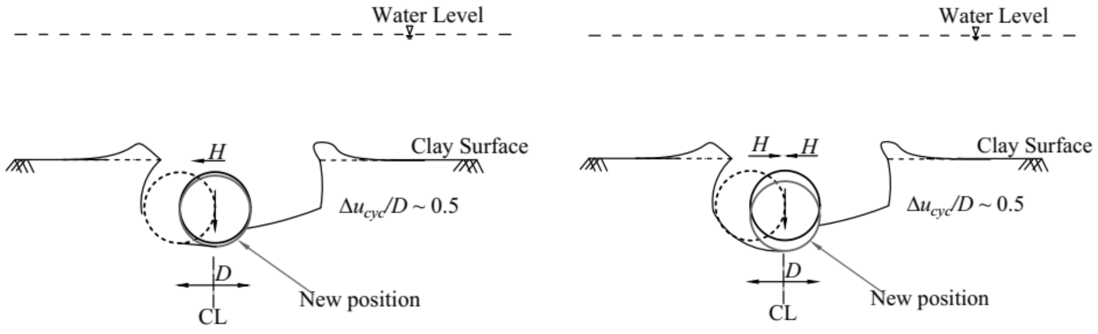

j) Test 2c, $u/D \sim 0.5$.

k) Test 2d, $\Delta u_{cyc}/D \sim 0.25$, new $w/D = 1.316$.

Figure 8.2 Continued.

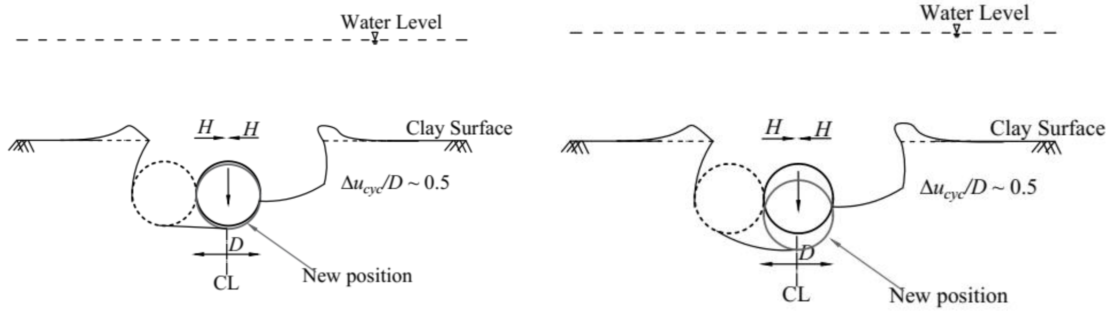

l) Test 2e, *u/D* ~ 1.0.

m) Test 2f, $\Delta u_{cyc}/D$ ~ 0.5, new *w/D* = 1.525.

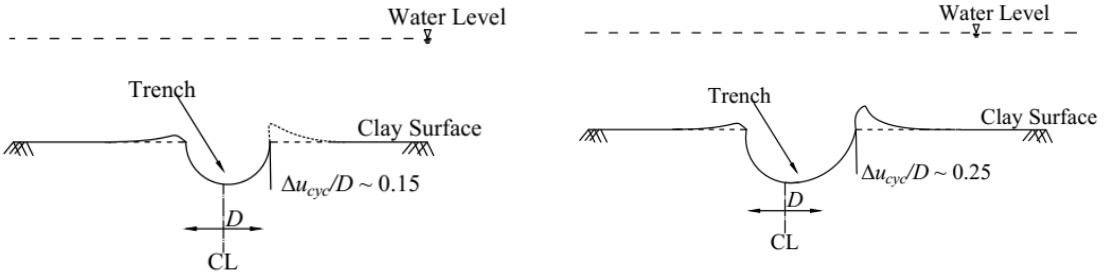

n) Trench after Test 1b, new *w/D* = 0.49.

o) Trench after Test 1d, new *w/D* = 0.757.

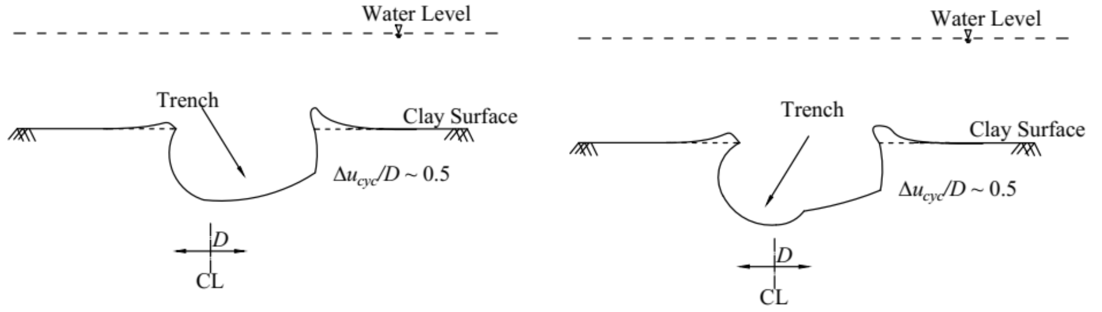

p) Trench after Test 1f, new *w/D* = 1.07.

q) Trench after Test 2b, new *w/D* = 1.167.

Figure 8.2 Continued.

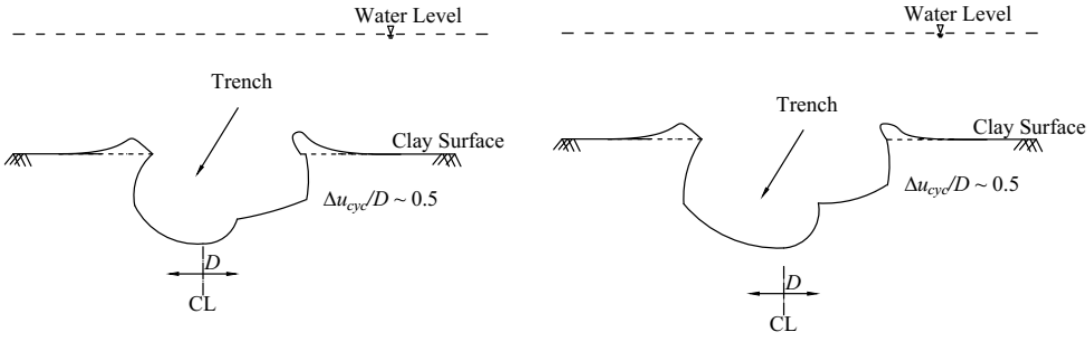

r) Trench after Test 2d, new *w/D* = 1.316. **s) Trench after Test 2f, new *w/D* = 1.525.**

Figure 8.2 Continued.

From Figure 8.2 a, *w* is embedment of the pipe from the surface of the soil, *H* is the horizontal force per unit length, *V* is the vertical force per unit length, *D* is the pipe diameter, and *u* is the lateral movement from the front face of the pipe.

a) Test 1a. **b) Test 1a.**

Figure 8.3 Photographs are taken during testing.

c) Test 1b. **d) Test 1d**

e) Test 2a **f) Test 2f**

g) After finishing the zig-zag test program

Figure 8.3 Continued.

8.5. Results and Data Interpretation

In the following sections, the findings of the entire test program will be explained in detail.

8.5.1. Series 1 and Series 2: Zig-zag Loading Tests

Series 1 is conducted under applying controlled displacement of 1.5 mm/sec in the lateral direction while releasing the vertical restriction to permit the pipe settle under its own weight during the lateral movements, introducing the zig-zag motions. These tests aimed to measure the horizontal resistance, monitor the shape of the trenches and berms formed during zig-zag movements, and find the new embedment depths, *w/D* after each test.

8.5.1.1. Series 1 (Test 1a): Backbone Curve, *u/D* ~ 0.3 and *w/D* = 0.3

Usually, laying pipelines on seabed causes initial embedment due to their weight plus additional embedment caused by dynamic motions. The test pipe is embedded to a depth of 0.3 to simulate the initial vertical penetration. After that, the vertical restriction that connects the pipe to the loading system is released. Finally, a lateral displacement *u/D* ~ 0.3 is applied into the riser. Figure 8.4 (Test 1a) shows the backbone curve with the lateral resistance. After finishing Test 1a, the riser is dragged back to the centerline *u/D* = 0.0 as shown in Figure 8.2b. A trench of ~ 0.3 *D* is formed as a result of Test 1a. The vertical displacement is recorded using a precise laser displacement sensor.

8.5.1.2. Series 1 (Test 1b): Small Zig-zag Cyclic Amplitude $\Delta u_{cyc}/D$ ~ 0.15 and w/D = 0.3

The pipe is penetrated to a depth of $w = 0.3\ D$ with normalized ultimate resistance V_{max}/Ds_{u0} of ~ 4.5. The operating loads V_{op}/Ds_{u0} is about 0.5, which simulate light pipes. The initial overpenetration ratios $R = V_{max}/V_{op} = 6$.

In Test 1b, the riser is subjected to one-way of 50 load cycles of a small cyclic amplitude $\Delta u_{cyc}/D$ ~ 0.15 D. Figure 8.4 shows the lateral resistance of the backbone curve and the lateral resistance of the cyclic loading for $\Delta u_{cyc}/D$ ~ 0.15. A complete cycle shows a banana shape, which also is noticed in the lateral cyclic loading (Chapter 7). For the first few cycles, the pipe tends to rise consistent with the typical behavior of light pipes (Wang et al. 2010). Continuing towards more cycles, the pipe tends to move downward as shown in Figure 8.7. That can be attributed to two mechanisms: 1) trenching and 2) softening.

Trenching is where the soil is pushed aside due to the lateral movements. Softening is where dynamic pipe motion remolds the soil around the pipe. That leads to reduce bearing capacity as a result of the reduction in soil strength. These two mechanisms help to increase the pipe embedment depth. The lateral resistance drops sharply for the swept area (trench path) because the soil is swept to the other side and a berm is formed as shown in Figure 8.2c. From Figure 8.4, the resistance at the trench (u/D ~ 0.15) is reduced by about 70% (between the backbone curve and the first load cycle). Furthermore, it can be seen clearly that the resistance at the beginning of the trench (both directions of movements) approaches zero (because all the soil is swept to the other side during the movements), but it picks up some resistance while moving inside the trench because of the zig-zag movements. The pipe starts to sink while moving in the lateral direction. That can be seen as well when the pipe leaves the berm. This behavior is also noticed for the suction resistance.

Some similarities and comparisons between lateral cyclic loading in (Chapter 7) (Test 3a-d)) and series 1 (Test 1a) can be concluded From Chapter 7 and Figure 8.4 as follows:

1. A complete cycle shows a banana shape for both series.
2. The steady state for Test 3a-d of Chapter 7 is reached at the wake of the trench at a lateral resistance of about zero (after about 10 cycles), but the steady state for Test 1a is reached (after about 15 cycles) with non-zero lateral resistance because of the zig-zag loading.

The resistance at the berms (Figure 8.4) is reduced by about 46% during the first 10 cycles. After the first 10 load cycles, the resistance continues to decrease, but at a reduced rate to reach the steady-state at about 15 cycles as shown in Figure 8.4. This reduction in resistance is due to multiple reasons: 1) softening and remolding the soil by increasing the number of cycles, causing the reduction in the undrained shear strength (Al-Janabi and Aubeny 2019; Al-Janabi et al., 2019; 2019a), and 2) soil erosion as evidenced by cloudy waves arising when the pipe touched the soil berm. In other words, the soil erosion (scour) occurs during the cyclic loading (see

Figure 8.3). The pipe sank for 9.72 mm. The new dimensionless embedment depth (*w/D*) is ~ 0.49.

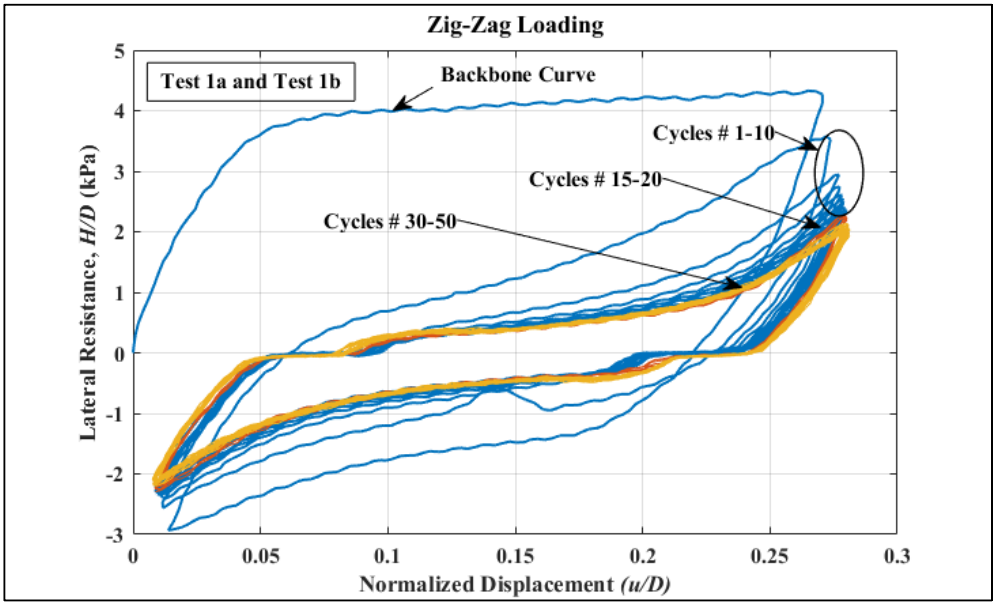

Figure 8.4 Backbone curve and hysteresis cycles (zig-zag loading).

8.5.1.3. Series 1 Test 1c: Monotonic tests (*u* ~ 0.5 D), new *w/D* ~ 0.49

The new embedment depth after Test 1b is 0.49 *D*. The pipe is kept unlocked and Test 1c is conducted by moving the pipe laterally into 0.5 *D* as shown in Figure 8.5. It is clear from Figure 8.5 that the lateral resistance of the backbone curve starts from negative resistance because Test 1c is conducted directly after 5b. The backbone curve tends to relax because of the trench forming as it is noticed in Lateral cyclic loading tests in Chapter 7.

8.5.1.4. Series 1 Test 1d: Medium zig-zag cyclic amplitudes $\Delta u_{cyc}/D$ ~ 0.25, *w/D* = 0.49

After conducting Test 1a, the pipe is returned to the starting point *u/D* = 0.0 and Test 1b is conducted. 50 load cycles are applied into the pipe with a small cyclic amplitude $\Delta u_{cyc}/D$ of ~ 0.15. The zig-zag loading led to trench formation as shown in Figure 8.2e.

Since there is no vertical restriction, the pipe sank deeper into the soil. From Figure 8.5, it can be seen that the lateral resistance drops to about 63% at *u/D* = 0.25 between the backbone curve and the first load cycle. Furthermore, it is clear that the resistance at the beginning of the cycles (both directions of movements) approaches zero (because all the soil swept to the other side during the movements), but it picks up some resistance while moving inside the trench. This behavior is similar to Test 1b. The steady-state is reached after about 15 cycles as shown in Figure 8.5. At the end of this test, the embedment depth *w/D* is ~ 0.757.

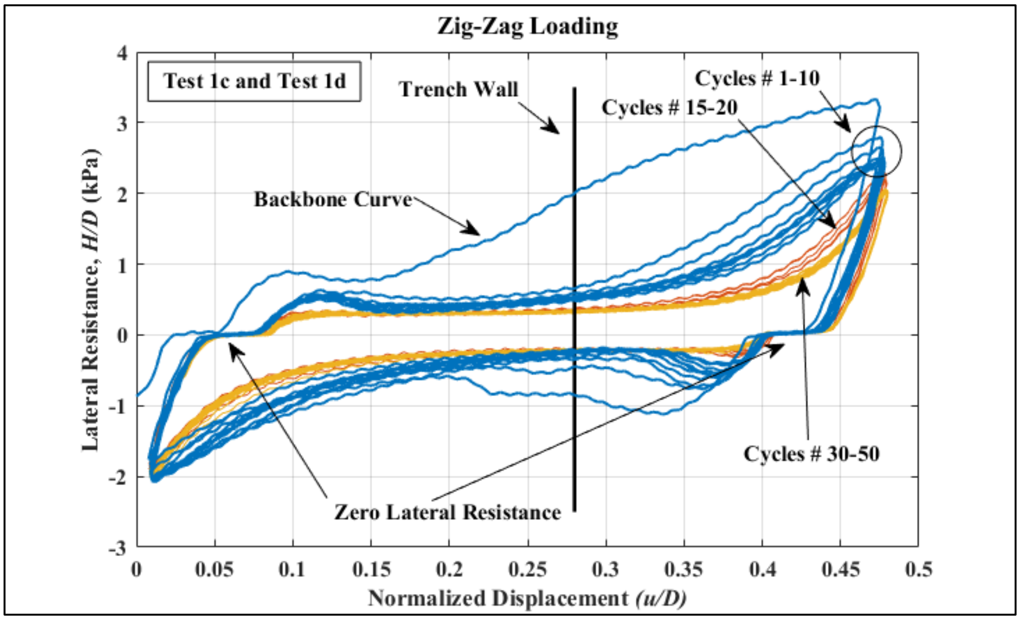

Figure 8.5 Backbone curve and hysteresis cycles (zig-zag loading).

8.5.1.5. Series 1 Test 1e: Large Lateral Monotonic *u/D* of ~ 1.0, new *w/D* = 0.757

After conducting Test 1d, Test 1c is conducted. The riser model is subjected to horizontal displacement *u/D* of ~ 1.0 (lateral direction) and its own weight (vertical direction). At the end of this test, the pipe is at the zero position and the new vertical embedment is recorded.

8.5.1.6. Series 1 Test 1f: Large zig-zag cyclic loading tests amplitudes $\Delta u_{cyc}/D$ ~ 0.5, w/D ~ 0.757

Another 50 load cycles are applied into the riser (Test 1f) with large lateral displacement amplitudes $\Delta u_{cyc}/D$ of ~ 0. 5 (Table 8.1). The testing produce of the series 1 led to the formation of a wide, deep trench as shown in Figure 8.2g. Figure 8.6 shows that the lateral resistance drops to about 36% at $u/D = 0.5$ (between the backbone curve and the first load cycle). At the end of this test, the entire pipe is covered by soil and the new embedment depth w/D is 1.07. Figure 8.11 shows the reduction in the lateral resistance at the berm while increasing the number of cycles. A minimum resistance occurred at about ~ 15 cycles. After that, soil resistance began to increase under continued cyclic loading, possibly due to the pipe penetrated into the soil while moving laterally. This behavior occurred for the large cyclic amplitudes $\Delta u_{cyc}/D$ of ~ 0. 5 as shown in Figure 8.10.

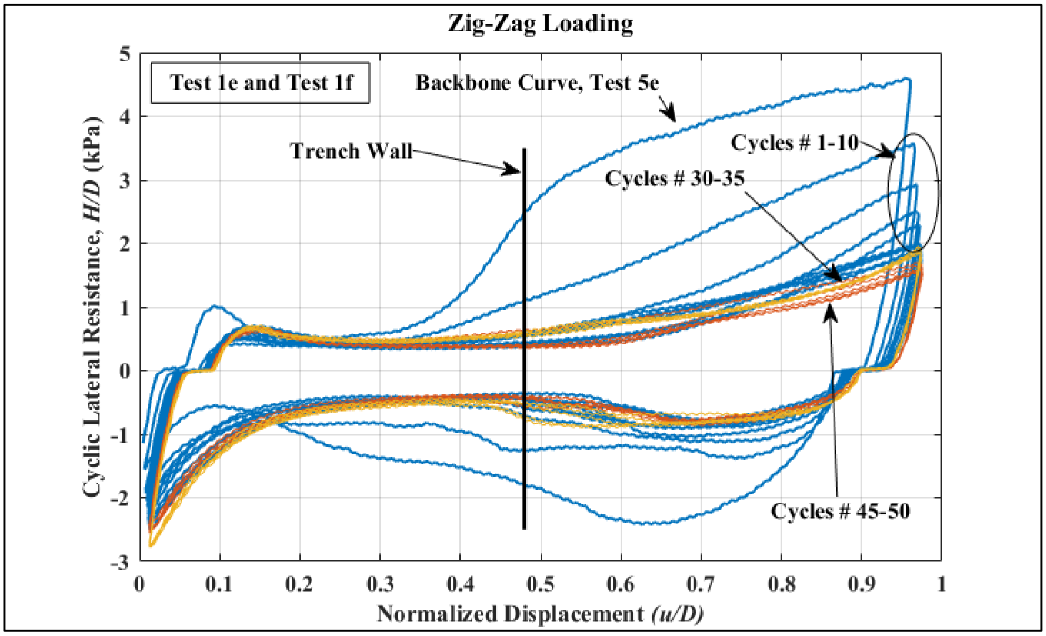

Figure 8.6 Backbone curve and hysteresis cycles (zig-zag loading).

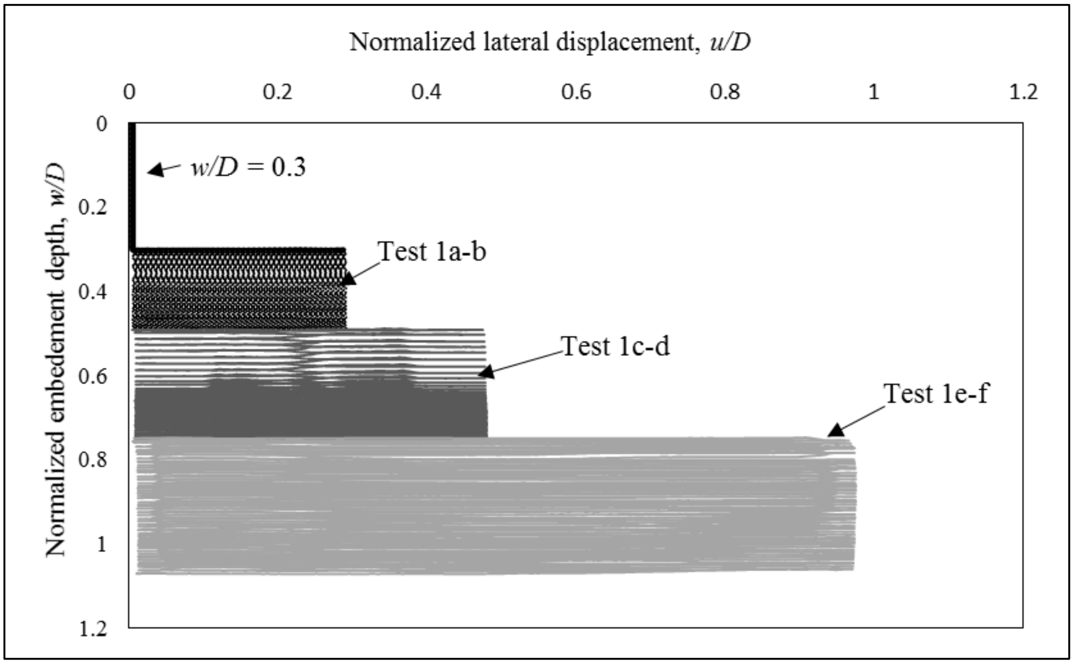

a) Pipe invert trajectory vs. normalized lateral displacement.

Figure 8.7 Pipe trajectory (series 2).

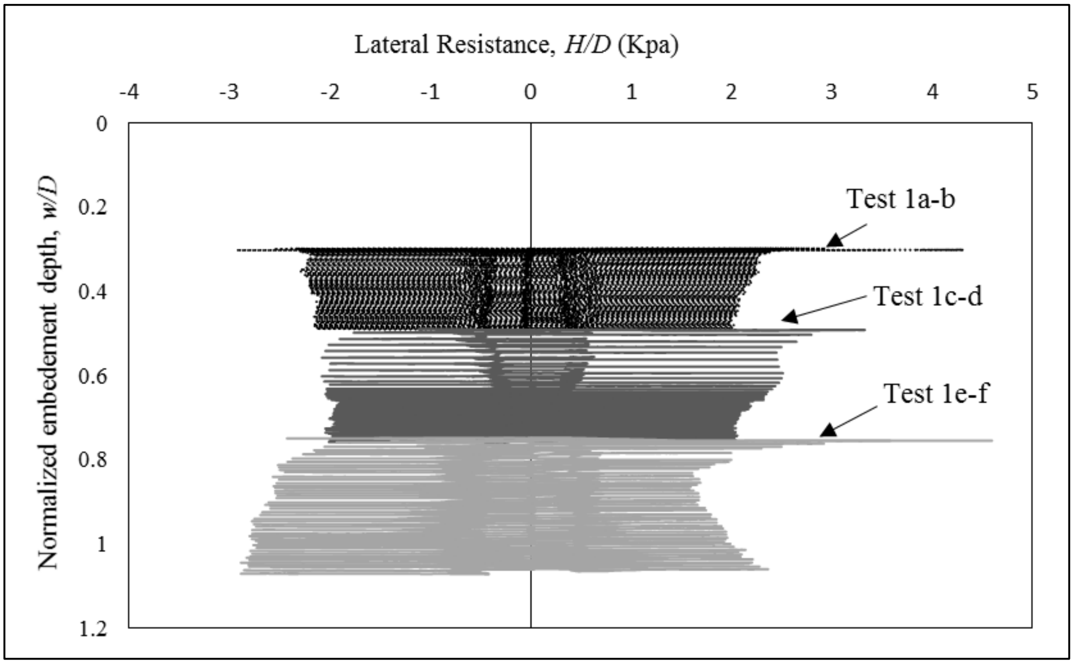

b) Pipe invert trajectory vs. lateral resistance.

Figure 8.7 Continued.

8.5.2. Series 2: Zig-zag Loading

Six tests in total are carried out in series 2. the same exact procedure of series 1 is followed but in the opposite direction. After finishing tests 5f of series 1, the new embedment depth is 1.07.

8.5.2.1. Series 2 (Test 2a): Backbone Curve, *u/D* ~ 0.3 and New *w/D* = 1.07

After conducting Test 1f of series 1, Test 2a is conducted in the opposite direction (~ 0.3 *D*).

The pipe is embedded to a depth of 1.07 due to Test 1f. After that, the vertical restriction that connects the pipe to the system is released. Figure 8.8 (Test 2a) shows the backbone curve with the lateral resistance. After finishing Test 2a, the riser is dragged back to the centerline *u/D* = 0.0 as shown in plot (b) of Figure 8.2h and Figure 8.3e.

8.5.2.2. Series 2 (Test 2b): A Small Zig-zag Cyclic Amplitude $\Delta u_{cyc}/D$ ~ 0.15, w/D ~ 1.07

The riser is subjected to 1-way of 50 load cycles of a small cyclic amplitude $\Delta u_{cyc}/D$ ~ 0.15 D. For the first few cycles, the pipe tends to rise due to the behavior of light pipes. Continuing towards more cycles, the pipe tends to move downward for the reason explained previously as shown in Figure 8.12. Figure 8.8 shows the lateral resistance of the backbone curve and the lateral resistance of the cyclic loading for $\Delta u_{cyc}/D$ ~ 0.15. Figure 8.4 and Figure 8.8 show that the reduction in soil resistance during cyclic loading is greatest at shallow depths and decreases somewhat with increasing penetration. For example, the resistance is reduced by about 70% and 57% for penetration depths 0.3 D and 1.07 D, respectively between the backbone curve and the first load cycle at u/D = 0.15. The pipe sank for 4.91 mm. The new dimensionless embedment depth w/D ~ 1.17.

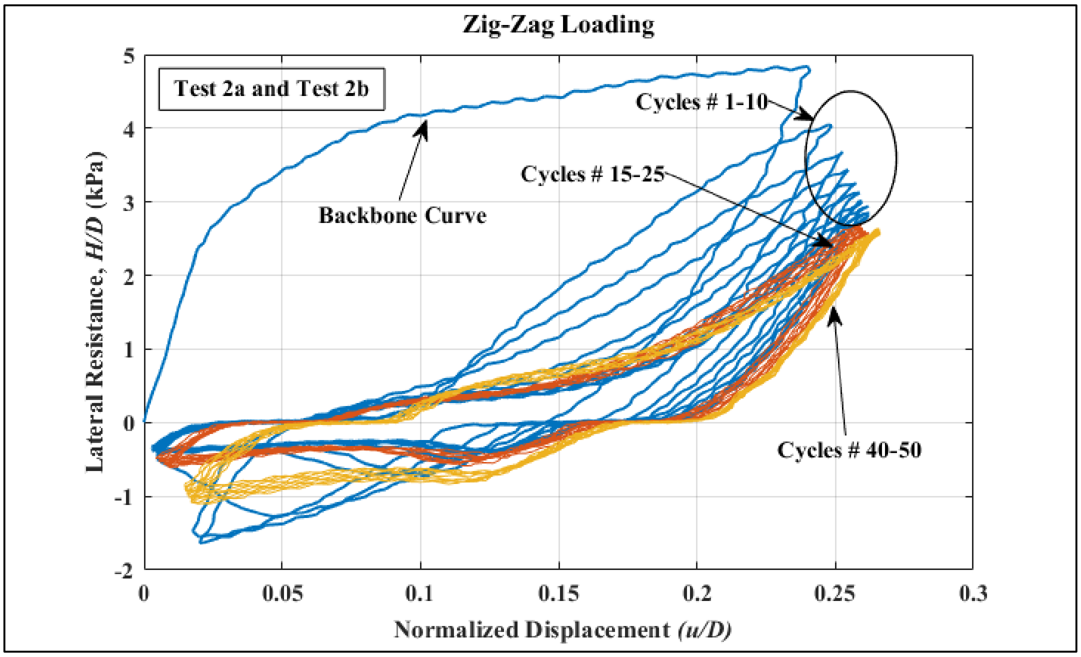

Figure 8.8 Backbone curve and hysteresis cycles (zig-zag loading).

8.5.2.3. Series 2 Test 2c: Monotonic tests (y ~ 0.5 D), new w/D = 1.167

Figure 8.9 shows behavior similar to series 1, but with greater mobilized lateral resistance, Likely due to the greater embedment depths.

8.5.2.4. Series 2 Test 2d: Medium zig-zag cyclic amplitudes $\Delta u_{cyc}/D$ ~ 0.25, *w/D* = 1.167

50 load cycles are applied into the riser with a small cyclic amplitude $\Delta u_{cyc}/D$ of ~ 0.15. Figure 8.5 and Figure 8.9 show that the reduction in soil resistance during cyclic loading is greatest at shallow depths and decreases somewhat with increasing penetration. For example, the resistance reduces by about 63% and 45% for penetration depths 0.49 *D* and 1.167 *D*, respectively, between the backbone curve and the first load cycle at *u/D* = 0.3. The pipe sank 7.595 mm, corresponding to a dimensionless embedment depth *w/D* ~ 1.316.

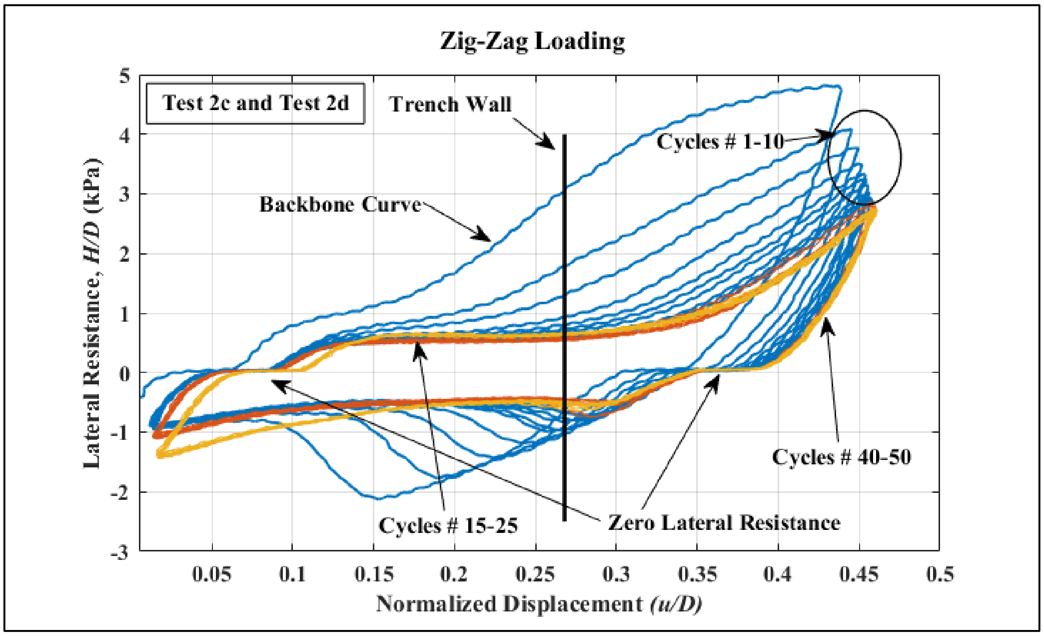

Figure 8.9 Backbone curve and hysteresis cycles (zig-zag loading).

8.5.2.5. Series 2 Test 2e: Large Lateral Monotonic u/ D of ~ 1.0, new w/D = 1.316

The riser model is subjected to lateral displacement *u/D* of ~ 1.0. Figure 8.21 shows the trench that is formed after conducting Test 2e

8.5.2.6. Series 2 Test 2f: Large zig-zag cyclic loading tests amplitudes $\Delta u_{cyc}/D$ ~ 0.5, *w/D* = 1.316

Another 50 load cycles are applied into the riser (Test 2f) with large lateral displacement amplitudes $\Delta u_{cyc}/D$ of ~ 0. 5 (Table 7.4). Figure 8.10 shows that the lateral resistance drops to about 43% at *u/D* = 0.5 (between the backbone curve and the first load cycle). At the end of this test, the entire pipe is covered by soil and the final embedment depth *w/D* is 1.525. Behavior is similar to Test 1f, where the steady-state reached at 15 cycles. After that, the resistance started to gain some strength while increasing the number of cycles as shown in Figure 8.11.

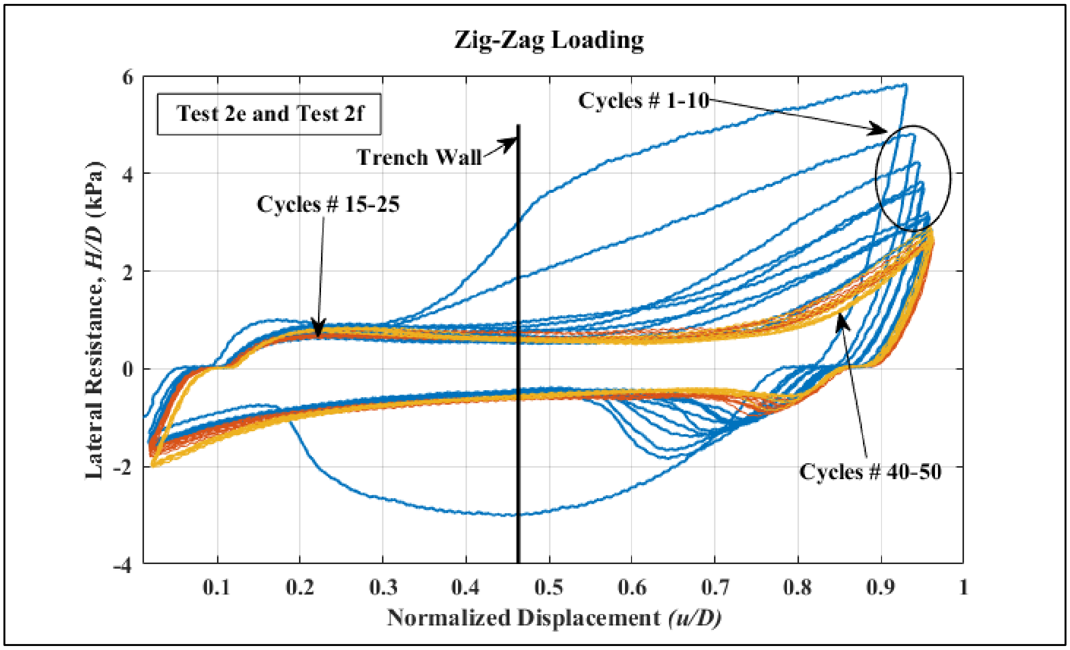

Figure 8.10 Backbone curve and hysteresis cycles (zig-zag loading).

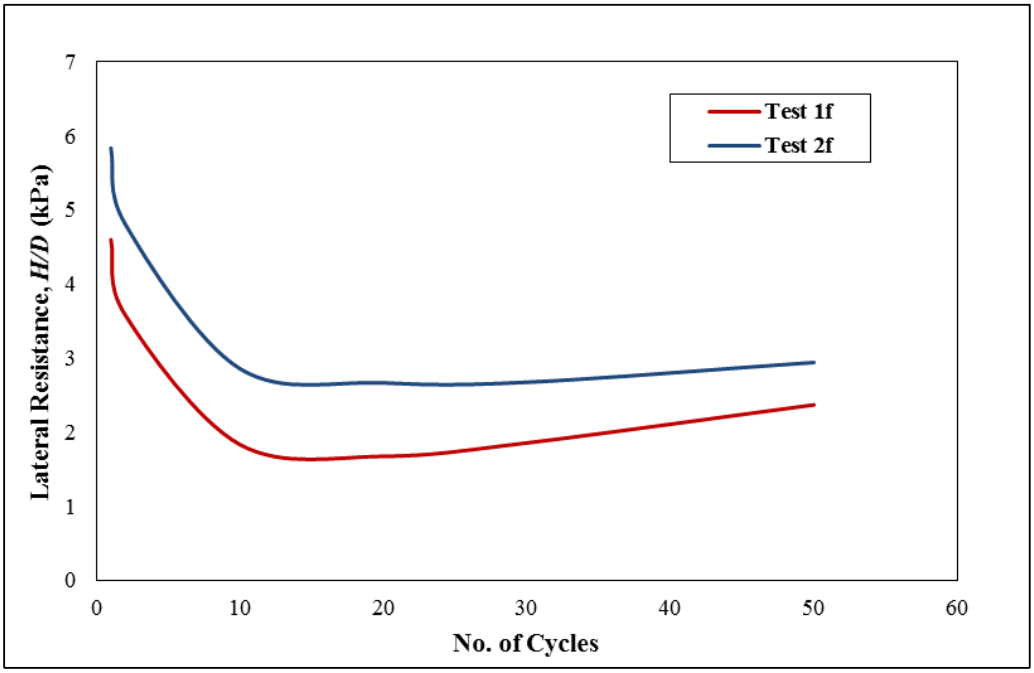

Figure 8.11 Lateral resistance vs. number of cycles Test 1f and Test 2f.

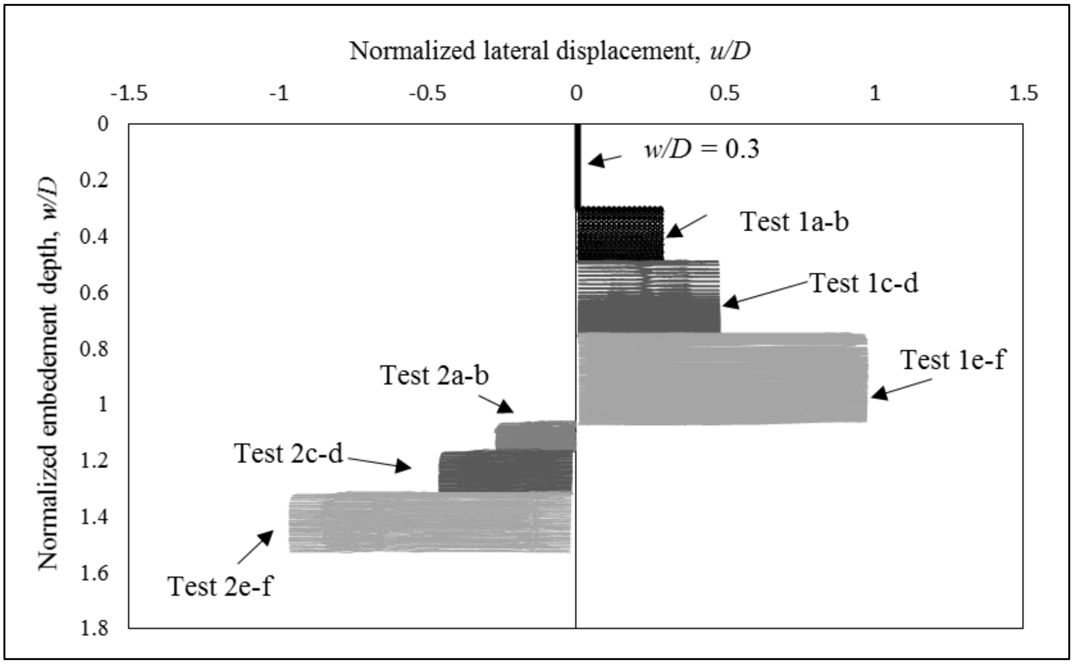

a) Pipe invert trajectory vs. normalized lateral displacement.

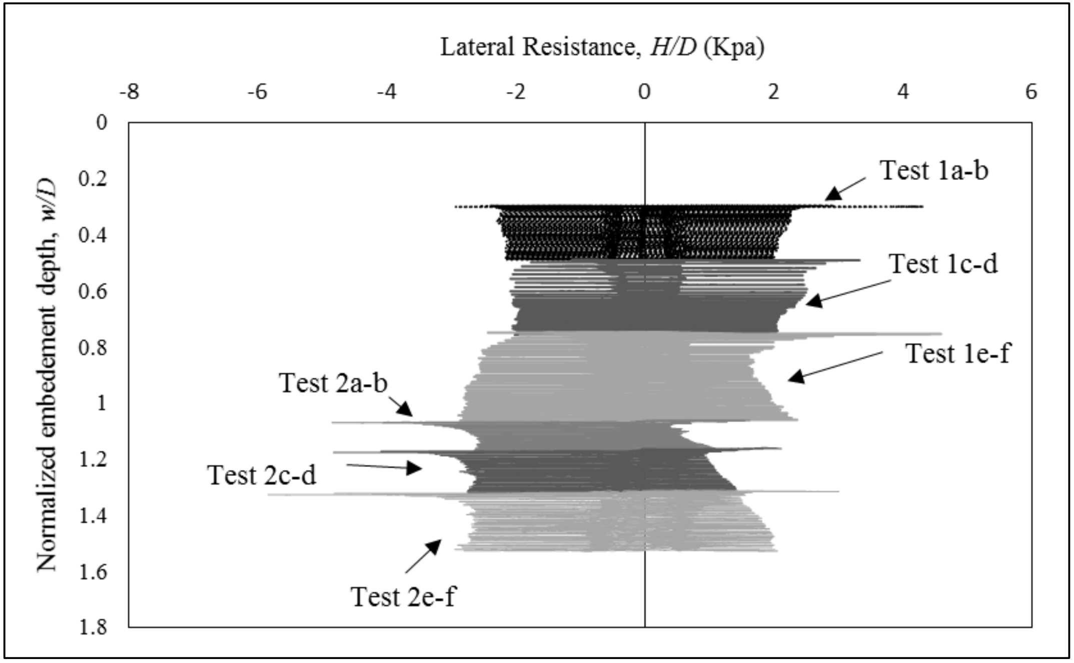

b) Pipe invert trajectory vs. lateral resistance.

Figure 8.12 Pipe trajectory (series 2-3).

8.6. Nomenclature

D	Pipe Diameter
GoM	Gulf of Mexico
H	Lateral Soil Resistance
H_1	Maximum Lateral Soil Resistance
L	Pipe Length
N	Number of Cycles
SCR	Steel Catenary Riser
s_u	Undrained Shear Strength
s_{u0}	Undrained Shear Strength at the surface
TDZ	Touch Down Zone
u	Lateral Displacement
u_1	Maximum Lateral Displacement
w	Embedment Depth
Δu_{cyc}	Lateral Cyclic Displacement Amplitude

8.7. References

Al-Janabi, H. A. & Aubeny, C. P. (2019). Experimental Measurement of Thixotropy and Sensitivity in Gulf of Mexico Clay. In The International Society of Offshore and Polar Engineers Conference, 2019-TPC-0593. Honolulu, HI, USA.

Al-Janabi, H. A., Aubeny, C. P., Chen J., Luo M. (2019a) Experimental Measurement of Monotonic and Cyclic Lateral Resistance of Steel Catenary Risers at Touchdown Zone in Gulf of Mexico Clays. Submitted to the Canadian Gerotechnical Journal.

Al-Janabi, H. A., Aubeny, C. P., Chen J., Luo M. (2019) Experimental Measurement of Touchdown Zone Stiffness for SCR in Gulf of Mexico Clay. Offshore Technology Conference, OTC-29504-MS. Houston, TX, USA.

Aubeny, C. P., Shi, H., & Murff, J. D. (2005). Collapse loads for a cylinder embedded in trench in cohesive soil. *International Journal of Geomechanics*, *5*(4), 320-325.

Bruton, D. A., White, D., Langford, T., & Hill, A. J. (2009, January). Techniques for the assessment of pipe-soil interaction forces for future deepwater developments. In *Offshore Technology Conference*. Offshore Technology Conference.

Bruton, D., White, D., Cheuk, C., Bolton, M., & Carr, M. (2006, January). Pipe/soil interaction behavior during lateral buckling, including large-amplitude cyclic displacement tests by the safebuck JIP. In *Offshore Technology Conference*. Offshore Technology Conference.

Chatterjee, S., White, D. J., & Randolph, M. F. (2012). Numerical simulations of pipe-soil interaction during large lateral movements on clay. *Géotechnique*, *62*(8), 693.

Chatterjee, S., White, D. J., & Randolph, M. F. (2013). Coupled consolidation analysis of pipe–soil interactions. *Canadian Geotechnical Journal*, *50*(6), 609-619.

Chen JB, Newlin J, Luo M, Zhang H, Hadley C and Hu S. (2019) Practice of Riser-Soil Interactions at Touch Down Zones for Steel Catenary Risers. Offshore Technology Conference, OTC-29553-MS. Houston, TX, USA.

Chen JB, Xu FB, Newlin J, Zhang H, Shuang H and Luo M. (2019a) Large Deformation Finite Element Analysis of Riser-Soil Interactions With Strain-Softening Soils. Offshore Technology Conference, OTC-29376-MS. Houston, TX, USA.

Langford, T., & Aubeny, C. P. (2008, January). Model tests for steel catenary riser in marine clay. In *Offshore Technology Conference*. Offshore Technology Conference.

Merifield, R., White, D. J., & Randolph, M. F. (2008). The ultimate undrained resistance of partially embedded pipelines. *Géotechnique*, *58*(6), 461-470.

Randolph, M. F., & White, D. (2008, May). Pipeline embedment in deep water: processes and quantitative assessment. In *Offshore Technology Conference*. Offshore Technology Conference.

Verley, R., & Lund, K. M. (1995). *A soil resistance model for pipelines placed on clay soils* (No. CONF-950695-). American Society of Mechanical Engineers, New York, NY (United States).

Wang, D., White, D. J., & Randolph, M. F. (2010). Large-deformation finite element analysis of pipe penetration and large-amplitude lateral displacement. *Canadian Geotechnical Journal*, *47*(8), 842-856.White, D. J., & Cheuk, C. Y. (2008). Modelling the soil resistance on seabed pipelines during large cycles of lateral movement. *Marine structures*, *21*(1), 59-79.

White, D. J., & Cheuk, C. Y. (2008). Modelling the soil resistance on seabed pipelines during large cycles of lateral movement. *Marine structures*, *21*(1), 59-79.

Yafrate, N., DeJong, J., DeGroot, D., & Randolph, M. (2009). Evaluation of remolded shear strength and sensitivity of soft clay using full-flow penetrometers. *Journal of Geotechnical and Geoenvironmental Engineering*, *135*(9), 1179-1189.

Zhang, J., Stewart, D. P., & Randolph, M. F. (2002). Modeling of shallowly embedded offshore pipelines in calcareous sand. *Journal of geotechnical and geoenvironmental engineering*, *128*(5), 363-371.

Murff, J. D., Wagner, D. A., & Randolph, M. F. (1989). Pipe penetration in cohesive soil. *Géotechnique*, *39*(2), 213-229.

9. CONCLUSION

9.1. Experimental Measurement of Thixotropy and Sensitivity in Gulf of Mexico Clay

Cyclic full-flow penetrometer (T-bar penetrometer) and miniature vane shear tests are performed at Texas A&M University in high plasticity Gulf of Mexico clay to evaluate its thixotropic properties. This thrust area has evaluated the thixtropy strength regain, and acquired sensitivities using two different methods to estimate the T-bar remolded bearing factor under a prolonged period of time of about 4 months using two different apparatus. The test program adds to the database evaluating the influence of thixotropy effect with time. The findings on strength recovery are particularly important, as this has been a major source of uncertainty in prior investigations due to the short in database. The finding of this study can be concluded as:

1. The net penetration resistance of the T-bar penetrometer (Equation 4.1) is about 2.5-3% less in resistance than the measured penetration resistance. This agrees with Yafrate et al. (2009).
2. The degradation in resistance varies depending on curing time of curing, and sensitivity as shown in plot (a) and (b) of Figure 4.24.
3. The greatest resistance degradation is in the first few cycles. This degradation continues to slightly decrease to reach an apparent steady-state after about 5-10 cycles. This trend is observed in both this study and previous studies as shown in plot (a) and (b) of Figure 4.24.

4. For T-bar tests, the gain in strength due to thixotropy effect under a long-time period is about 0 to 30% during the first day and it continues to increase sharply to about 45% for the first 6 days. That increment keeps increasing gradually to reach about 78% after 114 days T-bar tests.
5. For miniature vane shear tests, the gain in strength due to thixotropy under prolonged time is about 23% to 30% for the first few hours ~3 hours to 24 hours. After 30 days, the gain in strength continues to increase to reach about 81% at 112 days.
6. For the sensitivity:
   - a- For T-bar tests, the acquired sensitivity after a specific time (AS_t) is predicted. The gain in strength using the T-bar penetrometer continues to increase after 114 days. However, a future study to cover more curing time will be necessary.
   - b- For vane shear tests, the acquired sensitivity after time ($AS_{t(MVT)}$) is predicted as well, but it has been noticed that there is a small increment in the strength after 30 days. Therefore the sensitivity from MVT is predicted to be ~ 1.81 and it is used to evaluate the remolded T-bar factor $N_{T\text{-}bar(r)}$ using Equation 4.8.

Acquired sensitivity using Equation 4.8 as Yafrate et al. (2009) suggested, gives a very good fit with the MVTs data. Therefore, the correction from Equation 4.8 should be considered. In a future study, Equation 4.8 might be adjusted after obtaining additional data.

9.2. Experimental and Numerical Investigation of The Performance of Piles and Suction Caissons Subjected To Inclined Cyclic Loading in Cohesive Soils

The paper has presented 1-g model tests in fine-grained soil (Gulf of Mexico clay) as a means for calibrating the constitutive model (nonlinear kinematic hardening model) where the calibrated model was match to monotonic and cyclic lateral and vertical loading tests as well as pullout tests. This calibrated model can be a benchmark to investigate the accumulative displacements of pile and caissons due to vertical, lateral, and inclined loads, and a parametric study using a 3-*D* finite element model using non-uniform load amplitudes. The study was conducted to evaluate 1) the lateral and vertical resistance of monotonic loading as well as the pullout resistance 2) the degradation of the lateral and vertical resistance with an increasing number of cycles, and 3) the plastic deformations using non-uniform load amplitudes for different aspect ratios and load inclinations. Current methodologies use *p*-*y* curves, numerical methods, etc. for predicting pile displacements. These methods are not capable of predicting plastic cumulative deformations. The methodology for predicting cumulative cyclic deformations in this paper is recommended as a means for verifying that routine design procedures based on monotonic load capacity calculations lead to tolerable cumulative displacements. From the findings of this research the authors conclude the following:

1. Figure 5.17 and Figure 5.19 to Figure 5.21). The degradation is less pronounced while increasing the number of cycles (i.e. soil resistance approaches an apparent steady-state at about 20 cycles for the vertical cyclic loading and continues to slightly reduce for the lateral cyclic loading). For example, the reduction of

resistance after 10 load cycles is about 41% for the lateral cyclic loading, versus about 33% for the vertical cyclic loading.

2. The normalized resistance a) for the vented test tends to reach the peak load capacity and then drop rapidly because there is no resistance at the base of the caisson, and the vertical capacity is primarily due to internal and external friction (Colliat et al. 1995, 1997). The failure was captured at about 5% *D* for the same reason above (Figure 5.13a). b) for the sealed caissons, the load capacity tends to be somehow constant and then drops. This was likely because the vertical tension capacity for the sealed caisson includes the full bearing capacity of the caisson base and the internal friction capacity (Figure 5.13b-d). The failure was captured at about 20-25% *D*.
3. The calibrated model shows a very good fit between the experimental results and the FE results for the stress at zero plastic strain $\sigma_0 = 0.1\sigma_{max}$ (recommended values 0.1-0.3σ_{max} by Anastasopoulos et al. (2011)), $\alpha = 0.8$, E = C = 300 s_u, ν=0.45, $\gamma =$ (Equation 5.6). Degradation trends predicted by the FE analyses seem to match experimental measurements.
4. Soil resistance predictions in this study using FE model agree well with predictions with plastic limit analysis and a previous numerical within about 1% (Figure 5.9).
5. Applying small, non-uniform, load amplitudes packets to large load amplitudes (Figure 5.2a) shows a continuous increase in the cumulative deformations unlike applying large load amplitude packets to small load amplitudes packets (Figure 5.2b), which show the cumulative displacements sharply increased and

then started to reduce while decreasing the load amplitudes (Figure 5.26-Figure 5.30).

6. The permanent cumulative displacement for the aspect ratio, *L/D*, of 4 is larger than larger aspect ratios of 5 and 6. However, cumulative displacement is sensitive to the aspect ratio of the foundation.
7. The highest permanent displacement for all aspect ratios was at load angle of 20°.
8. Applying small load amplitudes in early loading history (Figure 5.2a) shows a slight increase in the cumulative displacement. The cumulative displacements continued to linearly increase while increasing the load amplitudes (F = 0.38 to 1.0 Fall) to be more sensitive at large load amplitudes (Figs. 27a-d).
9. The loss in the embedment increases by increasing the load angle. There is about 40% loss in embedment between $\psi = 20°$ and 45°. However, the cumulative vertical displacements are sensitive to the inclination load.
10. While numerical studies involving a large number of large amplitude loads may be useful for understanding the effects of certain variables (aspect ratio, load inclination) on cumulative deformations, actual anchors are seldom subjected to such load histories. More realistic simulations involve variable load amplitudes, with relatively few incidences of large amplitude loading.

Future tests are recommended with a large number of cycles for each packet to evaluate cumulative deformation.

9.3. Experimental Measurement of Touchdown Zone Stiffness for SCR in Gulf of Mexico Clay

Single gravity laboratory model tests are performed at Texas A&M University in high plasticity Gulf of Mexico clay to establish Touchdown Zone Stiffness for SCRs. Displacement-controlled loading is used in a series of monotonic and cyclic tests to evaluate rate effects, monotonic penetration resistance, vertical stiffness for displacement amplitudes ranging from 0.02-0.05 *D*, soil stiffness degradation with increasing numbers of load cycles, stiffness recovery during rest periods, and stiffness recovery under prolonged cyclic loading. Significant conclusions include:

1. The increase in bearing factor of monotonic tests due to the rate effects is about 11 to 27%, corresponding to a 15-fold increase in loading rate (Figure 6.8). While the resistance to uplift (suction) is sensitive to loading rate (Figure 6.10), the overall rate effect becomes less significant during cyclic loading primary due to cyclic degradation and erosion occurred during the test (plot (a) and plot (b) of Figure 6.10).
2. Soil resistance to monotonic penetration measured in this study agrees well with predictions from previous studies (Figure 6.9).
3. Soil resistance on a shallowly embedded (0.25 - 1*D*) pipe drops significantly during the first 10 load cycles (Figure 6.12a-c). The degradation is less pronounced at increased embedment depths. For example, the reduction of resistance after 10 load cycles is about 50% for a pipe embedded at 0.25*D*, versus about 40% for a

pipe embedded at a full diameter, 1D. With continued cycling of shallowly embedded pipes, the vertical resistance gradually declines and approaches zero after about 500 cycles for embedment less than 0.5D and 1000 cycles for an embedment equal to 1D.

4. For a deeply embedded (h/D = 2.0) pipe subjected to large amplitude (0.05D) cyclic displacements, soil resistance degrades rapidly (by about 33%) during the first few cycles (Figure 6.12d). After about 60 cycles the soil resistance very gradually decays until it approaches a constant value of about 50% of the original resistance after 1000 load cycles. No detectable erosion occurred during this test.
5. For a small cyclic amplitude Dy_{cyc}/D = 2% at shallow embedment h/D = 0.5, Figure 6.14 shows the pattern of degradation in soil resistance to be similar to that of large amplitude cyclic loading Dy_{cyc}/D = 5% at deep penetration h/D = 2.0. The soil resistance degrades by 30-40% during the first 5-10 cycles. After about 60 cycles the soil resistance degrades very slowly to a non-zero steady-state condition. No detectable erosion occurred during this test.
6. When pause periods are interspersed between packets of large-amplitude (0.05D) cyclic loading (Tests 11a-j, Figure 6.17 and Figure 6.18), the reconsolidation following the rest periods led to a short-term increase the soil secant stiffness and soil resistance that rapidly declines upon resumed cyclic loading; however, the degraded resistance is only slightly greater than the pre-rest period levels. With continued cyclic loading followed by rest periods, the soil stiffness gradually

trends upward. This behavior is believed to be due to the fact that settlement of the pipe is permitted to occur during the rest periods.

When rest periods are interspersed between packets of small-amplitude cyclic loading, $\mathrm{D}y_{cyc}/D$ = 2% (Figure 6.19, Tests 12a-d), there is a small regain in the resistance after the initial rest period. In fact, the soil resistance actually declined during the rest period, likely due to swelling uplift of the pipe. Subsequent rest periods showed increases in soil resistance of 18 and 30%, corresponding to rest periods of 3.5 hours and 16 hours.

9.4. Experimental Measurement of Monotonic and Cyclic Lateral Resistance of Risers and Pipelines in Gulf of Mexico Clays

This paper enhances the state of knowledge for pipe-soil interaction in soft clay with a new set of test data illustrating the complex load-displacement response of both shallowly and deeply embedded pipe segment undergoing small and large amplitude cyclic lateral movements, with periods of consolidation. From the findings of this research the authors conclude the following:

1. A 15-fold increase in penetration rate results in a 15-27% increases in the vertical bearing factor during initial monotonic penetration (Figure 7.7a).
2. Lateral resistance increases with increasing vertical penetration (Figure 7.8a). This study considered embedments w/D = 0.5 and 1, over which range the lateral resistance increased by 34-40%.
3. The initial lateral breakout resistance generally compares well with previous studies (Figure 7.8a).

4. The lateral residual resistance increases with lateral displacement, mainly due to the increasing berm size resulting from the fixed vertical position of the pipe segment.
5. Cyclic lateral movements show rapid degradation (after forming the trench) of the mid-sweep resistance to about 70% and 45% of the soil resistance at embedment depths of 0.5 *D* and 1.0 *D*, respectively (Figure 7.11). Similar behavior occurs when berm resistance mobilizes, but the degradation is less pronounced. This is mainly due to soil softening, removal of the soil from the trench, and consolidation of the soil downward away from the pipe.

Consolidation periods between cyclic loading leads to both strengthening of the soil and settlement of the pipe, leading to increased lateral resistance (Figure 7.14b).

9.5. Cyclic Loading of Pipelines/Risers in Cohesive Soils

Single gravity laboratory model tests are performed at Texas A&M University in high plasticity Gulf of Mexico clay at the Touchdown Zone for SCR to evaluate the lateral resistance of monotonic loading, the lateral cyclic resistance, zig-zag loading, the degradation of the lateral resistance by increasing the number of cycles for both the trenches and the berms, and the strength recovery after releasing the pipe for a period of time. From the findings of this research the authors conclude the following:

1. At the beginning of the series 1, the pipe is embedded into 0.3 *D* and it let to be free under its own weight. The final embedment depth is 1.525, so it sank for about w/D ~ 1.225 at the end of series 2.

2. Soil resistance on a shallowly embedded pipe dropped significantly between the backbone curve and the first load cycle (trench path). The degradation is less pronounced at increased embedment depths.
3. A complete cycle showed a banana shape for lateral (zig-zag) cyclic loading.
4. The resistance at the beginning of the trench (both directions of movements) approached zero (because all the soil swept to the other side during the movements), but it picked up some resistance while moving inside the trench.
5. The trench continued to become wider and deeper because of the zig-zag movement as shown in Figure 8.2 and
6. Figure 8.3.
7. The pipe is covered by a thin layer of muddy soil because of the erosion (scour).
8. The steady-state reached at 15 cycles (Figure 8.11). After that the resistance started to gain some strength while increasing the number of cycles. That is likely because the pipe penetrates deeper into the soil when moving in zig-zag motion.
9. The reduction in soil resistance at the trench path during cyclic loading is greatest at shallow depths and decreases somewhat with increasing penetration (during the zig-zag motion). For example, the resistance reduced by about 70% and 57% for penetration depths 0.3 D and 1.07 D, respectively between the backbone curve and the first load cycle at $u/D = 0.15$. That applies to the entire series 1 and series 2 (Figure 8.4 and Figure 8.8).

10. For the first few cycles, the pipe tended to rise in a manner typical of the behavior of light pipes. With continued cycling, the pipe tended to move downward as shown in Figure 8.7 and Figure 8.12.

Figure 8.12 depicts that the pipe dived deeper during series 1 (Tests 1a-f) than series 2 (Tests 2a-f) due to the increase in strength.